SPINEL COATINGS AND CRYSTAL STRUCTURE OF CU-MN-O

SPINEL COATINGS FOR SOLID OXIDE FUEL CELL INTERCONNECTS AND CRYSTAL STRUCTURE OF CU-MN-O

By
PING WEI, M.A.SC.

A Thesis
Submitted to the School of Graduate Studies
In Fulfilment of the Requirements for the Degree
Doctor of Philosophy

McMaster University
© Copyright by Ping Wei, May 2009

DOCTOR OF PHILOSOPHY (2009) McMaster University
(Departmen of Materials Science and Engineering) Hamilton, Ontario

TITLE: Spinel Coatings for Solid Oxide Fuel Cell interconnects and Crystal Structure of Cu-Mn-O

AUTHOR: Ping Wei, M.A.Sc. (McMaster University)
SUPERVISOR: Professor Anthony Petric
NUMBER OF PAGES: Viii, 152

Abstract

Long-term stability and chromium (Cr) contamination are two major concerns for application of chromium-bearing metallic materials as interconnects of solid oxide fuel cells (SOFCs) at intermediate temperature (~800°C). Copper-manganese (Cu-Mn) and cobalt-manganese (Co-Mn) spinel can be promising coating materials for the metallic interconnects as they show high electrical conductivities. The first objective of this research is to develop an economical and convenient method through which the spinel coatings can be applied to the metallic substrates. The investigations on the crystal structure of $Cu_xMn_{3-x}O_4$ spinel, e.g., structure symmetry and cation distributions, have always been controversial, which hinders the total understanding of the detailed structure of the material. In order to resolve the inconsistency, in-situ neutron and X-ray diffraction were employed to determine the structure of the spinel.

A novel method was developed to obtain high quality manganese coating without any additives (sulphur or selenium compounds). Cu-Mn and Co-Mn spinel coatings were applied to metallic coupons by electrodeposition and subsequent annealing. The method is convenient and easy to control. The performance testing showed that the area specific resistances (ASRs) of the coated samples (0.003 $\Omega \cdot cm^2$) are much lower than that of the uncoated UNS 430 (0.189 $\Omega \cdot cm^2$) after oxidation at 750°C for 1500 hours. Moreover, both spinel coatings can effectively suppress the outward diffusion of Cr, which resulted in reduction of Cr contamination significantly. The oxidation studies of Cu-Mn coating revealed the transformation mechanisms of Cu-Mn coating to the spinel. In-situ neutron and X-ray diffraction analysis clarified the crystal symmetry of $Cu_xMn_{3-x}O_4$ spinel and $CuMnO_2$ at high temperatures. Rietveld refinement revealed the cation distribution of Cu and Mn ions on tetrahedral and octrahedral sites of $Cu_xMn_{3-x}O_4$ spinel, which was compared to values in the literatures.

Acknowledgements

I would like to express my sincere gratitude to my supervisor, Dr. Anthony Petric, for his guidance and support. His help, stimulating suggestions and encouragement helped me in all the time of my research and writing of this thesis. I learn from him not only the knowledge, but also the research spirits.

I also want to thank all the other people who gave me the possibility to complete this thesis, Dr. Mario Bieringer (University of Manitoba), who did in-site X-ray diffraction analysis for me, and Mr. Lachlan M. D. Cranswick (Canadian Neutron Beam Centre), who helped me analyze samples with neutron diffraction and refine the diffraction data. Their efforts and help are really appreciated.

I want to furthermore thank Dr. O. E. Hileman for his valuable advice on the electrochemistry experiments, Dr. I. David Brown, who gave me valuable information about the crystal structure, Dr. James Britten, who gave me permission to use the computers in his lab to do X-ray data analyses and Dr. Shahab Derakhshan for his assistance in doing refinement of the diffraction data. I want to thank Mr. Wenhe Gong for helping me do phase identification of X-ray data, and Mr. Doug Culley, Ed McCaffery, Steve Koprich, Chris Butcher for their timely technical assistance in this project.

I am grateful for the financial support of the Natural Sciences and Engineering Research Council of Canada and the collaboration with Versa Power Systems.

I also would like to thank the colleagues from our group, Dr. Boris E. Martin, Dr. Reza Bateni, Joshua Deng, etc., for their cooperation and valuable help during my research. The service and friendship from the people in the MSE department is greatly appreciated.

Especially, I would like to give my special thanks to my family (my wife, Lili Zhang and my daughter, Emily), my parents and grandmother whose patient love enabled me to complete this work.

Table of Contents

List of Figures

List of Tables

Chapter 1

Introduction

1.1 Background

A solid oxide fuel cell (SOFC) is a complex ceramic device which consists of three main components: an anode, electrolyte and cathode. Only since the 1960s, has the SOFC have been considered as a possible future energy technology due to advances in materials and especially materials chemistry. The voltage obtained from a single cell under load is approximately 1 V. Therefore, it is necessary to connect the cells in electrical series to obtain the output power suitable for commercial use. The interconnect is a component that separates the cells into units but connects them electrically. Over the past several decades, efforts in interconnect development have been primarily focused on the family of compound ceramic oxides with perovskite structure. Only a few such oxide systems can satisfy the rigorous requirements for the interconnect materials in SOFCs. Lanthanum chromite ($LaCrO_3$) doped with strontium, or calcium ($La_{1-x}(Sr,Ca)_xCrO_3$) is the preferred ceramic interconnect material for SOFCs operating above 800°C since it exhibits sufficient electronic conductivity under fuel and oxidant atmospheres, adequate stability in the fuel cell environment, and reasonable compatibility with other cell components. However, this material is difficult to fabricate and deforms due to the loss of oxygen at the fuel side, and the price of precursor powder is high. Another disadvantage of these materials is their poor tolerance to sudden temperature changes. Therefore, high cost and inferior workability of the ceramics are major restrictions in the production of large components.

Since 1990, significant progress has been made toward reducing the operating temperature of SOFCs (below 800°C) while still keeping the same level of performance (Feng 1994; Ishihara 1994; Huang 1998; Huang 1996; Souza 1997). The reduction of SOFC operating temperature enables the use of low cost metallic materials, such as Cr-based, Ni-based and Fe-based alloys as interconnect materials due to their superior electronic and heat conduction, and low cost (Huang 2000; Linderoth 1996). Now, ferritic stainless steel has become the standard for interconnects in solid oxide fuel cells (SOFCs) due to its matching coefficient of thermal expansion, and high resistance to oxidation (Brylewski 2001; Horita 2002; Linderoth 1996). The main problems with these materials are their poor long-term stability and chromium volatility. It has been demonstrated that chromia-forming alloys will form volatile Cr(VI) species under SOFC operating environments (Dulieu 1998; Urbanek 2002), which results in chromium poisoning of the cathode and deterioration of cell performance. Moreover, Cr_2O_3 is a poor conductor with an electrical conductivity of 10^{-1}-10^{-2} S/cm at 800°C (Park 1989; Tsai 1995), and hence the area specific resistance (ASR) of the interconnects and oxide electrodes approaches the tolerance limit for practical SOFCs (Oishi 2000). Therefore, a protective coating for the metallic interconnect, which is also electronically conductive, non-volatile and chemically compatible with other cell components, is the most direct

solution to the problem. Moreover, the protection layer should possess low chromium cation diffusivity and low oxygen ion diffusivity.

Research was carried out on rare earth oxide coatings, such as yttria-silver and praseodymia coatings, for 430 stainless steel interconnects, as part of my masters thesis. The lowest ASR obtained at 750°C after 744 hours was 0.09 $\Omega \cdot cm^2$, but as the coatings were very thin, the outward transport of Cr was not suppressed (Wei 2005). Many studies have been done on perovskite coatings for metallic interconnects (Kim 2004; Zhu 2004; Przybylski 2004; Quaddakers 1996; Yoo 2001). However, the application of perovskite layers is more difficult. Several investigations have shown that a cobalt-manganese spinel coating is an effective barrier to chromium migration, decreasing oxidation and improving electrical conductivity of the cell (Chen 2005; Simner 2005; Larring 2000; Yang 2005).

The primary purpose of this research was to develop an economical and convenient method for developing copper-manganese (Cu-Mn) and cobalt-manganese (Co-Mn) spinel coatings on metallic substrates and to study their performance and properties, e.g., electrical conductivity, oxidation behavior.

Spinel have the general formula AB_2O_4, where A and B are divalent and trivalent cations, respectively. Since the physical properties of a spinel depend not only on the kind of cations in the spinel but also on their distribution within the interstices, it is important to know the cation distribution and its effect on the physical properties. The structure and ionic configuration of $Cu_xMn_{3-x}O_4$ have been studied over a long time as they have exceptionally high electrical conductivity (Kolomiets 1957; Buhl 1969; Verwey 1936; Verwey 1947; Verwey 1954; Stokman 1951; Zaslavskii 1969), but the results are ambiguous. It is accepted that $CuMn_2O_4$ is not a totally normal spinel with inversion degree varying from 12 to 30% as determined by x-ray and neutron diffraction of quenched samples (Aoki 1965; Buhl 1969; Radhakrishnan 1974; Zaslavskii 1969). Recently, the crystal structure of $Cu_xMn_{3-x}O_4$ has been studied in detail due to their high catalytic activity for oxygen reduction as a cathode material (Martin 2007). The quenched samples were analyzed by neutron diffraction. Although some useful information was obtained, the Cu-Mn spinel lattice presents very significant electronic mobility, which renders quenching from elevated temperature impractical. The proposed model provides only a first approximation of the thermodynamic behavior and cation/valence distribution, with thermodynamic parameters for the redox reaction consistent with calculated values. Exact determination of the dynamics of cation site distribution will require in-situ neutron diffraction at elevated temperature.

Another purpose of this research was to investigate the structure, e.g., the cation distribution of Cu-Mn spinel through in-situ neutron diffraction, and determine phase boundaries of the Cu-Mn-O system at intermediate temperatures through in-situ neutron and x-ray diffraction.

1.2 Objectives and organization of the thesis

The objectives of the work are as follows:

1. Develop cobalt-manganese and copper-manganese metallic coatings on UNS 430 stainless steel substrate through a convenient and economical method;
2. Develop a process which can be applied to transform the metallic coatings to the corresponding spinel layers without damaging their integrity;
3. Test the performance of two spinel layers under oxidation conditions;
4. Investigate arrangement of cations and extent of spinel solid solution in Cu-Mn-O through in-situ neutron and x-ray diffraction analyses.

A literature review of the research is included in Chapter 2. Chapter 3 describes the sample preparation procedure for the different experiments. In addition, sample analyses methods, e.g., in-situ neutron and x-ray diffraction, are briefly introduced. Chapter 4 focuses on experimental results and discussion on eletrodeposition, electrical conductivity measurement, and transformation mechanisms of metallic coatings to the spinel. In chapter 5, in-situ x-ray diffraction and neutron diffraction data are analyzed. The Cu-Mn-O phase diagram is re-constructed based on in-situ x-ray diffraction. The crystal structures of $Cu_xMn_{3-x}O_4$ and $Cu_{1+x}Mn_{1-x}O_2$ solid solutions are studied. Cation distribution in $Cu_xMn_{3-x}O_4$ solid solutions is calculated based on in-situ neutron diffraction data refinement.

Chapter 2

Literature Review

2.1 Interconnect materials of Solid Oxide Fuel Cells (SOFCs)

Metallic materials are commonly used for the interconnects of solid oxide fuel cells (SOFCs) at intermediate temperatures. However, the problems with the metallic materials persist, even with decreasing temperatures.

2.1.1 Problems with metallic interconnects

Decreased operating temperature of SOFCs allowed substitution of heat-resistant alloys for ceramic materials as interconnects (Fergus 2005; Yang 2003) and ferritic stainless steels with optimized alloy element additions are considered to be the best candidate materials for the interconnect application, with the following properties (Linderoth 1996; Linderoth 1996; Brylewski 2001; Horita 2002; Kakowaki 1993):

- chemical stability due to the formation of a Cr_2O_3 scale at elevated temperature in air, as well as in H_2-H_2O and H_2-H_2O-H_2S gas mixtures
- thermal expansion coefficient close to that of other cell components, e.g., 10×10^{-6} K^{-1} for YSZ versus $9\text{-}12\times10^{-6}$ K^{-1} for Fe-Cr alloys for temperatures up to 1000°C
- considerably lower cost of fabrication compared with ceramics
- excellent machinability, scale-up feasibility and gas tightness

2.1.1.1 Oxidation behavior of metallic interconnects

The corrosion behavior of ferritic stainless steels under consideration has been studied in air (Young 2001; iffard 2004; Velasco 2004; Horita 2002; Petit 2004; Kurokawa 2004; Yang 2005) and in H_2/H_2O as well as in mixtures containing sulphur, e.g. $H_2/H_2O/H_2S$ at elevated temperatures (Abellan 2002; Przybylski 1999; Brylewski 2001). It was shown that these materials exhibit high oxidation resistance by forming stable chromium oxide on their surface. Once formed, the Cr_2O_3 scale adheres strongly to the metal surface and becomes essentially impermeable to corrosive gases (Wagner 1951). Consequently, this scale can act as a diffusion barrier for oxygen on the cathode interconnect, protecting the alloy from rapid oxidation during operation. Since an oxide layer inevitably forms on the surface of metals in oxidizing atmospheres, the ideal situation is that the metallic interconnect possesses sufficient oxidation resistance over the projected service lifetime (40,000 h) of SOFCs. Ferritic stainless steels are attractive and suitable for interconnects in SOFCs. However, the electrical conductivity of a thermally grown chromia layer is reported to be very low, $\sim10^{-4}\text{-}10^{-5}$ $S \cdot cm^{-1}$ at 750-800°C (Virkar 2000; Armstrong 2005), although other references put the resistivity closer to 10^{-2} $S \cdot cm^{-1}$ (Samsonov 1973; Huang 2001). It has been demonstrated that the

chromia scales on stainless steels can grow to micrometers or even tens of micrometers after thousands of hours in the SOFC environment, which increases the overall cell resistance and consequently causes unacceptably high degradation rates in SOFC stack performance (Abellan 2002; Honegger 2001; Huang 2000; Brylewski 2001; Zhu 2003; Yang 2003). As a rule of thumb, an area specific resistance (ASR) value of 0.1 $\Omega \cdot cm^2$ is considered to be the acceptable upper limit for fuel cell operation (Zhu 2003). Therefore, an improvement in electronic conduction of the oxide scale is required.

2.1.1.2 Chromium contamination

Although the evidence suggests that it is possible to increase the electrical conductivity of Cr_2O_3 through doping with other elements, other concerns remain with ferritic stainless steels such as their long-term stability and compatibility issues, which are related to Cr volatility. Under cathodic conditions, volatile Cr (VI) species are generated from the Cr_2O_3 layer (Dulieu 1998; Greiner 1995; Urbanek 2000; Kofstad 1996; Kock 1995):

$$2Cr_2O_3(s) + 3O_2(g) \leftrightarrow 4CrO_3(g) \quad (2.1)$$

$$2Cr_2O_3(s) + 3O_2(g) + 4H_2O(g) \leftrightarrow 4CrO_2(OH)_2(g) \quad (2.2)$$

$$Cr_2O_3(s) + O_2(g) + H_2O(g) \leftrightarrow 2CrO_2OH(g) \quad (2.3)$$

All of the above processes are reversible, and therefore, the high-temperature oxidation of chromia-forming alloys indeed involves both scale formation and volatilization of oxides and oxyhydroxides. The electrochemical performance of SOFCs is severely deteriorated by the presence of gaseous chromium oxides and chromium oxyhydroxides at the cathode side of the fuel cell. Furthermore, over long-term exposure during SOFC operation, the oxide layer on ferritic stainless steel may react with the $LaMnO_3$ cathode and thus reduce the performance of the stack. Indeed, it was found that during thermal exposure, a duplex outer layer scale of Mn-Cr spinel and Cr_2O_3 inner layer were formed by interaction of stainless steel with the $LaMnO_3$ component (Ueda 2000; Quadakkers 2000). The Cr_2O_3 deposition at the interface between the $La_{0.85}Sr_{0.15}MnO_3$ (LSM) and the YSZ electrolyte causes an increase in both concentration and activation polarization (Matsuzaki 2000). For example, Cr species that evaporate from the steel at operating temperatures poison the electrode performance, in particular the oxygen reduction reaction at the cathode. Moreover, the electrical resistance of Cr_2O_3 is proportional to its thickness, and the ASR (area-specific resistance) of bare alloy with oxide electrodes approaches the tolerance limit for practical SOFCs quickly (Oishi 2000). Until recently, chromium-bearing metallic interconnects could only be applied to SOFCs operating below 700°C (Brylewski 2001).

2.1.2 Possible solutions for metallic interconnects

In order to improve the conductivity and suppress growth of Cr_2O_3 scale, many researchers have tried doping Cr_2O_3 with different elements, e.g., Fe_2O_3 (Footner 1967), La_2O_3, Y_2O_3 and NiO (Nagai 1983) , CoO (Saprykin 1997; Zhu 2003), Gd_2O_3, Sm_2O_3

(Nagai 1985), MgO (Holt 1997), and TiO_2 (Holt 1999). The doped materials did increase the electrical conductivity of Cr_2O_3 to a certain extent. However, doping still cannot solve the problem of gaseous chromium species evaporation.

Another approach is to design new alloys or hybrid interconnect materials with improved performance over the present ferritic stainless steels. Although development of new alloys is costly, some work is still under way. Manganese has been used as an alloying addition in several newly developed ferritic compositions (Abeilan 2001; Horita 2003; Quadakkers 2000). One such alloy is Crofer22 APU, a commercially available Fe-Cr-Mn steel developed specifically for SOFC applications. Simner et al. (2005) studied SOFC performance with this alloy as the cathode current collector at 750° C. Three cathodes were tested: $(La_{0.8}Sr_{0.2})_{0.99}MnO_3$, $(La_{0.8}Sr_{0.2})_{0.99}FeO_3$, and $(La_{0.6}Sr_{0.4})_{0.98}Fe_{0.8}Co_{0.2}O_3$. The results showed that the use of Crofer22 alloy as cathode current collector resulted in severe performance degradation at 750°C for the three cathode materials due to Cr poisoning. The mechanisms could be attributed to Cr volatilization and recondensation throughout the cathode, and/or solid-state reaction of the Cr-containing oxide scales with the adjacent cathode.

An alternative method to reduce the oxidation kinetics of metallic interconnects and suppress the loss of Cr through evaporation is the application of protective coatings. The coatings should be dense, electronically conductive, non-volatile and chemically compatible with other cell components at operating temperatures and atmospheres, have high electronic conductivity and slow ionic diffusion to reduce oxidation kinetics. Two classes of materials that are thermodynamically stable, bond well to metals, and exhibit acceptable conductivity are spinel and perovskite phases containing transition metal elements (Armstrong 2005). Many studies have been done based on this concept (Armstrong 2005; Larring 2000). Some La-based perovskite conducting thick films, e.g., $(La,Sr)CoO_3$ and $(La,Ca)CrO_3$ films, due to their high electronic conductivity, thermal expansion match and a relatively high chemical stability at 923–1173 K (Abellan 2002; Przybylski 2000; Przybylski 1999; Minh 1995; Brylewski 2003; Brylewski 2001), have been popular candidates.

Przybylski et al. (2004) studied La-based perovskite thick films, $(La,Sr)CoO_3$ and $(La,Ca)CrO_3$, on Fe-25Cr steels, and found that the ASR value of the tested Fe-25Cr steel coated with the La-based perovskites did not exceed the value of the currently applied commercial ceramic interconnect based on lanthanum chromium doped with strontium, and is relatively stable at 800°C in air. The maximum testing time during the studies was less than 300 hours. Research on different coatings of mainly $LaCoO_3$ and $LaCrO_3$ perovskites has been done in order to reduce the chromium evaporation (Batawi 1999; Schmidt 1995; Badwal 1997; Quadakkers 1996; Quadakkers 1996). These layers may reduce the resistance between the cathode and interconnect by increasing the contact area. However, interdiffusion of cations through the layers and formation of new interfacial layers may cause long-term problems. Zhu et al. (Zhu 2004) investigated the feasibility of depositing a thin, dense, conductive $LaCrO_3$-based coating on ferritic stainless steel using different methods. The results showed that the sol–gel coatings improved the oxidation resistance and scale adhesion of the alloy substrate after cyclic oxidation in air at 800°C, and the coated samples showed much lower electrical resistance compared to

the uncoated samples after similar thermal exposure for 100 h at 850°C. Kim et al. (2004) investigated the effect of $(La_{0.85}Sr_{0.15})_{0.9}MnO_3$ (LSM) coating on the electrical conductivity of SUS 430 stainless steel in air at 750°C. The LSM-coated UNS 430 was heat-treated in air at 1000°C after sintering, and maintained an almost constant ASR value of 0.074 $\Omega \cdot cm^2$ for 2600 h. Larring and Norby (2000) investigated the spinel and perovskite functional layers between Plansee Ducrolloy alloy Cr-5wt%Fe-1wt%Y_2O_3 (Plansee) and ceramic $(La_{0.85}Sr_{0.15})_{0.91}MnO_3$ cathode materials by means of electrical resistance measurements at 900°C in air humidified with 2% H_2O and with a dc load of 100 mA/cm^2. Their results showed that one sample of Plansee alloy with plasma-sprayed $La_{0.9}Sr_{0.1}CrO_3$ and a contacting layer of $La_{0.8}Sr_{0.2}CoO_3$ exhibited little degradation, estimated to be 0.066 $\Omega \cdot cm^2$ after 10,000 h. Coatings forming $MnCr_2O_4$ spinel and using $La_{0.8}Sr_{0.2}CoO_3$ as a contacting layer showed a low estimated degradation of 0.04-0.06 $\Omega \cdot cm^2$ after 10,000 h. Another spinel $(Co,Mn)_3O_4$ layer which is dense and adheres well to the Plansee alloy surface appeared to reduce Cr diffusion significantly, and when used together with a mixed perovskite made of 1:1 LSM and $La_{0.8}Sr_{0.2}CoO_3$ as a contacting layer, exhibited an estimated ASR of 0.024 $\Omega \cdot cm^2$ after 10,000 h.

It can be seen from many studies that perovskite coatings on metallic interconnects do lower the interfacial contact resistance, but cell performance may still be degraded by gaseous chromium contamination. Moreover, perovskite overlay coatings can have a thermomechanical stability problem during thermal cycling due to poor adhesion and/or coefficient of thermal expansion mismatch (Yang 2005). Rare earth oxide coatings, e.g., yttria-silver and praseodymia coatings, have been tried and the performance of coated samples did show better performance than bare ones, but the thin layer could not suppress outward diffusion of chromium (Wei 2005).

It was originally suggested by Larring and Norby that spinel such as $MnCo_2O_4$ could be promising coating materials for metallic interconnects (Larring 2000). Simner et al. (2005) investigated long-term performance of anode-supported thin-film YSZ-based SOFCs utilizing a ferritic stainless steel cathode current collector (Crofer22 APU) coated with a protective $(Mn,Co)_3O_4$ spinel to prevent Cr volatilization. Two kinds of cathode materials were used: La(Sr)FeO_3 (LSF) and La(Sr)MnO_3 (LSM). The results showed that $Mn_{1.5}Co_{1.5}O_4$ coating effectively mitigated Cr volatilization even at 800°C over long time periods (1000 h) when LSM cathodes were used. For LSF cathodes, rapid degradation was observed but the mechanism was not investigated. Chen et al. (2005) used a Mn-Co-O spinel coating on a 430 stainless steel in order to slow down the chromia scale formation. Their experiments showed that the area specific resistance (ASR) of uncoated UNS 430 at 800°C for 180 h was about one order of magnitude higher than those of the coated samples. The ASR for the coated sample, initially oxidized for 60 h at 800°C, followed by an additional cyclic oxidation at 850°C for 120 h, is as low as 2.5×10^{-3} $\Omega \cdot cm^2$, which is the lowest value obtained so far for coated UNS 430 at 850°C. By modeling, they predicted an ASR of approximately 0.5 $\Omega \cdot cm^2$ after 50,000 h in air at 850°C.

Recent research on spinel systematically studied the conductivity and thermal expansion coefficients of the possible candidates, namely, those containing divalent and trivalent cations. Based on research of manganite, ferrite, aluminate, and chromite

transition metal spinel systems (Hang 2005; Petric 2007), several were particularly attractive due to their relatively high electrical conductivity and matching TEC, namely, $Co_xMn_{3-x}O_4$ and $Cu_xMn_{3-x}O_4$. The conductivities of $Co_xMn_{3-x}O_4$ and $Cu_xMn_{3-x}O_4$ are shown in Fig. 2.1 and 2.2 (Martin 2007). It can be seen that these two materials have quite high conductivities in the SOFC operating temperature range. Studies on Co-Mn spinel coatings have demonstrated that the coating can effectively stop chromium migration, decrease oxidation and improve electrical conductivity of the cell (Chen 2005; Simner 2005; Larring 2000; Yang 2005). Therefore, these materials could be candidate materials for coatings on metallic interconnects.

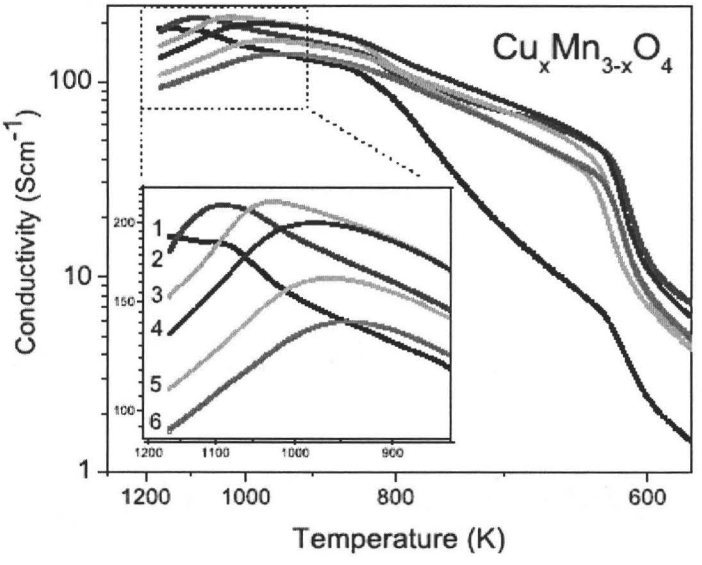

Figure 2.1 Electrical conductivity of $Cu_xMn_{1-x}O_4$ in air: (1) x = 1.08, (2) x = 1.19, (3) x = 1.28, (4) x = 1.47, (6) x = 1.58 (Martin 2007)

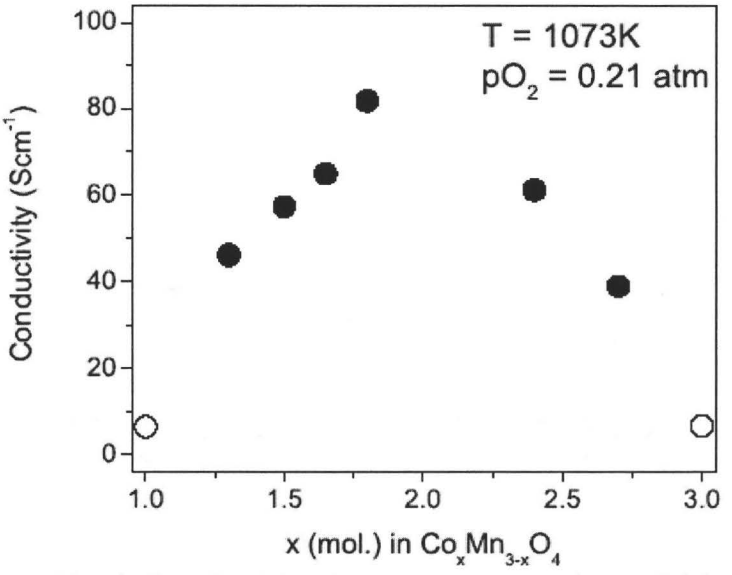

Figure 2.2 Electrical conductivity of $Co_xMn_{3-x}O_4$ at 800 degree Celsius in air (Martin 2007)

2.2 Electrodeposition of metallic coatings

Many methods have been tried to form protective oxide coatings for metallic interconnects, e.g., pulsed injection metal organic chemical vapor deposition (Burriel 2005), slurry coating (Kim 2004; Yang 2005), screen-printing (Przybylski 2004), thermal spray (Schiller 2000), reactive formation and sol-gel coating (Zhu 2004), etc., and the coated samples showed better performance than uncoated ones. Although these methods showed some success, they also had some drawbacks, e.g., the process itself is hard to control, a special experimental set-up is needed, and applying coatings to a surface with intricate shape is difficult. The electroplating method is attractive because it is a very mature technology, easy to control and economical. Moreover, it can be applied to parts with complicated shape, which can be the case for metallic interconnects. However, electroplating is simpler for metallic coatings than oxide coatings but metallic coatings can be converted to oxides afterwards, as will be described later.

As described above, Cu-Mn and Co-Mn spinel have some promising features as interconnect coatings and can be applied by electrodeposition of metallic layers. Electrodeposition of alloys is well known, and the most important practical consideration involved in the codeposition of two metals is that their deposition potentials be fairly close together. As the first step, the difference in electrochemical potential can be used as an approximate (rough) estimate of the difficulty of codeposition. However, equilibrium potential merely indicates the energy change that accompanies a reaction and it does not define the conditions under which the reaction can occur. The equilibrium electrode potentials of Mn/Mn^{2+}, Cu/Cu^{2+} and Co/ Co^{2+} are – 1.18 V, 0.337 V and –

0.277 V respectively (Brenner 1963). Clearly there is a large difference between Mn and Cu equilibrium potentials, and Mn and Co equilibrium potentials. According to the Nernst equation at 25°C:

$$E = E_0 - \frac{0.059}{n} \lg \alpha \quad (2.4)$$

where n is the number of equivalents per mole, and α is activity of the ion. Changes in the equilibrium potential of a metal are proportional to the log of the activity of the ion in solution. A hundred-fold decrease in the concentration of a divalent salt of the more noble metal would make the potential of the electrode only about 0.06 V more negative. Furthermore, the use of a dilute solution of the more noble metal in an alloy bath is impracticable, as when the concentration of the more noble metal is less than 1% that of the other, the concentration changes so rapidly during deposition that alloys of reproducible composition can not be obtained. In reality, many electrodeposited metals are obtained from solution in which the metal is present in the form of a complex, known as a chelating agent, instead of in the form of simple ions. The big advantage of baths of complex ions for alloy plating is that, in such baths, it is possible to bring the electrode potentials of metals closer together, which makes codeposition feasible. However, real application of alloy electrodeposition is very difficult in fact, and control of the composition of the alloys is almost impossible. Electrodeposition of alloys requires much practical knowledge of the electrochemistry of the elements, the solubility of their salts and the chemistry of their complexes. Due to the lack of quantitative guiding principles, a large number of tests might be needed. Moreover, a large portion of the alloy plating procedures in the literature is of no practicable value because they only yield very thin deposits of the alloy (Brenner 1963), to say nothing of quantitatively controlling alloy composition. Based on this information, the coating approach selected was to electroplate Mn, Co and Cu separately.

2.2.1 Electrodeposition of manganese

In electroplating, normally, aqueous solutions containing chemical compounds of the metals to be deposited, and having good electrical conductivity, are used for the electrodeposition of metals. It is well known that Mn is the most electronegative metal that can be electrodeposited from aqueous solution. Research on electrodeposition of Mn and its alloys began half a century ago (Oaks 1936;Dean 1952; Bradt 1937), and most of the literature is concerned with practical issues in electrowinning of Mn (Araujo 2006; Mantell 1967; Coleman 1984; Harris 1977; Ilea 1997; Iwasaki 1968; Mantell 1966; Mantell 1969; Mitsui Mining and Smelting Co. 1982; Reynolds 1983; Tilak 1962). Recently, research on the electrodeposition of Mn using modern electroanalytical techniques has been reported (Gong 2002; Gonsalves 1990). Normally, Mn deposition can be obtained through the use of Mn sulfate and chloride, together with corresponding ammonium salts (Mantell 1967; Oaks 1936; Lewis 1976; Lewis 1976; Díaz-Arista 2006; Dean 1952). The addition of ammonium sulfate to the Mn electrolyte can prevent

precipitation of Mn hydroxides during electrodeposition and improves the conductivity of the solution (Oaks 1936; Dean 1952). It was reported that ammonium salts can be used to suppress precipitation of manganous hydroxide even when the pH value of manganous salt solutions is raised to about 9 in the absence of air. In the presence of air, the solution becomes gradually unstable due to the precipitation of Mn hydroxide when its pH is above 6.5 (Gong 2002). Moreover, the buffering effect of ammonium sulphate at various Mn concentrations was also demonstrated. It was believed that the presence of NH_4^+ appeared to increase the difficulty with which hydrogen ions are discharged (Dean 1952). Recent research showed that ammonium sulfate increases Mn ion discharge ability and provides a desirable buffering effect at pH 2-3.5 and 6-7, and the presence of ammonium sulfate is essential to grow Mn coatings with good coverage (Gong 2002).

Although much has been published in this field, it is difficult to obtain Mn coatings with uniform quality from readily available reagent grade chemicals at the laboratory scale. Mn metal deposition is very sensitive to any amount of impurity. Impurities of different metallic ions and evolution of hydrogen lower the current efficiency by about 50 percent (Murti 1986). The impurities having the more detrimental effect are Fe, Co, Ni, Sb, As and Cu. It is believed that the deleterious impurities show low hydrogen overpotential in basic medium, and contribute to high hydrogen gas release and low current efficiency of the process (Araujo 2006). Normally, acceptable Mn coatings can be obtained by adding controlled levels of sulfur or selenium compounds as additives. In general, these additives increase current efficiency, and decrease the deleterious effects of the impurities. According to the literature (Lewis 1976), high cathode current efficiencies (85-90%) can be obtained at selenium levels of 0.03-0.06 g/L. However, the application of the additives leads to contamination of the Mn metal product (Ilea 1997; Gamburg 1999). Although selenium additives are more effective than sulfur compounds (Lewis 1976), the advantages of using selenium compounds are countered by the danger of selenium inclusion in the product at significantly higher levels than sulfur levels. These substances in the Mn deposits definitely decrease corrosion protection. Moreover, these additives are toxic and dangerous to the environment. Therefore, it was necessary to develop a new method for depositing high quality Mn coatings at room temperature without the use of additives.

2.2.2 Electrodeposition of cobalt

Electrodeposition of iron-group metals (iron, cobalt, nickel) has been studied for a long time (Cui 1990; Dille 1997; Floate 2002; Gomez 2002; Jartych 2002; Jartych 2001; Meguid 2003; Pradhan 2001; Sasaki 1998; Schindler 1997) and focused mainly on development of thin films (< 1 um). For application of thick coatings (at least several microns) following the procedures described in the literature, spallation and detachment of the deposit occurred in my preliminary tests. Therefore, it was necessary to develop a new approach for Co electroplating.

2.3 Transformation of metallic coatings to spinel

In order to transform metallic coatings to the spinel, oxidizing them at high temperature was necessary. Up to now, there is no literature in this field and there are few papers reporting oxidation behavior of Co-Mn alloys and Cu-Mn alloys.

Gesmundo et al. (1979) studied the oxidation of Co-Mn alloys in the range up to 48 at % Mn at 750-950°C and found that the phases formed in the scale and the cation concentration was dependent on oxidation time. The formation of a continuous layer of spinel would be favored on the more Mn-rich alloys. Narita et al. (1987) investigated oxidation of Co-Mn at higher temperatures (1000-1200°C), and found that when the spinel $(Co,Mn)_3O_4$ is continuous and parallel to the alloy-scale interface, it can cause a significant reduction in the parabolic rate constant of the oxidation curve, which can be attributed to a blocking effect of cation diffusion in spinel. Decreased temperature and increased oxygen pressure promote the formation of spinel oxides (Ansel 1993; Gesmundo 1979; Nanni 1978; Narita 1987). The Cu-Mn-O system has some interesting features: both metals can form more than one oxide; Cu and Mn oxides are mutually soluble to some extent. Therefore, the oxidation behavior of Cu-Mn alloys is complex. Ansel et al. (1993) studied the oxidation behavior of Cu-Mn alloys (Mn content less than 40 at%) in the range of 600-850°C in pure oxygen. They also found that Cu-Mn spinel formed more easily at higher Mn concentration and higher temperatures.

As little research has been done in the field, the oxidation behavior of Cu-Mn and Co-Mn alloys are still not well depicted, but we have some idea about the conditions under which spinel scales could form: high Mn concentration and intermediate temperature. For this thesis, the target compositions of Cu-Mn spinel and Co-Mn spinel are 43 at% Cu and 58 at% Co (the spinel with these compositions give high electrical conductivities), which clearly meet the needs of composition requirements for the formation of spinel scales.

2.4 Crystal structure analyses

2.4.1 Crystal structure of Cu-Mn spinel

Spinel is a large class of compounds isotypic with the mineral spinel $MgAl_2O_4$. The most common oxide spinel have the general formula AB_2O_4, where A and B are divalent and trivalent cations, respectively. The crystal structure of spinel was determined independently by Bragg(Bragg 1915) and Nishikawa(Nishikawa 1915). The majority of spinel compounds belong to the space group Fd3m. The ideal "normal" structure can be thought of as being based on a cubic close-packed array of oxide ions, with A^{2+} ions occupying tetrahedral holes and B^{3+} ions occupying octahedral holes. The primitive unit cell is illustrated in fig. 2.3; it is broken into eight octants, of which there are only two kinds, shown on the left. When compounds of general formula AB_2O_4 adopt the "inverse" structure, half of the B^{3+} ions now occupy tetrahedral sites, and the remaining half, together with the A^{2+} ions, occupy the octahedral sites. These materials

have found a wide and increasing application as oxidation catalysts and oxide electrode materials.

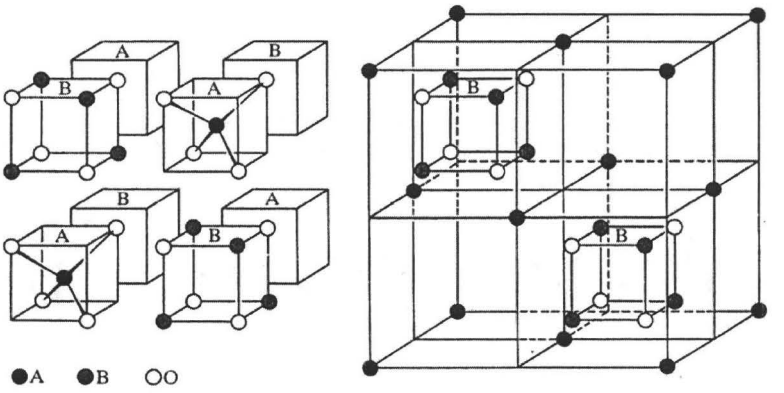

Figure 2.3 Spinel structure

$CuMn_2O_4$ is a spinel that is not well known but has interesting physical and crystallographic properties (Brabers 1973; Fierro 2006; Gillot 1997; Gillot 1991; Radhakrishnan 1977; Vandenberghe 1976; Vandenberghe 1976; Waskowska 2001). Copper and manganese oxide based catalysts were proposed for the removal of air pollutants like carbon monoxide and nitrous oxides from exhaust gas (Broemme 1985; Fierro 2006). Moreover, Cu-Mn spinel has high catalytic performance for steam reforming of methanol (Papavasiliou 2005). It is also known that Cu-Mn spinel exhibits high electrical conductivity (~ 200 $S \cdot cm^{-1}$@ 1073K), and its catalytic activity for oxygen reduction is comparable to that of lanthanum manganese perovskite (LSM) and stoichiometric $CoFe_2O_4$ and Co_2MnO_4 spinel at intermediate temperature, which make it a promising cathode material for SOFCs (Martin 2007). Interesting physical and crystallographic properties were expected in view of the presence of two kinds of Jahn-Teller (J-T) ions in these materials, e.g., Mn^{3+} and Cu^{2+}. In systems containing two types of Jahn-Teller ions, their interaction makes it difficult to predict the structure type as a function of temperature and Jahn-Teller ion concentration. Moreover, the possible presence of copper and manganese ions in different oxidation states (Cu^{+}, Cu^{2+}, Mn^{2+}, Mn^{3+}, Mn^{4+}) with different site preference energies makes the situation more complicated. Therefore, investigation of the cation oxidation state and site distribution in Cu-Mn spinel is crucial from the point of view of understanding the detailed structure of the materials.

Sinha et al. (1958) first reported that $CuMn_2O_4$ has the "normal" spinel structure with cubic symmetry. Ghare et al. (1968) proposed that at low temperature the ionic configuration is close to $(Cu^{+})[Mn^{3+}Mn^{4+}]O_4$ and it changes to $(Cu^{2+})[Mn_2^{3+}]O_4$ at temperatures greater than 600 K, where the symbols in parentheses refer to tetrahedral (A) sites and those in brackets represent octahedral [B] sites of the spinel structure. They mentioned that the change of the ionic configuration was due to a transformation $Cu^{1+} + Mn^{4+} \rightarrow Cu^{2+} + Mn^{3+}$ taking place at 600 K. Miyahara (1961, 1962) also

reported that copper manganite has cubic symmetry but they only proposed a formula $(Cu^{2+})[Mn_2^{3+}]O_4$. They explained the cubic structure as arising from two opposing effects, namely, the distortion with c/a>1 due to Mn^{3+} ions at B-sites compensated by an opposing distortion with c/a<1 caused by Cu^{2+} at the A-sites, with the result that the macroscopic structure remains cubic. However, other authors reported that $CuMn_2O_4$ with cubic structure could not be prepared (Blasse 1966; Buhl 1969), and Buhl (1969) obtained the compound only with tetragonal structure by quenching from temperatures between 750-940°C.

The investigations on the cation valences and cation distribution of copper manganese spinels are also controversial. Bhandage et al. (1975) studied the magnetic susceptibility and electrical conductivity of the $Cu_xCd_{1-x}Mn_2O_4$ system. Based on magnetic behavior and high electrical conductivity of $CuMn_2O_4$, they proposed the following configuration for $CuMn_2O_4$:

$$(Cu^{+}_{1-y-z}Cu^{2+}_{z}Mn^{3+}_{y})[Cu^{2+}_{y}Mn^{3+}_{1+z}Mn^{4+}_{1-y-z}]O_4 \quad (2.5)$$

where y ~ 0.30 and z ~ 0.10. Kshirsagar et al. (1971) studied several manganites through electrical resistivity measurements, and suggested that $CuMn_2O_4$ has the following cation distribution:

$$(Cu^{+}_{z}Cu^{2+}_{1-z})[Mn^{4+}_{z}Mn^{3+}_{2-2z}]O_4 \quad (2.6)$$

where $0 < z < 0.1$. Gillot et al. (1991; 1997) investigated $Cu_xMn_{3-x}O_4$ ($0 < x < 1$) solid solutions through thermogravimetry measurements, infrared spectrometry and electrical property measurements based on the samples quenched to room temperature after annealing in the temperature range of 900-1250°C for several hours and proposed the following cation distributions for $Cu_xMn_{3-x}O_4$ solid solutions for $x < 0.6$ (2.7) and $x > 0.6$ (2.8):

$$(Cu^{+}_{x}Mn^{2+}_{1-x})[Mn^{3+}_{2-x}Mn^{4+}_{x}]O_4 \quad (2.7)$$

$$(Cu^{+}_{x-y}Mn^{2+}_{1-x+y})[Cu^{2+}_{y}Mn^{3+}_{2-x-y}Mn^{4+}_{x}]O_4 \quad (2.8)$$

where y represents a low value (less than 0.2). Vandenberghe et al. (1976) studied $Cu_xMn_{3-x}O_4$ solid solutions and some similar Cu and Mn containing spinel through X-ray, thermal expansion measurements, infrared absorption and magnetic measurements. They believed that the ionic distribution over tetrahedral and octahedral sites can change at temperatures above 300°C through reactions (2.9) and (2.10):

$$Cu^{+}_{tetr} + Mn^{4+}_{oct} \Leftrightarrow Cu^{2+}_{oct} + Mn^{3+}_{tetr} \quad (2.9)$$

which shifts to the right at higher temperatures, and

$$Mn^{3+}_{tetr} + Mn^{3+}_{oct} \Leftrightarrow Mn^{2+}_{tetr} + Mn^{4+}_{oct} \quad (2.10)$$

which shifts to the right for the manganese rich compounds. Based on the above reactions, they proposed the following formula:

$$(Cu_{\alpha}^{+}Mn_{1-\alpha-\beta}^{3+}Mn_{\beta}^{2+})[Cu_{x-\alpha}^{2+}Mn_{3-2x-\beta}^{3+}Mn_{x+\alpha+\beta-1}^{4+}]O_4 \qquad (2.11)$$

for the ionic configuration in the $Cu_xMn_{3-x}O_4$ system, and the parameters α and β in the expression described by the equilibria of the two reactions. Radhakrishnan et al. (1977) studied $CuMn_2O_4$ through neutron diffraction and proposed the following ionic formula:

$$(Cu_{0.5}^{2+}Cu_{0.25}^{+}Mn_{0.25}^{3+})[Cu_{0.25}^{2+}Mn_{1.50}^{3+}Mn_{0.25}^{4+}]O_4 \qquad (2.12)$$

They believed that the high conductivity of the compound represented the presence of Mn^{4+} ions in the system. The presence of Mn^{4+} ions in turn produces an equivalent amount of Cu^{+} ions in order to keep the charge balanced. The only way to place these ions without violating the concept of site preference is to allow Cu^{+} ions to co-exist on the tetrahedral sites along with Cu^{2+} ions, while Mn^{4+} ions coexist with Mn^{3+} on the octahedral sites (Radhakrishnan 1977).

Dubrovina et al. (2001) recently studied the $Cu_xMn_{3-x}O_4$ system through high temperature X-ray diffraction, and found that the samples with x=0.5, 0.75, and 1.0 have the cubic spinel structure at 900°C in air. However, quenching in air gave rise to tetragonal distortion with c/a>1 (Dubrovina 1981), which is consistent with the previous result on quenched samples (Broemme 1985; Buhl 1969; Kharroubi 1991; Vandenberghe 1973). Taking into account both the site preference energy of each ionic species and the electroneutrality condition, they proposed an ionic configuration:

$$(Cu_{a}^{+}Cu_{b}^{2+}Mn_{1-a-b}^{2+})[Cu_{x-a-b}^{2+}Mn_{2(1-x)+a+2b}^{3+}Mn_{x-b}^{4+}]O_4 \qquad (2.13)$$

As the oxygen deficiency in the system is fairly low (Dubrovina 1981), only slightly greater than the average standard deviations (± 0.02) in the a and b parameters, it is ignored in the expression. They suggested that the combination of competitive effects of Jahn-Teller ions from tetrahedral and octahedral sites and thermal disordering might play a key role in determining the equilibrium structure of $Cu_xMn_{3-x}O_4$ solid solutions. In the absence of thermal disordering, the competing cooperative effects on tetrahedral and octahedral sublattices decide the structure of the solid solutions, e.g., quenched samples (Dubrovina 2001). Maunders et al. (2008) investigated the electronic structure of $Cu_{1.2}Mn_{1.8}O_4$ based on quenched samples by using electron energy loss spectroscopy. They determined the Mn components to be 55% Mn^{4+}, 37% Mn^{3+} and 8% Mn^{2+} and Cu to be present as Cu^{2+}, but they did not find any detectable Cu^{+} component. Dorris et al. (1988) studied electrical properties and cation valency in Mn_3O_4, and found the high electrical conductivity could be well explained by the following disproportionation reaction (2.14), and conduction between octahedral Mn^{4+} and Mn^{3+} by means of electron holes:

$$2Mn^{3+} \leftrightarrow Mn^{2+} + Mn^{4+} \qquad (2.14)$$

Moreover, they proposed a structure for divalent substituted manganites NMn_2O_4:

$$(N^{2+}_{1-y}Mn^{2+}_{y})[N^{2+}_{y}Mn^{2+}_{z-y}Mn^{3+}_{2-2z}Mn^{4+}_{z}]O_4 \qquad (2.15)$$

Waskowska et al. (2001) studied $CuMn_2O_4$ and found that the compound had cubic symmetry. Cu ions were present in two valence states, Cu^{2+} and Cu^{+}, in $CuMn_2O_4$ based on X-ray photoelectron spectroscopy (XPS). They explained the observed symmetry as being due to a spin superexchange process via the common O^{2-} ion linking the tetrahedral-site (A-site) cation to the octahedral-site (B-site) cation in the spinel structure: $Mn^{3+}_{A} - O^{2-} - Mn^{3+}_{B} \rightarrow Mn^{2+}_{A} - O^{2-} - Mn^{4+}_{B}$. The replacement of Mn^{3+} by the JT inactive Mn^{2+} and Mn^{4+} decreases the fraction of Jahn-Teller ions at the octahedral sites to a level below the critical amount of about 55%, which is necessary for tetragonal distortion. They proposed the following ionic configuration for $CuMn_2O_4$ at normal pressure, assuming the interaction $Cu^{+}_{letr} + Mn^{4+}_{oct} \Leftrightarrow Cu^{2+}_{oct} + Mn^{3+}_{letr}$:

$$(Cu^{+}_{0.2}Mn^{2+}_{0.8})[Cu^{2+}_{0.8}Mn^{3+}_{0.2}Mn^{4+}_{1.0}]O_4 \qquad (2.16)$$

It is clear that above investigations give conflicting results for the crystal structure, the cation distribution among octahedral and tetrahedral sites and especially the valences of Cu and Mn in copper manganite (Broemme 1985; Gillot 1997; Lenglet 1985; Radhakrishnan 1977; Vandenberghe 1973). These differences might arise from the fact that spinel structure is very versatile and hence features like stoichiometry, cation oxidation state and site distribution are strongly dependent on the preparation method, sintering temperature, sintering time and subsequent treatments (Vandenberghe 1973). Therefore, in-situ analyses at high temperatures is necessary to clarify the ionic configuration of $Cu_xMn_{3-x}O_4$ solid solutions. However, a precise determination of the degree of inversion by X-ray diffraction is difficult because of the similarity of the scattering factors of Cu and Mn atoms. Neutron diffraction is more appropriate as Cu and Mn have neutron scattering lengths of opposite sign [b(Cu) = 0.76×10^{-12}, b(Mn) = -0.36×10^{-12} cm] (Vandenberghe 1976) to obtain the precise Cu and Mn distribution and other crystallographic parameters aided by Reitveld structure refinement. In this study, in-situ neutron diffraction was used to determine the structure of the $Cu_xMn_{3-x}O_4$ system at high temperatures.

2.4.2 Cu-Mn-O phase diagram

The phase equilibrium in the Cu-Mn-O system in air above 750°C has been studied by Driessens and Rieck (1967) (fig. 2.4). They found that a cubic spinel could be prepared if an excess of copper was used. It was deduced that on the manganese rich side of $CuMn_2O_4$ ($x < 1$), the cubic spinel structure is stable at high temperatures (> 900°C). On the copper rich side ($x > 1$) the stability area becomes narrow and falls with

increasing Cu composition. Vandenberghe et al. (1973) studied the stability range of the cubic spinel structure below 700°C through more reactive mixtures of Cu and Mn hydroxides prepared by coprecipitation (fig. 2.5). They found that quenched single phase specimens were tetragonal at room temperature for $x<1.06$, and cubic for $x\geq1.06$. Clearly, the stability range of the spinel structure for compositions $x > 1$ obtained by Vandenberghe el al. (1973) is much larger than that reported by Driessens and Rieck (1967).

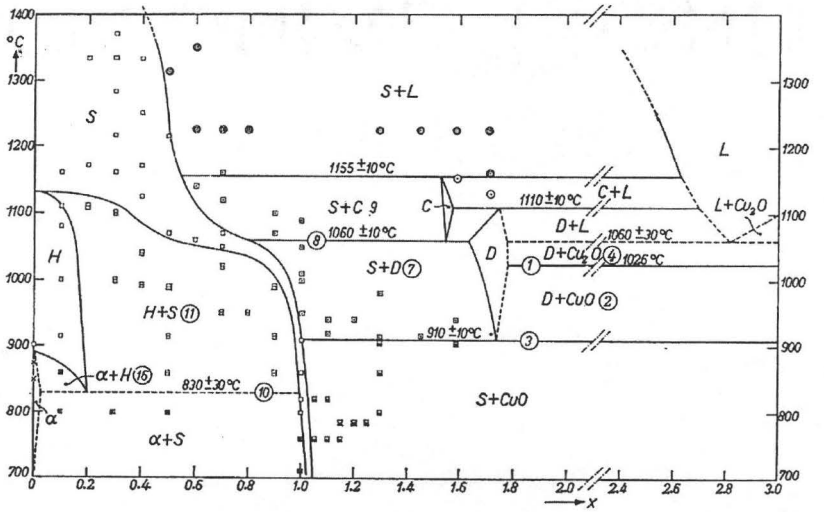

Figure 2.4 Phase equilibria in the system Cu-Mn-O(Driessens 1967)

Recently, Martin et al. (2007) reinvestigated the phase boundary of spinel in the Cu-Mn-O system in the intermediate temperature range, and the results match those from Vandenberghe et al. (1973). However, it is clear that the range of spinel stability has not been established, and some conflicting results about phase boundaries and crystal structures still exist. For example, it is unclear if the tetragonal or cubic spinel structure is stable in $Cu_xMn_{3-x}O_4$ solid solutions for values of x near 1 (Vandenberghe 1973). Golikov et al. (1994) showed that the Cu-Mn-O system is unique because its cooling from an equilibrium state to room temperature at any rate attainable in practice is accompanied by a variation in its phase composition. Therefore, the only way to further refine the phase diagram is through in situ investigation of the existing phase equilibria. In this investigation, in-situ X-ray diffraction was used to analyze the phase transformation at intermediate temperatures.

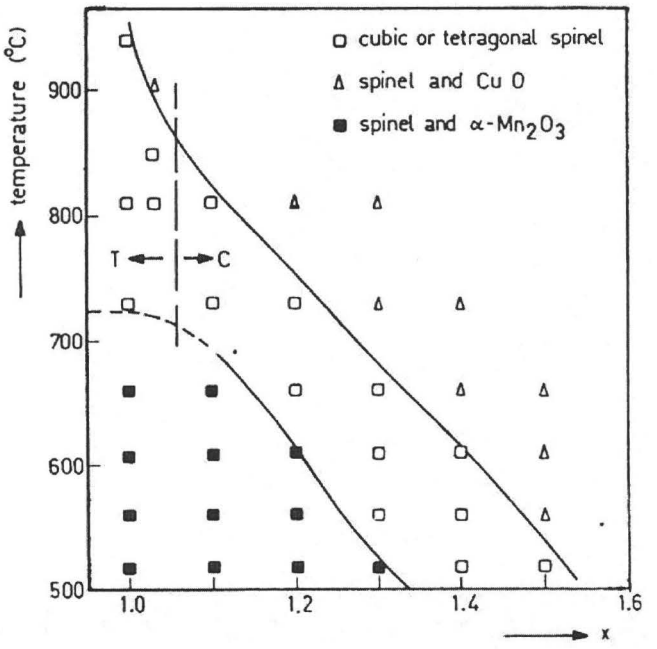

Figure 2.5 Stability of the cubic spinel structure ($Cu_xMn_{3-x}O_4$) in air (Vandenberghe 1973)

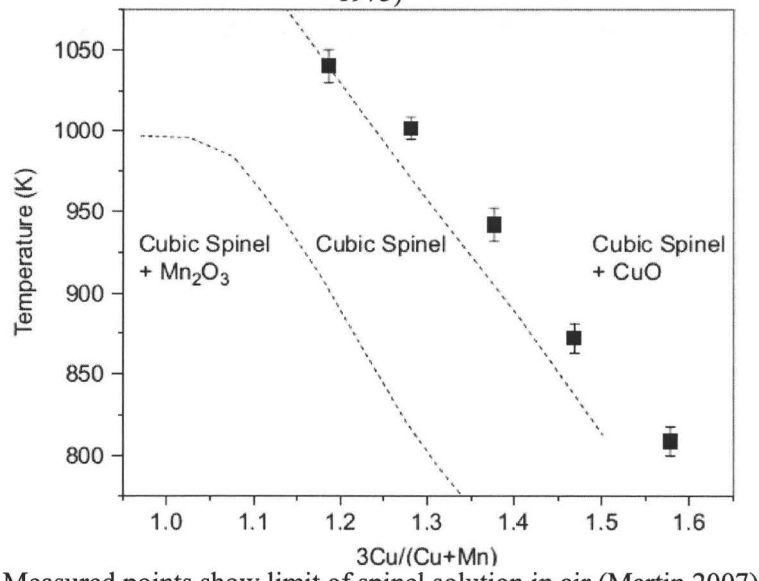

Figue 2.6 Measured points show limit of spinel solution in air (Martin 2007). Dotted lines are taken from Vandenberghe el al. (1973)

2.4.3 $CuMnO_2$ structure

Driessens et al. (1967) investigated the interaction of copper and manganese oxides in air between 750°C and 1400°C and reported $Cu_{1+x}Mn_{1-x}O_2$ to be a crednerite-like phase with monoclinic structure ($0 < x < 0.06$) and a delafossite-like phase with hexagonal structure ($0.08 < x < 0.12$).

Table 2.1 Compositions of reaction products for synthesis carried out in air

Nominal composition		Product compositions
$0 \leqslant x < 0.1$		$Cu_{1+x}Mn_{1-x}O_2$ (crednerite) + $Cu_yMn_{3-y}O_4$ (spinel)
$0.1 \leqslant x \leqslant 0.13$		$Cu_{1+x}Mn_{1-x}O_2$ (crednerite)
$0.13 < x \leqslant 0.20$	$T < 1030\,^{\circ}C$	$Cu_{1+x}Mn_{1-x}O_2$ (crednerite) + CuO
	$T > 1030\,^{\circ}C$	$Cu_{1+x}Mn_{1-x}O_2$ (crednerite) + Cu_2O

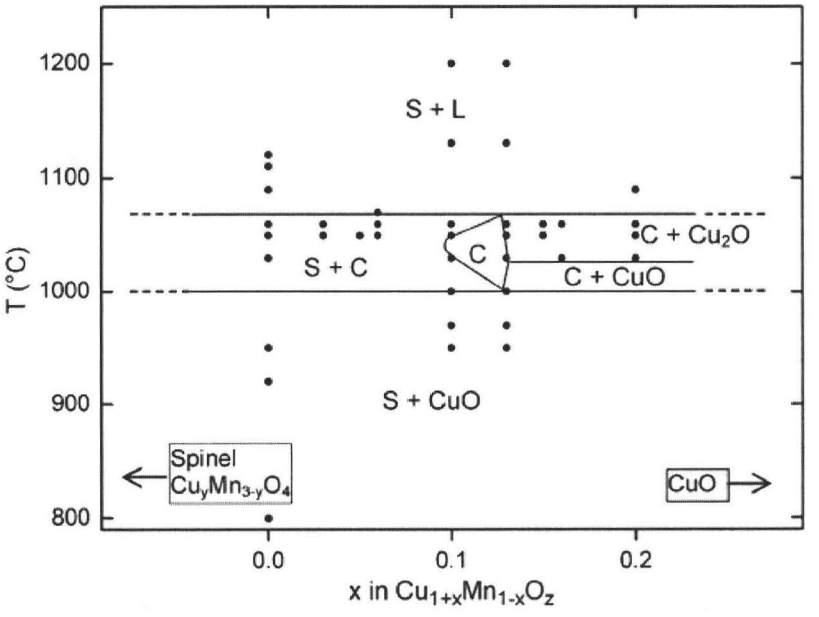

Figure 2.7 Phase diagram for $Cu_{1+x}Mn_{1-x}O_2$ ($0 < x < 0.2$) in air (C=crednerite, S=spinel, L=liquid) (Trari 2005)

Trari et al. (2005) prepared $Cu_{1+x}Mn_{1-x}O_2$ solid solutions by solid state reaction. After annealing at high temperatures, the samples were rapidly cooled to room temperature and analyzed by X-ray. They reported that solid solutions of $Cu_{1+x}Mn_{1-x}O_2$ with $0.2 \geq x \geq 0$ show single phase products; for $x \geq 0.2$, the limiting phase $Cu_{1.2}Mn_{0.8}O_2$

coexists with the oxides Mn_2O_3, CuO and Cu_2O based on the samples prepared in evacuated silica tubes. For preparations carried out in air, the phases are shown in table 2.1.

According to their results, solid solutions of $Cu_{1+x}Mn_{1-x}O_2$ have monoclinic crednerite structure (space group C2/m). Based on the results in table 2.1, thermogravimetric analyses (TGA) and differential thermal analyses (DTA), they reported the phase diagram in Fig. 2.7. The stability range of the solid solutions of $Cu_{1+x}Mn_{1-x}O_2$ in air has a very narrow composition range ($0.1 \leq x \leq 0.15$). Clearly, there is disagreement between the results from Driessens et al. (1967) and Trari et al. (2005). In order to clarify the phase equilibrium at the mid-composition of the Cu-Mn-O system, in-situ X-ray diffraction was used.

Chapter 3

Sample preparation and analyses

3.1 Sample preparation for electrodeposition of metallic coatings

For electrodeposition experiments, small coupons with dimensions 10×20×1 mm, cut from commercial ferritic UNS430 stainless steel sheets, were used. The nominal composition of the steel is shown in table 3.1. Each coupon was polished with 400 grit SiC paper and then cleaned in acetone in an ultrasonic bath and rinsed in water and alcohol. No other surface treatment was used.

Table 3.1 Standard UNS 430 stainless steel composition in wt.%

Element	Fe	C	Mn	Si	P	S	Cr	Ni
wt %	balance	< 0.12	<1.00	<1.00	<0.040	<0.030	16-18	<0.75

For manganese deposition, the experimental preparation was as follows: $MnSO_4 \cdot H_2O$ (Alfa Aesar, 98+%) and $(NH_4)_2SO_4$ (BDH) were used as supplied. Each catholyte sample consisted of 200 g/L $MnSO_4 \cdot H_2O$ and 150 g/L $(NH_4)_2SO_4$, dissolved in deionized water (D.I. water). The catholyte was adjusted to 3.20 ± 0.05 pH by adding dilute sulfuric acid. Each anolyte sample contained 150 g/L $(NH_4)_2SO_4$ in D.I. water. Two 4×50×1 mm platinum foil anodes, located on each side of the sample, were used in order to obtain complete coverage of the cathode. The anolyte was separated from catholyte by fine porosity glass frit tubes. UNS 430 stainless steel was chosen as the cathode for this study. All the experiments were carried out at room temperature. The electrolysis experiments were carried out in a 400 ml beaker. The electrochemical process consisted of two steps: pre-electrolysis of the catholyte followed by deposition of the Mn. Pre-electrolysis of the solution is a purification method that was developed in the thesis and applied before electrodeposition to remove impurities. The procedure was as follows. A UNS 430 coupon was inserted into the solution at a current density of 150 mA/cm^2 for 30 minutes. During the process, a copious amount of brown precipitate formed in the solution, and the pH of the solution rose to 6.20. Centrifuging was used to separate the precipitates, and the solution was filtered through 1 μm filter paper. The process was repeated once more after the pH was adjusted to 3.20 ± 0.05 by dilute sulfuric acid. The brown precipitates were washed with deionized water 5 times, and dried in a desiccator for several days for XRD analyses. After the pre-electrolysis and pH adjustment, the catholyte was used for Mn electrodeposition. During the deposition process, the catholyte was vigorously mixed by a magnetic stirrer.

After deposition, the samples were cleaned with D.I. water, dried in air for 30 minutes, and stored in a desiccator. An EG&G A273 potentiostat/galvanostat in galvanostatic mode was used as power supply. The current efficiency was calculated from the weight gain of the samples. The influence of the parameters, e.g., initial pH

value of the solution, deposition time and current density, on the current efficiency of Mn electrodeposition was also studied, and the working potential of the UNS 430 stainless steel substrate was measured.

For the working electrode potential measurement, a three-electrode cell was used. A platinum foil was used as the counter electrode which was separated from the working electrode by a diaphragm to avoid the contamination of solution and a saturated calomel electrode (SCE) was used as the reference electrode which was in a different compartment, separated from the working electrode by a Luggin capillary; the working electrode potential cited in the text was measured against the SCE reference.

3.2 Sample preparation for electrical conductivity measurement

For electrical conductivity measurement, commercial UNS 430 stainless steel rods were chosen as the substrate. The rod sample was 6.3 mm in diameter and 200 mm in length. The analyzed composition of the steel is shown in table 3.2. One end of each rod was polished with 400 grit SiC paper, and then cleaned in acetone in an ultrasonic bath and rinsed in water and alcohol. Metallic coatings were applied to the polished surface of the rod samples by electroplating. For Co-Mn spinel coating, samples were first plated with cobalt, then with manganese. For Cu-Mn spinel coating, samples were coated with copper, then with manganese.

As Mn, Cu and Co have much larger thermal expansion coefficients (TECs) than that of metallic interconnects of SOFCs, the mismatch between the metallic coatings and metallic interconnects can cause high stress, which can result in spallation and detachment of the coatings and subsequently formed oxide layers. In order to increase the bonding between metallic coatings and substrate, an alloying process was used to transform separate layers of Cu, Mn and Co to Cu-Mn and Co-Mn alloy coatings. After electroplating, the coated rods were annealed at 800°C in an argon atmosphere for 2 hours to produce alloy coatings. After cooling, a thin layer of Pt paste was applied to the coated ends as an electrical junction. After drying at 200°C, four pairs of stainless steel rod samples were placed end to end in a furnace, as described in (Wei 2007) (fig. 3.1). The electrical conductivity was measured at 750°C in air 4 days later in order to make sure that the metallic thin films have transformed to the spinel coatings. A constant DC current of 100 mA was applied, and the voltages of the samples recorded by a 4 channel voltage recorder (Omega). The resulting ASR values were used to compare electrical conductivity of the samples.

Table 3.2 Analyses of UNS 430 Stainless Steel Composition by ICP (in wt.%)

Element	Fe	C	Mn	Si	P	S	Cr	Ni	Mo	Cu	V
wt %	balance	0.049	0.351	0.205	0.017	0.004	17.47	0.304	0.024	0.112	0.047

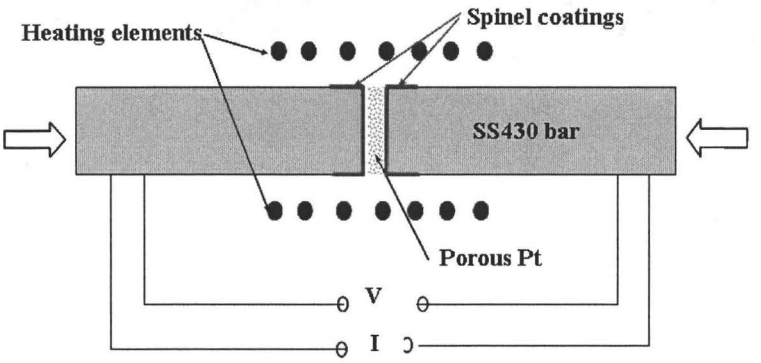

Figure 3.1 Experimental set-up for electrical conductivity measurement

3.3 Sample preparation for studying transformation mechanisms

Commercial ferritic UNS 430 stainless steel coupon samples with dimensions 10×20×1 mm were prepared for oxidation testing, and the composition is shown in table 3.2. Each coupon was polished with 400 grit SiC paper and then cleaned in acetone in an ultrasonic bath and rinsed in water and alcohol. No other surface treatment was used. After application of Mn, Co and Cu metallic coatings, the samples were oxidized in air at a heating rate of 3°C/min within the temperature range 600-950°C. The samples were periodically cooled to room temperature and weighed. In order to specifically study the transformation mechanism of Cu-Mn at 750 °C, the samples were put into a furnace at temperature, and air quenched to obtain readings. A digital balance with a read-out of 0.0001 g was used.

3.4 Sample preparation for in-situ neutron and X-ray diffraction

Samples for in-situ neutron and X-ray diffraction analyses were prepared from high purity CuO and MnO_2 through solid state reaction (table 3.3). Stoichiometric amounts of the oxides were mixed in a Nalgene container. In order to achieve intimate mixing of the constituent oxides, the powders were ball milled in 100% anhydrous ethanol with 5 mm diameter yttria stabilized zirconia balls (TOSOH Ceramics). Pure ethanol was added to facilitate mixing and flowing of the powder out of the container after mixing. Milling of powders was performed for 24 hours. After the milling, the powders were transferred to porcelain dishes and heated to approximately 80°C on a hot plate to evaporate the ethanol.

During pressing, a cylindrical die was used and uniaxial pressing was performed on a manually operated press (Model K, F.S. Carver Inc., Summit, N.J, U.S.A) to form the green body. The pressure was maintained around 80-100 MPa. No organic binder was used during the process. The pressed samples were annealed at different temperatures in order to obtain pure spinel. The annealing temperatures and time were

determined based on the previous research on Cu-Mn-O system (Broemme 1985; Vandenberghe 1973) (table 3.4).

The composition of the samples was confirmed by inductively coupled plasma optical emission spectrometry (ICP-OES). It is clear that the compositions of the powder samples were controlled very well (table 3.5). The samples were heated to the corresponding annealing temperatures at a heating rate of 5°C/min. After annealing, they were quenched to room temperature in air. Afterwards, the samples were ground into powder and put into quartz tubes (fig. 3.2). The tubes were sealed with a reduced pressure of air inside to compensate for volume expansion and maintain a pressure near one atmosphere during high temperature (600-800°C) testing. After neutron analyses, the powder samples were analyzed by high temperature x-ray diffraction analyses at the University of Manitoba.

The XRD analyses of the samples before in-situ neutron analyses is shown figs. 3.3-3.7. It can be seen that for $Cu_{0.8}Mn_{2.2}O_4$, $Cu_{1.0}Mn_{2.0}O_4$ and $Cu_{1.1}Mn_{1.9}O_4$, pure spinel was obtained, while for $Cu_{1.3}Mn_{1.7}O_4$, spinel plus Mn_2O_3 was obtained and the sample of $Cu_{1.4}Mn_{1.6}O_4$ consisted of spinel, CuO and Mn_2O_3.

Table 3.3 Nature and purity of the powders for neutron and x-ray diffraction

Powder	Purity, %	Mesh	Manufacturer
CuO	99.7	200	Alfa Aesar, U.S.A
MnO_2	99.9	325	

Table 3.4 Preparation of the samples for Neutron and X-ray diffraction analyses

Nominal composition	Annealing temperature (°C)	Time (days)
$Cu_{0.8}Mn_{2.2}O_4$	900	3
$Cu_{1.0}Mn_{2.0}O_4$	850	3
$Cu_{1.1}Mn_{1.9}O_4$	790	4
$Cu_{1.3}Mn_{1.7}O_4$	690	5
$Cu_{1.4}Mn_{1.6}O_4$	550	20

Table 3.5 Composition analyses of the powders by ICP

Sample	Cu	Mn
$Cu_{0.8}Mn_{2.2}O_4$	0.80298	2.19702
$Cu_{1.0}Mn_{2.0}O_4$	1.00708	1.99292
$Cu_{1.1}Mn_{1.9}O_4$	1.10771	1.89229
$Cu_{1.3}Mn_{1.7}O_4$	1.30893	1.69107
$Cu_{1.4}Mn_{1.6}O_4$	1.43347	1.56653

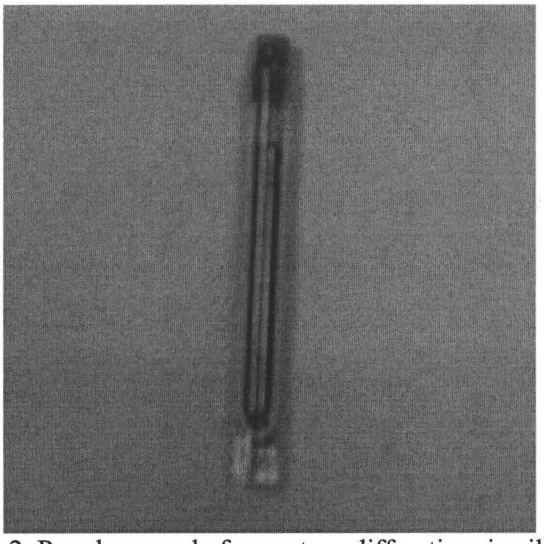

Figure 3.2 Powder sample for neutron diffraction in silica tube

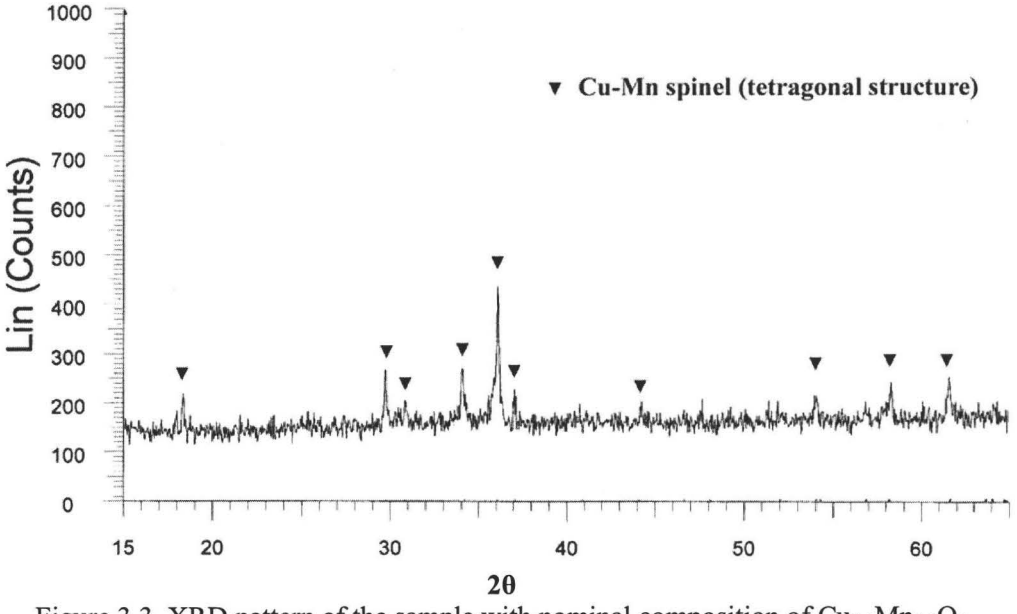

Figure 3.3 XRD pattern of the sample with nominal composition of $Cu_{0.8}Mn_{2.2}O_4$

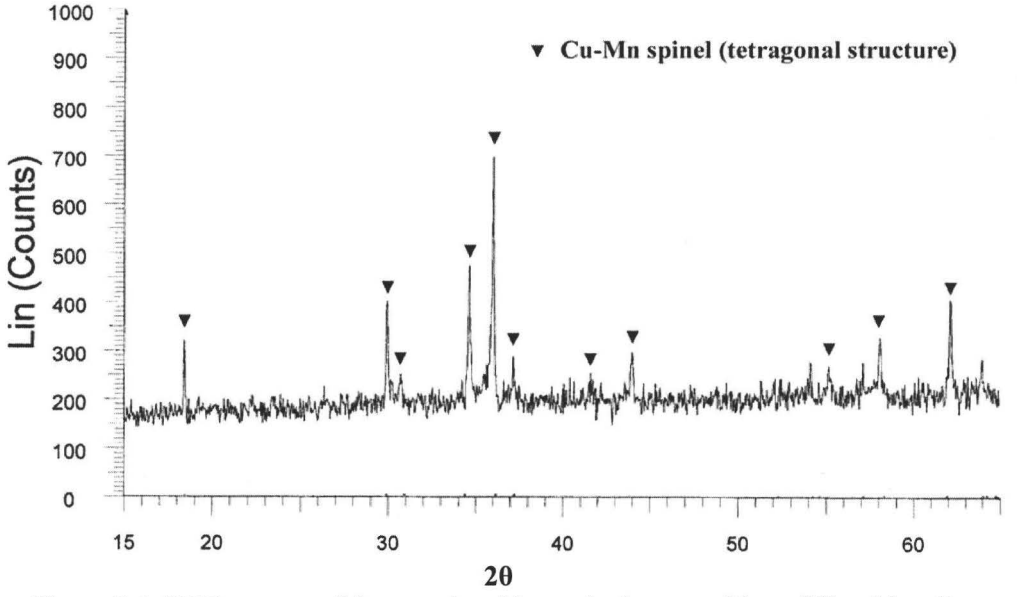

Figure 3.4 XRD pattern of the sample with nominal composition of $Cu_{1.0}Mn_{2.0}O_4$

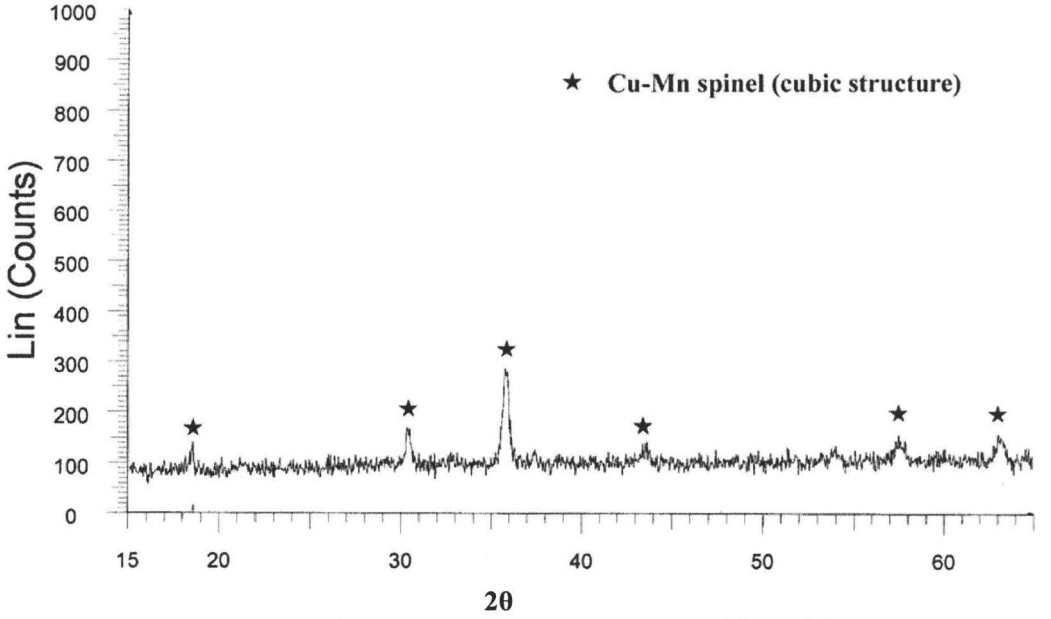

Figure 3.5 XRD pattern of the sample with nominal composition of $Cu_{1.1}Mn_{1.9}O_4$

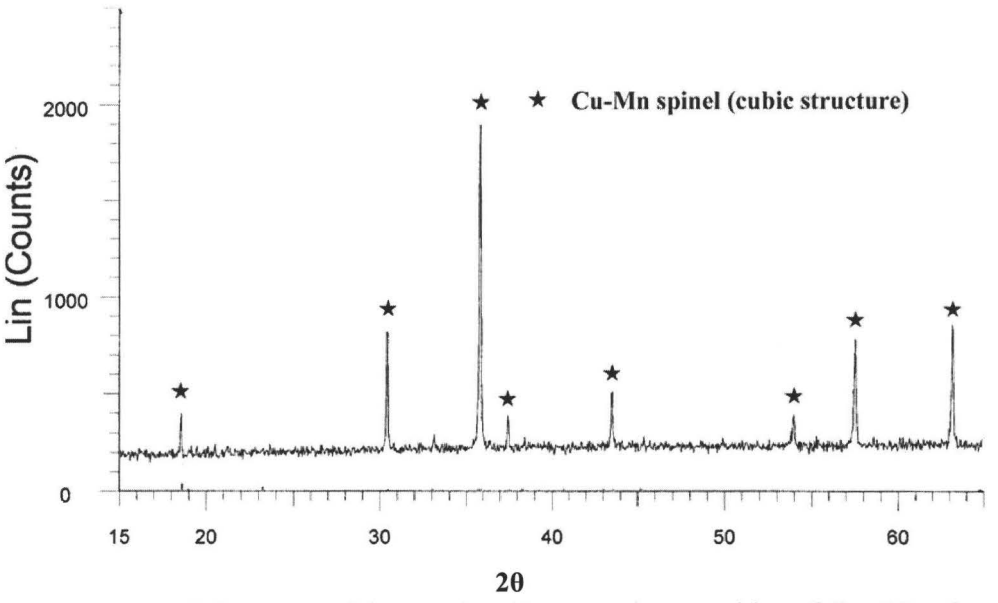

Figure 3.6 XRD pattern of the sample with nominal composition of $Cu_{1.3}Mn_{1.7}O_4$

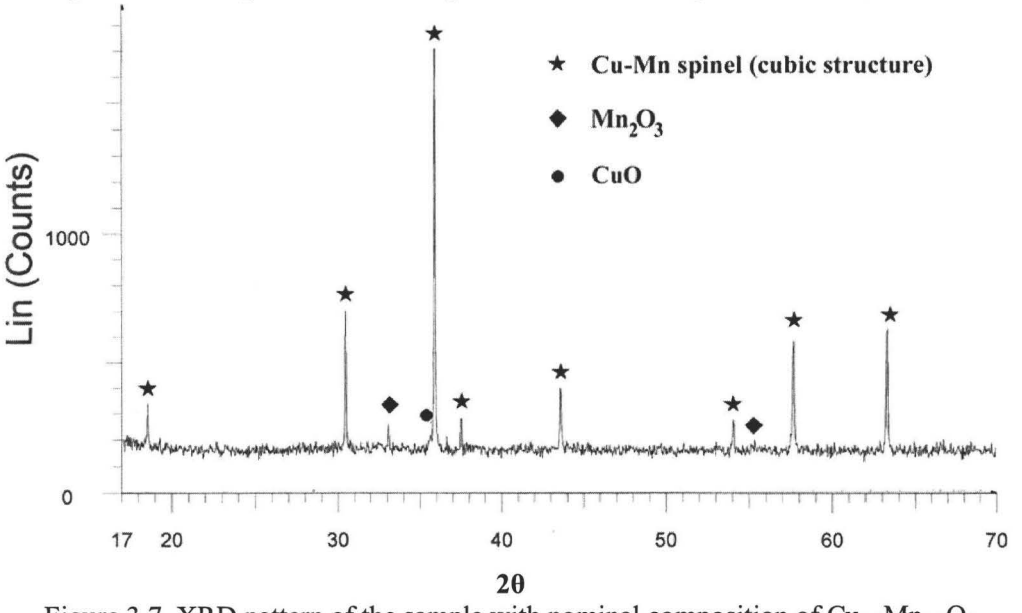

Figure 3.7 XRD pattern of the sample with nominal composition of $Cu_{1.4}Mn_{1.6}O_4$

3.5 Sample analyses

Microstructure analyses was done by a Philips 515 scanning electron microscope (SEM). The spinel composition was analyzed by energy dispersive spectrometry (EDS), and the composition of Cu-Mn spinel powder samples were analyzed by inductively coupled plasma optical emission spectrometry (ICP-OES). The phase content was determined by a Bruker D8 Advanced x-ray diffractometer. The impurity content of $MnSO_4 \cdot H_2O$ for electrodeposition was analyzed using ICP-OES, inductively coupled plasma mass spectrometry (ICP-MS) or instrumental neutron activation analyses (INAA). In-situ X-ray diffraction analyses was conducted by using a PANalytical X'Pert Pro System at the University of Manitoba. Cu $K\alpha_1$ was used for analyses and $K\alpha_2$/ $K\alpha_1$ intensity ratio was 0.5. Diffraction patterns were acquired within the 2θ range from 10°-70° with step time of 50 seconds. The diffraction data were analyzed by phase identification software of EVA using JCPDS database at McMaster University.

In order to study the cation distribution in $Cu_xMn_{3-x}O_4$ solid solutions, in-situ neutron diffraction was performed due to the similarity of X-ray scattering power of copper and manganese. The analyses was conducted at the Canadian Neutron Beam Centre, NRC, Chalk River, on the C2 Spectrometer equipped with a silicon monochromator. Diffraction patterns were acquired for $0° < 2\theta < 120°$ using two different wavelengths: 1.32927 Å and 2.37083 Å. Rietveld refinement was performed using the General Structure Analyses System (GSAS) package with EXP Graphic Users Interface (EXPGUI).

Chapter 4

Spinel Coatings for metallic interconnects

4.1 Electrodeposition of manganese on UNS 430 stainless stee

The composition of laboratory grade $MnSO_4 \cdot H_2O$ as analyzed by ICP-OES, ICP-MS and INAA is shown in table 4.1. It can be seen that the largest concentration among the impurities is that of Fe at 0.112 wt%. During the pre-electrolysis process, no Mn deposit was obtained on the sample surface, while a substantial amount of brown precipitate formed as described above. XRD patterns of the brown precipitates are shown in fig. 4.1. The as-obtained precipitates exhibited an amorphous pattern. After heating at 600°C for one hour, a pattern matching Fe_2O_3 appeared, indicating the brown precipitates were iron oxides or hydroxides. It is believed that impurities in the solution, especially iron, hinder the formation of a Mn deposit and must be removed.

In acidic solution, the parasitic electrode reaction at the cathode is hypothesized to be:

$$nH_2O + Fe^{n+} + ne^- \rightarrow Fe(OH)_n \downarrow + \frac{n}{2} H_2 \uparrow \qquad (4.1)$$

where 'n' could be 2 or 3. Since large amounts of hydrogen gas evolve at the cathode surface, hydroxide ions (OH^-) should be abundant in this region, which results in a local pH increase of the catholyte. According to the Pourbaix diagram, the formation of insoluble iron(II) hydroxide is very possible (Pourbaix 1966). When these precipitates were heated to 600°C in air, they dehydrated and oxidized to form Fe_2O_3. In previous studies of MnO_2 deposition, Fe impurities were also found to be responsible for the efficiency decrease of deposit formation (Pilla 2004). It is reported that hydrolytic removal of iron from Mn sulfate solution is a common practice (A.G.Kholmogorov 2000).

After filtering, the solution was used as the catholyte for Mn deposition. As a result of preliminary studies, several factors were identified as important for the production of a coherent, uniform deposit of a silvery white Mn product at high current efficiency; namely, initial pH level of the catholyte, the applied current density, and the duration of electrolysis. The current efficiency as a function of initial catholyte pH level was investigated at a current density of 120 mA/cm^2. The deposition time was set at 5 minutes. After deposition, homogeneous and silvery bright Mn deposits were obtained on all samples. The measured values of current efficiency in Table 4.2 show little change at pH values in the range of 2.80 – 6.16. The surface morphology of the samples is shown in fig. 4.2. It is clear that there was no significant difference in surface morphology of the Mn deposit as a function of initial pH of the solution, in contrast to the literature (Gong 2002). As a lower overvoltage for hydrogen evolution was observed at pH 2-3, compared with pH values of 3.7, 5.0, and 7.5 (Gong 2002), which resulted in increased hydrogen evolution, and Mn dissolution, solutions with pH 2-3 should be

avoided. In order to obtain maximum current efficiency, the influence of current density on Mn deposition was studied. The pH value of the solution was adjusted to 3.20. Table 4.3 shows that current efficiency initially increased with current density. However, when current densities exceeded 120 mA/cm^2, a lower current efficiency was obtained and black deposits formed at the edges of the samples. It is known that at low current densities, the efficiency of Mn deposition is affected by self-dissolution of the film. As both water electrolysis and Mn dissolution contribute to hydrogen evolution, the hydrogen evolution rate is high and the Mn deposition rate appears low (Gong 2002). Black deposits on the cathode at too high current densities are well documented (H.H.Oaks 1936), and recent research also demonstrated the formation of black films at edges of samples at curent densities above 150 mA/cm^2 (Gong 2002). These black films were amorphous and contained oxyhydroxides that are known to greatly inhibit crystal growth, which decreases the current efficiency.

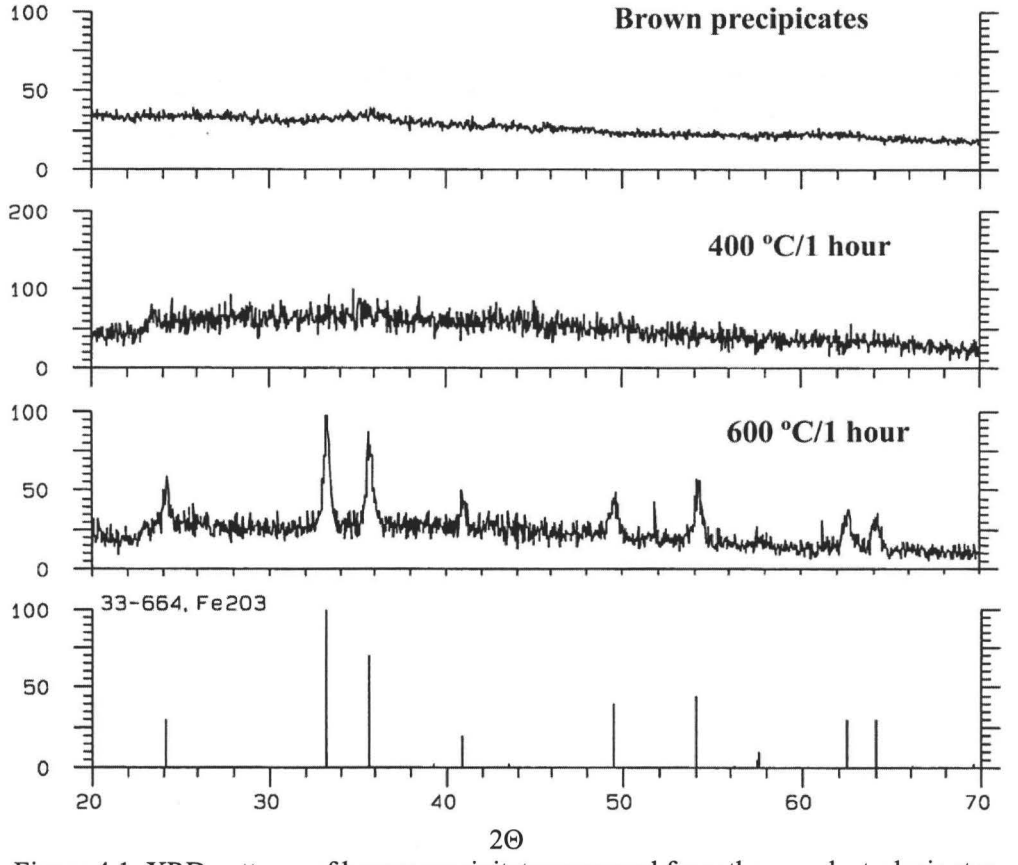

Figure 4.1 XRD patterns of brown precipitates removed from the pre-electrolysis step and exposed to different levels of heat treatment, compared with a file of 33-664 in JCPDS database

Table 4.1 Elemental analysis of impurities in $MnSO_4 \cdot H_2O$ (ppm by wt)

Li	**Be <1**											B	C	N	O
Na 220	**Mg <60**											**Al 630**	**Si 280**	**P <44**	S
K 250	**Ca <70**	**Sc <1**	**Ti 18**	**V <5**	**Cr 60**	Mn	**Fe 1120**	**Co <1**	**Ni 20**	**Cu <10**	**Zn <30**	**Ga 9**	**Ge <0.5**	**As 5**	**Se 8**
Rb <1	**Sr <2**	**Y <0.5**	**Zr <4**	**Nb <0.2**	**Mo 8**	Tc	Ru	Rh	Pd	**Ag <0.5**	Cd	**In <0.1**	**Sn <1**	**Sb 0.4**	Te
Cs <0.1	**Ba 5**	**Lu <0.002**	**Hf <0.1**	**Ta <0.01**	**W <0.5**	Re	Os	Ir	Pt	Au	Hg	**Tl <0.05**	**Pb <5**	**Bi <0.1**	Po
Fr	Ra	Lr	Rf	Db	Sg	Bh	Hs	Mt	Ds	Rg					

Lanthanoids	**La**	**Ce**	**Pr**	**Nd**	Pm	**Sm**	**Eu**	**Gd**	**Tb**	**Dy:**	**Ho:**	**Er**	**Tm**	**Yb**
	<0.05		**<0.01**	**<0.05**		**<0.01**	**<0.005**	**<0.01**					**<0.005**	**<0.01**
Actinoids	Ac	**Th <0.05**	Pa	**U 0.02**	Np	Pu	Am	Cm	Bk	Cf	Es	Fm	Md	No

Table 4.2 Current efficiency of Mn deposition as a function of pH at current density of 120 mA/cm^2

Initial pH value of catholyte	2.80	3.20	3.58	4.40	5.75	6.16
Current efficiency (%)	60	62	62	62	61	60

Table 4.3 Current efficiency of Mn deposition as a function of current density for 5 minutes

Current density (mA/cm^2)	50	100	120	150	200
Current efficiency (%)	20	53	64	52	50

Table 4.4 Current efficiency of Mn deposition as a function of electrolysis time

Deposition time (min)	1	5	10
Current efficiency (%)	37	64	71

The variation of current efficiency with time for Mn deposition was also investigated at a current density of 120 mA/cm^2, shown in Table 4.4. It can be seen that as deposition time increased, the current efficiency also increased, which is consistent with the previous observation that there are differences in current efficiencies between short duration experiments and much longer times (Lewis 1976). In order to investigate the reason why deposition time influences the current efficiency, the surface morphology of Mn deposits was periodically analyzed by SEM (Figures 4.3 and 4.4). An incomplete Mn coating can be seen after one minute deposition (Fig. 4.3-a, b). The coating at the edge is more uniform than that in the center (Fig. 4.3-c, d), which correlates with the deposition rate at the edges being higher than that in the center. EDS analyses demonstrated that the fine and large crystals in Figure 4.3 are all Mn crystals. Accordingly, we conclude that Mn crystals nucleate on the surface, and grow until they contact each other. However, after 5 minutes of deposition, there is no difference in coating morphology between the edge and the center (Figure 4.4), and the coating totally covers the surface. Comparing fig. 4.3 with fig. 4.4, it can be seen that Mn deposits are more uniform after long duration than short deposition times. Fig. 4.5 shows a cross-section image of Mn coatings after 5 minutes deposition.

According to the data, the longer the deposition time, the higher the current efficiency of deposition. The reason could be that Mn has higher catalytic activity for Mn plating and a slightly higher overpotential for H^+ reduction than stainless steel (Conway 1992; Mantell 1966; Gong 2002; Ilea 1997). Due to increasing the hydrogen overvoltage and higher catalytic activity of Mn deposition, the reduction of Mn ions was favored over that of hydrogen ions after the initial layer of Mn was deposited. The working potential of 430 stainless steel during Mn deposition was measured by using a three-electrode cell at a current density of 120 mA/cm^2 and pH of 3.20. The potential was –1.362 V.

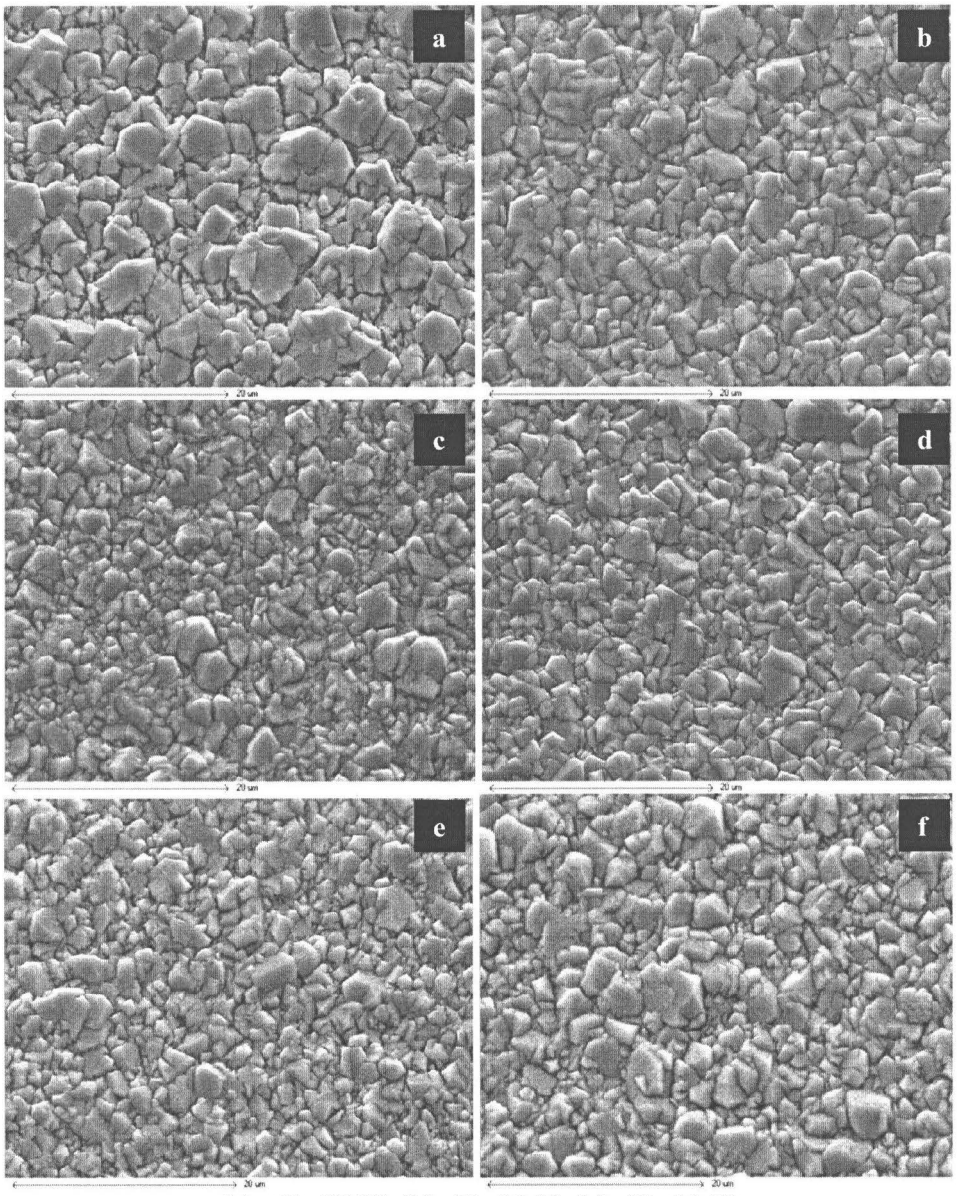

(a) pH of 2.80 (b) pH of 3.20 (c) pH of 3.58
(d) pH of 4.40 (e) pH of 5.75 (f) pH of 6.16

Fig. 4.2 Surface morphology of Mn coating at different pH values of the solution (All deposits were obtained after 5 min deposition at 120 mA/cm^2)

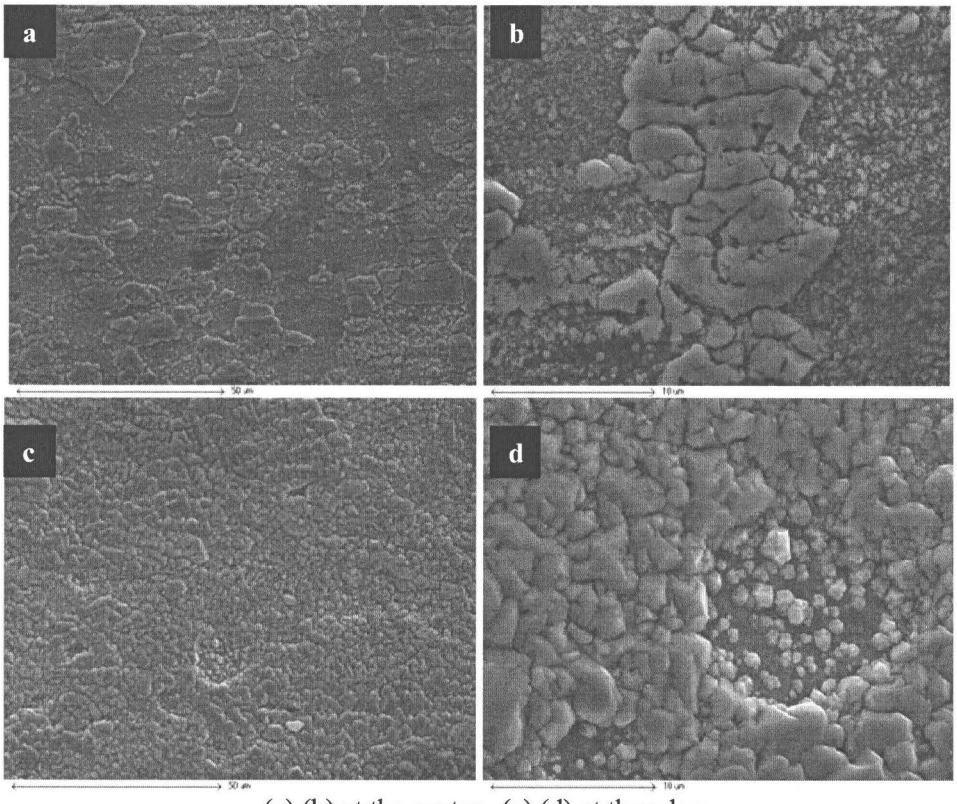

(a),(b) at the center (c),(d) at the edge

Figure 4.3 Surface morphology of Mn deposit after 1 min deposition

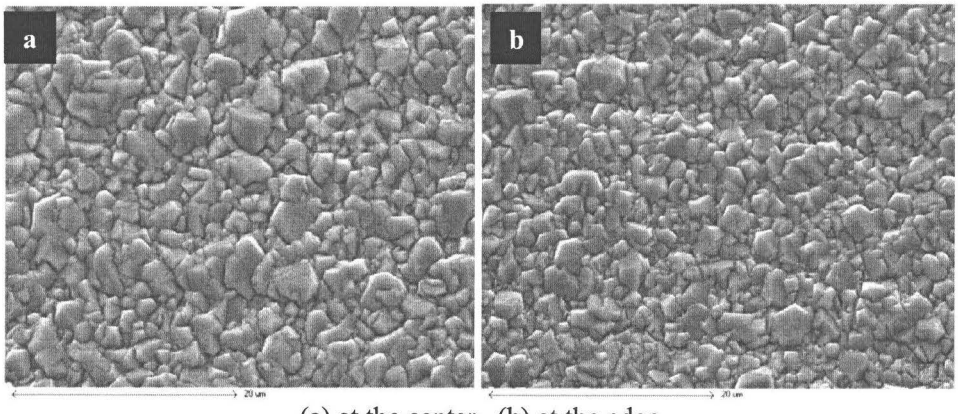

(a) at the center (b) at the edge

Figure 4.4 Surface morphology of Mn deposit after 5 min deposition

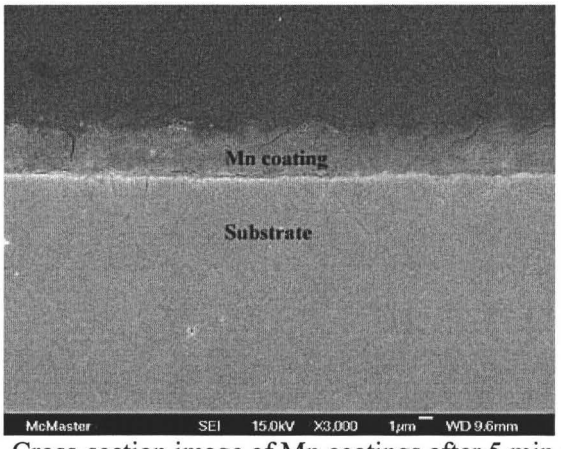

Figure 4.5 Cross-section image of Mn coatings after 5 min deposition

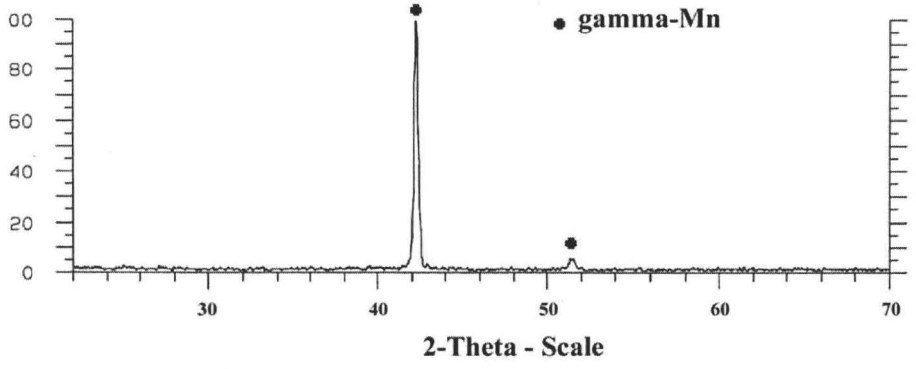

Figure 4.6 XRD pattern of fresh Mn deposit

The crystal structure of the fresh Mn deposit and the deposit after 3 months elapsed were compared. XRD results showed that the fresh deposit was gamma Mn, stabilized by the high hydrogen content of the electrolytic process (Potter 1945); after 3 months, it turned to alpha Mn (fig. 4.6-4.7).

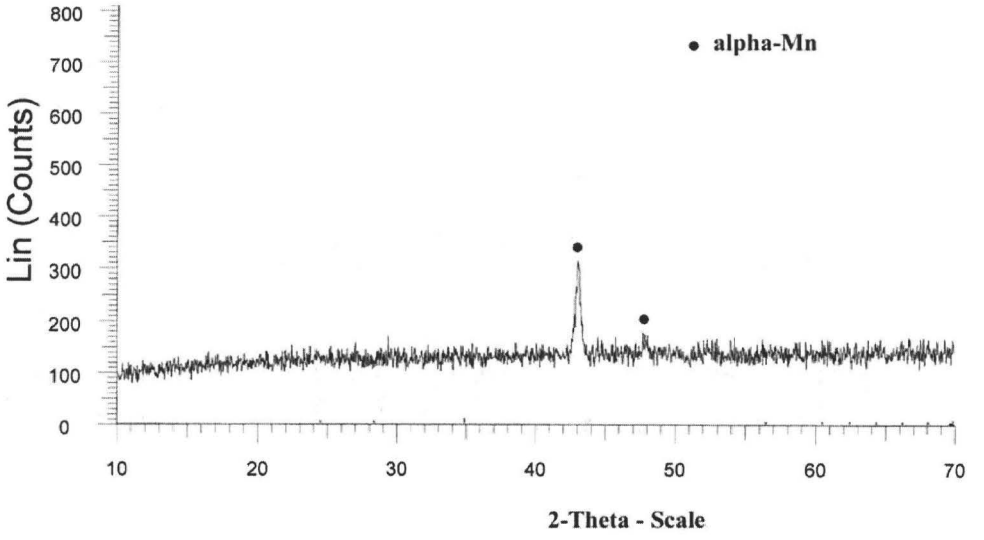

Figure 4.7 XRD pattern of Mn deposit after 3 months in air

4.2 Electrodeposition of Cobalt and Copper on UNS 430 stainless steel

Most studies of electrodeposition of iron-group metals (iron, cobalt, nickel) have focused on application of thin films (< 1 um) (Cui 1990; Dille 1997; Floate 2002; Gomez 2002; Jartych 2002; Jartych 2001; Meguid 2003; Pradhan 2001; Sasaki 1998; Schindler 1997). When I used the procedure in the literature to grow thick coatings (at least several microns), there was always spallation and detachment of the coatings. Therefore, based on information from the literature, the following recipe for the Co electrolyte was developed in this work: an aqueous solution of $CoCl_2 \cdot 6H_2O$ (Alfa Aesar) at a concentration of 300 g/L, and HBO_3 at a concentration of 30 g/L (BDH). The current density used was 15 mA/cm^2. For electrodeposition of Cu (Basu 2005), aqueous solution of $CuSO_4 \cdot 6H_2O$ (Alfa Aesar) at a concentration of 200 g/L, and concentrated H_2SO_4 at a concentration of 40 g/L was used. The current density was 48 mA/cm^2. D.I. water was used as solvent. All electroplating experiments were carried out at room temperature.

4.3 Electrodeposition of Co-Mn and Cu-Mn metallic thin films

In order to produce Cu-Mn and Co-Mn spinel coatings, the corresponding metallic thin films must be plated. As Mn can easily dissolve in acidic aqueous solution, and the solutions for Co and Cu deposition are acidic, Cu and Co coatings were electrodeposited as the first layer. Mn was coated on top of them. The experimental set-up of Cu and Co deposition is the same as that for Mn deposition except that no frit glass tube was needed. For fresh solutions, the deposition rates of Co, Cu and Mn are shown in table 4.5. For every experiment, six samples were used. It was observed that the Mn deposition rate is a little higher on Cu and Co coating than it was on 430 stainless steel,

which means that Cu and Co substrates favor Mn deposition. In order to produce 30 um thick oxide coatings, the corresponding metallic thin films with a thickness near 10 um are necessary.

Table 4.5 Deposition rate of metallic thin films

Coating	substrate	Sample	Current density (mA/cm^2)	Deposition rate ($g/min \cdot cm^2$)
Cobalt	430 stainless steel	1	15	0.00019
		2		0.00020
		3		0.00020
		4		0.00019
		5		0.00020
		6		0.00019
Copper		1	48	0.000947
		2		0.000948
		3		0.000948
		4		0.000962
		5		0.00095
		6		0.000976
Manganese		1	120	0.0013
		2		0.0013
		3		0.0013
		4		0.0014
		5		0.00134
		6		0.00129
Manganese	Copper coated 430 stainless steel	1	120	0.00140
		2		0.00139
		3		0.001439
		4		0.001429
		5		0.001424
		6		0.001414
Manganese	Cobalt coated 430 stainless steel	1	120	0.001538
		2		0.001511
		3		0.001621
		4		0.00159
		5		0.00159
		6		0.00139

Based on the above information about the deposition rates, the deposition time for Cu and Co coatings was set at 4 minutes and 30 minutes respectively, and the deposition time for Mn was set at around 3 minutes in order to get compositions with high electrical conductivity (for Cu-Mn spinels, $Cu_{1.3}Mn_{1.7}O_4$; for Co-Mn spinels, $Co_{1.75}Mn_{1.25}O_4$). However, since many factors can influence the electrodeposition rate, e.g., solution

temperature, concentration, stirring rate, surface roughness, the molar ratio of Cu to Mn and Co to Mn could not be controlled with high accuracy. Co-Mn and Cu-Mn metallic thin films are shown in figure 4.8. It is clear that fresh Mn deposit can be easily oxidized.

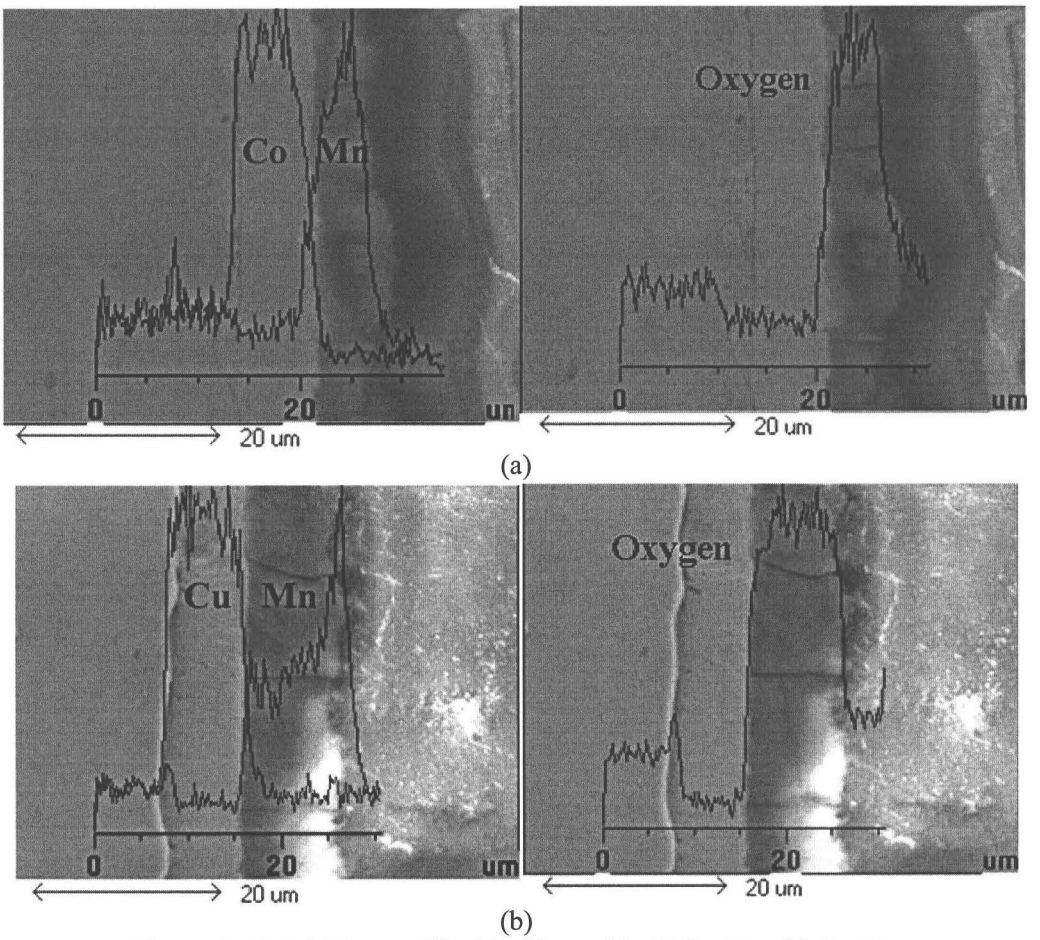

Figure 4.8 Multiple metallic thin films with (a) Co-Mn (b) Cu-Mn

4.4 Co-Mn and Cu-Mn spinel coatings formation

In order to determine the mechanism of conversion of metal to spinel, test coupons were electrodeposited with Co-Mn and Cu-Mn metallic thin films and then they were heated to 750˚C slowly for transformation. It was found that spalling of the coating occurred in many samples after oxidation. It was deduced that spallation was due to the stress resulting from the thermal expansion coefficients (TECs) mismatch of Cu, Co and Mn oxides with that of UNS 430 stainless steel. In order to reduce the stress, the coated samples were annealed at 800˚C in argon for 2 hours in order to form Cu-Mn and Co-Mn

alloys on the surface and improve the bonding between the metallic thin films and substrate. The idea is that when the alloys are oxidized in the air, the metallic elements in the alloys will be oxidized simultaneously and the spinel coatings can form through reactions among the oxides immediately. As the TECs of Cu-Mn and Co-Mn spinel are close to that of the substrate, the stress due to the TECs mismatch can be greatly reduced. The experiments showed that spallation was greatly alleviated through annealing at 800˚C in argon. Line scan analyses of the cross-section of Cu-Mn and Co-Mn coated coupons after annealing are shown in figs. 4.9 and 4.10. It can be seen that the surface of the metallic thin films was a little oxidized (fig. 4.9). Compared with fig. 4.8, it can be seen that annealing at 800˚C in Ar significantly improves the bonding: the gap between the metallic thin films and substrate disappeared. Moreover, the metallic thin films diffused into each other, and formed an alloy layer on the surface.

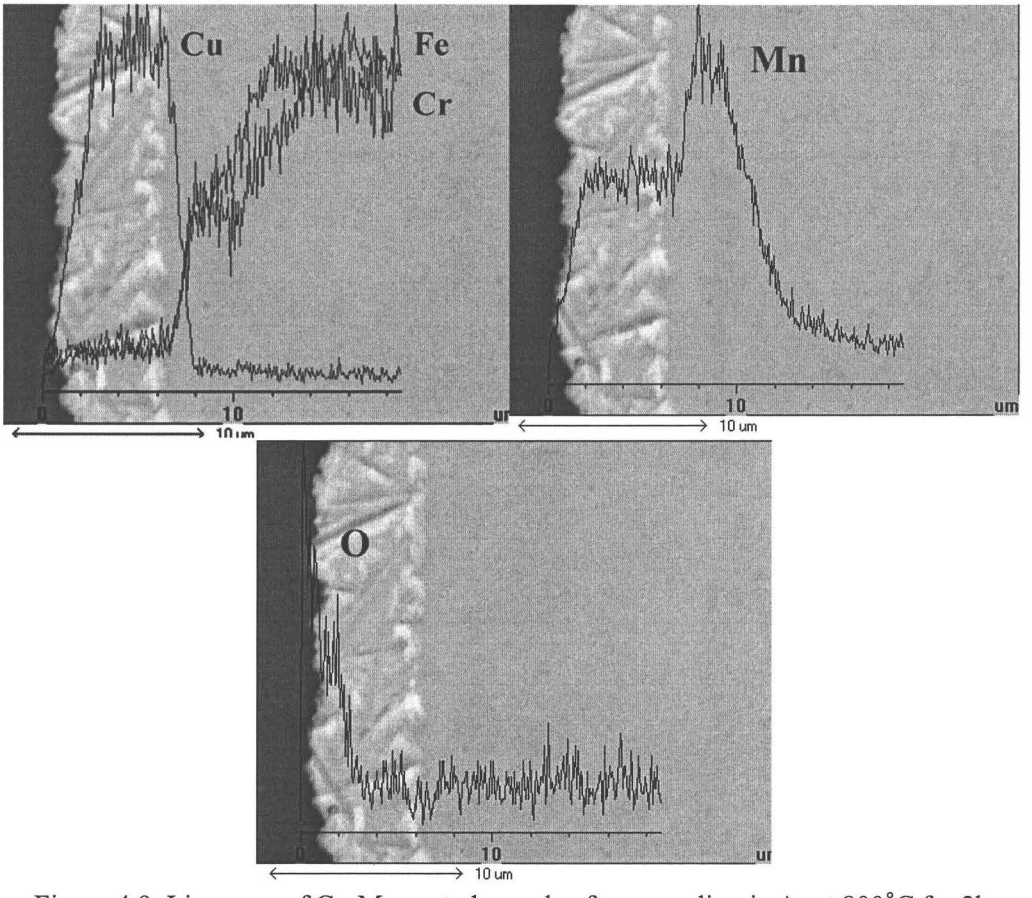

Figure 4.9 Line scan of Cu-Mn coated sample after annealing in Ar at 800˚C for 2h

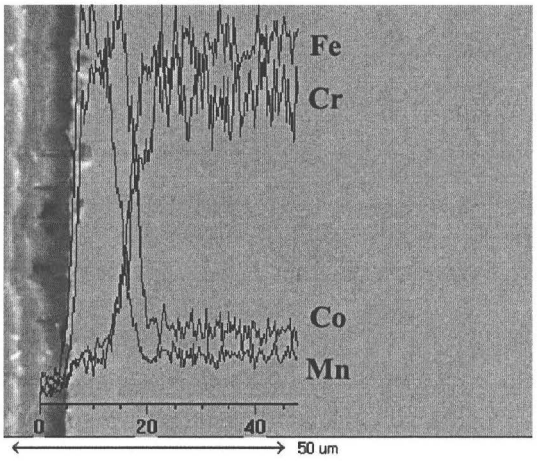

Figure 4.10 Line scan of Co-Mn coated sample after annealing in Ar at 800°C for 2h

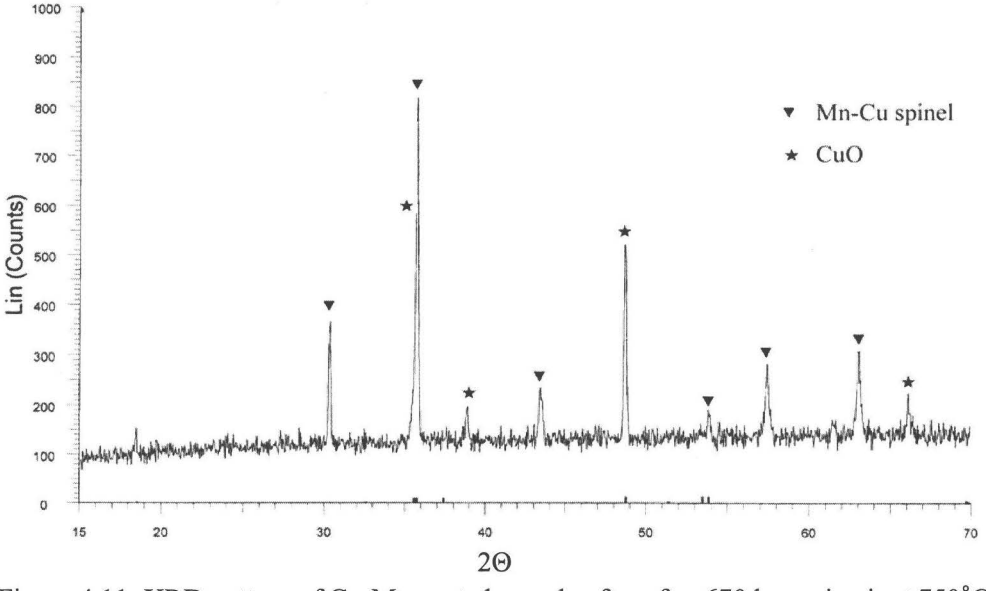

Figure 4.11 XRD pattern of Cu-Mn coated sample after after 670 hours in air at 750°C

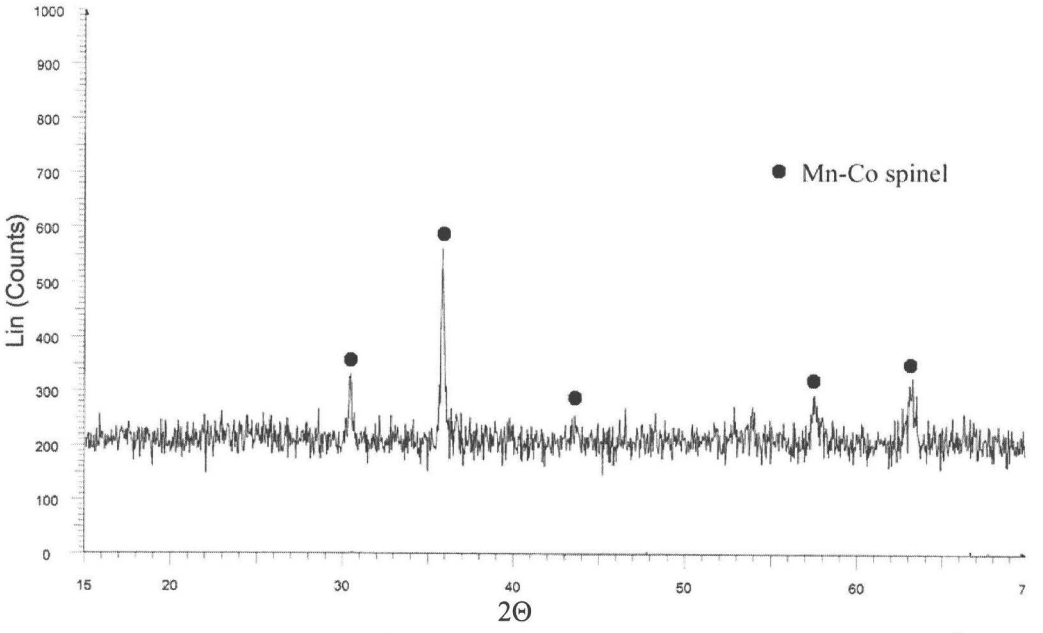

Figure 4.12 XRD pattern of Co-Mn coated sample after 670 hours in air at 750°C

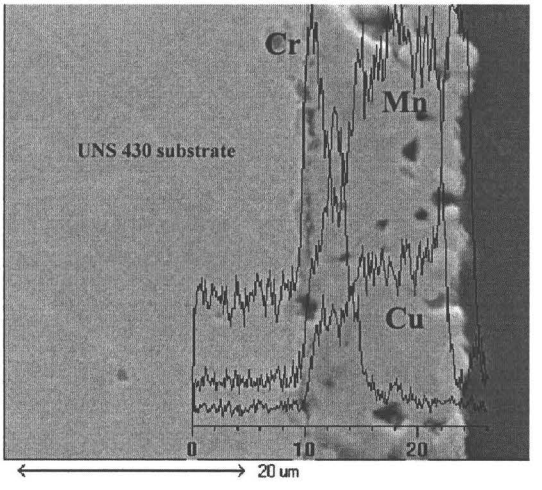

Figure 4.13 Line scan analyses of Cu-Mn spinel coating after 670 hours in air at 750°C

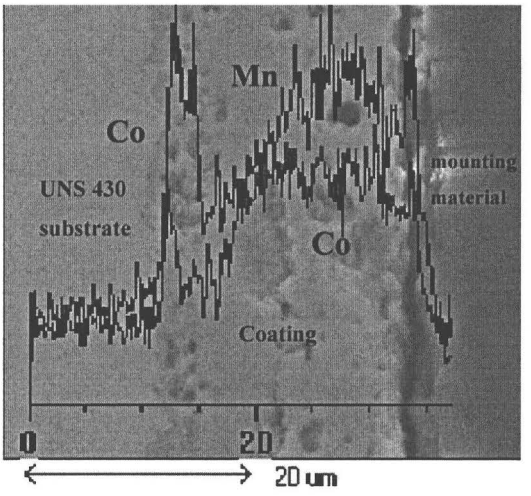

Figure 4.14 Line scan analyses of Co-Mn spinel coating after 670 hours in air at 750°C

For Cu-Mn coating, Cu diffused outward and Mn diffused inward, forming a homogeneous solid solution of Cu-Mn near the surface. It can be seen that the concentration of Mn in Cu-Mn solid solution was lower than that in Fe-Cr alloy. The reason is not clear. A possible explanation is that the chemical potential of Mn in Cu-Mn solid solution is higher than that in Fe-Cr alloy at the same concentration of Mn. Therefore, Mn diffuses from the Cu-Mn alloy into the Fe-Cr alloy, which results in lower Mn concentration in Cu-Mn. Fig. 4.10 shows that Co and Mn coatings form a solid solution at the surface during the annealing. After 670 hours oxidation at 750°C, XRD analyses (Figs. 4.11 and 4.12) demonstrated that Cu-Mn and Co-Mn metallic thin films have transformed to the corresponding spinel. Line scan analyses showed that surface layers were composed of Cu-Mn and Co-Mn oxides (figures 4.13 and 4.14). The spinel coatings are continuous and relatively dense. Based on the above results, it is clear that spinel coatings can be formed through the method of electroplating and subsequent heat treatment.

4.5 Electrical conductivity measurement

The rod samples which were used for electrical conductivity measurement followed the same sample procedure as the coupons. After annealing, the samples were heated to 750°C at a heating rate of 3°C/min. The area specific resistances (ASR) of the rod samples after oxidation for 1500 hours in air at 750°C are shown in fig. 4.15. The data recording started at the fourth day of the experiment. It is assumed that the resistivity of the metallic substrate is negligible compared to that of the oxide layer thermally grown on the surface of the steel. It can be seen that the steel with Cu-Mn and Co-Mn spinel coating shows no apparent change of ASR, while uncoated steel shows gradual increase in ASR. After oxidation at 750°C for 1500 hours, the ASR of both

samples with Cu-Mn and Co-Mn spinel coatings was 0.003 $\Omega \cdot cm^2$, while the ASR of uncoated steel was 0.189 $\Omega \cdot cm^2$. The uncoated sample shows a resistance increase by a factor of approximately 60 over the coated samples. Chen et al. (2005) showed that the ASR of 430 stainless steel with Co-Mn spinel coating at 850°C was 0.0025 $\Omega \cdot cm^2$, but the sample was initially oxidized for 60 h at 800°C, followed by an additional cyclic oxidation at 850°C for 120 h.

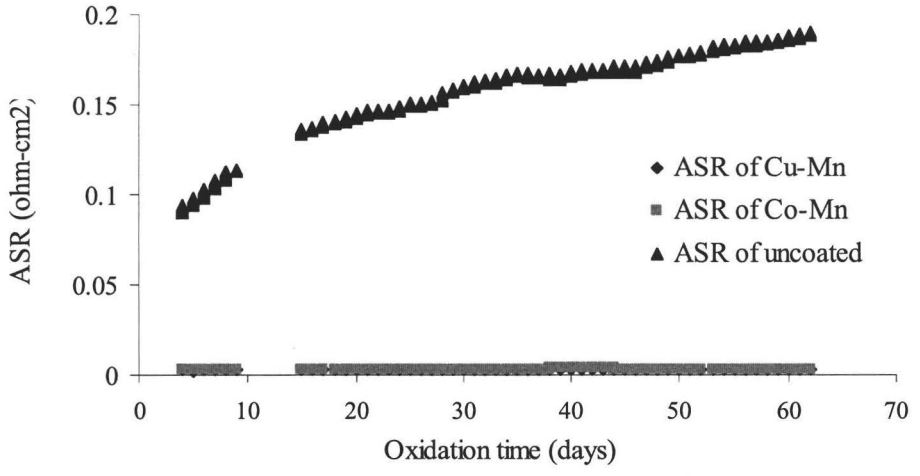

Figure 4.15 ASRs of the coated samples with oxidation time

The cross-sections of the rod samples are shown in Figs. 4.16 and 4.17. From fig. 4.16, it can be seen that the oxide scales on Cu-Mn coated samples were composed of two layers. The line scan analysis shows that the top layer was mainly Cu-Mn oxide with some dissolved iron, and the bottom layer was Cu-Mn-Cr-Fe mixed oxide. A cross-section of the sample of Co-Mn spinel is shown in fig. 4.17. According to the line scan analyses, the oxide scale on the surface was composed mainly of Mn and Co with little dissolution of iron. Cr oxide forms only at the interface between the spinel and substrate. A cross-section of uncoated samples is shown in fig. 4.18. It can be seen that a thin layer of Cr oxide has formed on the surface. Based on these results, the spinel coating can effectively reduce the contact resistance of UNS 430 stainless steel.

Comparing the Co-Mn and Cu-Mn coated samples with the uncoated sample, it can be seen that the ASRs of the coated samples are much lower than that of the uncoated UNS 430 sample (fig. 4.15). According to the line scan analyses (fig. 4.16), after 1500 hours oxidation, a Cu-Mn-Cr-Fe oxide mixture forms at the interface between Cu-Mn spinel and the substrate, while a very thin layer of Cr oxide forms at the interface between Co-Mn spinel and the substrate (fig. 4.17). Therefore, the line scan analyses confirm the previous assertion that Co-Mn spinel is better able to impede the inward diffusion of oxygen than Cu-Mn spinel. Literature data on the electrical conductivity shows that Cu-Mn spinel has higher conductivity than Co-Mn spinel. (Ling 2005). However, the measurement showed no significant difference of electrical conductivity

between Cu-Mn and Co-Mn coated samples. For 430 stainless steel with Co-Mn spinel coating, the literature (Chen 2005) shows a very similar ASR value to this study. However, their testing temperature, pre-oxidation process, and duration time were totally different.

For the uncoated samples, the oxide forming on the surface is normally Cr_2O_3 (Kurokawa 2004). As the electrical conductivity of Cr_2O_3 is much lower than those of Cu-Mn and Co-Mn spinel, it is not strange that the ASR of uncoated samples is much higher than those of the samples with Cu-Mn and Co-Mn spinel coatings. Comparing the cross-sectional images of the Co-Mn coated sample with that of the uncoated sample (figs. 4.17 and 4.18), it can be seen that the Cr oxide forming on the surface of the uncoated sample has almost the same thickness as that growing at the interface of the Co-Mn coated sample. The white external layer is Pt paste in figs. 4.16-4.18.

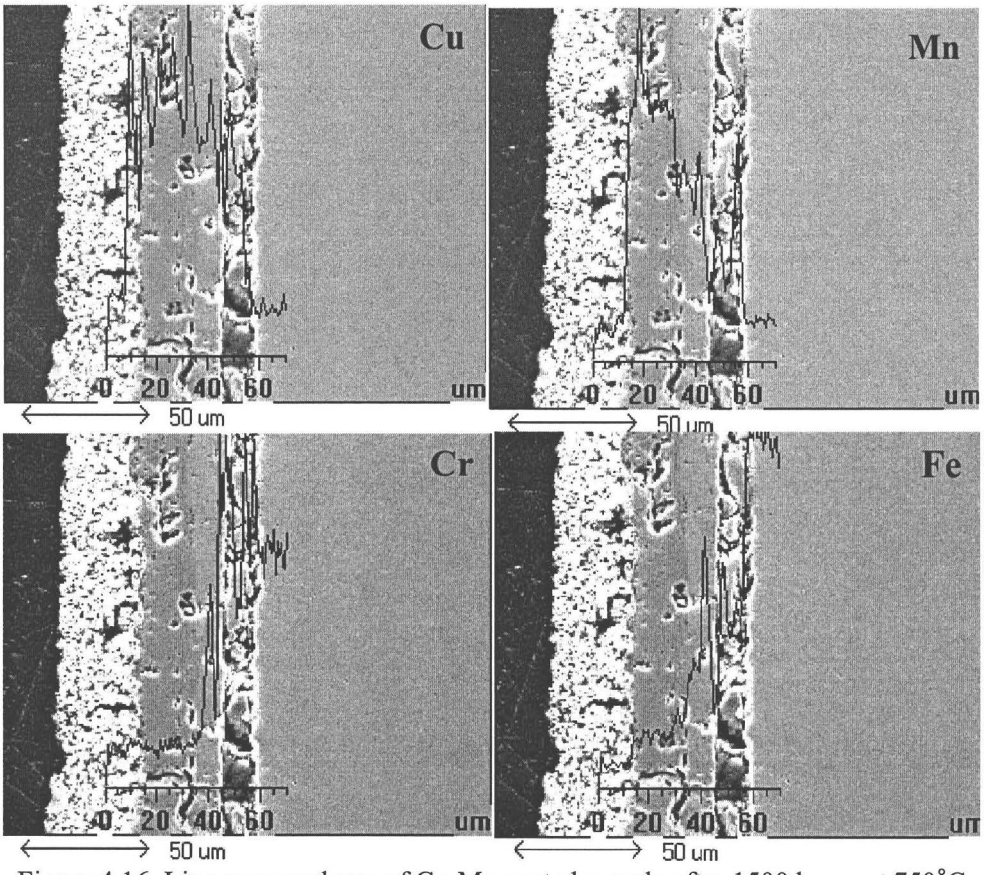

Figure 4.16 Line scan analyses of Cu-Mn coated sample after 1500 hours at 750°C

It is clear that the Cr oxide growing at the interface of the Co-Mn coated sample is not Cr_2O_3; otherwise, the ASR of the sample should be higher. Based on line scan

analyses, the Co content at the interface is higher than that of Mn. According to the data (Ling 2005), Co-Cr spinel has a conductivity of 7.1 S/cm at 800°C, and its stability is relatively high, which means that its formation is highly probable. Therefore, it was deduced that the oxide formed at the interface between Co-Mn spinel and the substrate was Co-Cr spinel.

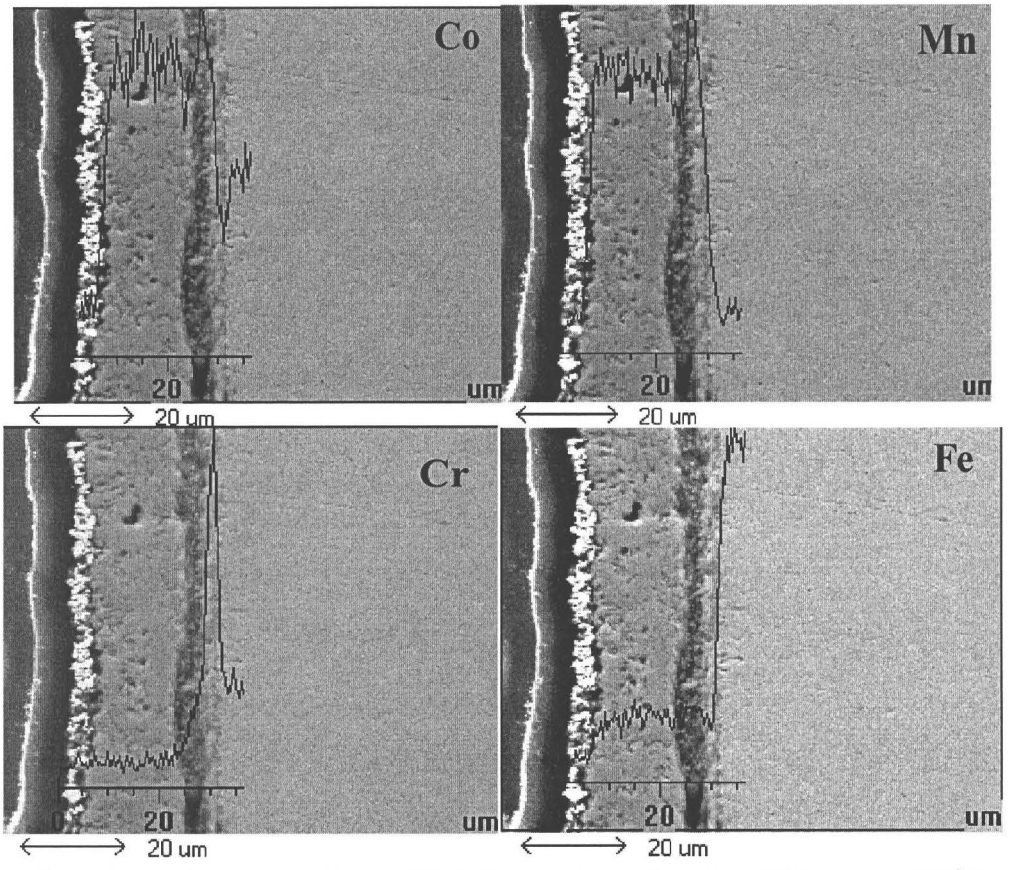

Figure 4.17 Line scan analyses of Co-Mn coated samples after 1500 hours at 750°C

In order to validate the assumption, point analyses at every micron were done by EDS (fig. 4.19). "0" μm in the graph represents the interface between Co-Mn spinel and the substrate on the left side. It is clear that an oxide rich in Cr exists only up to 2 μm from the interface. The dissolution of Fe in the spinel is very low, and the concentration of Cr in the spinel is lower than Fe. There is a Cr depletion zone in the substrate within 1 um of the interface, which is due to the formation of Cr-rich oxides at the interface. Semi-quantitative EDS analyses seems to support the idea that a mixed spinel $(Mn,Co,Fe,Cr)_3O_4$ has replaced the corundum layer, but further quantitative analyses is required.

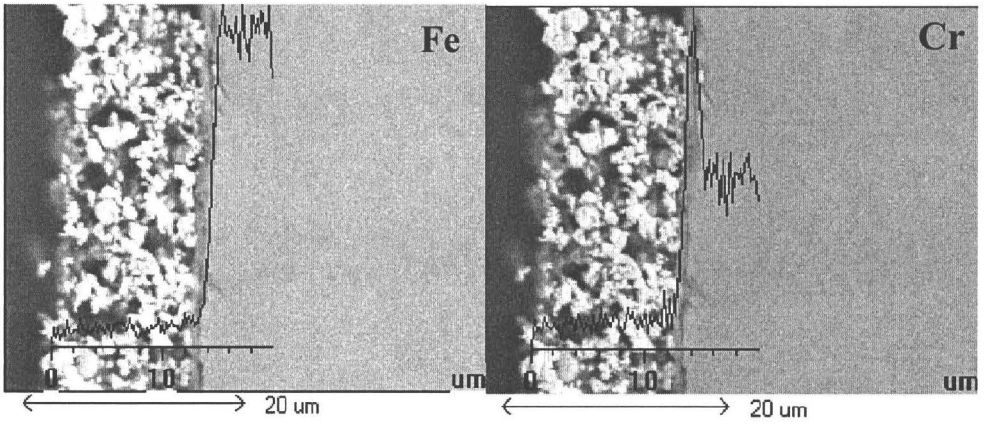

Figure 4.18 Line scan analyses of uncoated sample after 1500 hours in air at 750°C

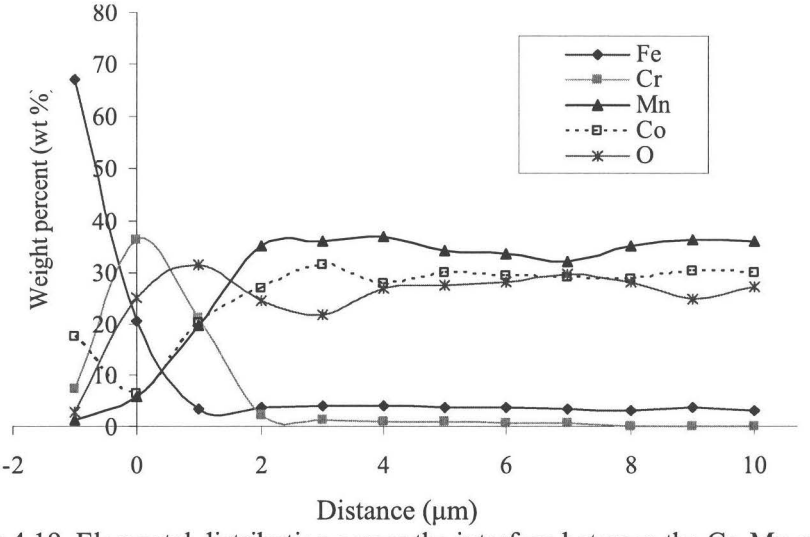

Figure 4.19 Elemental distribution across the interface between the Co-Mn spinel coating and substrate

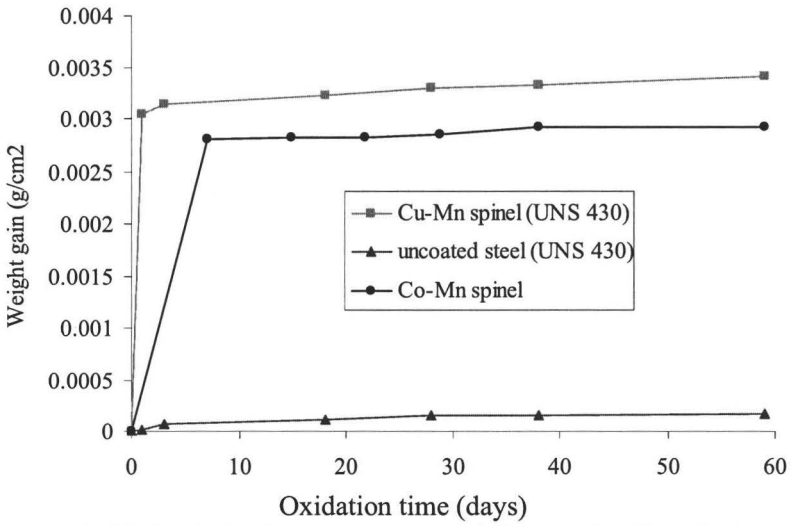

Figure 4.20 Oxidation behavior of UNS 430 stainless steel with and without spinel coatings at 750°C

4.6 Oxidation behavior of Cu-Mn and Co-Mn coated samples

In order to study the oxidation behavior of Co-Mn and Cu-Mn coated samples, the coupons were annealed at 800°C in argon for two hours before oxidation, following the same sample preparation procedure as that of the rod samples. After that, the samples were heated to 750°C at a heating rate of 3°C/min. The oxidation behavior of the coupon samples with and without the spinel coatings at 750°C is shown in fig. 4.20. It is clear that weight gains of the coated samples increase insignificantly after the first few days oxidation, which means that protective coatings have formed. It can be seen that, compared with the uncoated sample, weight gains of the coated samples are much higher. This should be related to the transformation process of the metallic thin films to spinel. The metallic thin films oxidized to form the corresponding oxides at first, and then these oxides reacted with each other to form the spinel. Considering the thickness of the spinel layers was much larger than that of Cr_2O_3 which formed on the bare sample surface, it is not unexpected that the weight gains of the coated samples are much higher than that of the uncoated samples. Surface morphologies of the coupon samples after annealing for 670 hours at 750°C in air are shown in fig. 4.21. It can be seen that both surfaces were covered with dense oxide crystals. XRD patterns (Figs. 4.11 and 4.12) demonstrated that the Cu-Mn and Co-Mn spinels formed on the surface. Even after 59 days oxidation at 750°C, the coatings maintained good bonding with the substrate (Figs. 4.22 and 4.23). It is clear that both spinel coatings can effectively improve oxidation resistance of the substrate (fig. 4.20).

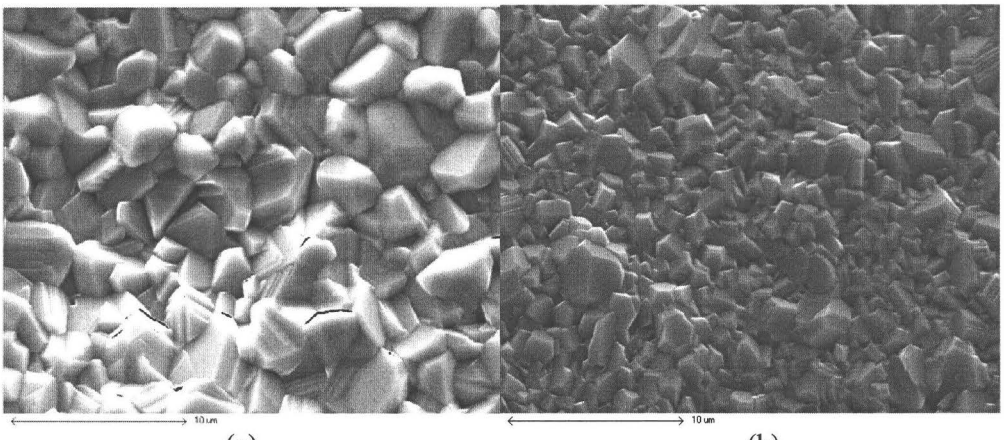

(a) (b)

Figure 4.21 Surface morphology of spinel coatings (a) Cu-Mn spinel (b) Co-Mn spinel

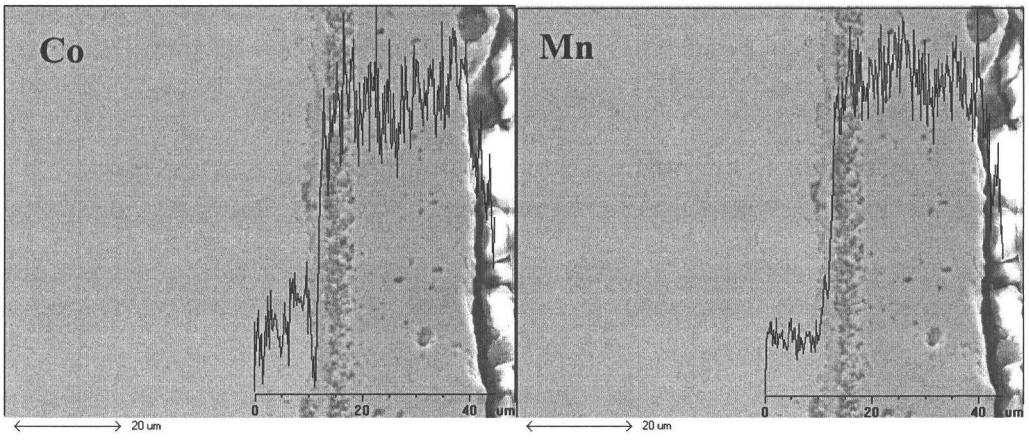

Figure 4.22 Line scan analyses after oxidation at 750°C for 1500 hours (Co-Mn)

4.7 Transformation mechanisms of Cu-Mn metallic thin films to the spinel coating

Although the method to obtain the spinel coatings on the metallic substrate has been presented, the mechanism of transformation from metal to spinel was unknown. Moreover, further improvement on coating quality is necessary for real applications. If we compare cross-section images of the coated samples (figs. 4.16-4.17), we can see that oxidation behavior of Cu-Mn coated samples is more complicated than that of Co-Mn coated samples. Therefore, Cu-Mn coated coupons were chosen for the study in order to understand the transformation mechanism from metallic thin films to spinel coatings.

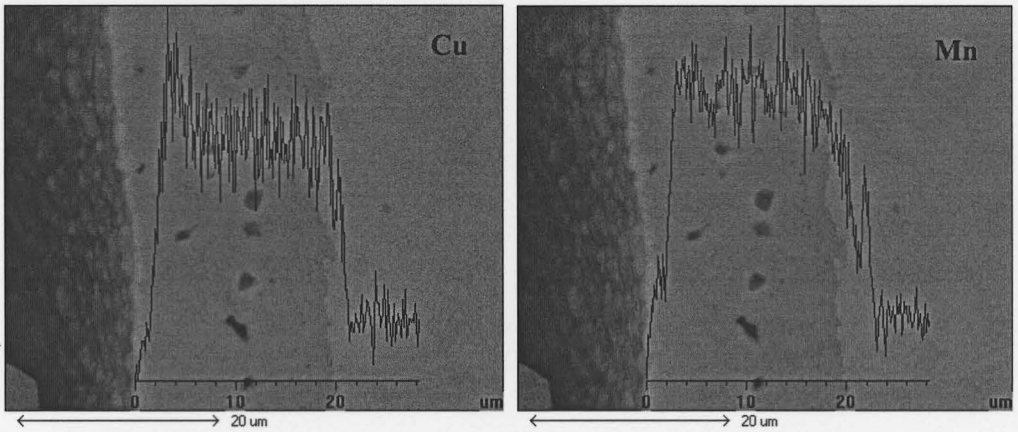

Figure 4.23 Line scan analyses after oxidation at 750°C for 1500 hours (Cu-Mn)

4.7.1 Oxidation of Cu-Mn coatings at different temperatures

The surface morphologies of the coated samples after oxidation at different temperatures are shown in fig. 4.24. It can be seen that as the oxidation temperature increases, the grain size of the oxides on the top surface increases. There were cracks on the oxide layer after oxidation at 950°C. The weight gains of the coated samples are shown in fig. 4.25 and table 4.6. It is clear that the weigh gains increase with oxidation temperature. At oxidation temperatures below 850°C, after an initial quick increase, the weight gain approached a constant value with time but oxidation at 950°C resulted in a continuous weight increase.

Table 4.6 Weight gains of coated samples at different temperatures

Temp./time (h)	600°C/96 hours	750°C/208 hours	850°C/120 hours	950°C/24 hours
Weight gain (g/cm^2)	0.0030	0.0030	0.0066	0.0122

As discussed before, weight gains of the coated samples included those due to oxidation of the metallic thin films, which resulted in the initial high oxidation rate. The higher levels of weight gains at higher temperatures (850°C, 950°C) can be correlated to the oxidation of the substrate. Cross-sectional images also showed that the thickness of the oxide scales at 850°C and 950°C was much larger than those at 600°C and 750°C (fig. 4.26). After oxidation at 950°C, cracks occurred in the oxide layer (fig. 4.26), and they probably happened during cooling to room temperature. Line scan analyses showed that a transition layer formed between the top dense coating and substrate at 850°C and 950°C (fig. 4.27 and 4.28). The layer was composed mainly of Fe-Cr oxides with dissolved Cu and Mn, which meant that the formation of the transition layer was due to oxidation of the substrate. Clearly, the Cu-Mn spinel coating on the surface can effectively protect the

substrate based on the insignificant variation of the weigh gains after its formation at temperatures up to 850°C (fig. 4.25).

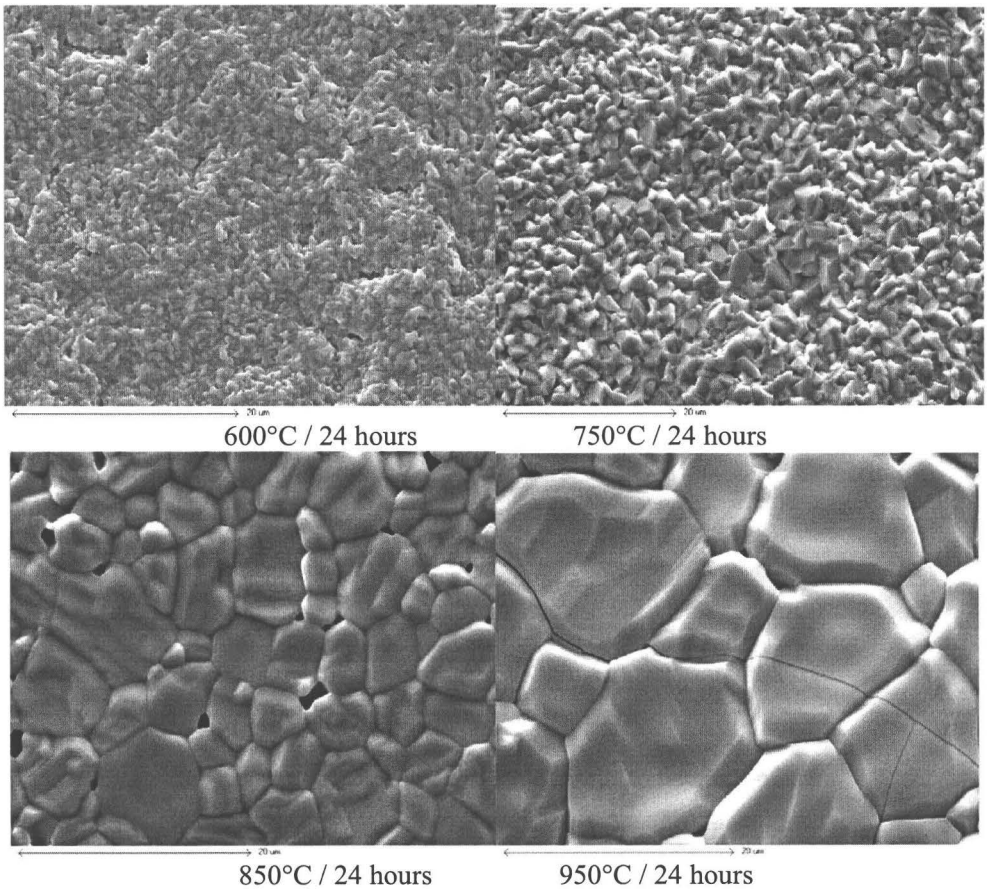

600°C / 24 hours 750°C / 24 hours

850°C / 24 hours 950°C / 24 hours

Figure 4.24 Surface morphology of Cu-Mn coated samples

At 950°C, formation of the cracks in the spinel coating facilitated the inward diffusion of oxygen during cycling, and resulted in further increase of the weight gain during the subsequent oxidation periods. It was proposed that the transition layer forming at 850°C and 950°C should happen before the formation of the spinel coatings. Otherwise, the weight gain should keep increasing with time at 850°C. Clearly, the transformation of the metallic coating to the spinel coating took some time, during which there was no protection for the substrate. This resulted in heavier oxidation of the substrate with increasing temperature, which is consistent with the results from fig. 4.25.

Comparing the curve at 600°C with that at 750°C in fig. 4.25, it can be seen that the weight gain at 600°C at last reaches the same level as that at 750°C. As 600°C is a relatively low temperature, the oxidation of the substrate during the spinel transformation process should be very small. Thus, we can conclude that the total weight gain of the

oxidation at 750°C is due to the oxidation of the metallic thin films. The oxidation of the substrate at this temperature during the transformation process is negligible. At 600°C, XRD analyses showed that the coating was composed of Mn_2O_3, CuO, a tetragonal phase, and a cubic phase Cu-Mn spinel within the first 6 hours oxidation. The tetragonal and cubic phases could be Cu-Mn solid solution or Mn_3O_4.

The Mn-O phase diagram (fig. 4.33) shows Mn_3O_4 with cubic structure exists only at temperatures above 1170°C. The later high-temperature x-ray diffraction data show that Cu-Mn spinel with tetragonal symmetry can only occur with Cu less than 0.8. Therefore, high concentrations of Cu in the coating can't lead to formation of Cu-Mn spinel with tetragonal symmetry. Therefore, the cubic phase is Cu-Mn spinel and the tetragonal phase is Mn3O4. After 24 hours, Mn3O4 was gone and the remaining phases were Mn2O3, CuO and Cu-Mn spinel (fig. 4.29). Even after 96 hours at 600°C, there was no significant change of the phases in the oxide scale.

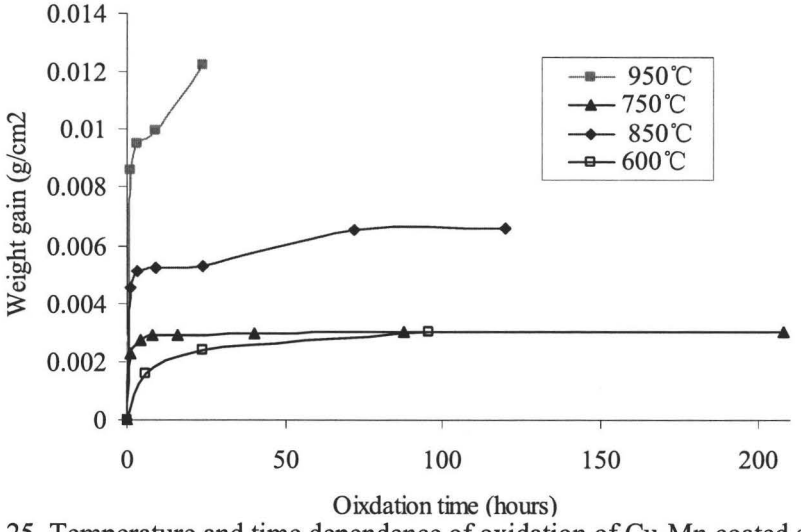

Figure 4.25 Temperature and time dependence of oxidation of Cu-Mn coated stainless steel

According to the Gibbs phase rule, three phases can't coexist in a binary system except at an invariant temperature. Obviously, the equilibrium state was not reached in the experiment. The initial oxidation of copper and manganese coatings led to formation of Mn3O4 and CuO, both of which were not equilibrium phases at this temperature. As oxidation continued, Mn3O4 disappeared and CuO reacted with Mn2O3 to form spinel. At 750°C, the oxide scales consisted of CuO and Cu-Mn spinel (fig. 4.30) after one day, and this did not change even after 59 days oxidation (fig. 4.31), which means that transformation of Cu-Mn metallic thin films to the spinel took one day or less. This result is consistent with that shown in fig. 4.25, where the weight gain at 750°C did not change after 24 hours oxidation as the spinel coating prevented the substrate from further oxidation.

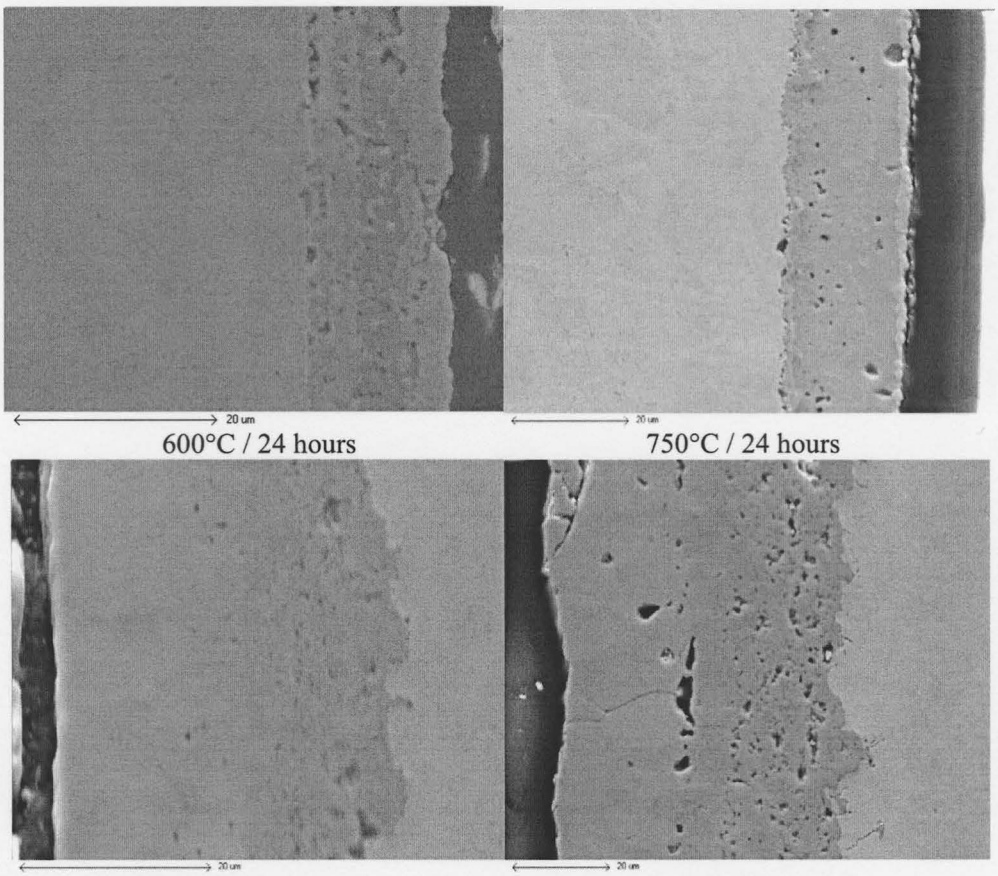

Figure 4.26 Cross-sectional images of Cu-Mn coated samples

A single Cu-Mn spinel phase formed on the surface after oxidation at 950°C for one day (fig. 4.32). Fig. 4.33 shows a line scan analyses after oxidation at 600°C for 1 day. Clearly, Cu and Mn compositions in the coating were not homogeneous. The outer and inner layers were rich in Cu and the middle was mainly Mn. There was rapid outward diffusion of Cu through Mn. EDS analyses showed that the inner layer (next to the substrate) was composed of Mn, Cu, Fe, Cr and oxygen, and it is hard to tell which phases existed in this layer (table 4.7). The middle layer was a solid oxide solution of Cu in Mn, and the top layer contained mainly Cu and a little Mn. If we combine the analyses from XRD and EDS, the phases at the top layer should be Mn_2O_3, CuO and Cu-Mn spinel, but it was difficult to locate the spinel. Formation of the oxides is due to inward diffusion of oxygen. Clearly, the diffusion rate of Mn in Cu is much lower than that of Cu in Mn.

After oxidation at 750°C for one day or more, the phases were CuO and Cu-Mn spinel (fig. 4.30 and 4.31). Line scan analyses showed that the outer surface was rich in Cu. In other areas, the distribution of Cu and Mn was homogeneous (fig. 4.23 and 4.35).

The longer the oxidation time, the more homogeneous the distribution of elements in the oxide scales (fig. 4.23). EDS analyses (table 4.8) suggests that the top surface is CuO with some dissolved Mn, and the bottom layer is spinel phase, which is consistent with XRD analyses (fig. 4.30).

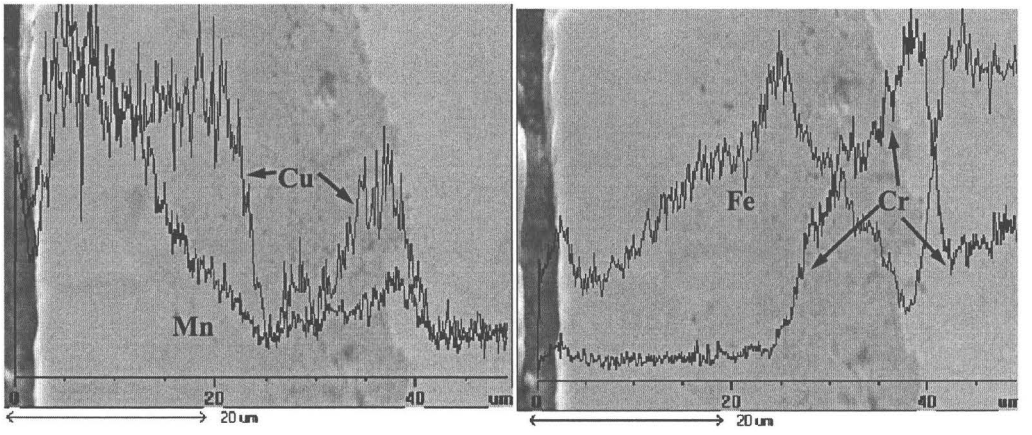

Figure 4.27 Line scan analyses after oxidation at 850°C for 1 day

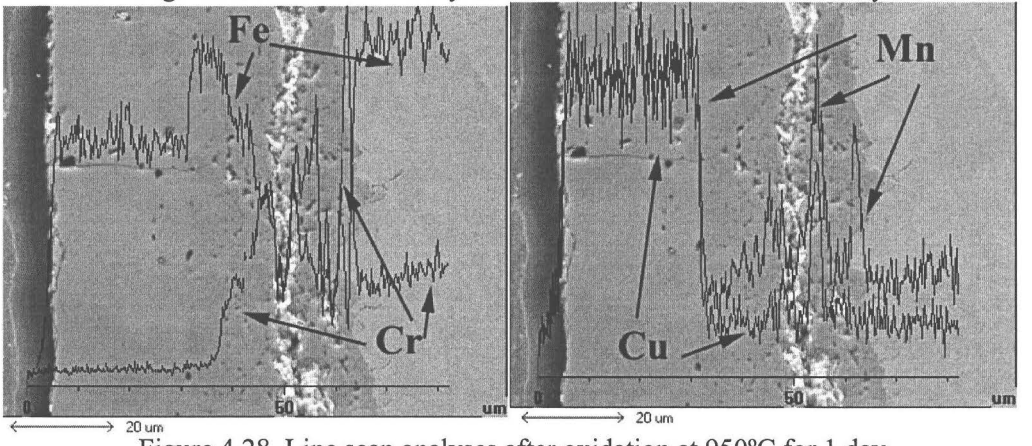

Figure 4.28 Line scan analyses after oxidation at 950°C for 1 day

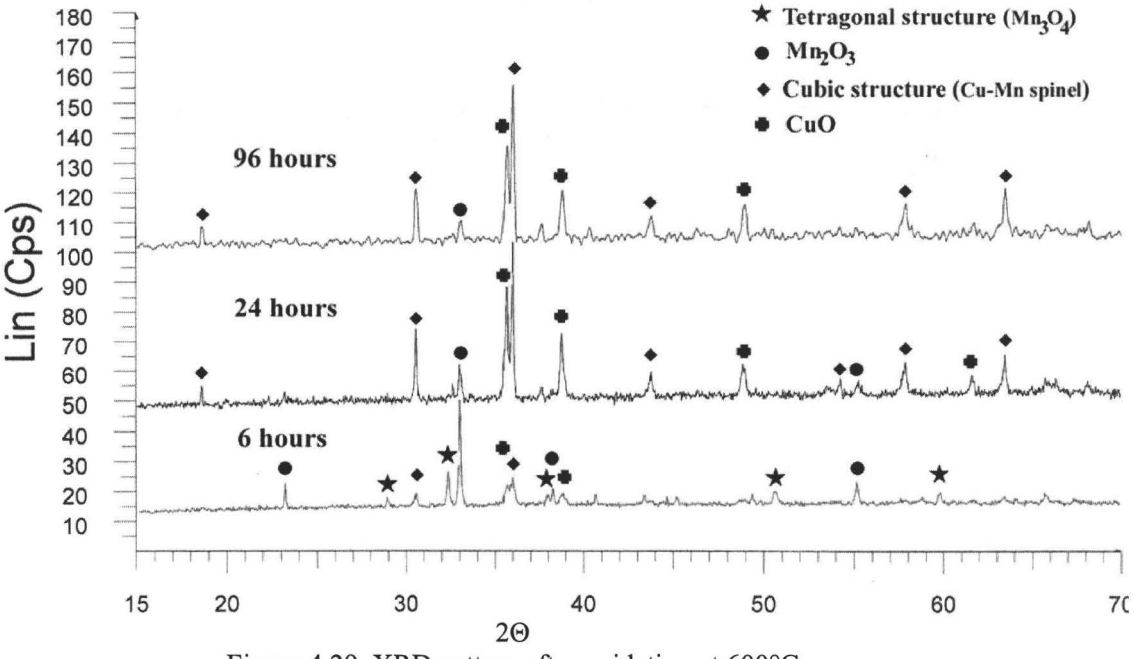

Figure 4.29 XRD pattern after oxidation at 600°C

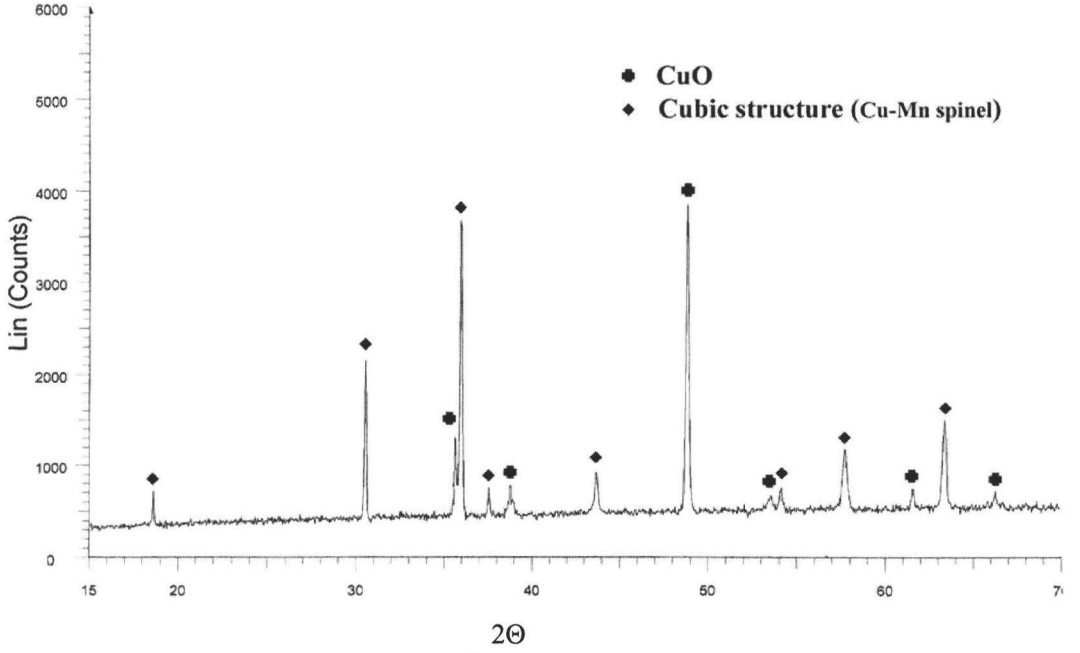

Figure 4.30 XRD pattern after oxidation at 750°C for one day

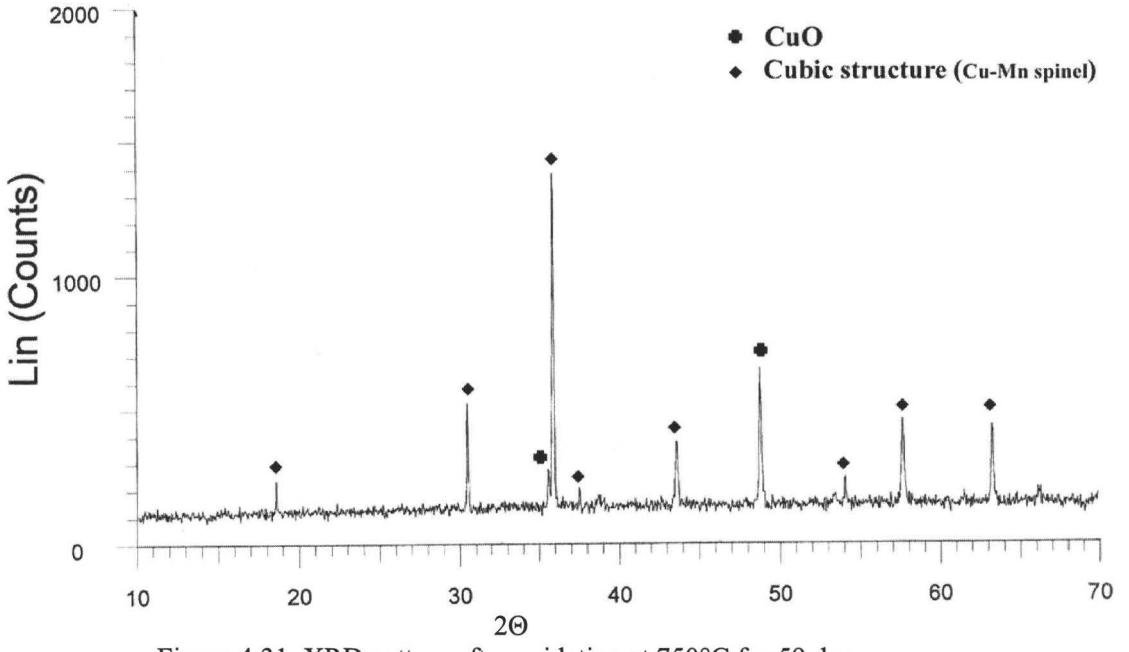

Figure 4.31 XRD pattern after oxidation at 750°C for 59 days

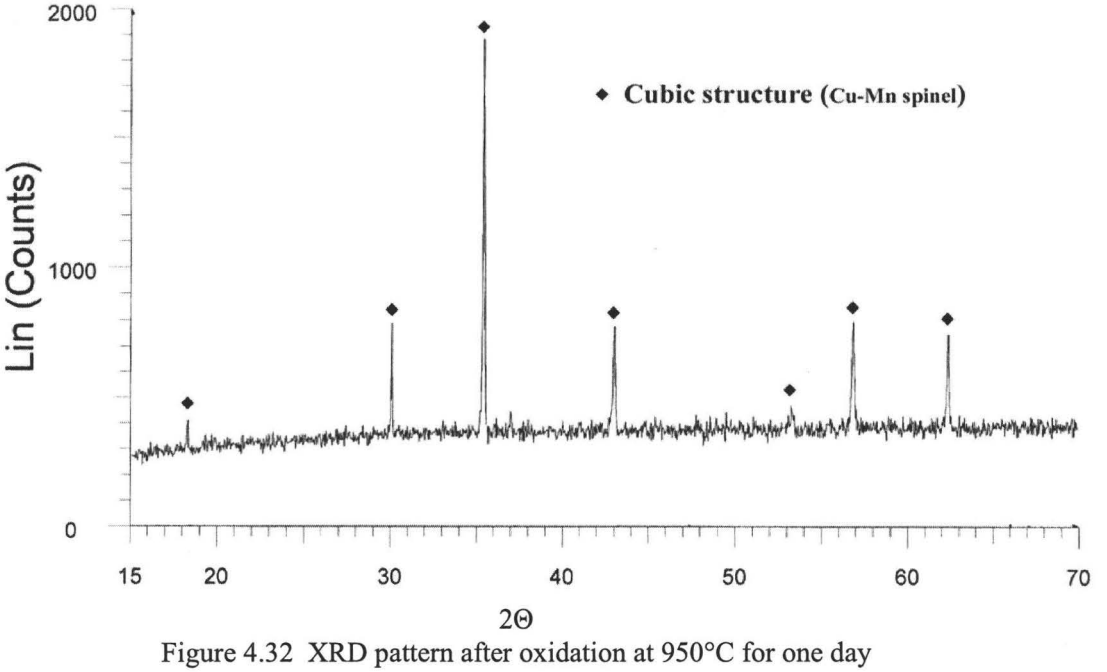

Figure 4.32 XRD pattern after oxidation at 950°C for one day

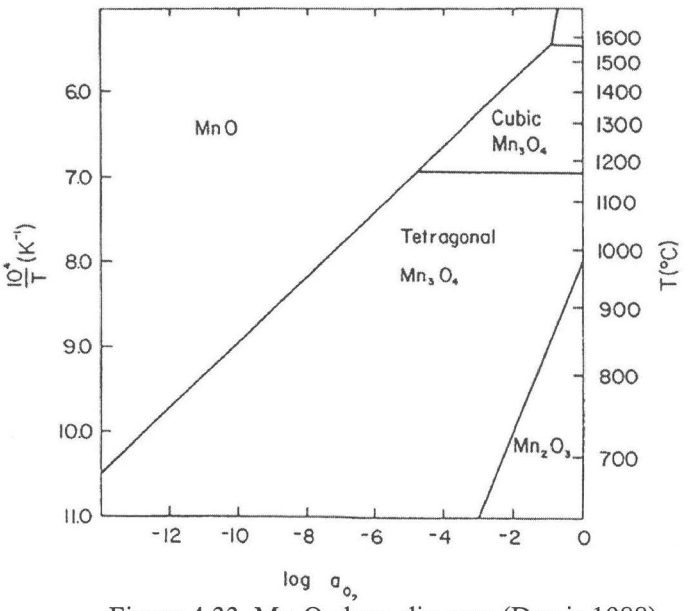

Figure 4.33 Mn-O phase diagram (Dorris 1988)

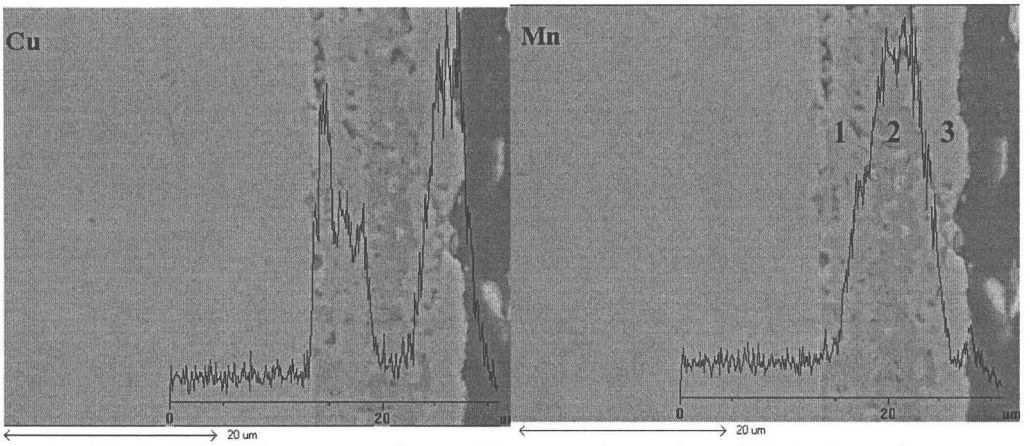

Figure 4.34 Line scan analyses of the coated sample at 600°C after 1 day

Table 4.7 EDS analysis of the oxide layers after oxidation at 600°C for 1 day

	1		2		3	
Elements	Wt%	At%	Wt%	At%	Wt%	At%
O	14.09	37.94	20.47	14.32	13.29	37.30
Cr	2.25	1.87	0.42	0.48		
Mn	7.36	5.77	72.75	79.93	12.76	10.43
Fe	29.00	22.37	0.21	0.22		
Cu	47.30	32.06	6.16	5.06	73.94	52.27

Table 4.8 EDS analysis of the oxide layers after oxidation at 750°C for 1 day

	Top thin layer		Bottom layer	
Element	Weight%	Atomic%	Weight%	Atomic%
O K	19.68	49.20	25.68	55.89
Mn K	2.27	1.65	38.53	24.42
Cu K	78.05	49.15	34.73	19.03
Fe K			1.06	0.66

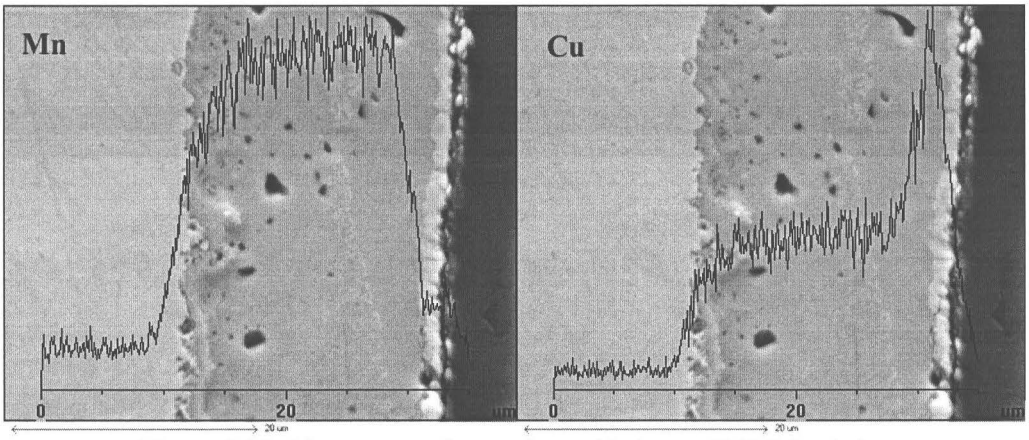

Figure 4.35 Line scan analyses after oxidation at 750°C for 1 day

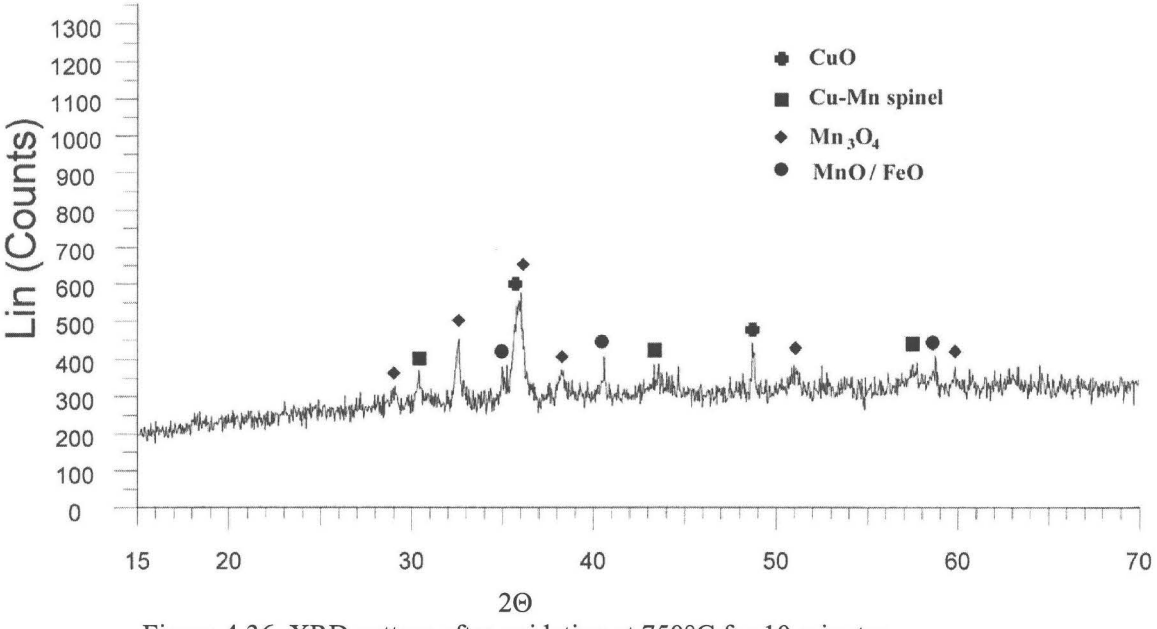

Figure 4.36 XRD pattern after oxidation at 750°C for 10 minutes

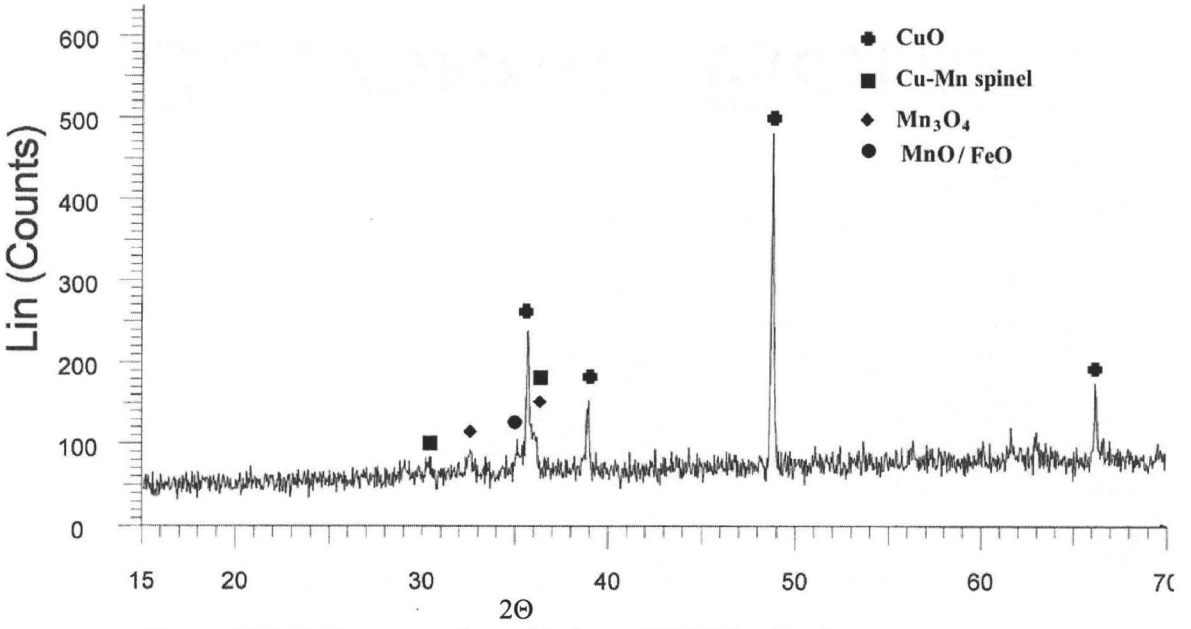

Figure 4.37 XRD pattern after oxidation at 750°C for 60 minutes

4.7.2 Transformation mechanisms studying at 750°C

Based on the previous analyses, the formation of the spinel needs some time, and 750°C is an optimum temperature for transformation of the metallic thin films to the spinel layers. Higher temperature caused heavy oxidation of the substrate ($\geq$ 850°C), and lower temperatures ($\leq$ 600°C) needed longer time to form the protective layer. In order to investigate the details of the transformation at 750°C, two samples were put into a furnace after 750°C was reached, and held for 10 or 60 minutes. XRD analyses showed that MnO, Mn_3O_4, CuO and Cu-Mn spinel formed in the coating within the first 10 minutes (fig. 4.36). After 60 minutes, the phases did not change, but the intensity of CuO increased very quickly (fig. 4.37).

EDS results are shown in tables 4.9 and 4.10. Gold in the EDS analyses came from the sputtered gold film. After 10 minutes oxidation, the top surface consisted of MnO and Mn_3O_4 (fig. 4.38a and table 4.9a). Next to it is $(Fe,Mn)_2O_3$ (point 2 in fig. 4.38b). Point 3 (fig. 4.38b) consists of metallic copper and (Fe,Mn)O, and point 5 contains metallic copper and $(Fe,Cr,Mn)_3O_4$. Clearly, most of the copper (white area in the middle represented by points 3 and 5) still exists in metallic form within the initial 10 minutes. A grey area surrounded by points 3 and 5 (point 4) shows FeO plus CuO. The layer next to the substrate is $(Fe,Cr,Mn)_3O_4$. All the phases in the oxides are shown in fig. 4.39 based on EDS analyses. It can be seen that the manganese coating is quickly oxidized but most of the copper remains in its metallic form after the first 10 minutes of oxidation. Iron diffuses outward through copper and forms iron oxides underneath the

manganese oxides. Chromium does not diffuse outward but forms an oxide layer next to the substrate.

Table 4.9a EDS analysis of the oxide scale after 10 minutes at 750°C

	1a		1b	
Elements	Wt%	At%	Wt%	At %
O	27.15	56.45	22.92	50.78
Cr	0.15	0.10		
Mn	59.51	36.04	70.71	45.63
Fe	11.94	7.11	5.14	3.26
Cu	0.26	0.14	0.25	0.14
Au	0.98	0.17	0.98	0.18

Table 4.9b EDS analysis of the oxide scale after 10 minutes at 750°C

	2		3		4		5		6	
Elements	Wt%	At %	Wt%	At %	Wt%	At %	Wt%	At %	Wt%	At%
O	30.55	60.70	1.32	5.07	21.77	49.67	5.57	18.76	28.22	57.41
Cr	0.28	0.17	0.47	0.55	1.18	0.83	4.00	4.14	24.26	15.19
Mn	28.22	16.33	1.38	1.54	12.50	8.30	2.26	2.21	3.78	2.24
Fe	39.35	22.40	3.49	3.83	57.16	37.36	7.85	7.57	42.25	24.63
Cu	0.44	0.22	91.77	88.52	6.35	3.65	79.03	66.96	0.83	0.42
Au	1.16	0.19	1.57	0.49	1.03	0.19	1.29	0.35	0.67	0.11

Table 4.10 EDS analysis of the oxide scale after 60 minutes at 750°C

	1		2		3		4		5	
Elements	Wt%	At%	Wt%	At%	Wt%	At%	Wt%	At%	Wt%	At%
O	13.27	40.36	20.69	50.18	19.40	48.00	8.27	27.12	23.31	52.89
Cr			0.30	0.22	0.63	0.48	7.75	7.82	22.84	15.94
Mn	4.32	3.83	16.12	11.39	5.42	3.90	1.92	1.83	1.44	0.95
Fe	1.19	1.04	50.84	35.33	63.85	45.25	12.42	11.66	43.64	28.36
Cu	66.86	51.22	1.23	0.75	0.51	0.32	59.08	48.76	0.63	0.36
Au	14.36	3.55	10.81	2.13	10.18	2.05	10.56	2.81	8.14	1.50

After one hour oxidation, a CuO layer forms on the outer surface (point 1 in fig. 4.40 and table 4.10). Points 2 and 3 (fig. 4.40) are a mixture of FeO and Mn_3O_4. Point 4 (fig. 4.40) contains metallic copper plus $(Fe,Cr)_3O_4$, and point 5 is $(Fe,Cr)_3O_4$. All the phases in the oxide layers are shown in fig. 4.41. Clearly, copper diffuses very quickly outward through manganese and iron oxide and forms CuO at the top surface, but some as-deposited copper coatings remain unoxidized. $(Fe,Cr)_3O_4$ forms at the interface between the oxides and substrate, and there is no outward diffusion of chromium.

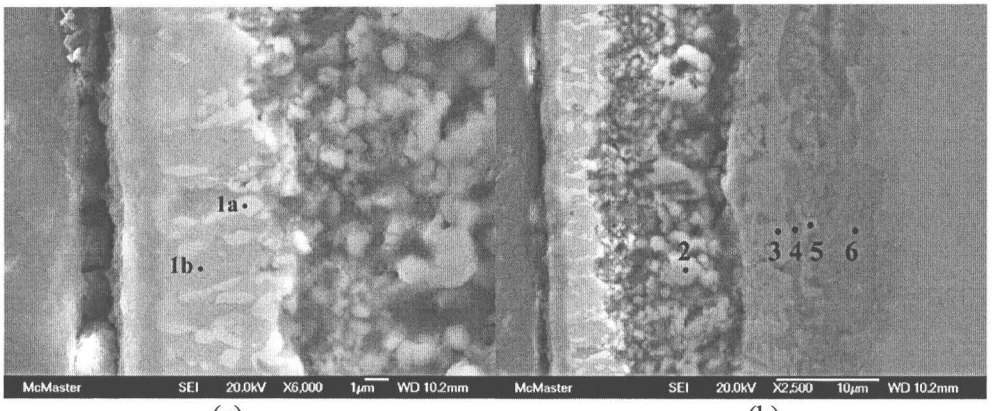

(a) (b)

Figure 4.38 Cross section after 10 minutes oxidation at 750°C

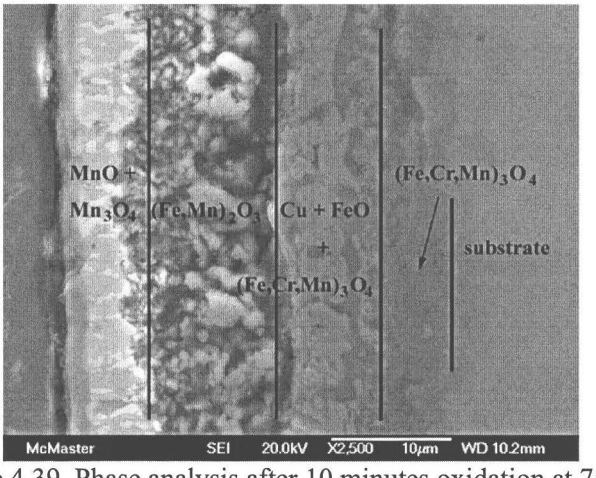

Figure 4.39 Phase analysis after 10 minutes oxidation at 750°C

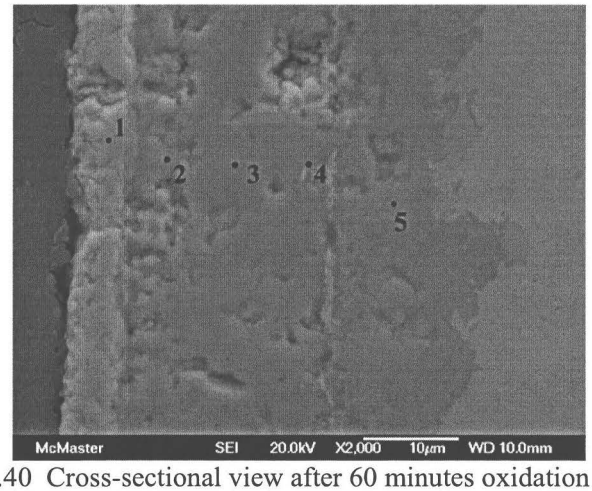

Figure 4.40 Cross-sectional view after 60 minutes oxidation at 750°C

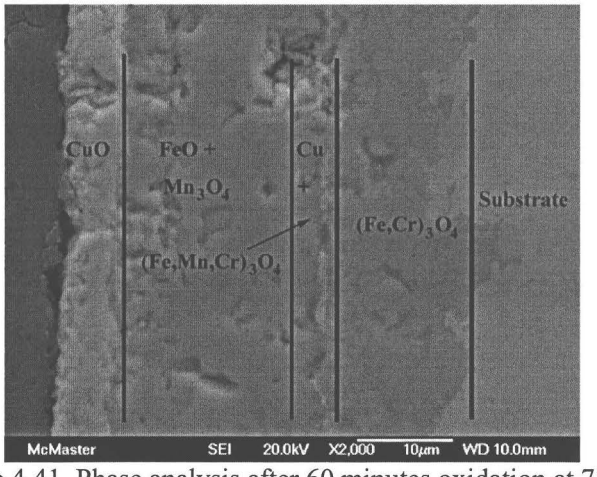

Figure 4.41 Phase analysis after 60 minutes oxidation at 750°C

Clearly, EDS results (fig. 4.39 and 4.41) are quite consistent with XRD data (fig. 3.36 and 3.37). Moreover, based on XRD analysis, there is CuO existing in the oxides after the first 10 minutes oxidation. However, no detectable amount of CuO is determined by EDS (fig. 4.39). This is probably because the amount of Cu-Mn spinel and CuO in the oxides is very low at the initial oxidation stage, which makes their analyses through EDS difficult. XRD analyses shows that the amount of CuO at the surface increases significantly after 60 minutes oxidation (fig. 4.37), compared with that after 10 minutes oxidation (fig. 4.36). EDS also found a thick CuO layer formed on the top surface. Based on this information, it is deduced that CuO forms at the surface through outward diffusion of copper. As manganese oxides and iron oxides are more stable than copper oxides, the formation of copper oxides inside the coating is not favored. After 24 hours oxidation, the oxide structure is composed of a thin CuO layer at

the top surface and thick bottom layer of Cu-Mn spinel (fig. 4.35 and table 4.12). Formation of Cu-rich oxide on the top surface was also reported in the literatures when studying oxidation of Cu-Mn alloys (Ansel 1993; Nanni 1979). Clearly, Cu-Mn spinel layer forms through reactions between copper oxides and manganese oxides. As CuO is scare at the initial oxidation stage, Cu-Mn spinel is not detectable by EDS. Oxidation of manganese, iron and the metallic substrate is through inward diffusion of oxygen. The nature and sequence of formation of the underlying layers correspond to the formation of oxides which are more stable. The chemical potential of oxygen from the external surface decreases to the alloy interface.

If we compare the phases at 600°C with those at 750°C, we find that the oxide scales consist of Mn_3O_4, Mn_2O_3, CuO and very little Cu-Mn spinel within the first 6 hours of oxidation at 600°C. 24 hours later, Mn_3O_4 disappears. Mn_2O_3, CuO and spinel phase exist after 96 hours oxidation at 600°C (fig. 4.29), while MnO, Mn_3O_4, CuO and the spinel formed within the first hour of oxidation at 750°C (fig. 4.37). Clearly, Mn_2O_3 persists at low temperature (600°C), while Mn_3O_4 are the stable phases at the higher temperatures and lower oxygen pressure, which is consistent with the phase diagram (figs. 2.4 and 2.5). The literature (Ansel 1993) mentions that for Cu-36%Mn (atomic weight percent) alloys oxidized at 760°C for 100 hours, the outside layer was $Cu_xMn_{3-x}O_4$ and the internal layer was MnO, between which was a layer of Mn_3O_4. This supports the observation that MnO + Mn_3O_4 are more stable than Mn_2O_3 at 750°C.

According to a refinement of the partial Cu-Mn-O phase diagram (Broemme 1985; Vandenberghe 1973) (fig. 4.40), for the composition prepared in this thesis ($Cu_{1.3}Mn_{1.7}O_4$), the equilibrium phase is pure spinel at 600°C but at 750°C and 950°C, the phases are CuO and spinel. As the diffusion rate is low at 600°C, the equilibrium state clearly was not reached after 96 hours. The phases detected at 750°C were consistent with the phase diagram, and the phases did not change even after 59 days oxidation, which means that one day is enough for Cu-Mn-O system to reach the equilibrium state. However, the results at 950°C were not consistent with the phase diagram. The oxide scale was composed of a single Cu-Mn spinel phase after oxidation at 950°C for one day. Based on the results of the experiment at 750°C, the equilibrium state should have also been reached after one day at 950°C. The discrepancy between these results and the phase diagram (Vandenberghe 1973) could be due to the upper phase boundary of Cu-Mn-O being incorrect or the amount of CuO in the oxide scale being too low to be detected by XRD. An analysis of the experimental results revealed that oxidation of the metallic thin films was quite complicated, and a clear understanding of the mechanisms requires knowledge of the main features of the ternary Mn-Cu-O phase diagram and of the thermodynamic properties of the phases. As this system is intricate and our knowledge of it is still inadequate, a further investigation of the system was necessary.

4.8 Conclusions

An electrolysis method was developed for the removal of deleterious components of catholyte solutions prior to Mn deposition. Bright silvery and uniform Mn deposits

were obtained on UNS 430 stainless steel from the resulting beneficiated solutions prepared from reagent grade $MnSO_4$. The results show that the current efficiency of Mn deposition is influenced by the applied current density and the elapsed electrolysis time. The initial pH level of the catholyte solution does not show significant influence on current efficiency and surface morphology of Mn deposits over the pH range of 2.80 – 6.16. The maximum current efficiency of Mn deposition was obtained at a current density of 120 mA/cm^2. Current efficiency increases with increased deposition time.

Cu-Mn and Co-Mn spinel coatings were formed by a method of electroplating and subsequent heat treatment. Clearly, annealing at 800°C in Ar is beneficial to form a strong bond between the coatings and substrate. Spinel coatings can provide an effective electronic path to the metallic substrate. It is also demonstrated that the outward diffusion of Cr can be virtually suppressed by the spinel coatings.

Transformation of Cu-Mn metallic thin films to the spinel coating occurs due to reactions between CuO and Mn oxides. 750°C is an optimum temperature at which metallic Cu-Mn coatings can transform into Cu-Mn spinel without clear oxidation of the substrate. The higher the oxidation temperature, the heavier the oxidation of the substrate. The manganese coating was oxidized to Mn_3O_4 plus MnO through inward diffusion of oxygen and CuO formed at the top surface through outward diffusion of copper. The oxidation of the metallic substrate is due to inward diffusion of oxygen. Some iron diffused from the substrate into the spinel coating during the transformation; chromium was confined to the metal substrate/coating interface.

Chapter 5

Arrangement of Cations and Extent of Spinel Solid Solution in the Cu-Mn-O System

5.1 Background introduction

Based on the results from previous chapters, it can be seen that both Cu-Mn and Co-Mn spinels are promising coating materials for metallic interconnect of SOFCs. Cu-Mn spinel was found to have the highest electrical conductivity among spinel (225 S/cm at 750°C), much higher than that of Co-Mn spinel (60 S/cm at 800°C) (Petric 2007). This value is close to the electrical conductivity of the most popular cathode material, strontium doped lanthanum manganite (LSM) (290 S/cm at 1000°C) (Minh 1995). However, the mechanism of high conductivity in Cu-Mn spinel is not clear. The crystal structure information of the material is the key to understand its electrical properties. Moreover, for its application as a protective coating, it is very important to know single phase spinel boundary in Cu-Mn-O system as previous research (Martin 2007) has shown that its conductivity decreases as the second phase appears.

Investigation of the oxidation behaviors and electrical conductivities of the spinel coatings was described in chapter 4. In this chapter, high temperature x-ray and neutron diffraction analyses were used to study cation distribution in Cu-Mn spinel and phase boundary in Cu-Mn-O system. As Cu-Mn spinel coating was thick (~30 μm), the crystallographic information obtained from powder method can be applied to understanding the physical properties of the spinel coating.

5.2 In-situ XRD results

The sequence of X-ray analyses is shown schematically in fig. 5.1. All samples were initially equilibrated as single phase spinel and quenched. Each sample was then analyzed by X-ray diffraction at a series of temperatures. For $Cu_{0.8}Mn_{2.2}O_4$, the powder sample was heated to 900°C within a few seconds, and then the temperature was decreased in steps of 25°C to 600°C. After analysis at 600°C, within a few seconds, the sample was reheated directly to 900°C and then stepwise to 1150°C. For $Cu_{1.1}Mn_{1.9}O_4$, the starting point was 790°C, followed by analyses at temperatures decreasing to 535°C. Then, the temperature was increased to 790°C within a few seconds and stepwise to 1100°C. For $Cu_{1.3}Mn_{1.4}O_4$, the starting point was 750°C, and analysed with decreasing temperature to 375°C step by step. For $Cu_{1.4}Mn_{1.6}O_4$, two samples were tested. For the first one, the starting point was 550°C, and then the temperature was decreased gradually to 400°C. After that, temperature was increased to 550°C rapidly and further to 850°C step by step. For the second sample, the temperature was increased from room temperature to 1125°C step by step. Increasing and decreasing temperature from one step

to another takes only a few seconds. At each temperature, ten sets of data were collected and each set of data was collected for 24 minutes.

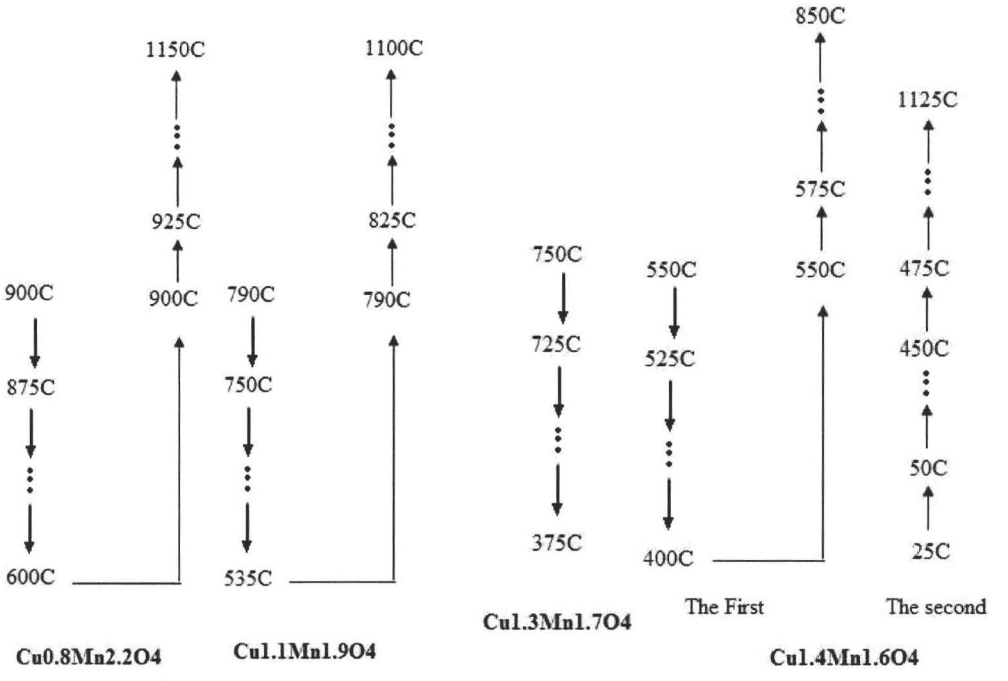

Figure 5.1 Sequence of temperatures for XRD measurement of each composition

5.2.1 The XRD analyses of $Cu_{1.1}Mn_{1.9}O_4$

The phase identification results of in-situ XRD data are shown in appendix 1. It can be seen that the phases at 535°C are Mn_2O_3 and cubic spinel. When temperature increases directly to 790°C, Mn_2O_3 quickly disappears, leaving only single spinel phase with cubic structure. From fig. 3.5, it can be seen that the spinel has cubic symmetry after quenching. A comparison of the patterns at 790°C at the beginning of the in-situ analyses and after 535°C shows that there is no difference between them, which means that the equilibrium state can be reached very quickly at this temperature. Single spinel phase with cubic symmetry exists at 725°C. As temperature decreases to 700°C, small peaks corresponding to Mn_2O_3 appear and the Mn_2O_3 phase becomes apparent at 675°C. Clearly, Mn_2O_3 starts forming at 700°C, and 700°C is regarded as the phase boundary between single phase (cubic spinel) and the two phase area (spinel plus Mn_2O_3). CuO and cubic spinel phase coexist at temperatures of 825°C and 850°C . As no CuO is found at 790°C, CuO may start forming at 825°C. Therefore, 825°C is taken as the phase boundary.

Phases at 925°C are CuO and cubic spinel. As temperature increases to 950°C, a third phase corresponding to $CuMnO_2$ with hexagonal structure appears and the amount of this phase further increases at 975°C. Meanwhile, the content of cubic spinel in the sample decreases markedly. As temperature further increases to 1000°C, CuO starts to disappear. At 1025°C, CuO can't be seen, which indicates that the phase boundary is near 1000°C. From 1000°C to 1100°C, the coexisting phases are cubic spinel and $CuMnO_2$ with hexagonal symmetry. The cubic spinel phase fraction begins to increase after 1075°C, which signals the limit of stability of $CuMnO_2$ and its transformation to spinel. Driessens et al. (Driessens 1967) investigated the interaction of copper and manganese oxides in air between 750°C and 1400°C and reported that $Cu_{1+x}Mn_{1-x}O_2$ was a crednerite-like phase with monoclinic structure ($0 < x < 0.06$) and a delafossite-like phase with hexagonal structure ($0.08 < x < 0.12$). At 1060±10°C, the delafossite structure transforms to the crednerite structure. Trari el al (2005) analyzed the structure of quenched samples of $Cu_{1+x}Mn_{1-x}O_2$ through X-ray diffraction, and found only the monoclinic distortion of crednerite. However, our in-situ X-ray analyses of $CuMnO_2$ did not detect monoclinic symmetry at temperatures up to 1100°C. It seems that the state of a sample can greatly influence the cation distribution in $CuMnO_2$, which is the same as the situation in $Cu_xMn_{3-x}O_4$ solid solutions. Quenching (metastable) normally decreases cell symmetry. This could be due to more Jahn-Teller ions, e.g., Mn^{3+}, which can form on octahedral sites and increase the degree of distortion. In order to accommodate these Jahn-Teller ions, the cell elongates along the c axis, resulting in tetragonal distortion. At high temperatures, as cations have more room, distortion is not necessary to accommodate these Jahn-Teller ions, and cubic symmetry can be maintained. The existence of three phases, CuO, cubic spinel and $CuMnO_2$, can only be explained by a non-equilibrium state.

5.2.2 The XRD analyses of $Cu_{0.8}Mn_{2.2}O_4$

X-ray diffraction analyses at 600°C shows that the phases are Mn_2O_3 and cubic spinel. Single spinel phase with cubic structure is present at 900°C and there is no difference between the patterns at 900°C at the beginning of the analyses and after analyses at 600°C. The Mn_2O_3 which coexists at 600°C disappears when temperature increases to 900°C, which means that the equilibrium state can be reached very quickly at this temperature. Figure 3.3 shows that the phase obtained after quenching in air from 900°C is tetragonal spinel. This study demonstrates that the structures obtained from in-situ and quenching experiments can be different.

Single spinel phase with cubic symmetry exists at 800°C. As temperature decreases to 775°C, small peaks corresponding to Mn_2O_3 appear and Mn_2O_3 phase becomes prominent at 750°C, which indicates that 775°C is the probable phase boundary between single phase (cubic spinel) and the two phase area (spinel plus Mn_2O_3). It can be seen that single spinel phase with cubic symmetry exists at 950°C. As temperature increases to 975°C, small peaks corresponding to $CuMnO_2$ with hexagonal symmetry appear, and this phase becomes more apparent at 1000°C, which means that $CuMnO_2$ with hexagonal structure forms at 975°C. Therefore, 975°C is regarded as the phase

boundary. As temperature increases from 1100°C to 1125°C, the amount of $CuMnO_2$ decreases. At 1150°C, only single spinel phase with cubic symmetry exists. Therefore, 1125°C is regarded as the transformation temperature.

5.2.3 The XRD analyses of $Cu_{1.3}Mn_{1.7}O_4$

For $Cu_{1.3}Mn_{1.7}O_4$, CuO and cubic spinel phase exist at 725°C and 750°C. As temperature decreases to 600°C, there is a small amount of CuO second phase, which disappears at 575°C. At 550°C, single spinel phase with cubic structure exists. Therefore, 575°C is taken as the phase boundary at this composition. As temperature further decreases to 450°C, only single spinel phase exists. At 425°C, a tiny peak corresponding to Mn_2O_3 phase occurs, and the peak grows at 400°C. Therefore, 425°C is regarded as the phase boundary. However, at these low temperatures, the degree of uncertainty is higher.

5.2.4 The XRD analyses of $Cu_{1.4}Mn_{1.6}O_4$

For this composition, two samples were analyzed in-situ. Although the heating processes were different, the patterns matched very well. It can be seen that the phases are CuO, cubic spinel and Mn_2O_3 at 675°C. At 700°C, Mn_2O_3 becomes less prominent and it disappears at 725°C. At temperatures below 700°C, three phases, CuO, cubic spinel and Mn_2O_3, coexist. This observation is consistent with that of $Cu_{1.1}Mn_{1.9}O_4$, in which Mn_2O_3 started to form when temperature decreased to 700°C. It is assumed that the existence of CuO at low temperatures is due to the sample preparation process. Fig. 3.7 revealed that there were small amounts of CuO in the quenched sample before thesis in-situ analyses. As the in-situ analyses started from low temperatures, CuO did not dissolve. Clearly, the equilibrium state had not been reached, and phase boundaries can't be determined at intermediate temperatures. At 900°C, there are two phases (CuO and cubic spinel) coexisting. As temperature increases to 925°C, CuO disappears and $CuMnO_2$ with hexagonal structure appears. At 950°C, the phases are $CuMnO_2$ and cubic spinel. Therefore, 925°C is the assumed phase transformation temperature for the onset of the $CuMnO_2$ phase. The $CuMnO_2$ peaks diminish as temperature further increases. At 1100°C, $CuMnO_2$ has almost vanished, and single spinel phase remains above 1125°C, from which 1100°C can be estimated as the phase boundary. Above 1125°C, single spinel phase with cubic structure is stable.

In the investigated temperature range, we can see three peaks at around 39.5°, 46° and 67.2° that can't be identified. Intensities of the peaks at 39.5° and 46° do not change with temperature and the intensity of the diffraction at 67° increases a little with temperature. Sometimes, this peak coincides with CuO, but clearly it does not belong to CuO as CuO disappears at temperatures higher than 925°C. These peaks are attributed to unknown impurity phases.

The phase boundaries from our XRD study and those from Vandenberghe et al (Vandenberghe 1973) are shown in tables 5.1 and 5.2 for comparison. The question mark appearing in table 5.1 for the sample of $Cu_{1.4}Mn_{1.6}O_4$ means an impurity phase which

could not be identified. It is clear that the spinel boundaries from our XRD data of $Cu_{0.8}Mn_{2.2}O_4$ and $Cu_{1.1}Mn_{1.9}O_4$ matched closely with the mid-composition investigation of Vandenberghe et al. (1973). However, at compositions of $Cu_{1.3}Mn_{1.7}O_4$ and $Cu_{1.4}Mn_{1.6}O_4$, there is poor match between our results and theirs. This difference could be due to a failure to reach equilibrium in the samples of $Cu_{1.3}Mn_{1.7}O_4$ and $Cu_{1.4}Mn_{1.6}O_4$ in our experiments at temperatures below 750°C.

Trari et al. (2005) found that above 1150°C, the following reaction occurs:

$$Cu_{1+x}Mn_{1-x}O_2 \rightarrow Cu_yMn_{3-y}O_4(spinel) + liquid \quad (5.1)$$

In my experiments on $Cu_{0.8}Mn_{2.2}O_4$, single spinel phase was found at temperatures above 1125°C. Liquid phase may also exist in this temperature range, but can't be identified by XRD. For $Cu_{1.1}Mn_{1.9}O_4$, as the highest temperature tested was 1100°C, nothing can be concluded. For $Cu_{1.4}Mn_{1.6}O_4$, it is clear that $CuMnO_2$ phase disappears, and single phase spinel forms at temperatures above 1100°C, which is consistent with the phase diagram (Trari 2005).

Table 5.1 Phase boundaries based on in-situ x-ray diffraction analyses

Lowest test temp. (°C)	Highest test temp (°C)	Sample	Phase region	Phase boundary (°C)
600	1150	$Cu_{0.8}Mn_{2.2}O_4$	Spinel + Mn_2O_3	600 - 775
			Spinel	775 - 975
			Spinel + $CuMnO_2$	975 – 1125
			Spinel	1125 - 1150
535	1100	$Cu_{1.1}Mn_{1.9}O_4$	Spinel + Mn_2O_3	535 - 700
			Spinel	700 - 825
			Spinel + CuO	825 - 950
			Spinel + CuO + $CuMnO_2$	950 - 1000
			Spinel + $CuMnO_2$	1000 - 1100
350	750	$Cu_{1.3}Mn_{1.7}O_4$	Spinel + Mn_2O_3	350 - 425
			Spinel	425 - 575
			Spinel + CuO	575 - 750
400	1125	$Cu_{1.4}Mn_{1.6}O_4$	Spinel + Mn_2O_3 + CuO+ ?	400 - 550
			Spinel + Mn_2O_3 + CuO+ ?	550 - 750
			Spinel + CuO+ ?	750 - 925
			Spinel + $CuMnO_2$+ ?	925 - 1100
			Spinel + ?	1100 - 1125

'?' means unknown impurity phase.

Table 5.2 Phase boundary of the single spinel from the literature (Vandenberghe 1973)

Composition	Cu0.8	Cu1.0	Cu1.1	Cu1.2	Cu1.3	Cu1.4
Single spinel phase area (°C)	800-1000	720-950	700-820	610-750	540-680	500-610

Table 5.3 Temperature range of $CuMnO_2$ formation

Sample	Phase region	Phase boundary (°C)
$Cu_{0.8}Mn_{2.2}O_4$	Spinel + $CuMnO_2$	975 – 1125
$Cu_{1.1}Mn_{1.9}O_4$	Spinel + CuO + $CuMnO_2$	950 - 1000
	Spinel + $CuMnO_2$	1000 - 1100
$Cu_{1.4}Mn_{1.6}O_4$	Spinel + $CuMnO_2$+ ?	925 - 1100

'?' means unknown impurity phase.

From table 5.3, it can be seen that the temperature at which $CuMnO_2$ forms in the compositions of $Cu_{0.8}Mn_{2.2}O_4$, $Cu_{1.1}Mn_{1.9}O_4$ and $Cu_{1.4}Mn_{1.6}O_4$ are consistently in the vicinity of 950°C. Therefore, it is assumed that the onset of $CuMnO_2$ formation is 950°C. The three-phase analyses of the $Cu_{1.1}Mn_{1.9}O_4$ sample at 950-1000°C might be due to a metastable state of the sample. Our experiments show that $Cu_xMn_{3-x}O_4$ spinels have tetragonal structure for $x \leq 1.0$ and cubic symmetry with $x > 1.0$ through quenching in air after annealing at high temperatures (fig. 3.3-3.7). The results are consistent with the literature (Dubrovina 2001; Vandenberghe 1973). The samples with nominal composition of $Cu_{1.3}Mn_{1.7}O_4$ and $Cu_{1.4}Mn_{1.6}O_4$ could not be annealed to pure spinel phase, but consist of a mixture of the spinel plus CuO, or the spinel and Mn_2O_3. This may be due to the slow diffusion at temperatures below 750°C, and consistent with the literature (Vandenberghe 1973). However, no matter what crystal symmetry the spinel have after quenching in air, they have cubic symmetry at high temperatures, and transformation of cubic to tetragonal structure was not observed by the in-situ X-ray diffraction analysis. These results are summarized by a Cu-Mn-O phase diagram calculated using FACTSage that included in-situ x-ray data and the subsequent neutron diffraction analyses (fig. 5.2).

5.2.5 Conclusions

The major finding was that the spinel boundaries from our XRD study matched closely with the mid-composition investigation of Vandenberghe et al. (Vandenberghe 1973). The inconsistency in phase identification at $x>1.1$ in $Cu_xMn_{3-x}O_4$ could be due to unattainability of the equilibrium state at intermediate temperatures. The phase transformation between cubic and tetragonal structure near $x=1.0$ in $Cu_xMn_{3-x}O_4$ solid solutions was not demonstrated by in-situ X-ray analyses. All the $Cu_xMn_{3-x}O_4$ solid solutions showed cubic symmetry. During heating to high temperatures, there is a decomposition of $CuMnO_2$ to cubic spinel, and the transformation temperature is estimated at 1125°C. This is quite consistent with previous results (Driessens 1967; Trari 2005). In-situ X-ray diffraction shows that $CuMnO_2$ at high temperatures in air has

hexagonal structure, and in the composition range investigated, $CuMnO_2$ with monoclinic structure was not found.

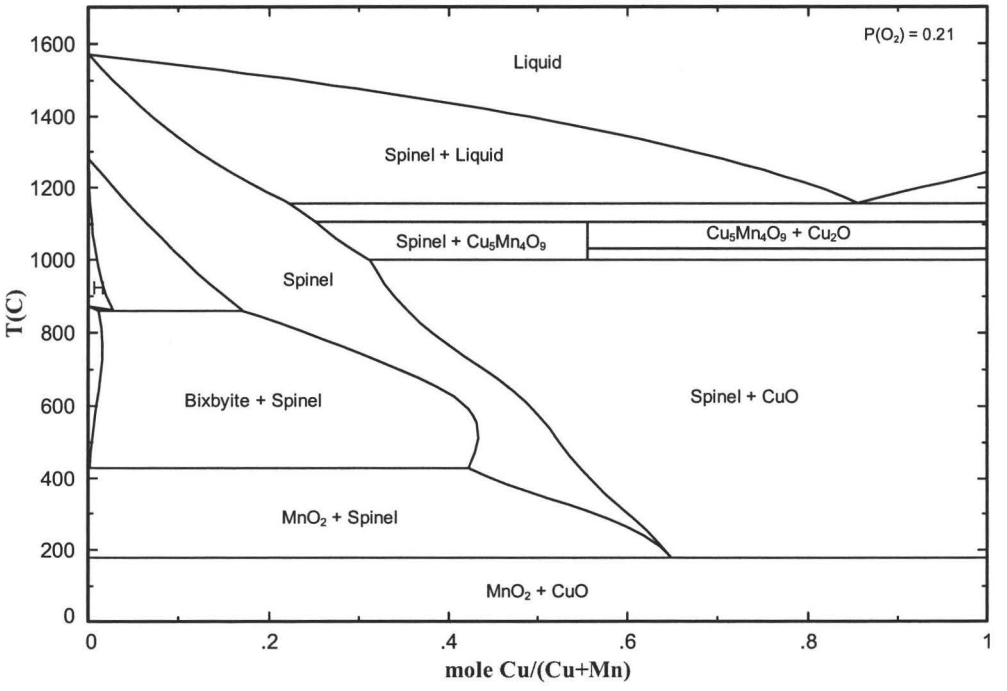

Figure 5.2 Cu-Mn-O phase diagram

5.3 In-situ neutron diffraction analyses

5.3.1 Experimental procedure

For in-situ high temperature neutron diffraction, $Cu_xMn_{3-x}O_4$ compounds were prepared by mixing CuO and MnO_2 following the standard ceramic technique. The mixtures were reacted in air at high temperatures in order to produce pure spinel phase according to the phase diagram (Martin 2007; Vandenberghe 1973). Based on previous literature, it is clear that different opinions exist regarding the cation distribution and valences of the cations in $Cu_xMn_{3-x}O_4$ solid solutions. It was suggested that the stoichiometry, cation oxidation state and site distribution in $Cu_xMn_{3-x}O_4$ solid solutions were strongly dependent on the preparation method, sintering temperature, sintering time and subsequent treatments (Vandenberghe 1973). Temperatures could also influence the cation valences and distributions in the compounds (Dorris 1988; Ghare 1968; Sinha 1958; Vandenberghe 1973; Vandenberghe 1976). As most of the previous research was based on quenched samples, in-situ analyses was considered an advantage to clarify the structure of $Cu_xMn_{3-x}O_4$ solid solution. Although some research has been done through in-situ X-ray diffraction to study the structure, as the difference between the scattering

powers of Cu and Mn in X-ray diffraction is small, the resolution is insufficient. Neutron diffraction, in many cases, can give an unambiguous picture of the cation distribution as neutron coherent scattering lengths of elements adjacent to each other in the periodic table may different significantly. In the case of $Cu_xMn_{3-x}O_4$ solid solution, as Cu and Mn have neutron scattering lengths with opposite signs, in-situ neutron diffraction is regarded as an appropriate technique to obtain precise information on cation distribution in $Cu_xMn_{3-x}O_4$ solid solutions and other crystallographic parameters.

In-situ neutron diffraction analysis was conducted at the Canadian Neutron Beam Centre. Two wavelengths were selected, 1.32927 Å and 2.37083 Å, so as to resolve low d-spacing with a maximum collection of 115°. In order to optimize the intensity of the signal and the accuracy of lattice parameter, the acquisition time was fixed at two hours. The spectra obtained with the smaller wavelength are shown in appendix 2, along with the refined difference spectra. Rietveld refinement was used to determine copper and manganese site distribution and lattice parameters.

5.3.2 Refinement results

The cation distribution and lattice parameters of the spinels based on Rietveld refinement using a model with $Fd\bar{3}m$ space group are shown in the following tables 5.4-5.11. Rp is the total R-factor and wRp is the weighted profile R-factor.

According to figs. 5.3 and 5.4, it can be seen that the cubic lattice parameter of the spinel phase increases with temperature, and decreases with increasing Cu content in $Cu_xMn_{3-x}O_4$ solid solutions. The cell parameter increases with temperature should be due to thermal expansion of the crystal structure. Vandenberghe et al. (1973) also observed that the lattice parameter diminished with increasing x in in $Cu_xMn_{3-x}O_4$ solid solutions, and they proposed that the copper ions will distribute in a specific way over the octahedral and tetrahedral sublattices, and the lattice parameter decreased with increasing tetrahedral copper concentration. The cation distribution from our refinement does show an increase of tetrahedral copper concentration as a function of copper content x in $Cu_xMn_{3-x}O_4$ solid solutions (tables 5.5, 5.7, 5.9 and 5.11). As ionic radii of Cu^+ and Cu^{2+} on tetrahedral sites are smaller than that of Mn^{2+} on the same sites (Shannon 1976), the lattice parameter decreases when copper ions replace manganese ions on tetrahedral sites.

Table 5.4 Lattice parameters of the spinel $Cu_{0.8}Mn_{2.2}O_4$

Temperature (°C)	700	800	900	1000
Spinel, cubic a = b = c (Å)	8.470	8.488	8.494	8.509
x in $Cu_xMn_{3-x}O_4$ spinel	0.7626	0.7768	0.7724	0.7518
Rp	0.0481	0.0476	0.05	0.0477
wRp	0.0624	0.0613	0.0635	0.0617

Table 5.5 Cation distribution in the spinel phase for the composition $Cu_{0.8}Mn_{2.2}O_4$

Temperature (°C)	Occupancy at tetrahedral sites		Occupancy at octahedral sites	
	Cu1	Mn1	Cu2	Mn2
700	0.5608	0.4392	0.1009	0.8991
800	0.5376	0.4624	0.1196	0.8804
900	0.5484	0.4516	0.1120	0.8880
1000	0.5242	0.4758	0.1138	0.8862

Table 5.6 Lattice parameters of the spinel $Cu_{1.0}Mn_{2.0}O_4$

Temperature (°C)	750	800	850	950
Spinel, cubic a = b = c (Å)	8.446	8.459	8.470	8.481
x in $Cu_xMn_{3-x}O_4$ spinel	0.9634	0.89	0.9084	0.9166
Rp	0.0528	0.055	0.056	0.0515
wRp	0.0671	0.073	0.0747	0.0663

Table 5.7 Cation distribution in the spinel phase for the composition $Cu_{1.0}Mn_{2.0}O_4$

Temperature (°C)	Occupancy at tetrahedral sites		Occupancy at octahedral sites	
	Cu1	Mn1	Cu2	Mn2
750	0.6630	0.3370	0.1502	0.8498
800	0.6554	0.3446	0.1173	0.8827
850	0.6554	0.3446	0.1265	0.8735
950	0.6526	0.3474	0.1320	0.8680

Table 5.8 Lattice parameters of the spinel $Cu_{1.1}Mn_{1.9}O_4$

Temperature (°C)	650	700	790	900	950
Spinel, cubic a = b = c (Å)	8.429	8.434	8.448	8.465	8.467
x in $Cu_xMn_{3-x}O_4$ spinel	1.0393	1.0003	1.0028	1.0034	1.0046
Rp	0.056	0.0521	0.05	0.054	0.0541
wRp	0.0716	0.0675	0.0641	0.0701	0.07

Table 5.9 Cation distribution in the spinel phase for the composition $Cu_{1.1}Mn_{1.9}O_4$

Temperature (°C)	Occupancy at tetrahedral sites		Occupancy at octahedral sites	
	Cu1	Mn1	Cu2	Mn2
650	0.7387	0.2613	0.1503	0.8497
700	0.7325	0.2675	0.1339	0.8661
790	0.712	0.288	0.1454	0.8546
900	0.7032	0.2968	0.1501	0.8499
950	0.7040	0.2960	0.1503	0.8497

Table 5.10 Lattice parameters of the spinel $Cu_{1.3}Mn_{1.7}O_4$

Temperature (°C)	RT	550	600	690	800	850
Spinel, cubic a = b = c (Å)	8.336	8.392	8.401	8.422	8.430	8.44
x in $Cu_xMn_{3-x}O_4$ spinel	1.1448	1.1535	1.1535	1.2265	1.2173	1.1919
Rp	0.0593	0.0584	0.0571	0.0573	0.0635	0.0587
wRp	0.0756	0.075	0.0738	0.0737	0.0801	0.0746

Table 5.11 Cation distribution in the spinel phase for the composition $Cu_{1.3}Mn_{1.7}O_4$

Temperature (°C)	Occupancy at tetrahedral sites		Occupancy at octahedral sites	
	Cu1	Mn1	Cu2	Mn2
25	0.8774	0.1226	0.1337	0.8663
550	0.8531	0.1469	0.1502	0.8498
600	0.8341	0.1659	0.1597	0.8403
690	0.8643	0.1357	0.1811	0.8189
800	0.8591	0.1409	0.1791	0.8209
850	0.8545	0.1455	0.1687	0.8313

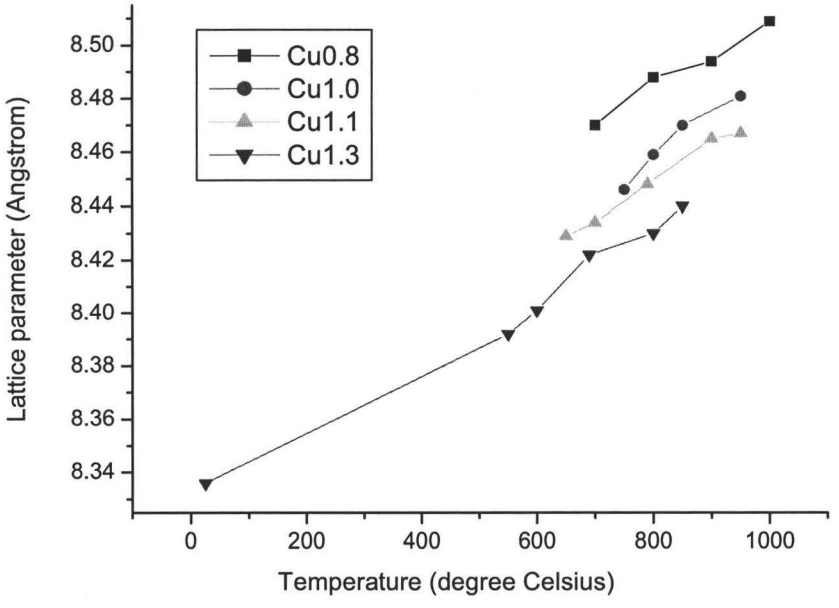

Figure 5.3 Lattice parameter of the spinel as a function of temperature

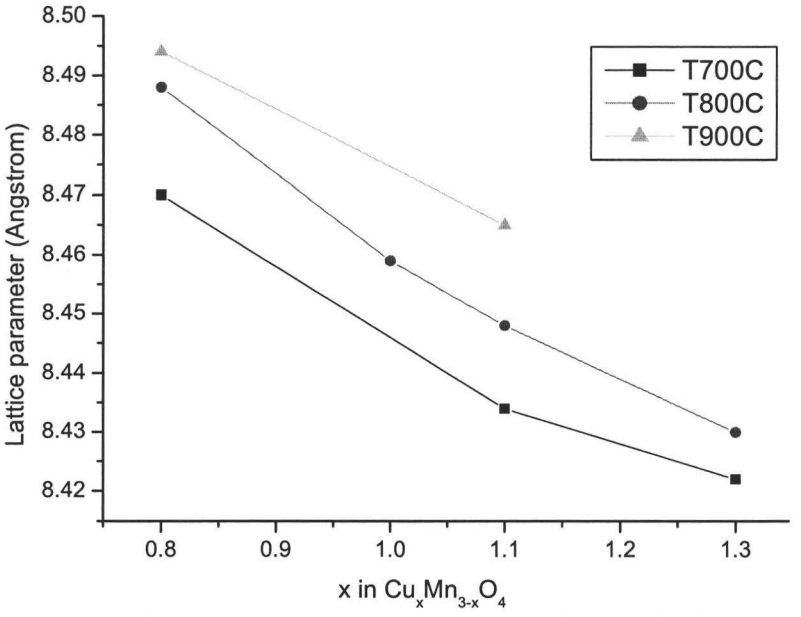

Figure 5.4 Lattice parameter of the spinel as a function of x in $Cu_xMn_{3-x}O_4$

In-situ neutron diffraction results confirm the findings of in-situ x-ray diffraction that $Cu_xMn_{3-x}O_4$ solid solutions have cubic structure at high temperatures. The literature (Vandenberghe 1973) mentioned that $Cu_xMn_{3-x}O_4$ solid solutions had cubic structure for $1.06 \leq x \leq 1.50$ and tetragonal structure for $0.98 \leq x < 1.06$ in $Cu_xMn_{3-x}O_4$ when quenched samples were used. However, this transformation of tetragonal symmetry to cubic structure of the spinel at x~1.0 in $Cu_xMn_{3-x}O_4$ solid solutions (Vandenberghe 1973) was not observed by our in-situ analyses.

Dubrovina et al. (2001) studied $Cu_xMn_{3-x}O_4$ solid solutions with compositions of $0.5 \leq x \leq 1.0$ at 900°C in air through in-situ x-ray diffraction and also found that $Cu_xMn_{3-x}O_4$ solid solutions had cubic structure at high temperature, but quenching in air gave rise to tetragonal distortion, which was confirmed in our experiments, e.g., $Cu_{0.8}Mn_{2.2}O_4$ and $Cu_{1.0}Mn_{2.0}O_4$ (fig. 3.3 and 3.4). The disagreement between our results and those in the literature (Buhl 1969; Vandenberghe 1973) demonstrated that quenching is not a suitable method to obtain correct information about crystal symmetry of $Cu_xMn_{3-x}O_4$ solid solutions at high temperatures. According to the phase diagram (fig. 4.33), Mn_3O_4 at intermediate temperatures has tetragonal structure and the cation distribution of $(Mn^{2+})[Mn^{3+}Mn^{3+}]O_4$ was proposed for this symmetry (Dorris 1988). That $Cu_xMn_{3-x}O_4$ spinel with the composition investigated show cubic structure means that there is a transformation of tetragonal to cubic symmetry, and this transformation should be related to the change of ionic configuration in $Cu_xMn_{3-x}O_4$. It is reasonably deduced that the transformation of tetragonal to cubic symmetry in $Cu_xMn_{3-x}O_4$ occurs at $x<0.5$ based on the results of Dubrovina et al. (2001) and ours at high temperatures.

Different ionic configurations have been proposed for $Cu_xMn_{3-x}O_4$ solid solutions (table 5.12). Cation distributions from our in-situ neutron analyses were compared with those of others (figs. 5.5-5.8). The label of 'Wei' in the ligend represents the data from our experiments. As cation distributions in $Cu_xMn_{3-x}O_4$ spinel did not show significant variation at intermediate temperatures in our experiments (tables 5.5, 5.7, 5.9 and 5.11), average values were taken for comparison with others. Symbols of 'Dubrovina' and 'DubrovinaQ' in the figures mean the data from in-situ analyses and room temperature analyses based on the quenched samples of Dubrovina et al. (2001).

According to figs. 5.5-5.8, it can be seen that the cation distributions from Maunders et al. (2008) (quenched samples), Dubrovina et al. (2001) (quenched samples), Radhakrishnan et al. (1977) and Vandenberghe et al. (1976) matched with our in-situ data better than others. Radhakrishnan et al. (1977) studied $CuMn_2O_4$ after quenching between 850 and 900°C through neutron diffraction, and the cation distribution was solved as $(Cu_{0.75}Mn_{0.25})[Cu_{0.25}Mn_{1.75}]$. Vandenberghe et al. (1976) reported a cation distribution of $(Cu_{0.76}Mn_{0.24})[Cu_{0.24}Mn_{1.76}]$ in $CuMn_2O_4$ through quenching from 940°C.

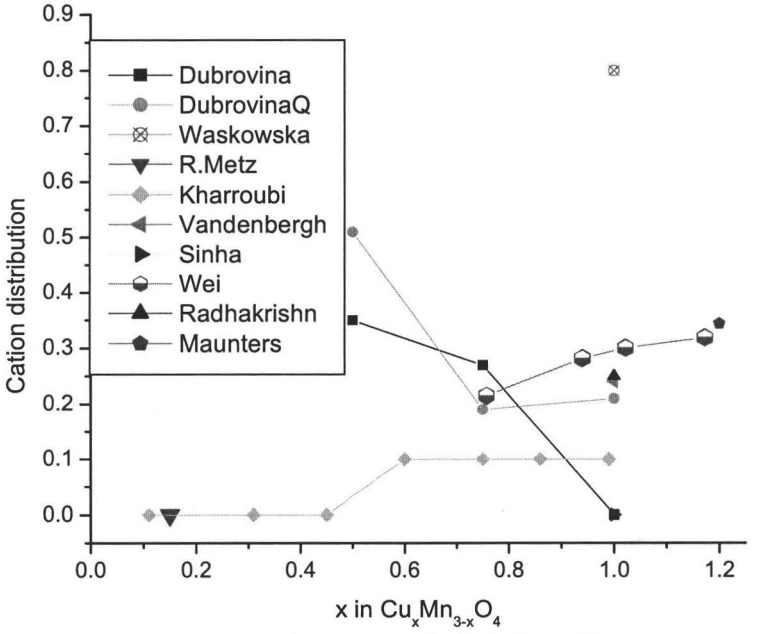

Figure 5.5 Copper cations on octahedral sites of $Cu_xMn_{3-x}O_4$

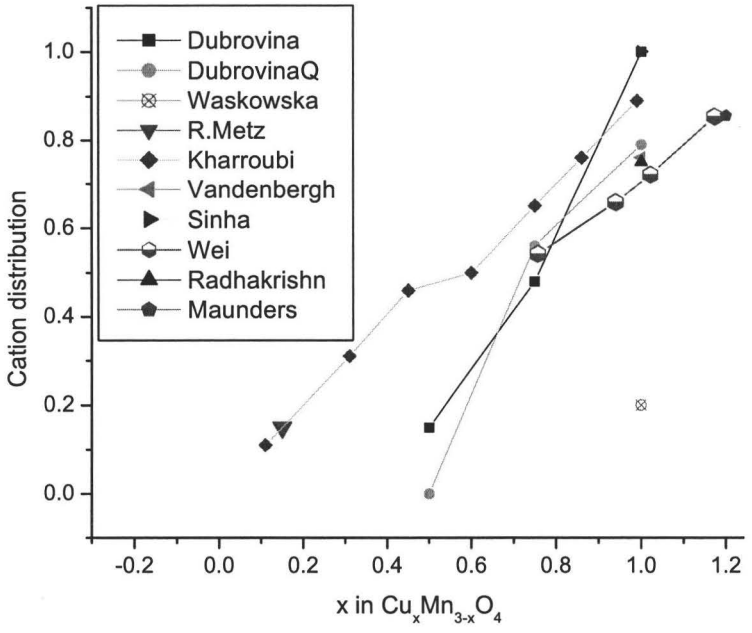

Figure 5.6 Copper cations on tetrahedral sites of $Cu_xMn_{3-x}O_4$

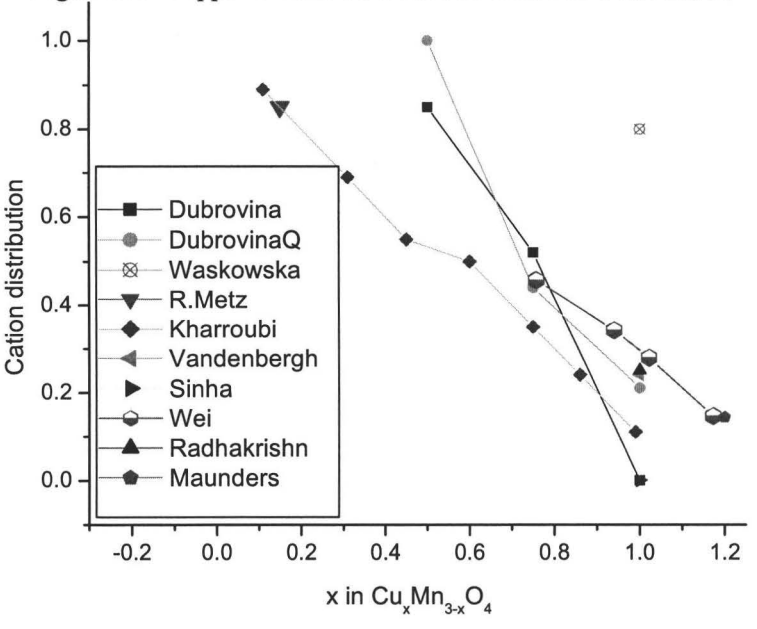

Figure 5.7 Manganese cations on tetrahedral sites of $Cu_xMn_{3-x}O_4$

Table 5.12 Cation distributions in $Cu_xMn_{3-x}O_4$

Reference	Year	x in $Cu_xMn_{3-x}O_4$	Cationic distributions
Maunders et al. (Maunders 2008)	2008	1.2	$(Cu^{2+}_{0.856}Mn^{2+}_{0.144})[Cu^{2+}_{0.344}Mn^{3+}_{0.666}Mn^{4+}_{0.99}]$ quenched
Dubrovina et al. (Dubrovina 2001)	2001	0.5	$(Mn^{2+}_{0.85}Cu^{+}_{0.15})[Cu^{2+}_{0.35}Mn^{3+}_{1.15}Mn^{4+}_{0.50}]$ at 900°C $(Mn^{2+}_{1.0})[Cu^{2+}_{0.51}Mn^{3+}_{0.98}Mn^{4+}_{0.51}]$ quenched
		0.75	$(Mn^{2+}_{0.52}Cu^{+}_{0.25}Cu^{2+}_{0.23})[Cu^{2+}_{0.27}Mn^{3+}_{1.21}Mn^{4+}_{0.52}]$ at 900°C $(Mn^{2+}_{0.44}Cu^{+}_{0.25}Cu^{2+}_{0.31})[Cu^{2+}_{0.19}Mn^{3+}_{1.37}Mn^{4+}_{0.44}]$ quenched
		1.0	$(Cu^{+}_{1.0})[Mn^{3+}_{1.01}Mn^{4+}_{0.99}]$ at 900°C $(Mn^{2+}_{0.21}Cu^{2+}_{0.79})[Cu^{2+}_{0.21}Mn^{3+}_{1.58}Mn^{4+}_{0.21}]$ quenched
Waskowska et al. (Waskowska 2001)	2001	x = 1	$(Cu^{+}_{0.2}Mn^{2+}_{0.8})[Cu^{2+}_{0.8}Mn^{3+}_{0.2}Mn^{4+}_{1.0}]$
R. Metz (Metz 2000)	2000	$0 \leq x < 0.3$	$(Cu^{+}_{x}Mn^{2+}_{1-x})[Mn^{3+}_{2-x}Mn^{4+}_{x}]$ quenched
		$0.3 \leq x < 1.0$	$(Cu^{+}_{x-y}Mn^{2+}_{1-x+y})[Cu^{2+}_{y}Mn^{3+}_{2-x-y}Mn^{4+}_{x}]$ quenched
Kharroubi et al. (Kharroubi 1991)	1991	$x < 0.6$	$(Cu^{+}_{x}Mn^{2+}_{1-x})[Mn^{3+}_{2-x}Mn^{4+}_{x}]$ quenched
		$1.0 > x > 0.6$	$(Cu^{+}_{x-y}Mn^{2+}_{1-x+y})[Cu^{2+}_{y}Mn^{3+}_{2-x-y}Mn^{4+}_{x}]$* quenched
Radhakrishnan et al. (Radhakrishnan 1977)	1977	x = 1	$(Cu^{2+}_{0.50}Cu^{+}_{0.25}Mn^{3+}_{0.25})[Cu^{2+}_{0.25}Mn^{3+}_{1.50}Mn^{4+}_{0.25}]$ quenched
Vandenberghe et al. (Vandenberghe 1976)	1976	x = 1	$(Cu^{+}_{0.76}Mn^{3+}_{0.24})[Cu^{2+}_{0.24}Mn^{3+}_{1.0}Mn^{4+}_{0.76}]$ quenched $(Cu^{+}_{0.76}Mn^{2+}_{0.24})[Cu^{2+}_{0.24}Mn^{3+}_{0.76}Mn^{4+}_{1.0}]$ quenched
Sinha et al. (Sinha 1958)	1958	x = 1	$(Cu^{+})[Mn^{3+}Mn^{4+}]$

*: y represents a low value (less than 0.20), and is taken as 0.1 in our calculations.

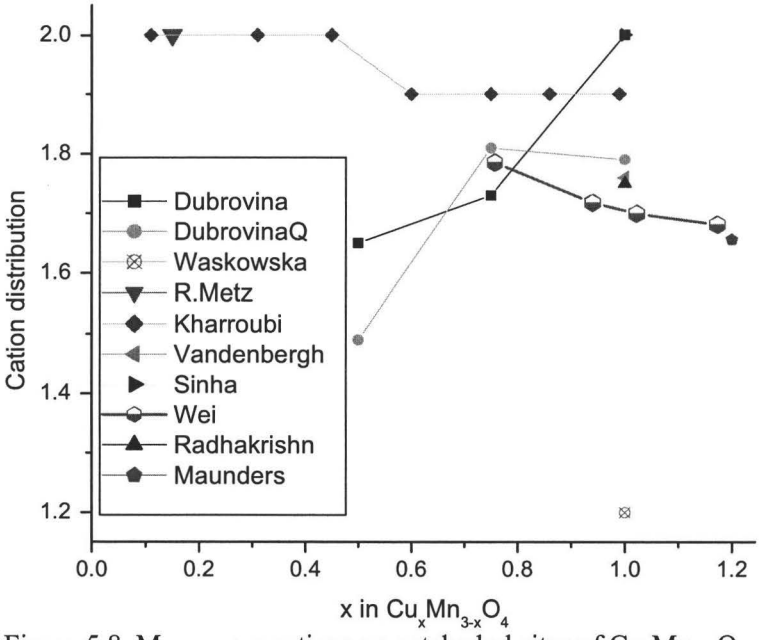

Figure 5.8 Manganese cations on octahedral sites of $Cu_xMn_{3-x}O_4$

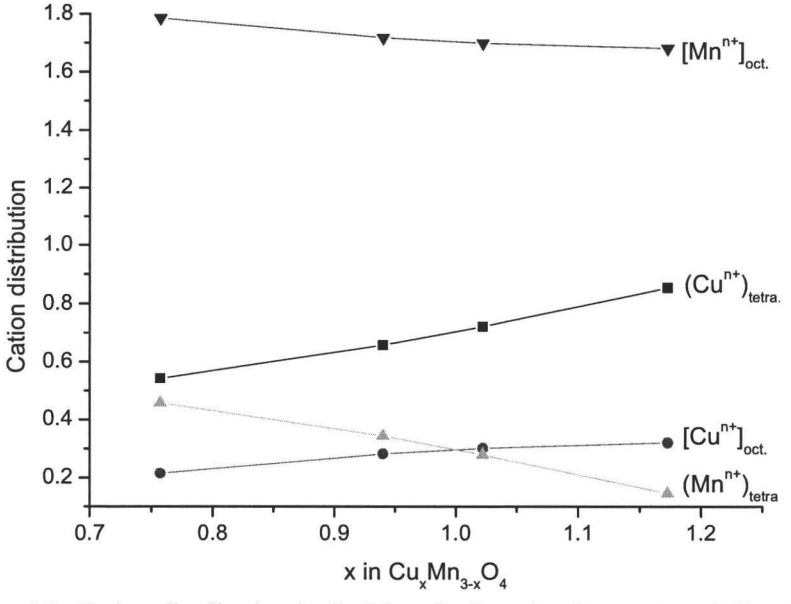

Figure 5.9 Cation distribution in $Cu_xMn_{3-x}O_4$ from in-situ neutron diffraction

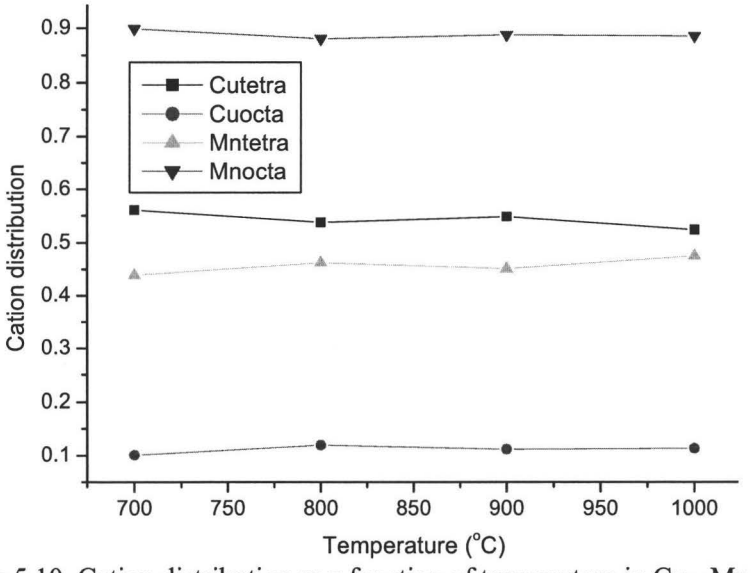

Figure 5.10 Cation distribution as a function of temperature in $Cu_{0.8}Mn_{2.2}O_4$

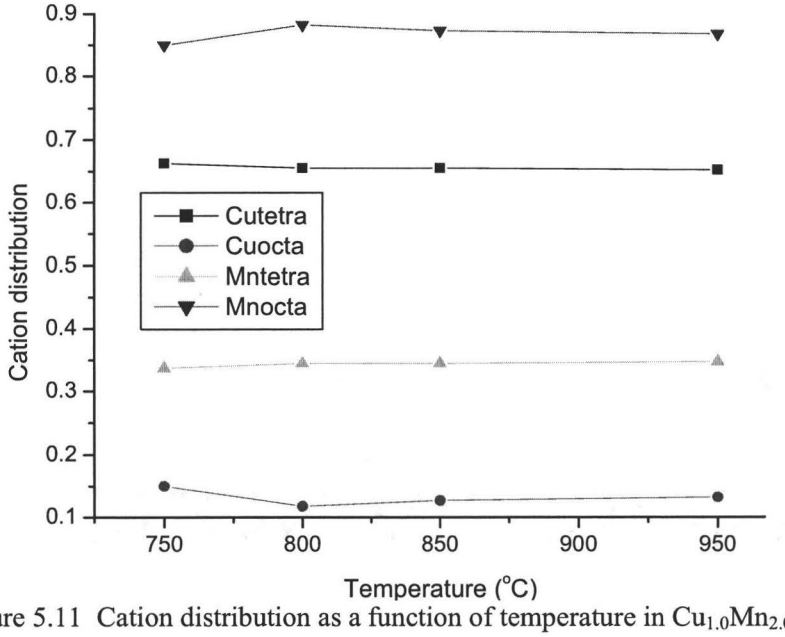

Figure 5.11 Cation distribution as a function of temperature in $Cu_{1.0}Mn_{2.0}O_4$

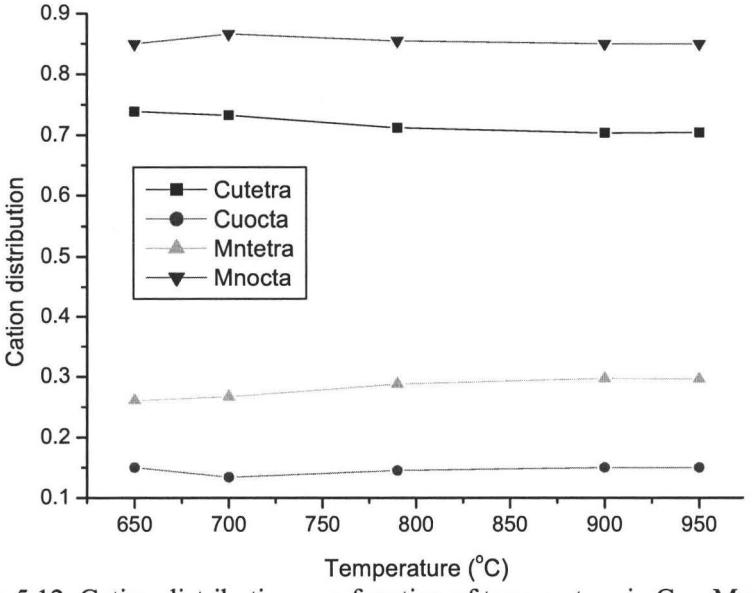

Figure 5.12 Cation distribution as a function of temperature in $Cu_{1.1}Mn_{1.9}O_4$

Although the cation distributions in $CuMn_2O_4$ from Vandenberghe et al. (1976) and Radhakrishnan et al. (1977) are consistent with each other, the ionic configurations they proposed are quite different (table 5.12). Our in-situ neutron diffraction analyses show that the sample with a nominal composition of $Cu_{1.1}Mn_{1.9}O_4$ has a cation distribution of $(Cu_{0.703}Mn_{0.297})[Cu_{0.30}Mn_{1.70}]$ at 900°C (table 5.9). The nominal spinel composition of $Cu_{1.1}Mn_{1.9}O_4$ has a refined composition of $Cu_{1.003}Mn_{1.997}O_4$. The difference of the cation distribution between our results and the literatures can be attributed to the state of the samples, either equilibrium state (in-situ analyses) or metastable state (quenching). The comparison demonstrates that quenching is unable to give accurate information about the cation distribution and crystal symmetry of the materials at high temperatures. Although quenching can freeze the cation distribution in $Cu_xMn_{3-x}O_4$ at high temperatures to some extent, for example, the cation distributions from Maunders et al. (2008), Vandenberghe et al. (1976), Dubrovina et al. (2001) (quenched samples), and Radhakrishnan et al. (1977) are very close to our in-situ analyses, caution must be taken where using quenched samples to study crystal structure of the materials, as most of the data from quenching experiments deviate significantly from the in-situ analysed data.

Dubrovina et al. (2001) mentioned that the competing cooperative effects of the Jahn-Teller ions on tetrahedral and octahedral sublattices play a decisive role in determining the structure of the solid solutions. Cubic symmetry existing at high temperatures while tetragonal structure existing in quenched samples could be attributed to a large entropy contribution to the free energy of the solid solution at high temperatures, which impedes interaction between Jahn-Teller ions. The thermal factor probably plays an important role in determining the equilibrium structure of $Cu_xMn_{3-x}O_4$

solid solutions at high temperatures. However, up to now, no suitable theory has yet been formulated to describe the combined effect of Jahn-Teller ions.

In-situ diffraction has been demonstrated as an effective method to provide direct information about crystal structure of materials at high temperature. As Cu and Mn have different neutron scattering lengths with opposite sign, in-situ neutron diffraction can give accurate and direct information about the structure and cation distribution in $Cu_xMn_{3-x}O_4$. However, as copper and manganese have multi valences, even neutron analyses can't provide comprehensive information about valence of copper and manganese ions on the octahedral and tetrahedral sites.

The complicated situation in $Cu_xMn_{3-x}O_4$ solid solutions where copper and manganese ions have multiple valences makes the determination of copper and manganese cation distributions in the spinel difficult. Since no technique is available which can give direct information about valence of elements at high temperatures in air, several methods have to be combined in order to get cation distribution in the solid solutions. Although $Cu_xMn_{3-x}O_4$ has been studied for long time, the results about their ionic configuration are always controversial, which means that not only the materials themselves are complicated, but also there is no developed theory which can give clear description about the relationship among their structure, sample state, composition and temperature. Although many mechanisms have been proposed, it is impossible to tell which is more accurate.

From previous neutron diffraction data on the cation distribution in $CuMn_2O_4$ (Buhl 1969; Radhakrishnan 1977; Zaslavskii 1969), it follows that the Cu ions have a preference for the tetrahedral sites. Our experiments also found that more Cu ions go to the tetrahedral sites than the octahedral sites with increasing x in $Cu_xMn_{3-x}O_4$ solid solutions. From fig. 5.9, it can be seen that at intermediate temperatures, the concentration of copper ions on tetrahedral and octahedral sites increases with increasing copper concentration in $Cu_xMn_{3-x}O_4$, and the former increases more quickly than the latter. The concentration of manganese ions on tetrahedral and octahedral sites decreases with increasing copper concentration, and the former decreases more quickly than the latter. It is possible that manganese ions move from the tetrahedral sites to octahedral sites. Vandenberghe et al. (1973) proposed the following equilibrium based on the above neutron diffraction analysis, taking into account a random distribution at high temperatures:

$$Cu_{tetra.} + Mn_{oct.} \Leftrightarrow Cu_{oct.} + Mn_{tetra.} \quad (5.2)$$

which shifts to the right at high temperatures. Based on magnetic susceptibility measurements on $CuMn_2O_4$, Vandenberghe et al. (1976) proposed the equilibria given by 5.3 and 5.4 in $Cu_xMn_{3-x}O_4$, while Dubrovina et al. (2001) proposed the equilibrium in 5.5.

$$Cu^{+}_{tetr} + Mn^{4+}_{oct} \Leftrightarrow Cu^{2+}_{oct} + Mn^{3+}_{tetr} \quad (5.3)$$
$$Mn^{3+}_{tetr} + Mn^{3+}_{oct} \Leftrightarrow Mn^{2+}_{tetr} + Mn^{4+}_{oct} \quad (5.4)$$

$$Cu^{+}_{tetr} + Mn^{4+}_{oct} \Leftrightarrow Cu^{2+}_{tetr.} + Mn^{3+}_{oct.} \quad (5.5)$$

Clearly, the mechanisms they proposed are different. Equation 5.4 shows that Mn^{3+} on tetrahedral and octahedral sites can transform to Mn^{2+} and Mn^{3+}, while equation 5.5 shows that Mn^{3+} only exists on octahedral sites, and transforms to Mn^{4+}. Dorris et al. (Dorris 1988) proposed the following equilibrium to explain the transformation of tetragonal to cubic structure in Mn_3O_4, and expanded the theory to other manganites.

$$2[Mn^{3+}]_{oct.} \Leftrightarrow [Mn^{2+}]_{oct.} + [Mn^{4+}]_{oct.} \quad (5.6)$$

It has been widely accepted that tetrahedral distortion in Mn-rich spinels can be attributed to octahedral Mn^{3+} on account of its $3d^4$ electronic configuration, which is consistent with equilibrium (5.5). As Mn^{3+} transforms to Mn^{2+} + Mn^{4+}, the concentration of Mn^{3+} decreases and the extent of tetragonal distortion decreases. When Mn^{3+} concentration falls below a critical concentration, the cubic structure replaces tetragonal distortion. Waskowska et al. (2001) also mention that the amount of the distorting ions is the key to crystal symmetry in $Cu_xMn_{3-x}O_4$. They estimated the critical fraction of distortive ions on octahedral sites to be about 55%. The replacement of Mn^{3+} by Mn^{2+} and Mn^{4+} plays a key role in suppressing the tetragonal distortion (Yamada 1996).

As variation of the cation distribution with temperature in $Cu_{0.8}Mn_{2.2}O_4$, $Cu_{1.0}Mn_{2.0}O_4$ and $Cu_{1.1}Mn_{1.9}O_4$ at high temperatures was not significant (figs. 5.10-5.12), no rule could be drawn based on those data. The cation distribution in $Cu_{1.3}Mn_{1.7}O_4$ showed a clear trend between room temperature and high temperatures. However, there is no clear trend in the variation at high temperatures (table 5.11), the reason for which is not clear. In order to avoid this problem, it was assumed that the cation distribution at 850°C was representative of high temperatures (table 5.11). It can be seen that $(Cu^{n+})_{tetra.}$ and $[Mn^{n+}]_{oct.}$ decrease, while $[Cu^{n+}]_{oct.}$ and $([Mn^{n+}]_{tetra.}$ increase as temperature increases. Clearly, Some Cu^{n+} ions transfer from tetrahedral to octahedral sites, and Mn^{n+} moves in the opposite direction at the same time as temperature increases. Buhl proposed the following thermally activated site exchange reaction (Buhl 1969):

$$Cu^{2+}_{tetra.} + Mn^{2+}_{oct.} \Leftrightarrow Mn^{2+}_{tetra.} + Cu^{2+}_{oct.} \quad (5.7)$$

It is clear that as temperature increases, the above equation shifts to the right side: $(Cu^{2+})_{tetra.}$ and $[Mn^{2+}]_{oct.}$ decrease, while $[Cu^{2+}]_{oct.}$ and $[Mn^{2+}]_{tetra.}$ increase with temperature.

Based on the above analyses, it is clearly seen that equation 5.2 can explain the cation distribution in $Cu_xMn_{3-x}O_4$ solid solutions. However, the valences which can be assigned to copper and manganese ions on both sides of the equation are not consistent, which makes final determination of the ionic configuration impossible. The compositions of the cubic spinel can be calculated based on the refined distribution for manganese and copper as well as the site multiplicity for tetrahedral and octahedral sites

following the equation: $Cu_{total} = Cu_{tet.} + Cu_{octa.}$. The compositions of the spinel based on refinement are quite different from ICP analyses (table 3.5). The probable explanation is that ICP analyses gives compositions of the whole sample, not a specific phase. Moreover, ICP analyses has a greater level of uncertainty.

Although the results of early studies on $Cu_xMn_{3-x}O_4$ solid solutions were controversial, they can provide some useful information on cation distribution of copper manganites:

- The tetragonal distortion of Mn-rich spinels can be attributed to octahedral Mn^{3+} (Dunitz 1957; Goodenough 1955);
- Manganese is present in the compounds in three valence states: Mn^{2+}, Mn^{3+} and Mn^{4+}. It is generally accepted that the high electrical conduction of copper manganites is dominated by thermally activated electron exchange between Mn^{3+} and Mn^{4+} ions on the octahedral sublattices;
- As Mn^{3+} and Mn^{4+} have high preferences for octahedral sites, the tetrahedral concentration of either species is expected to be very small (Dunitz 1957; Navrotsky 1967; O'Neill 1984);
- The presence of Mn^{4+} ions will result in an equivalent amount of Cu^{+} ions in order to keep the charge balance (Radhakrishnan 1977);
- It has been confirmed that Mn^{2+} has strong preference for tetrahedral sites (Lucchesi 1997). Therefore, Mn^{2+} will preferentially occupy tetrahedral sites;
- Copper can be present in two valence states, Cu^{+} and Cu^{2+}. If Cu^{+} exists, it will occupy tetrahedral sites due to its low octahedral site preference;
- Cu^{2+} also has a strong preference for octahedral sites, and competes with Mn^{3+} and Mn^{4+}, but its occupancy on tetrahedral sites is possible to a significant extent.

Determination of the concentration of each cation in $Cu_xMn_{3-x}O_4$ solid solutions is not available yet, as no theory can uniquely describe the equilibria between all species.

5.4 Conclusions

In-situ x-ray and neutron diffraction reveal that CuxMn3-xO4 spinel have cubic structure with x from 0.8 to 1.4 at high temperatures. CuMnO2 with hexagonal structure was detected at high temperatures, and monoclinic symmetry at the temperatures up to 1100°C was not observed in our in-situ x-ray diffraction analyses. Clearly, quenching (metastable) normally decreases cell symmetry of Cu-Mn oxides, and is not a reliable way to determine equilibrium structure in Cu-Mn-O system. High temperature neutron diffraction confirmed the x-ray diffraction results that Cu-Mn spinel has cubic symmetry. Cation distributions from refinement of high-temperature neutron diffraction data show that the cubic lattice parameter of the spinel phase increases with temperature, and decreases with increasing Cu content in $Cu_xMn_{3-x}O_4$ solid solutions. More Cu goes onto tetrahedral sites than octahedral sites. As Cu content in the solid solution increases, Cu concentration on tetrahedral sites increases more quickly than that on octahedral sites. Meanwhile, Mn was replaced by Cu, and its concentration decreases.

Chapter 6
Summary and conclusions

This work has developed a new method to obtain metallic manganese deposits through electrodeposition without any additives. Cobalt-manganese and copper-manganese spinel coatings were obtained by electrodeposition and subsequent oxidation. It was demonstrated that the spinel coatings can provide an effective electronic path to the metallic substrate and the outward diffusion of chromium can be virtually suppressed by the spinel coatings.

Studies on the transformation of copper-manganese metallic thin films to spinel show that manganese was oxidized through inward diffusion of oxygen and CuO formed by outward diffusion of copper. The reaction between manganese oxides and CuO resulted in the formation of the spinel. 750°C can be a suitable temperature at which metallic thin films transform to the spinel coatings. The higher oxidation temperature can result in formation of transition layer, which is due to oxidation of the substrate alloy.

In-situ x-ray and neutron diffraction analyses provide clear insights into the crystal structures of $Cu_xMn_{3-x}O_4$ solid solutions and $CuMnO_2$ at high temperatures. $Cu_xMn_{3-x}O_4$ spinel has cubic symmetry and $CuMnO_2$ has hexagonal structure at high temperatures. The following equation was confirmed by our in-situ analysis data in $Cu_xMn_{3-x}O_4$ solid solutions:

$$Cu_{tetra.} + Mn_{oct.} \Leftrightarrow Cu_{oct.} + Mn_{tetra.}$$

Many equilibrium reactions have been proposed for $Cu_xMn_{3-x}O_4$ solid solutions, but their applicability is in question, which makes determination of the concentration of manganese and copper ions on the tetrahedral and octahedral sites in $Cu_xMn_{3-x}O_4$ solid solutions difficult. Through comparing our in-situ data to those with quenched samples, we found that quenching can not prevent change of crystal symmetry of Cu-Mn oxides and is not a reliable way to determine equilibrium structure in Cu-Mn-O system.

As Cu-Mn spinel coating has a thickness of around 20 μm, its physical properties is the same as the bulk material. The crystal structure information obtained from the bulk materials can be extended to understanding of Cu-Mn spinel coating.

Bibliography

A.G.Kholmogorov, A.M.Zhyzhaev, U.S.Kononov, G.A.Moiseeva, and G.L.Pashkov: Hydrometallurgy **56:** 1-11, 2000.

A.I.Saprykin, J.S.Becker, U.V.D.Crone, and H.J.Dietze, F.: J.Anal.Chem. **358:** 145, 1997.

A.V.Virkar, and D.M.England: Solid State Fuel Cell Interconnector, United States Patent 6,054,231, 25 April 2000.

Abellan, J. P., V.Shemet, F.Tietz, L.Singheiser, W.J.Quadakkers, and A.Gil. *In* Proceedings 7th International SOFC VII, Tsukuba, Japan.

Ansel, D., Liu, J. W., Bohn, M., and Debuigne, J.: Oxidation of copper-manganese alloys under pure oxygen. Oxidation of Metals **39** (1/2)**:** 31-54, 1993.

Aoki, I.: J.Phys.Soc. Japan **20:** 871, 1965.

Araujo, J. A. M. d., Castro, M. d. M. R. d., and Lins, V. d. F. C.: Hydrometallurgy **84:** 204-210, 2006.

B.E.Conway, and B.V.Tilak: Advances in Catalysis, Academic Press, New York, 1992.

B.T.Kolomiets, I.T.Sheftel, and E.V.Kurlina: Soviet Phys.-Tech.Phys. **2:** 40-58, 1957.

Basu, R. N., Knott, N., and Petric, A.: Development of a CuFe2O4 interconnect coating. *In* Solid Oixde Fuel Cells IX, pp. 1859-1865.

Bhandage, G. T., and Keer, H. V.: Structural and magnetic properties of the CuxCd1-xMn2O4 system. J. Phys. C: Solid State Phys. **8:** 501-506, 1975.

Blasse, G.: J. Phys. Chem. Solids **27:** 383-389, 1966.

Brabers, V. A. M., and Vandenberghe, R. E.: Ionic order and cation valencies in the spinels Cu1.5Mn1.5O4 and CuGaMnO4. Physics Letters **44A** (7)**:** 493-494, 1973.

Bragg, W. H.: The structure of the spinel group of crystals. Philos. Mag. **30:** 305-315, 1915.

Brenner, A.: Electrodeposition of alloys Principles and Practice, Academic Press, New York and London, 1963.

Broemme, A. D. D., and Brabers, V. A. M.: Preparation and properties of copper and manganese containing mixed oxides. Solid State Ionics **16:** 171-178, 1985.

Brylewski, T., Nanko, M., Maruyana, T., and Przybylski, K.: Solid State Ionics **143:** 131, 2001.

Buhl, R.: J. Phys.Chem. Solids **30:** 805-812, 1969.

Burriel, M., Garcia, G., Santiso, J., Hansson, A. N., Linderoth, S., and Figueras, A.: Co3O4 protective coatings prepared by pulsed injection metal organic chemical vapour deposition. Thin Solid Films **473:** 98-103, 2005.

C.L.Mantell, and B.G.Shah: Trans.Metal.Soc.AIME **239** (4)**:** 591, 1967.

C.L.Mantell, and G.Rerment: Trans.Metall.Soc. **236:** 718, 1966.

C.Wagner: Diffusion and High-temperature Oxidation of Metals in Atom Movements, Am.Soc.Metals, Cleveland, Ohio, 1951.

Chen, X., Y.Hou, P., P.Jacobson, C., J.Visco, S., and Jonghe, L. C. D.: Solid State Ionics **176:** 423-433, 2005.
Chen, X., Y.Hou, P., P.Jacobson, C., J.Visco, S., and Jonghe, L. C. D.: Solid State Ionics **176:** 425-433, 2005.
Coleman, T. W., and Griffin, R. A.: Electrodepositing metallic manganese. *In* US Patent 4478697A, 1984.
Cui, C. Q., Jiang, S. P., and Tseung, A. C. C.: Electrodeposition of cobalt from aqueous chloride solutions. Journal of the Electrochemical Society **137** (11)**:** 3418-3423, 1990.
D.Dulieu, J.Cotton, and H.Greiner, Nantes, France, 1998.
D.Dulieu, J.Cotton, and H.Greiner. *In* Proceedings of Third European Solid Oxide Fuel Forum, Nantes, France, pp. 447.
D.J.Young, and O.Ahmed: Materials Science Forum **369-372:** 93, 2001.
Dille, J., Charlier, J., and Winand, R.: The structure and mechanical properties of thick cobalt electrodeposits. Journal of Materials Science **32:** 2637-2646, 1997.
Dorris, S. E., and Mason, T. O.: Electrical properties and cation valencies in Mn3O4. J. Am. Ceram. Soc. **71** (5)**:** 379-385, 1988.
Driessens, F. C. M., and Rieck, G. D.: Phase equilibria in the system Cu-Mn-O. Z. anorg. allgem. Chem. **351:** 48-62, 1967.
Dubrovina, I. N., Antonov, A. V., Balakirev, V. F., and Chufarov, G. I.: Effects of nonstoichiometry and quenching on the crystal structure of copper manganite. Dokl. Aakd., Nauk SSSR **260** (3)**:** 658-661, 1981.
Dubrovina, I. N., Balakirev, V. F., and Antonov, A. V.: Cation distribution in the CuxMn3-xO4 and CuMxMn2-xO4 (M=Cr, Al) spinel. Inorganic Materials **37** (1)**:** 76-81, 2001.
Dunitz, J. D., and Orgel, L. E.: Electronic properties of tansitin metal oxides-Distortions from cubic symmetry. J. Phys. Chem. Solids **3:** 20-29, 1957.
Dunitz, J. D., and Orgel, L. E.: Electronic properties of transition metal oxides. J. Phys. Chem. Solids **3:** 318-323, 1957.
E.Batawi, A.Plas, W.Strab, K.Honegger, and R.Diethelm, The Electrochemical Society Proceedings Series, Pennington, NJ, 1999.
E.Batawi, W.Glatz, W.Kraussler, M.Janousek, B.Doggwiler, and R.Diethelm, PV 99-19 pp., The Electrochemical Society Proceedings Series, Pennington,NJ, 1999.
E.J.W.Verwey, and J.H.de-Boer: Rec.Trav.Chim. **55:** 531-540, 1936.
E.J.W.Verwey, P.W.Haajman, and F.C.Romein: J.Chem.Phys. **16:** 181, 1947.
E.V.Potter, and R.W.Huber: Pyys.Rev. **68:** 24, 1945.
E.Verwey: Semiconducting Materials, Forengn Lit.Press, 1954.
F.Riffard, H.Buscail, E.Caudron, R.Cueff, C.Issartel, Messki, S. E., and S.Perrier: Materials Science Forum **461-464:** 175, 2004.
F.Stokman: Naturwissenschaft **150** (7)**:** 38, 1951.
F.Velasco, A.Gonzalez-Centeno, and A.Bautista: Materials Science Forum **461-464:** 1149, 2004.
Feng, M., and J.B.Goodenough: European J. Solid State and Inorganic Chemistry **T31:** 663, 1994.

Fergus, J. W.: Metallic interconnects for solid oxide fuel cells. Materials Science and Engneering A **397:** 271-283, 2005.

Fierro, G., Ferraris, G., Dragone, R., Jacono, L. L., and Faticanti, M.: Catal. Today **116** (1)**:** 38-49, 2006.

Floate, S., Hyde, M., and Compton, R. G.: Electrochemical and AFM studies of hte electrodeposition of cobalt on glassy carbon: an analysis of the effect of ultrasound. Journal of Electroanalytical Chemistry **523:** 49-63, 2002.

G.V.Samsonov: The Oxide Handbook, IFI Plenum, New York, 1973.

Gesmundo, F., Nanni, P., and Whittle, D. P.: High temperature oxidation of Co-Mn alloys. Corrosion Science **19:** 675-691, 1979.

Ghare, D. B., Sinha, A. P. B., and Singh, L.: Changes in valency state of ions in CuMn2O4 at high temperatures. J. Mater. Sci. **3:** 389-394, 1968.

Gillot, B., Buguet, S., and Kester, E.: Oxidation mechanism and valence states of copper and manganese in tetragonal CuMnO4. J. Mater.Chem. **7** (12)**:** 2513-2517, 1997.

Gillot, B., Kharroubi, M., Metz, R., Legros, r., and Rousset, A.: Electrical properties of copper manganite spinels CuxMn3-xO4 (0<x<1). Phys.stat.sol. **(a)124:** 317-325, 1991.

Golikov, Y. V., Ovchinnikova, L. A., Dubrovina, I. N., and Balakirev, V. F.: Phase diagram of the Cu-Mn-O system. Inorganic Materials **30** (10)**:** 1206-1211, 1994.

Gomez, E., and Valles, E.: Thick cobalt coatings obtained by electrodeposition. Journal of Applied Electrochemistry **32:** 693-700, 2002.

Gong, J., and Zangari, G.: Journal of the Electrochemical Society **149** (4)**:** C209, 2002.

Goodenough, J. B., and Loeb, A. L.: Theory of ionic ordering crystal distortion and magnetic exchange due to covalent forces in spinels. Phys. Rev. **98** (2)**:** 391-408, 1955.

H.Greiner, T.Grogler, W.Kock, and R.F.Singer, Teh Telectrochemical Society Inc., 1995.

H.H.Oaks, and W.E.Bradt: Trans.Electrochem.Soc. **69:** 567, 1936.

H.Ishihara, H.Matsuda, and Y.Takita: J.American Chemistry Society **116:** 3801, 1994.

H.Ling, and A.Petric. *In* Proceedings of the Ninth International Symposium on solid Oxide Fuel Cells, Pennington,NJ,USA, pp. 1866-1873.

H.Nagai, S.Ishikawa, N.Amano, and K.Shoji: Transactions of the Japan Insittute of Metals **26** (10)**:** 753, 1985.

H.Nagai, T.Fujikawa, and K.Shoji: Transactions of the Japan Insittute of Metals **24** (8)**:** 581, 1983.

H.Schmidt, B.Bruckner, and K.Fischer, PV 95-1 pp., The Electrochemical Society Proceedings Series, Pennington, NJ, 1995.

Hang, L., and Petirc, A. *In* Solid Oxide Fuel Cells IX, pp. 1866.

Harris, M., Meyer, D. M., and Auerswald, K.: J.the South African Institute of Mining & Metallurgy **77** (7)**:** 137, 1977.

Holt, A., and Kofstad, P.: Solid State Ionics **100:** 201, 1997.
Holt, A., and Kofstad, P.: Solid State Ionics **117:** 21, 1999.
Horita, T., Xiong, Y., Yamaji, K., N.Sakai, and Yokokawa, H.: Fuel cells 2002 **3-4** (2)**:** 189, 2002.
Huang, K., and J.B.Goodenough: Solid State Ionics **129:** 237, 2000.
Huang, K. Q., Tichy, R., and J.B.Goodenough: J.American Chemistry Society **81:** 2565, 1998.
Huang, P., and Petric, A.: J. Electrochemistry Society **143** (5)**:** 1644, 1996.
Ilea, P., Popescu, I.-C., Urda, M., and Oniciu, L.: Hydrometallurgy **46:** 149, 1997.
Iwasaki, I., and Carlson, W. J.: Continuous-weighing laboratory cell for electrowinning manganese. Transactions of the Society of Mining Engineers of AIME **241** (3)**:** 308, 1968.
J.-H.Park, and K.Natesan: Oxidation of Metals **33:** 31, 1989.
J.E.Lewis, P.H.Scaife, and D.A.J.Swinkels: J.Appl.Electrochem. **6:** 453, 1976.
J.E.Lewis, P.H.Scaife, and D.A.J.Swinkels: J.Appl.Electrochem. **6:** 199, 1976.
J.H.Kim, R.H.Song, and S.H.Hyun: Solid State Ionics **174:** 185-191, 2004.
J.H.Zhu, Y.Zhang, A.Basu, z.G.Lu, M.Paranthaman, D.F.Lee, and E.A.Payzant: Surf.Coat.Technol. **177-178:** 65-72, 2004.
J.H.Zhu, Y. Z., A.Basu, Z.G.Lu, M.Paranthaman, D.F.Lee, E.A.Payzant: Surface and Coatings Technology **177-178:** 65, 2004.
J.P.Abeilan, V.Shemet, F.Tietz, L.Singheiser, and W.J.Quadakkers. *In* Solid Oxide Fuel Cells VII, Pennington, NJ, pp. 811.
J.P.Petit, M.Mermoux, Y.Wouters, A.Galerie, and C.Chemarin: Materials Science Forum **461-464:** 681, 2004.
J.Urbanek, M.Miller, H.Schmidt, and K.Llipert, Lucene, Switzerland, 2000.
J.Urbanek, M.Miller, H.Schmidt, and K.Llipert. *In* Proceedings of Fourth European Solid Oxide Fuel Cell Forum, Lucene, Switzerland, pp. 503.
Jartych, E., Jalochowski, M., and Budzynski, M.: Influence of the electrodeposition parameters on surface morphology and local magnetic properties of thin iron layers. Applied Surface Sciences **193:** 210-216, 2002.
Jartych, E., Zurawicz, J. K., Maczka, E., and Borc, J.: Preparation of thin iron films by electrodeposition and characterization of their local magnetic properties. Materials Chemistry and Physics **72:** 356-359, 2001.
K.Honegger, A.Plas, R.Diethelm, and W.Glatz. *In* Solid Oxide Fuel Cells VII, Pennington, NJ, pp. 803.
K.Huang, P.Y.Hou, and J.B.Goodenough: Solid State Ionics **129:** 237, 2000.
K.Huang, P.Y.Hou, and J.B.Goodenough: Mater.Res.Bull. **36:** 81, 2001.
K.Przybylski, J.Morgiel, J.Prazuch, and T.Brylewski. *In* Proceedings of 3th Japanese-Polish Joint Seminar on Materials Analysis, Zakopane, Poland.
K.Przybylski, J.Prazuch, T.Brylewski, and T.Maruyama. *In* Proceedings 14th International Corrosion Congress, CorrISA, Cape Town, South Africa, pp. p.1.
K.Przybylski, T.Brylewski, and J.Morgiel: Materials Science Forum **461-464:** 1099-1106, 2004.

K.Przybylski, T.Brylewski, and J.Morgiel: Materials Science Forum **461-464:** 1099, 2004.

Kharroubi, M., Gillot, B., Legros, R., Metz, R., Vajpei, A. C., and Rousset, A.: An IR spectroscopic investigation of copper manganite CuxMn3-xO4 (0<x<1) spinels and their oxidation products. J. Less-Common Metals **175** (2)**:** 279-287, 1991.

Kim, J.-H., Song, R.-H., and Hyun, S.-H.: Effect of slurry-coated LaSrMnO3 on the electrical property of Fe-Cr alloy for metallic interconnect of SOFC. Solid State Ionics **174:** 185-191, 2004.

Kshirsagar, S. T., and Sabane, C. D.: Electrical conduction in tetragonally distorted manganite spinels. Japan. J. Appl. Phys. **10** (6)**:** 794-802, 1971.

Kurokawa, H., Kawamura, K., and Maruyama, T.: Solid State Ionics **168:** 13, 2004.

Kurokawa, H., Kawamura, K., and Mauyama, T.: Solid State Ionics **168:** 13-21, 2004.

Larring, Y., and Norby, T.: Spinel and Perovskite Functional Layers Between Plansee metallic Interconnect (Cr-5wt. % Fe-1wt. % Y2O3) and Ceramic (La0.85Sr0.15)0.91MnO3 Cathode Materials for Solid Oxide Fuel Cells. J. Electrochemistry Society **147:** 3251-3256, 2000.

Lenglet, M., Huysser, A. D., Kasperek, J., Bonnelle, J. P., and Durr, J.: Mater. Res. Bull. **20** (7)**:** 745-757, 1985.

Linderoth, S., Herdriksen, P. V., Morgensen, M., and Nolangvad: J. Materials Science **31:** 5077, 1996.

Lucchesi, S., Russo, U., and Giusta, A. D.: crystal chemistry and cation distribution in some Mn-rich natural and synthetic spinels. Eur. J. Mineral. **9:** 31-42, 1997.

M.Gonsalves, and D.Pletcher: Journal of Electroanalytical Chemistry and Interfacial Electrochemistry. **285** (1-2)**:** 185, 1990.

M.Ueda, and H.Taimatsu, Lucerne, Switzerland, 2000.

Mantell, C. L., and Ferment, G. R.: Transactions of the Metallurgical Society of AIME **236** (5)**:** 718, 1966.

Mantell, C. L., and Ferment, G. R.: Electrowinning manganese. US Patent 3455799 A, 1969.

Martin, B. E.: The Performance of Perovskites and Spinels as Catalysts for Oxygen Reduction in Solid Oxide Fuel Cell Cathodes. *In* Materials Science and Engineering, vol. Doctor of Philosophy, pp. 216, McMaster University, Hamilton, 2007.

Martin, B. E., and Petric, A.: Electrical properties of copper-manganese spinel solutions and their cation valence and cation distribution. J. Phys. Chem. Solids **68:** 2262-2270, 2007.

Maunders, C., Martin, B. E., Wei, P., Petric, A., and Botton, G. A.: Investigation of the electronic structure of the cubic spinel Cu1.2Mn1.8O4 using electron energy loss spectroscopy. Solid State ionics **179** (19-20)**:** 718-724, 2008.

Meguid, E. A. A. E., Rehim, S. S. A. E., and Moustafa, E. M.: Electroplating of iron from alkaline gluconate baths. Thin Solid Films **443:** 53-59, 2003.

Metz, R.: Electrical properties of NTC thermistors make of manganite ceramics of general spinel structure. Journal of Materials Science **35:** 4705-4711, 2000.

Mitsui Mining and Smelting Co., L.: Electrowinnig manganese from manganese nodules. Japanese Patent 57073194 A2, 1982.

Miyahara, S.: J. Phys. Soc. Japan **17** (B-I)**:** 181, 1962.

Miyahara, S., Muramori, K., and Tokuda, N.: J. Phys. Soc. Japan **16:** 1490, 1961.

Murti, R., Razdan, N., and E.Ermolina: Indian Journal of Technology **24:** 270, 1986.

N.Oishi, T.Namikawa, and Y.Yamazaki: Surf.Coat.Technol. **132:** 58-64, 2000.

N.Oishi, T.Namikawa, and Y.Yamazaki: Surface and Coatings Technology **132:** 58, 2000.

N.Q.Minh, and T.Tahahashi: Science and Technology of Ceramic Fuel Cells, Elsevier, Amsterdam, 1995.

Nanni, P., Viani, F., Elliott, P., and Gesmundo, F.: High-temperature oxidation of copper-manganese alloys. Oxidation of Metals **13** (2)**:** 181-195, 1978.

Narita, T., Ishikawa, T., Karasawa, S.-i., and Nishida, K.: Oxidation properties of Co-Mn alloys at temperatures from 1273 to 1473 K. Oxidation of Metals **27** (5/6)**:** 267-282, 1987.

Navrotsky, A., and Kleppa, O. J.: The themodynamics of cation distributions in simple spinels. J. Inorg. Nucl. Chem. **29:** 2701-2714, 1967.

Nishikawa, S.: Structure of some crystals of the spinel group. Proc.Math.Phys.Soc. Tokyo **8:** 199-209, 1915.

O'Neill, H. S. C., and Navrotsky, A.: Cation distributions and thermodynamic properties of binary spinel solid solutions. Am. Mineral. **69:** 733-753, 1984.

P.Díaz-Arista, R.Antaño-López, Y.Meas, R.Ortega, E.Chainet, P.Ozil, and G.trejo: Electrochimica Acta **51:** 4393-4404, 2006.

P.K.Footner, D.R.Holmes, and D.Mortimer: Nature **216:** 54, 1967.

P.Kofstad, Oslo, Norway, 1996.

P.Wei, I.Zhitomirsky, and A.Petric. *In* Proceedings of the Ninth International Symposium on solid Oxide Fuel Cells, Pennington, NJ, pp. 1851-1858.

Papavasiliou, J., Avgouropoulos, G., and Ioannides, T.: Steam reforming of methanol over copper-manganese spinel oxide catalysts. Catalysis Communications **6:** 497-501, 2005.

Petric, A., and Ling, H.: J. American Ceramic Society **90** (5)**:** 1515-1520, 2007.

Pilla, A. S., M.E.Duarte, M., and E.Mayer, C.: Journal of Electroanalytical Chemistry **569:** 7, 2004.

Pourbaix, M.: Atlas of Electrochemical Equilibria in Aqueous Solutions, Pergamon Press Ltd., Great Britain, 1966.

Pradhan, N., Singh, P., Tripathy, B. C., and Das, S. C.: Electrowinning of cobalt from acidic sulphate solutions-effect of chloride ion. Minerals Engineering **14** (7)**:** 775-783, 2001.

Przybylski, K., Brylewski, T., and Morgiel, J.: Int. Interfacial interactions between some La-based perovskite thick films and ferritic steel substrate with regard to the operating conditions of SOFC **461-464:** 1099-1106, 2004.
R.S.Dean: Electrolytic Manganese and Its alloys, The Ronald Press, New York, 1952.
Radhakrishnan, N. K., and Biswas, A. B.: J. Indian Chem. Soc. **LI:** 274, 1974.
Radhakrishnan, N. K., and Biswas, A. B.: A Neutron diffraction study of the spinel oxide CuMn2O4. Phys.stat.sol. **(a)44:** 45-48, 1977.
Reynolds, J. E., and Lombardo, N. J.: Manganese and zinc solvent extraction. US Patent 4423012 A, 1983.
S.C.Tsai, A.M.Huntz, and C.Dolin: Oxidation of Metals **43:** 581, 1995.
S.Linderoth, P.V.Herdriksen, M.Morgensen, and Nolangvad: J.Mat.Sci. **31:** 5077, 1996.
S.P.S.Badwal, R.Deller, K.Foger, Y.Ramprakash, and J.P.Zhang: Solid State Ionics **99:** 297, 1997.
S.P.Simner, M.D.Anderson, Xia, G.-G., Z.Yang, and J.W.Stevenson: Ceramic Engineering and Science Proceedings **26** (4)**:** 83, 2005.
S.P.Simner, M.D.Anderson, Xia, G.-G., Z.Yang, and J.W.Stevenson: Ceramic Engineering and Science Proceedings **26** (4)**:** 83-90, 2005.
Sasaki, K. Y., and Talbot, J. B.: Electrodeposition of iron-group metals and binary alloys from sulfate baths. Journal of the Electrochemical Society **145** (3)**:** 981-990, 1998.
Schiller, G., Henne, R., and Ruckdaschel, R.: Journal of Nuclear Materials **32:** 3, 2000.
Schindler, W., Schneider, O., and Kirschner, J.: Electrodeposition of ultathin magnetic films of Fe and Co. Journal of Applied Physics **81** (8)**:** 3915-3917, 1997.
Shannon, R. D.: Revised effective ionic-radii and systematic studies of interatomic distances in halides and chalcogenides. Acta Crystallographica Section A **32:** 751-767, 1976.
Simner, S. P., Anderson, M. D., Yang, G.-G., Pederson, L. R., and Stevenson, J. W.: SOFC performance with Fe-Cr-Mn alloy interconnect. Journal of the electrochemical society **152** (4)**:** A740-A745, 2005.
Sinha, A. P. B., Sanjana, N. R., and Biswas, A. B.: J. Phys. Chem. **62:** 191, 1958.
Souza, S. D., S.J.Visco, and Jonghe, L. C. D.: Solid State Ionics **98:** 57, 1997.
T.Brylewski, K.Przybylski, and M.Morgiel: Mater.Chem.Phys. **81:** 434, 2003.
T.Brylewski, M.Nanko, T.Maruyana, and K.Przybylski: Solid State Ionics **143:** 131, 2001.
T.Horita, Y.Xiong, K.Yamaji, and N.Sakai: J.Electrochem.Soc. **150:** A243, 2003.
T.Horita, Y.Xiong, K.Yamaji, N.Sakai, and H.Yokodawa: Fuel Cells **2** (3-4)**:** 189, 2002.
T.J.Armstrong, and M.Smith, The Electrochemical Society,Inc., 2005.
T.Kakowaki, T.Shiomitsu, E.Matsuda, H.Nakagawa, and H.Tsuneizumi: Solid State Ionics **67:** 65, 1993.

Tilak, B. V. K. S. R. A.: Journal of Scientific and Industrial Research, Section B: Physical Sciences **21D:** 56, 1962.

Trari, M., Topfer, J., Dordor, P., Grenier, J. C., Pouchard, M., and Doumerc, J. P.: Preparation and physical properties of the solid solutions Cu1+xMn1-xO2 (0<x<2). J. Solid State Chem. **178:** 2751-2758, 2005.

Vandenberghe, R. E., Brabers, V. A. M., and Robbrecht, G. G.: The preparation and the lattic parameters of cubic CuxMn3-xO4 spinels. Phys. Stat. Sol. **(a)16:** K117-K120, 1973.

Vandenberghe, R. E., Legrand, E., Scheerilinck, D., and Brabers, V. A. M.: Neutron diffraction study of the cation ordering in Cu1.5Mn1.5O4 and CuMn0.5Mn1.5O4. Acta. Cryst. **B32:** 2796-2798, 1976.

Vandenberghe, R. E., and Robbrecht, G. G.: On the stability of the cubic spinel structure in the system Cu-Mn-O. Materials Research Bulletin **8:** 571-580, 1973.

Vandenberghe, R. E., Robbrecht, G. G., and Brabers, V. A. M.: Structure and ionic configuration of oxidic copper-manganese spinels. Phys.stat.sol. **(a)34:** 583-592, 1976.

W.E.Bradt, and H.H.Oaks: Trans.Electrochem.Soc. **70:** 279, 1937.

W.H.Zhu, and S.C.Deevi: Mater.Res.Bull. **38:** 957, 2003.

W.J.Quadakkers, H.Greiner, W.Kock, H.P.Buchkremer, K.Hilpert, and D.Stover, 1 pp., European SOFC Forum, Oberrohrdorf, Switzerland, 1996.

W.J.Quadakkers, T.Malkow, and P.Albellan. *In* Proceedings of Fourth European Solid Oxide Feul Cell Forum, Lucene, Switzerland, pp. 827.

W.J.Quadakkers, H. G., M.Hansel, A.Pattanaik, A.S.Khanna, W.Mallener: Solid State Ionics **91:** 55, 1996.

W.J.Quaddakers, H.Greiner, M.Hansel, A.Pattanaik, A.S.Khanna, and w.Mallener: Solids State Ionics **91:** 55-67, 1996.

W.Kock, H.Martinz, H.Greiner, and M.Janousek, The Electrochemical Society Inc., 1995.

W.Z.Zhu, and S.C.Deevi: Materials Research Bulletin **38:** 957, 2003.

Waskowska, A., Gerward, L., Olsen, J. S., Steenstrup, S., and Talik, E.: CuMn2O4: Properties and the high-pressure induced Jahn-Teller phase transition. J. Phys.: Condens. Matter. **13:** 2549-2562, 2001.

Wei, P., Deng, X., Bateni, M. R., and Petric, A.: Oxidation and electrical conductivity behavior of spinel coatings for metallic interconnects of Solid Oxid Fuel Cells. Corrosion **63** (6)**:** 529-536, 2007.

Wei, P., Zhitomirsky, I., and Petric, A.: Proceedings of the Ninth Internationaly Symposium on Solid Oxide Fuel Cells 1851, 2005.

Y.Larring, and T.Norby: J.Electrochem.Soc. **149** (9)**:** 3251, 2000.

Y.Larring, and T.Norby: Journal of The Electrochemical Society **147** (9)**:** 3251-3256, 2000.

Y.Matsuzaki, and I.Yasuda: Solid State Ionics **132:** 271, 2000.

Y.Yoo, and M.Dauga. *In* Proceedings of the 7International Symposium on Solid Oxide Fuel Cells, Pennington, NJ, pp. 837-846.

Yamada, A.: Lattice instability in Li(LixMn2-x)O4. Journal of solid state chemistry **122:** 160-165, 1996.

Yang, Z., Weil, K. S., Paxton, D. M., and Stevenson, J. W.: Selection and evaluation of heat-resistant alloys for SOFC interconnect applications. Journal of the Electrochemical Society **150** (9)**:** A1188-A1201, 2--3.

Yang, Z., Xia, G., Simner, S. P., and Stevenson, J. W.: J. Electrochemistry Society **159** (9)**:** A1896-A1901, 2005.

Yang, Z., Xia, G., Simner, S. P., and Stevenson, J. W.: Thermal growth and performance of manganese cobaltite spinel protection layers on ferritic stainless steel SOFC interconnects. Journal of the Electrochemical Society **152** (9)**:** A1896-A1901, 2005.

Yu.D.Gamburg: Russian Journal of Applied Chemistry **72** (4)**:** 716, 1999.

Z.Yang, K.S.Weil, D.M.Paxton, and J.W.Stevenson: J.Electrochem.Soc. **150:** A1188, 2003.

Zaslavskii, A. I., and Plakhtii, V. P.: Soviet Phys. - Solid State **11:** 3, 1969.

Zhu, J. H., Zhang, Y., Basu, A., Lu, Z. G., Paranthaman, M., Lee, D. F., and Payzant, E. A.: LaCrO3-based coatings on ferritic stainless steel for solid oxide fuel cell interconnect applications. Surface and Coatings Technology **177-178:** 65-72, 2004.

Appendix 1

Phase Identification of In-Situ X-ray Diffraction Data

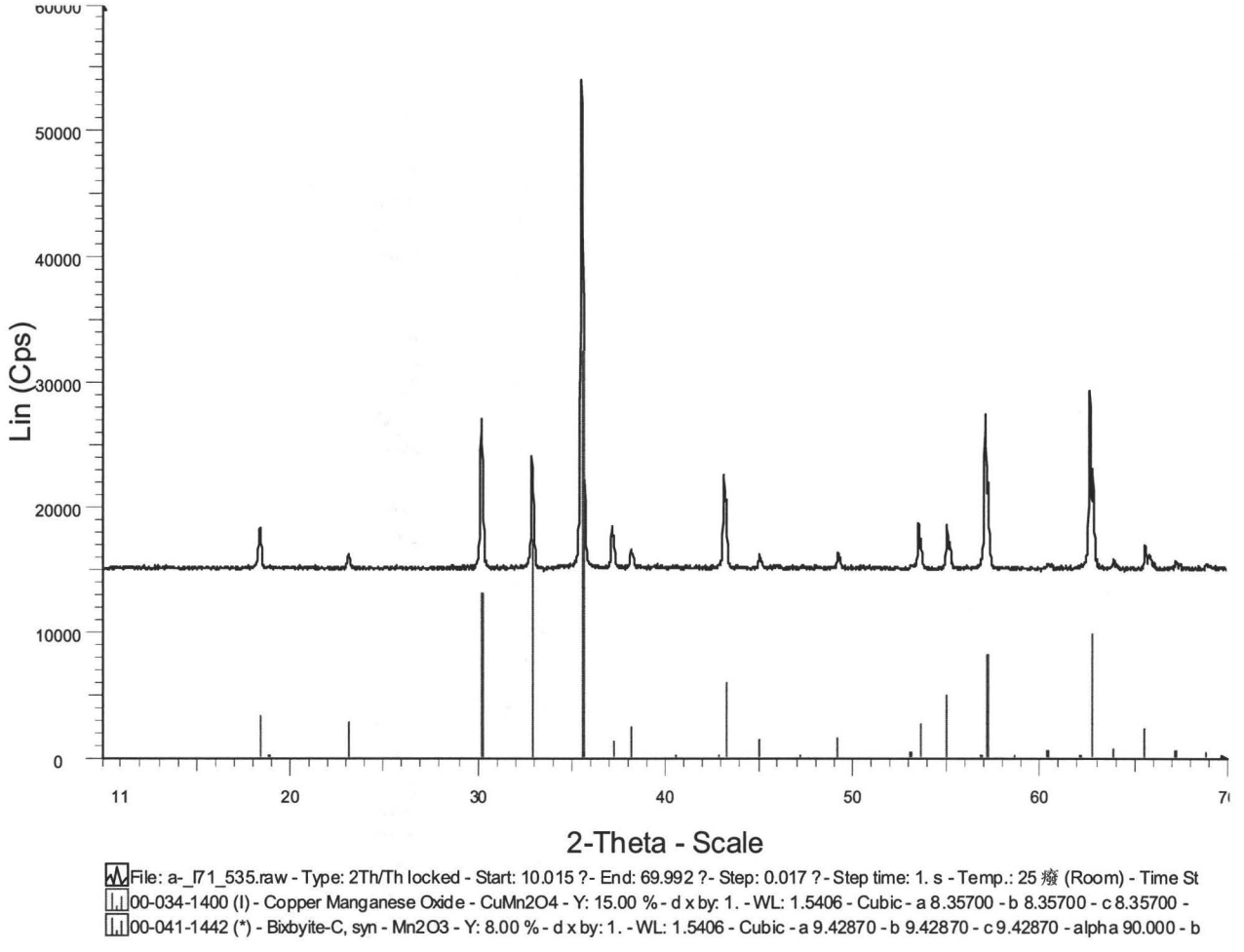

Figure 1 X-ray diffraction pattern of $Cu_{1.1}Mn_{1.9}O_4$ at 535°C

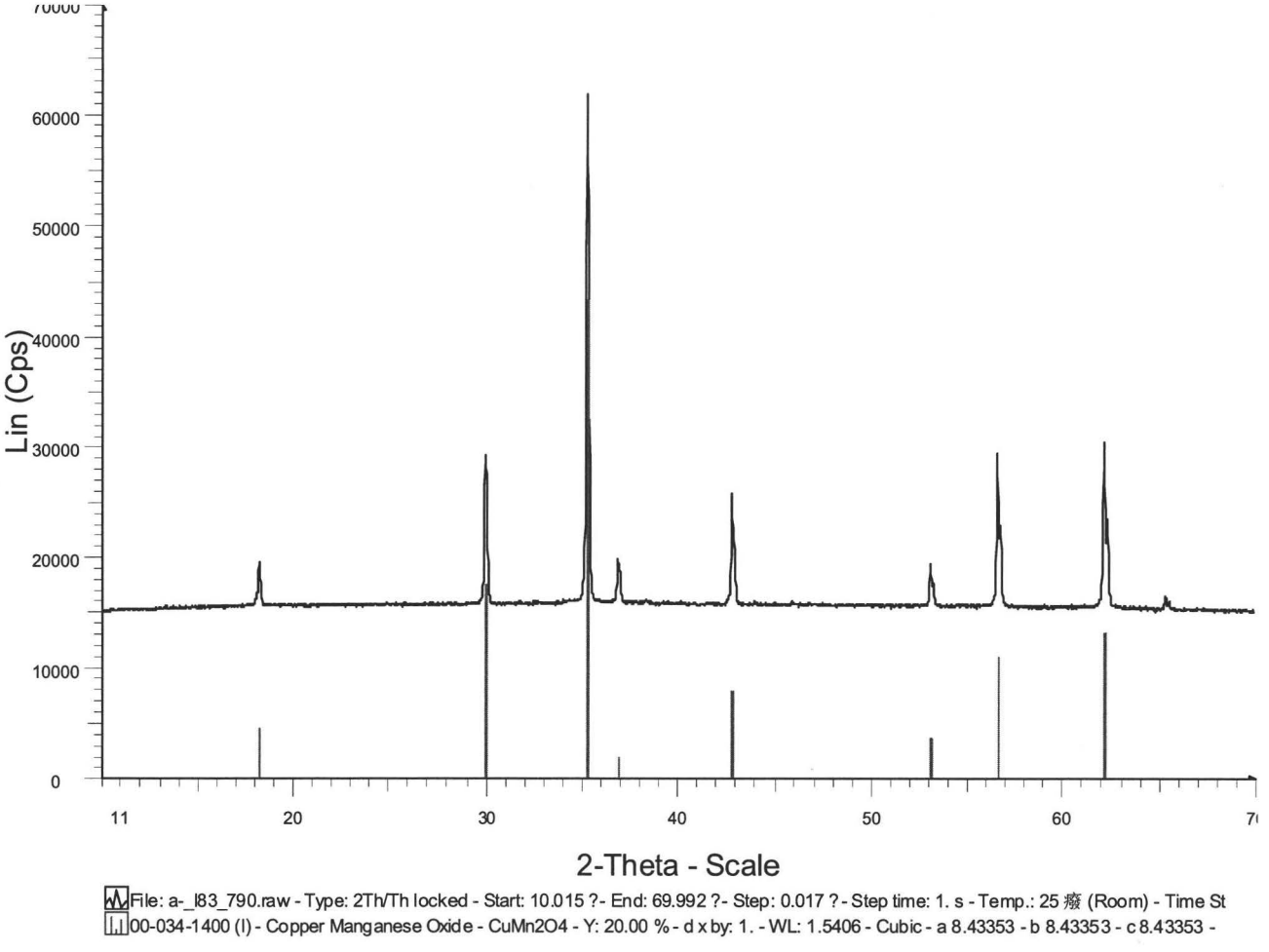

Figure 2 X-ray diffraction pattern of $Cu_{1.1}Mn_{1.9}O_4$ at 790°C after 535°C

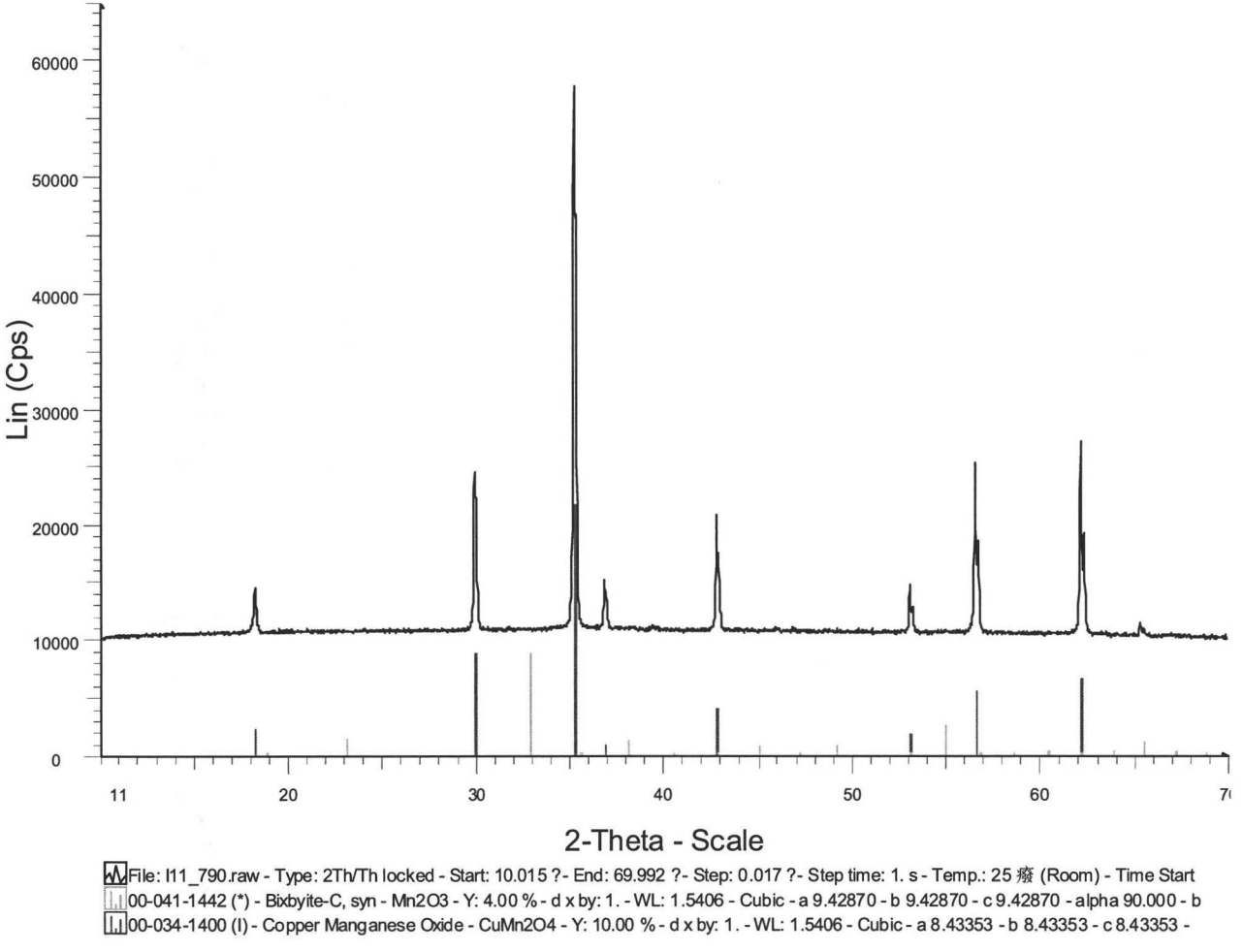

Figure 3 X-ray diffraction pattern of $Cu_{1.1}Mn_{1.9}O_4$ at 790ºC at the beginning

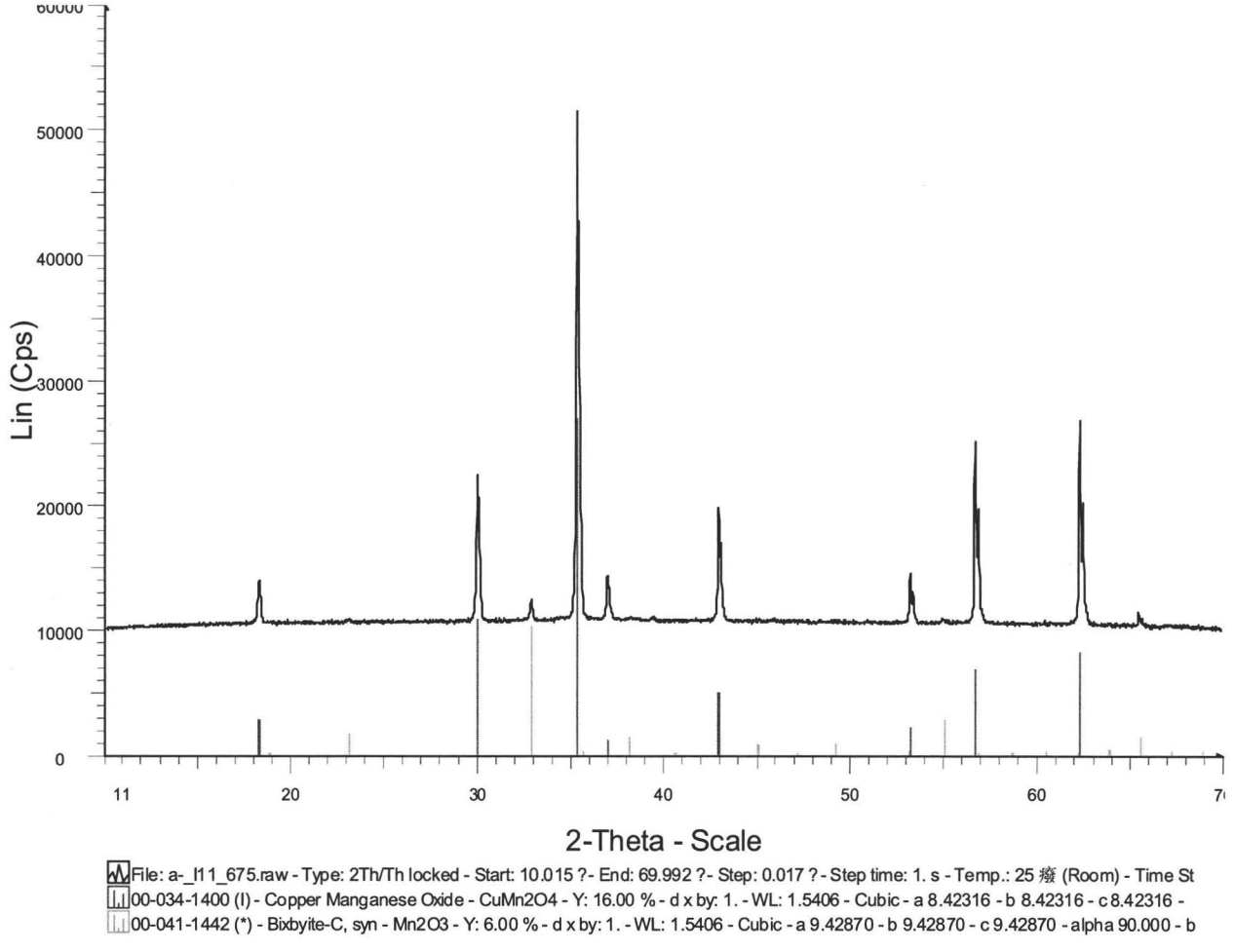

Figure 4 X-ray diffraction pattern of $Cu_{1.1}Mn_{1.9}O_4$ at 675°C

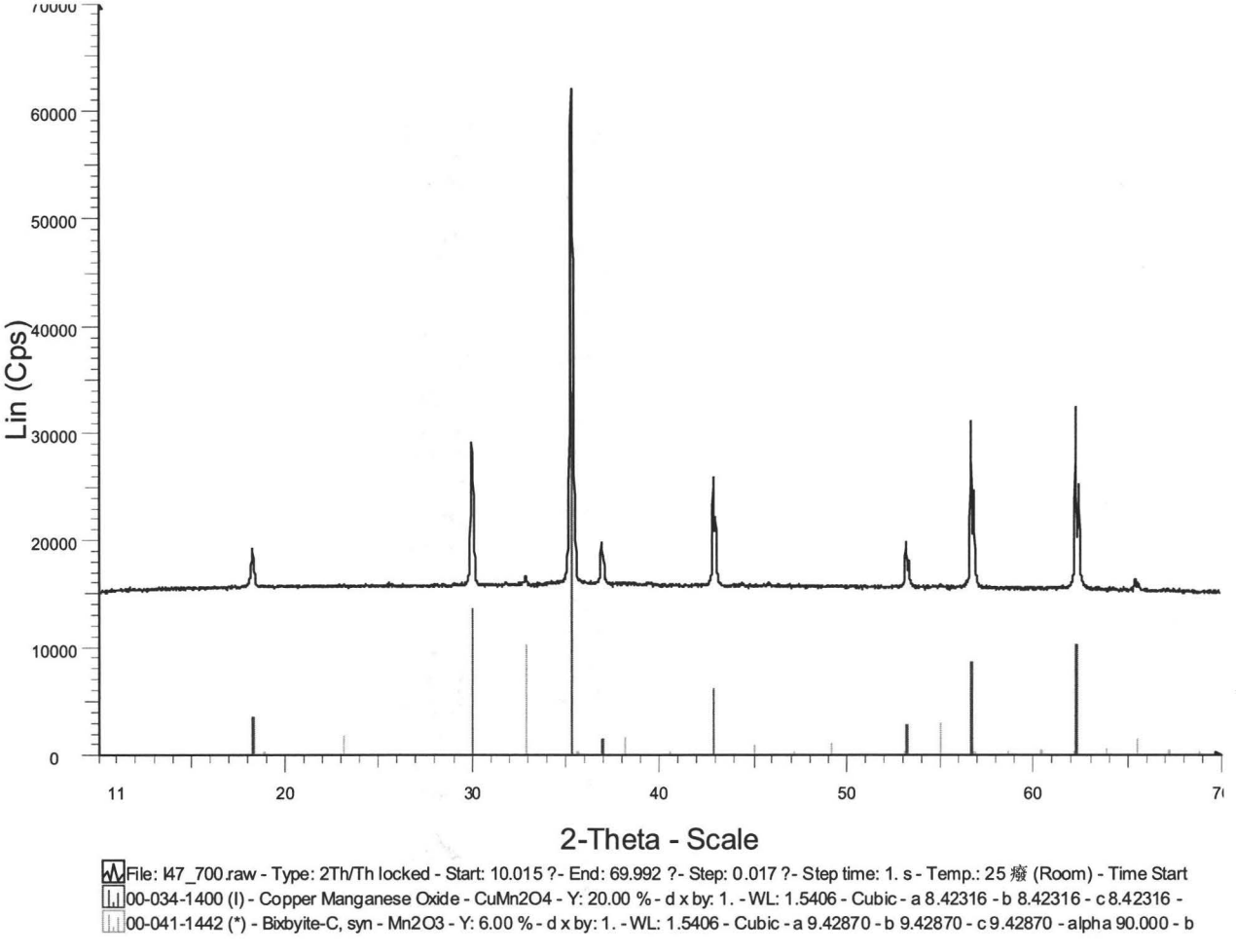

Figure 5 X-ray diffraction pattern of $Cu_{1.1}Mn_{1.9}O_4$ at 700°C

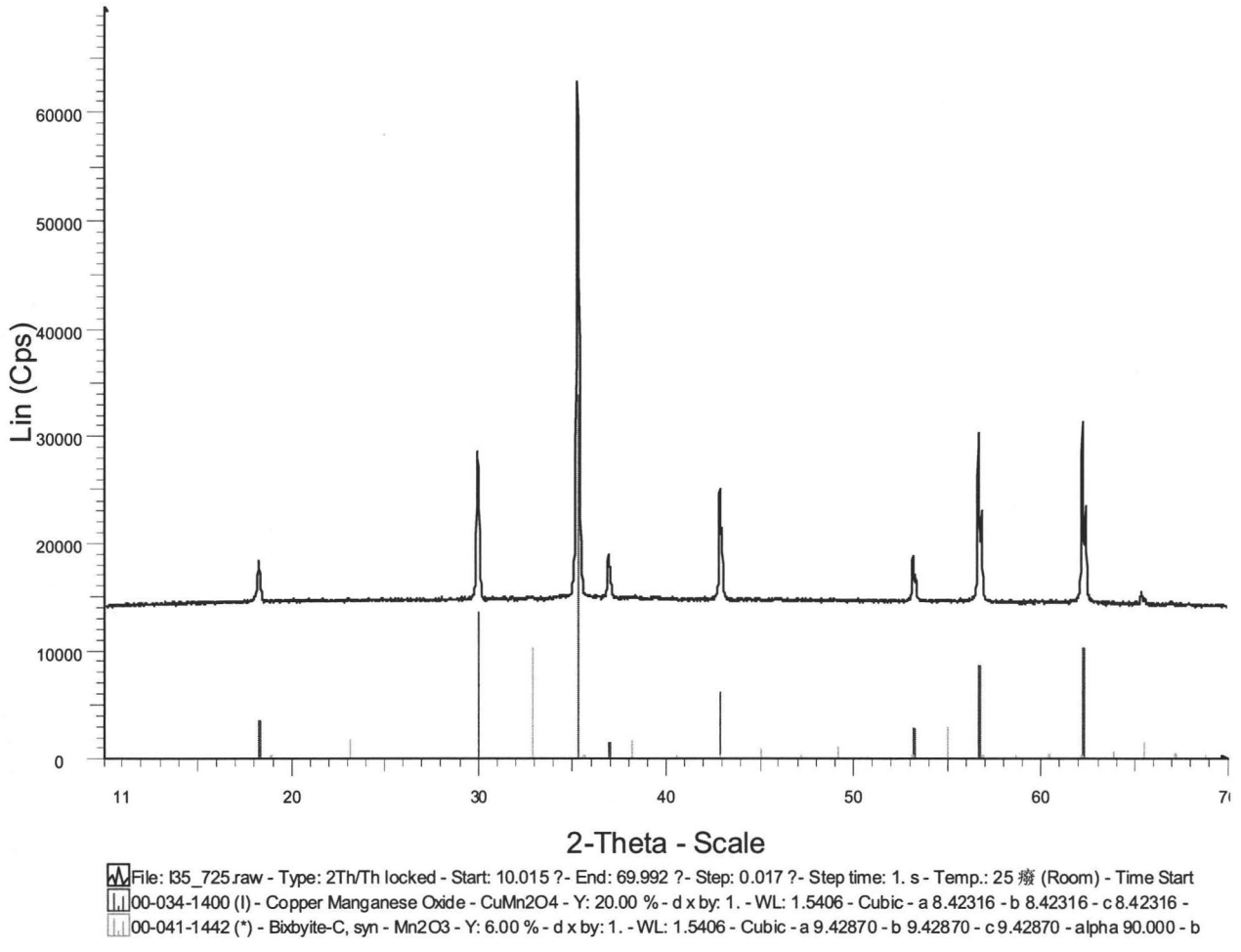

Figure 6 X-ray diffraction pattern of $Cu_{1.1}Mn_{1.9}O_4$ at 725°C

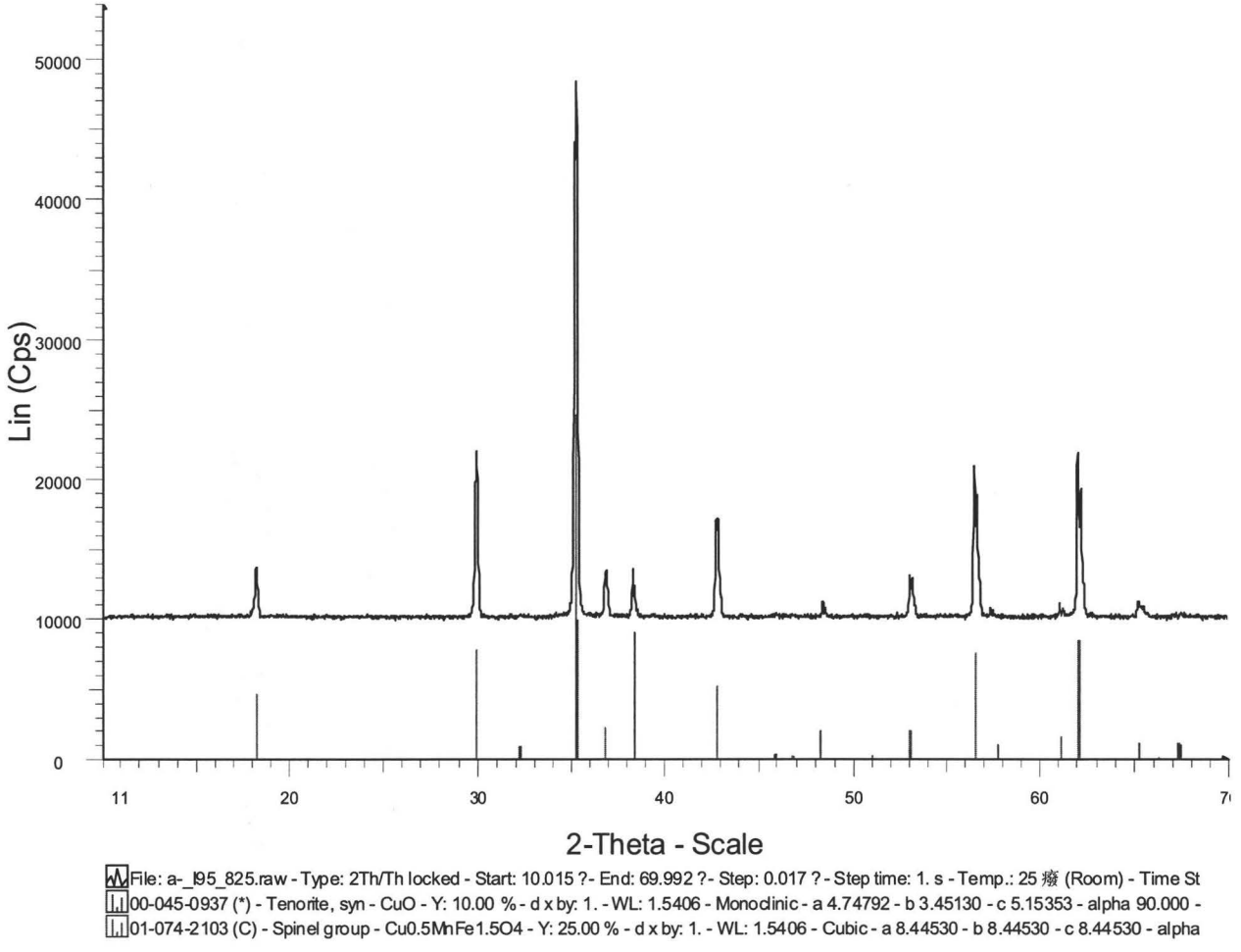

Figure 7 X-ray diffraction pattern of $Cu_{1.1}Mn_{1.9}O_4$ at 825°C

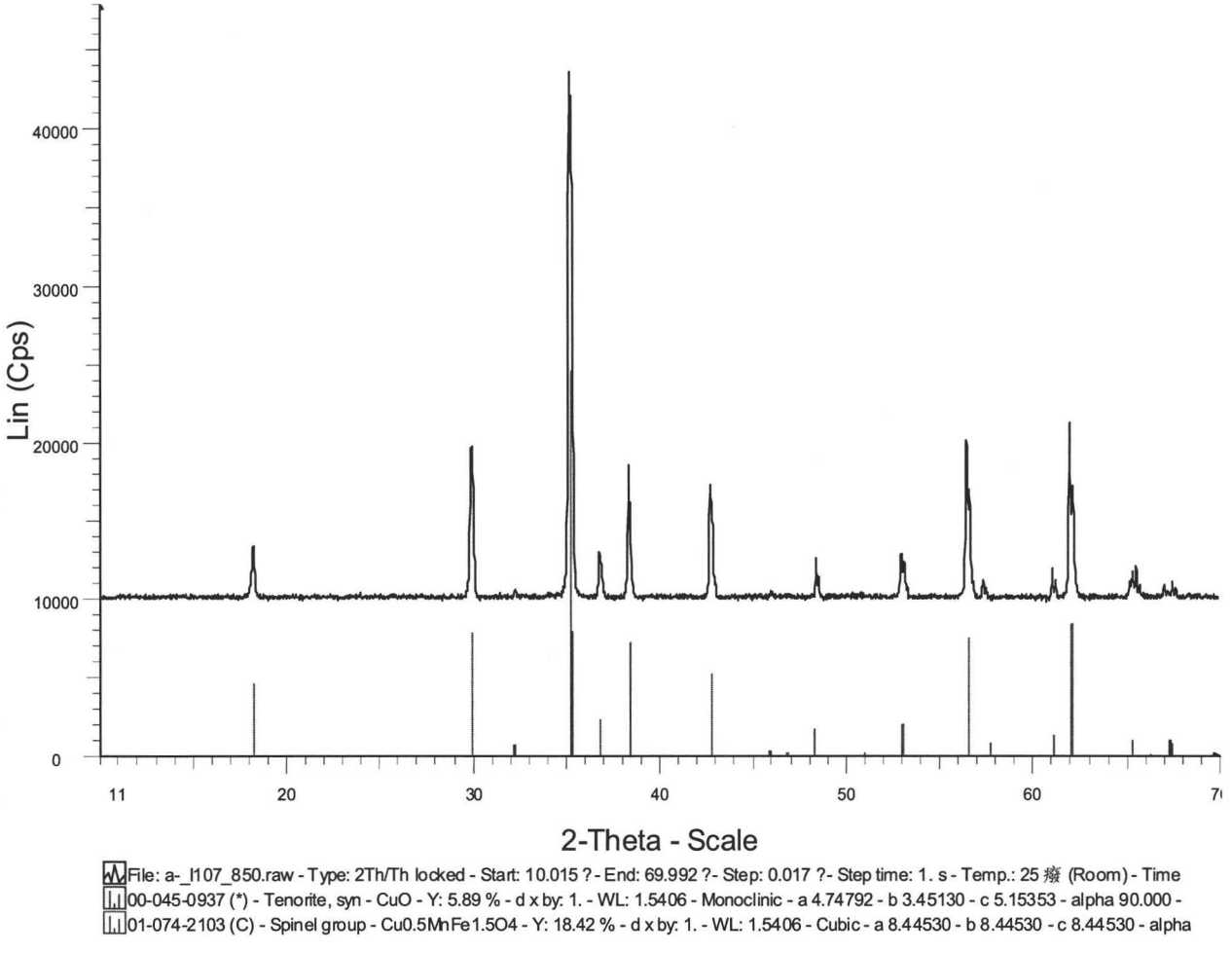

Figure 8 X-ray diffraction pattern of $Cu_{1.1}Mn_{1.9}O_4$ at 850°C

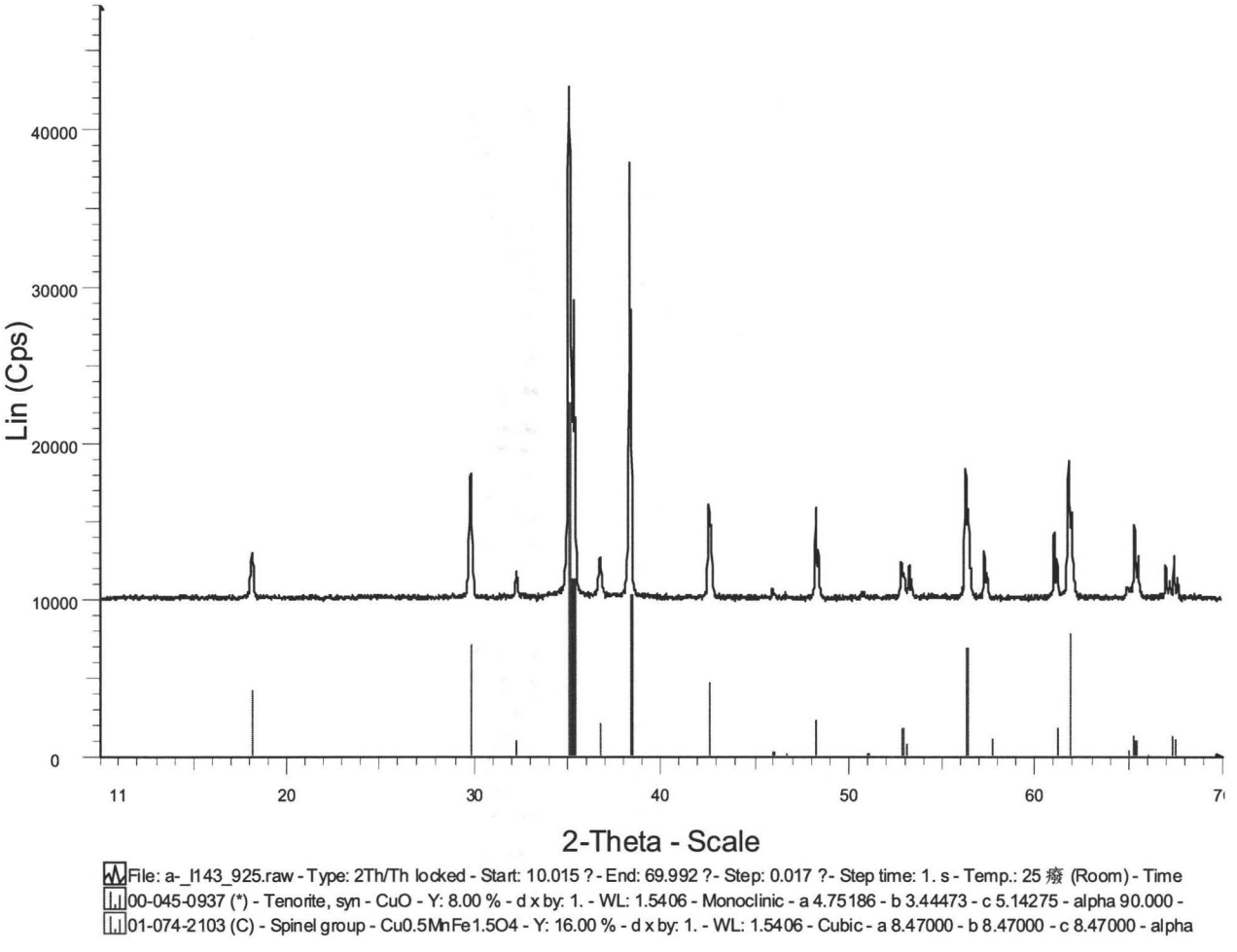

Figure 9 X-ray diffraction pattern of $Cu_{1.1}Mn_{1.9}O_4$ at 925°C

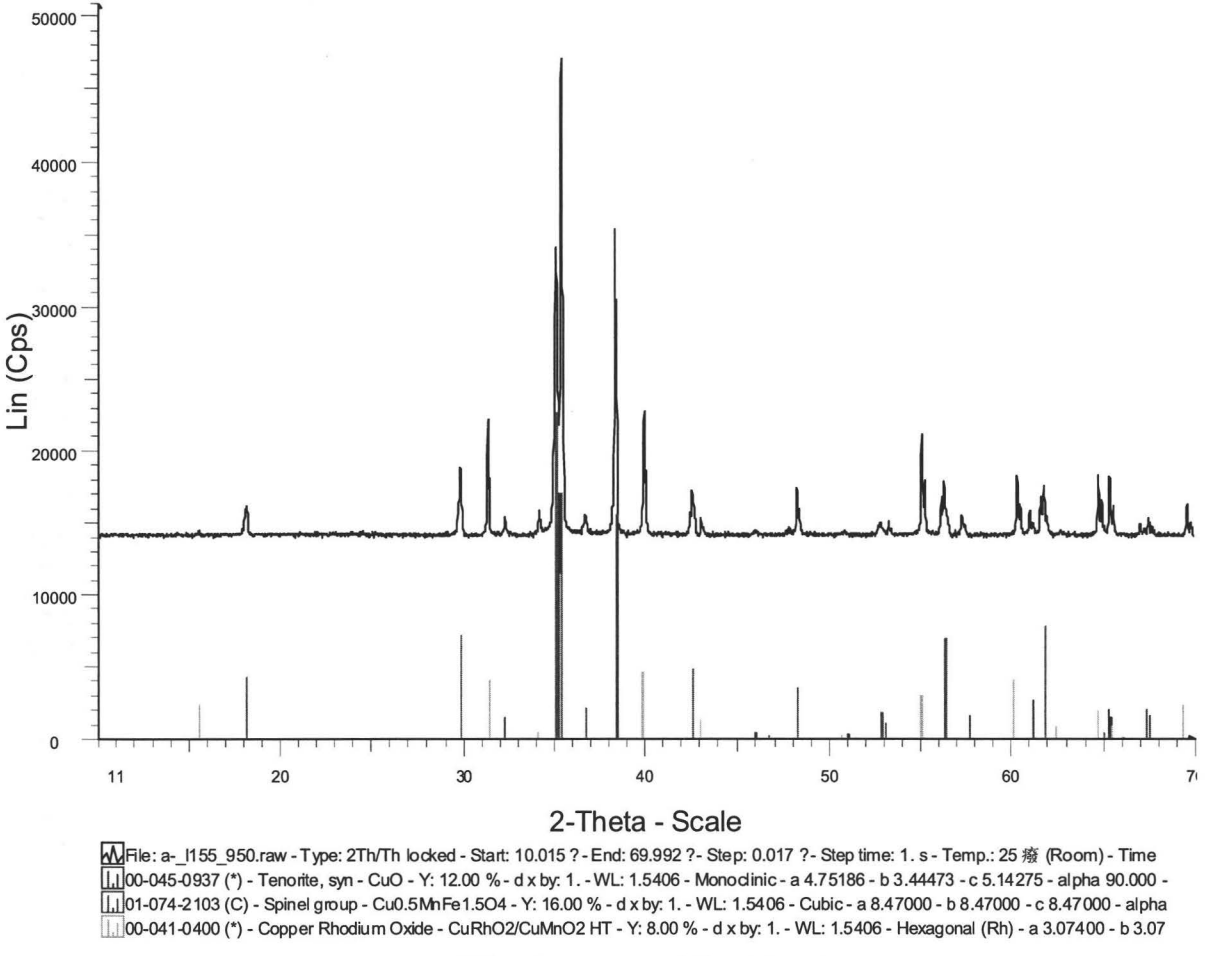

Figure 10 X-ray diffraction pattern of $Cu_{1.1}Mn_{1.9}O_4$ at 950°C

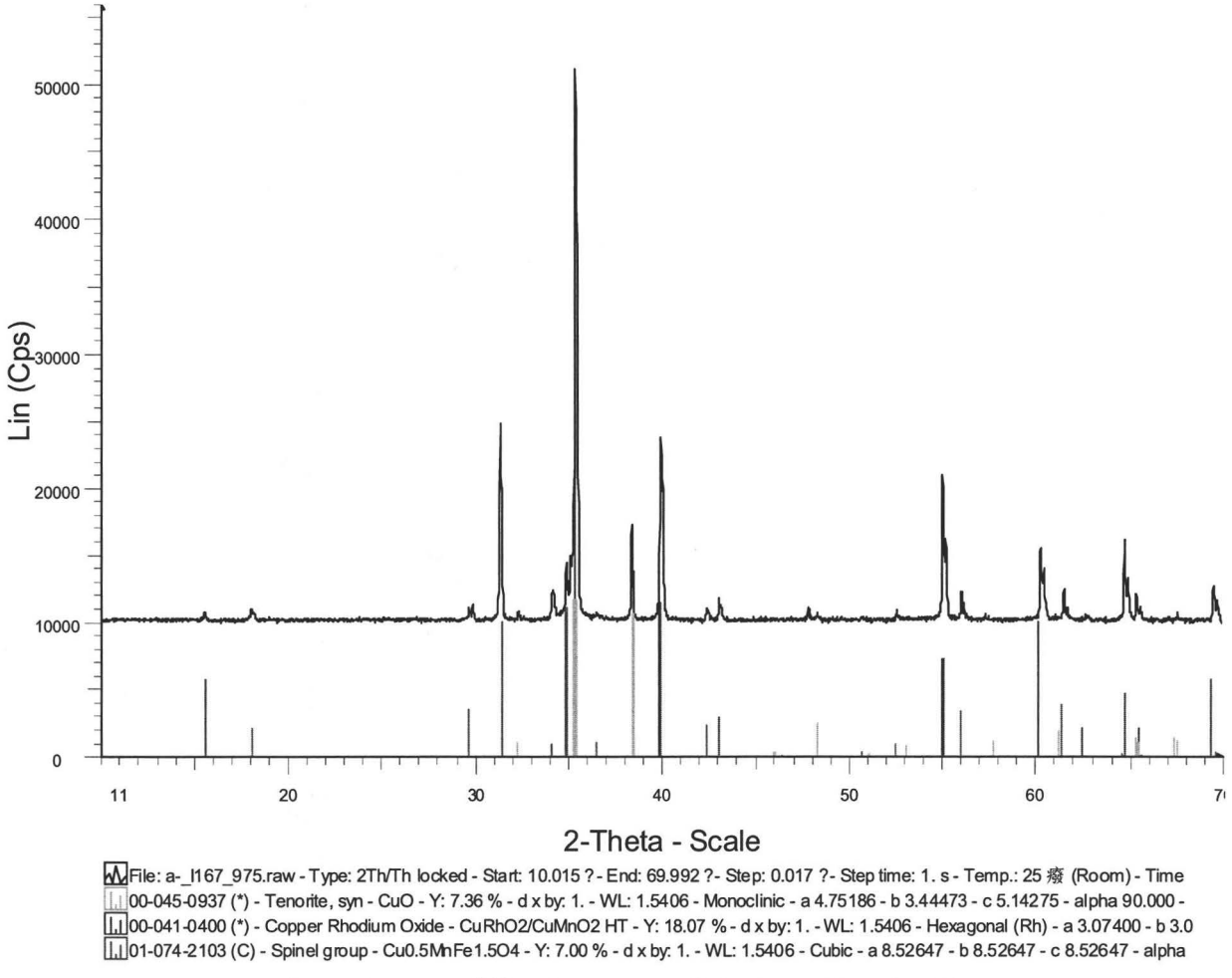

Figure 11 X-ray diffraction pattern of $Cu_{1.1}Mn_{1.9}O_4$ at 975°C

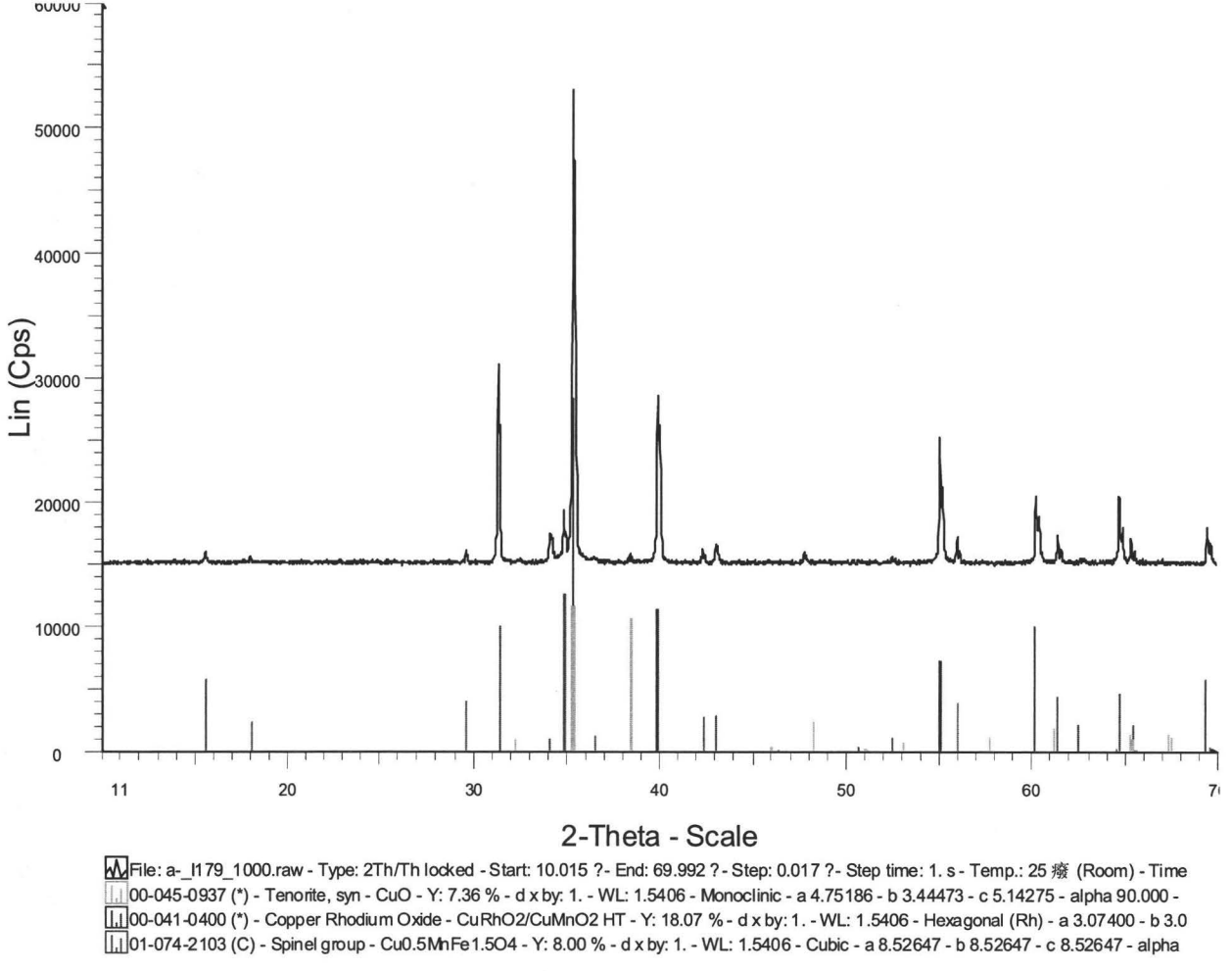

Figure 12 X-ray diffraction pattern of $Cu_{1.1}Mn_{1.9}O_4$ at 1000°C

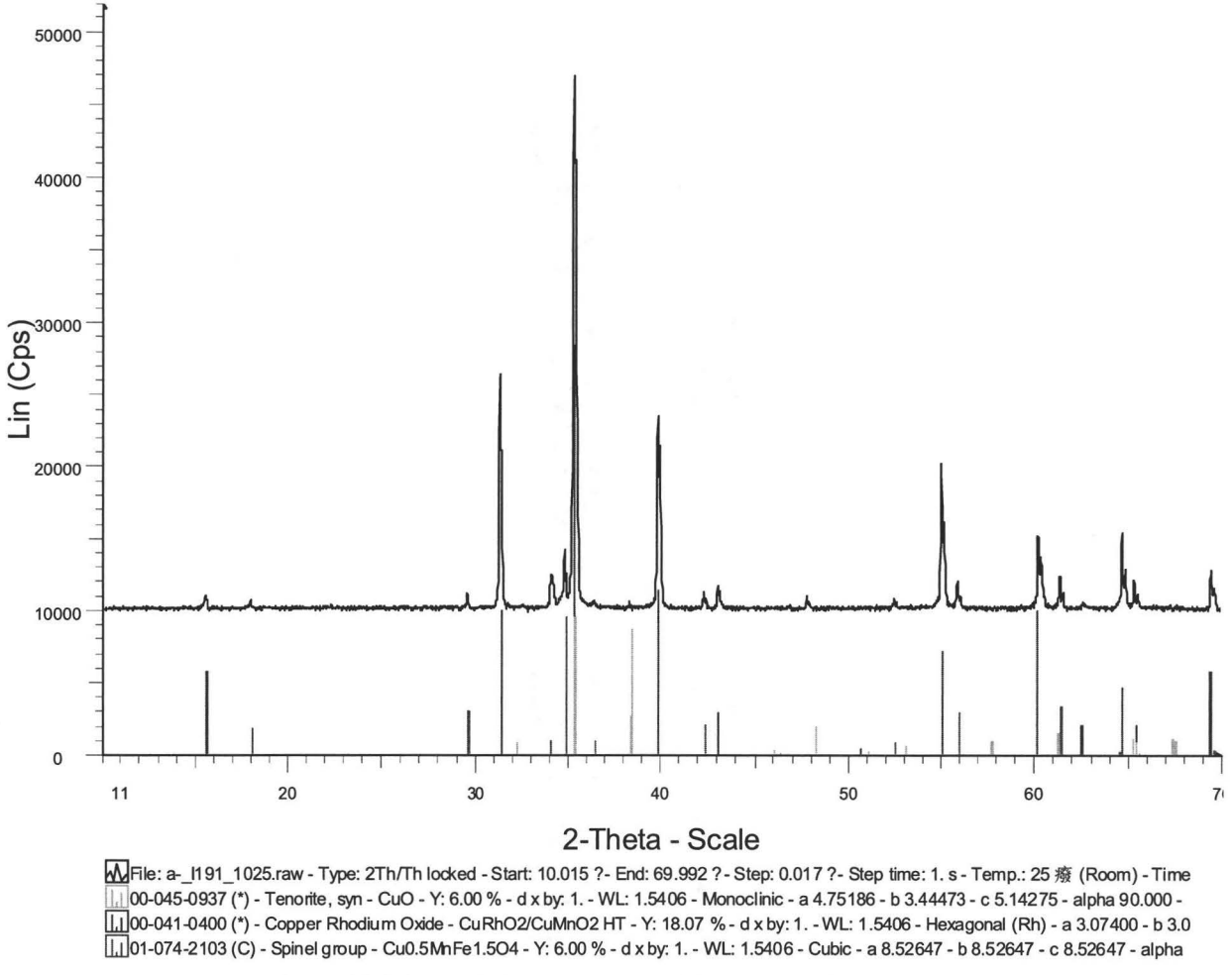

Figure 13 X-ray diffraction pattern of $Cu_{1.1}Mn_{1.9}O_4$ at 1025°C

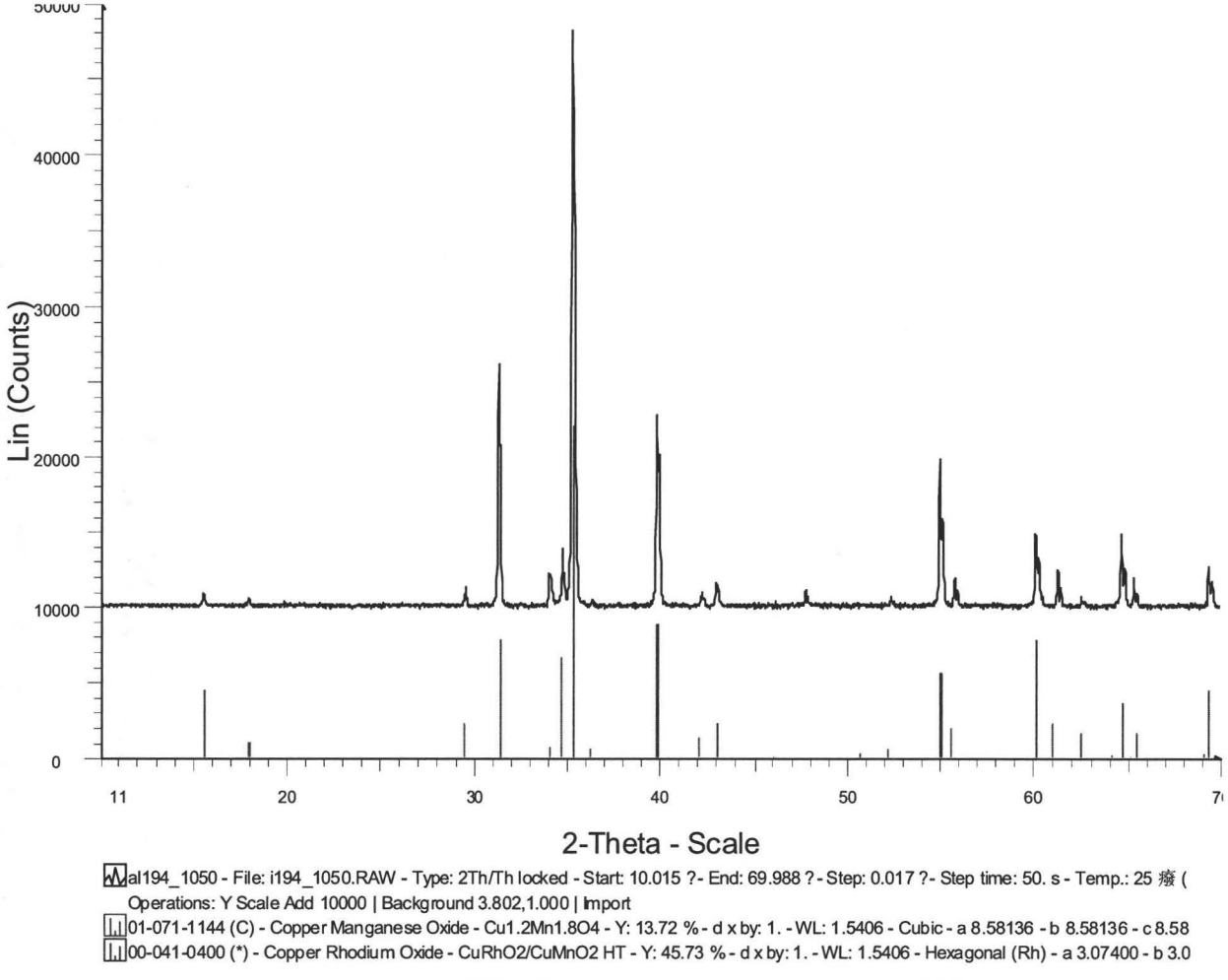

Figure 14 X-ray diffraction pattern of $Cu_{1.1}Mn_{1.9}O_4$ at 1050°C

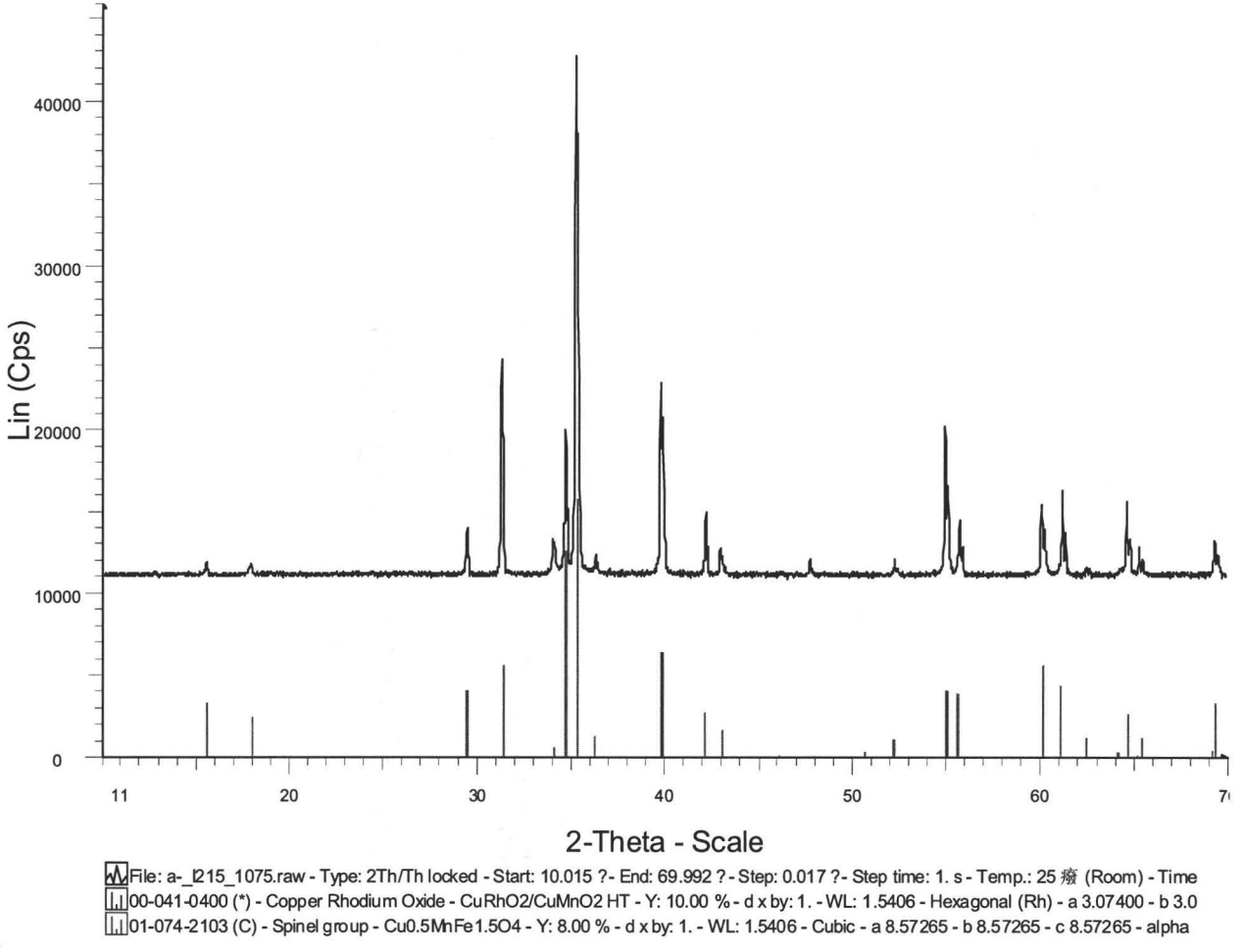

Figure 15 X-ray diffraction pattern of $Cu_{1.1}Mn_{1.9}O_4$ at 1075°C

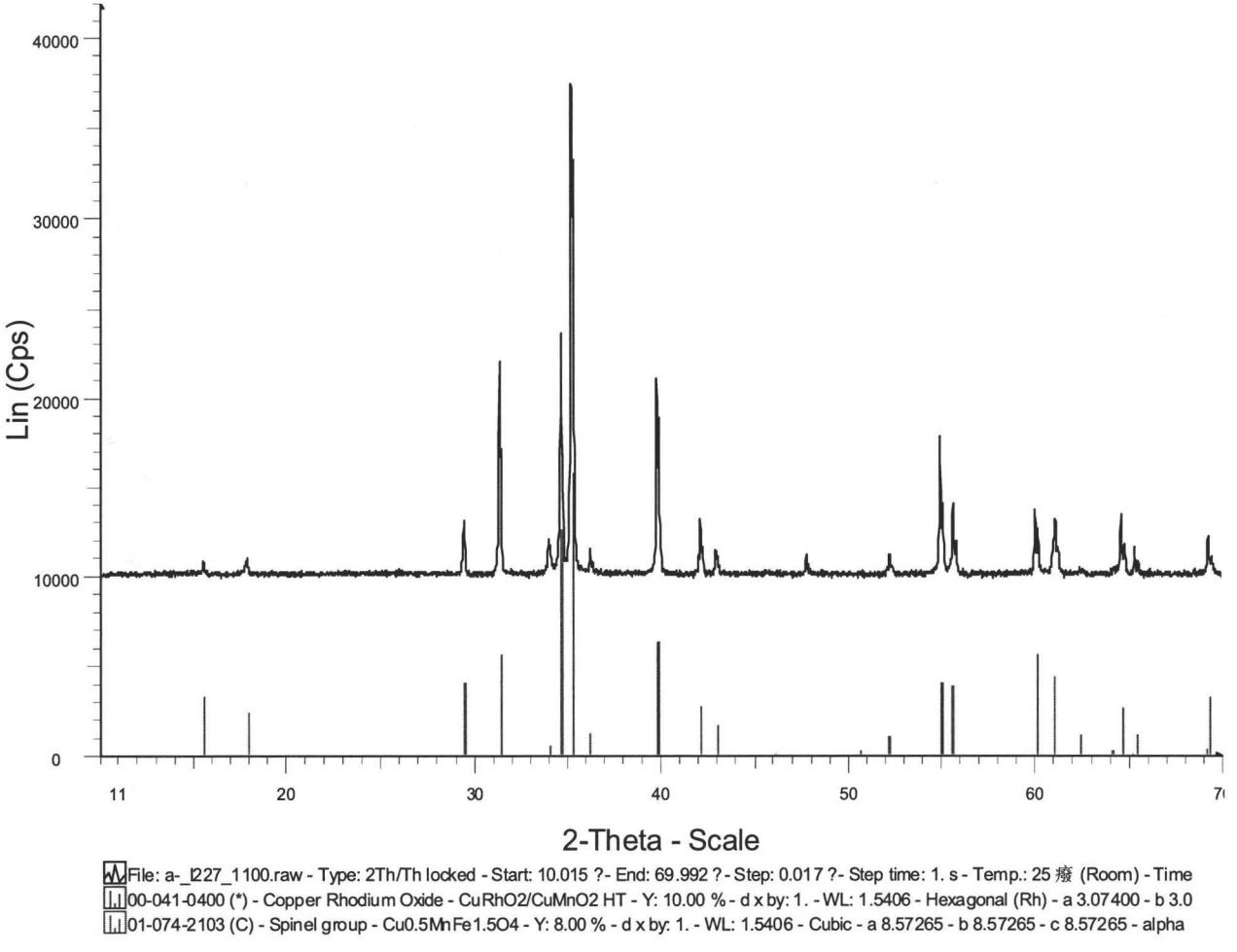

Figure 16 X-ray diffraction pattern of $Cu_{1.1}Mn_{1.9}O_4$ at 1100°C

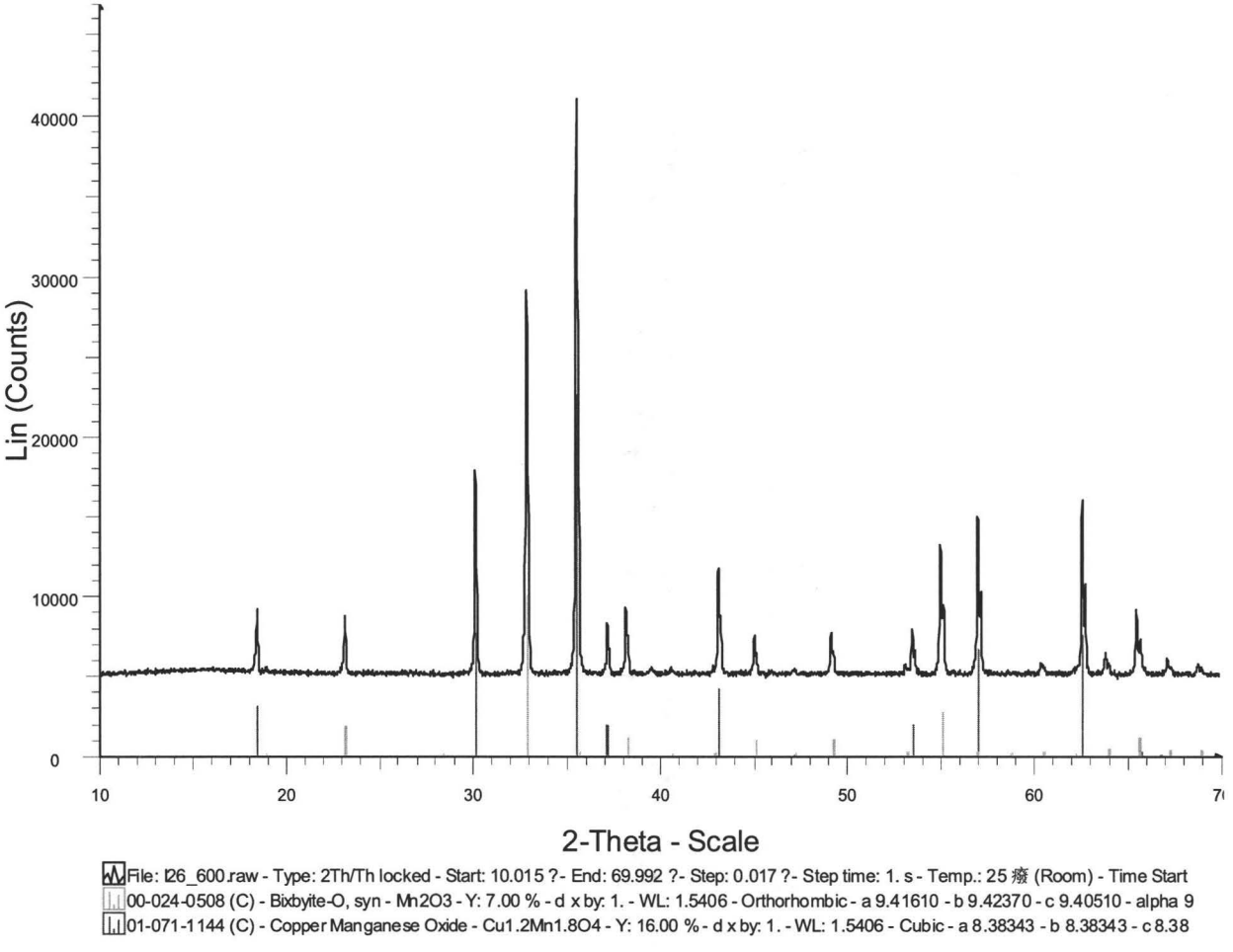

Figure 17 X-ray diffraction pattern of $Cu_{0.8}Mn_{2.2}O_4$ at 600°C

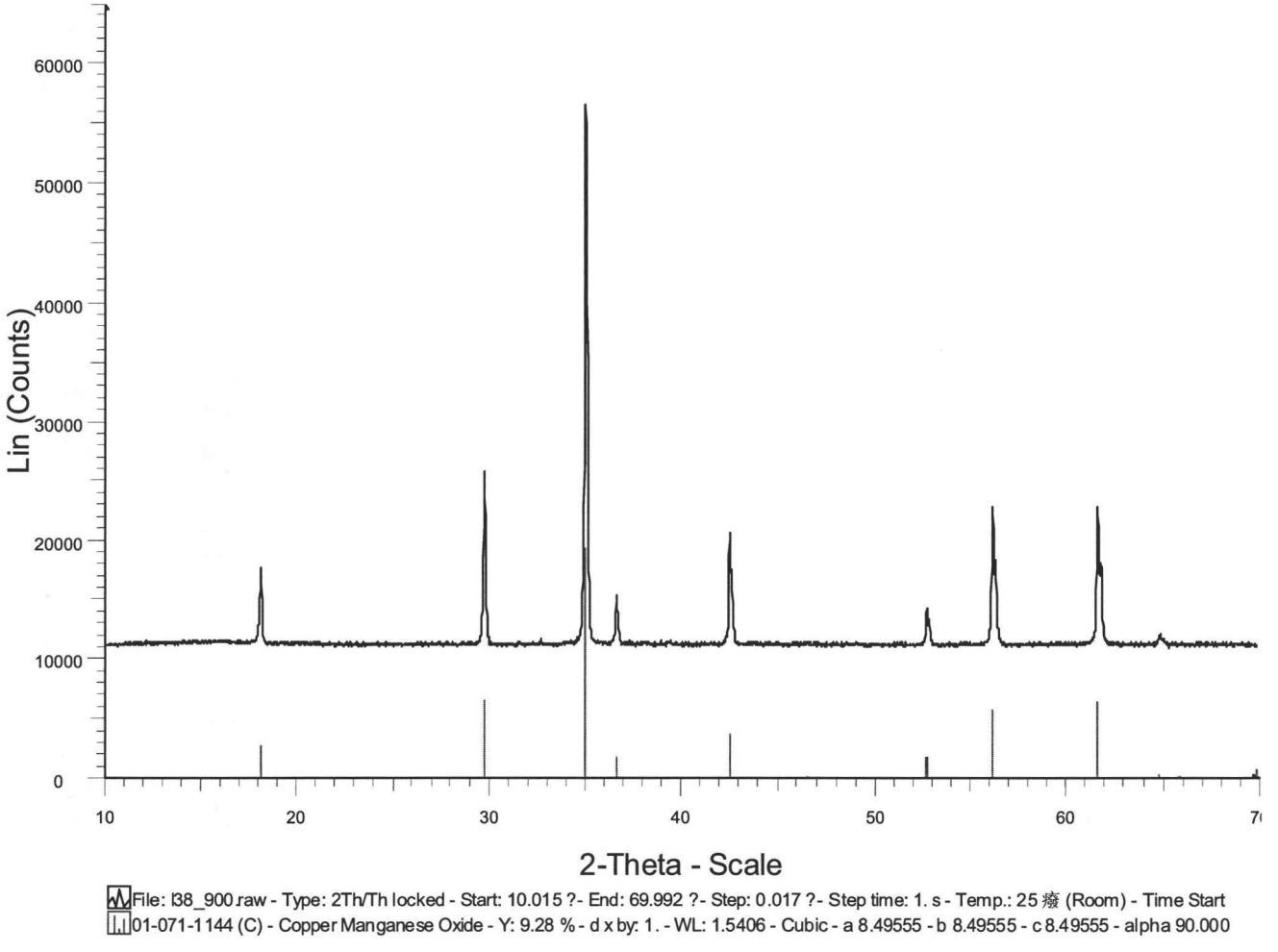

Figure 18 X-ray diffraction pattern of $Cu_{0.8}Mn_{2.2}O_4$ at 900°C after 600°C

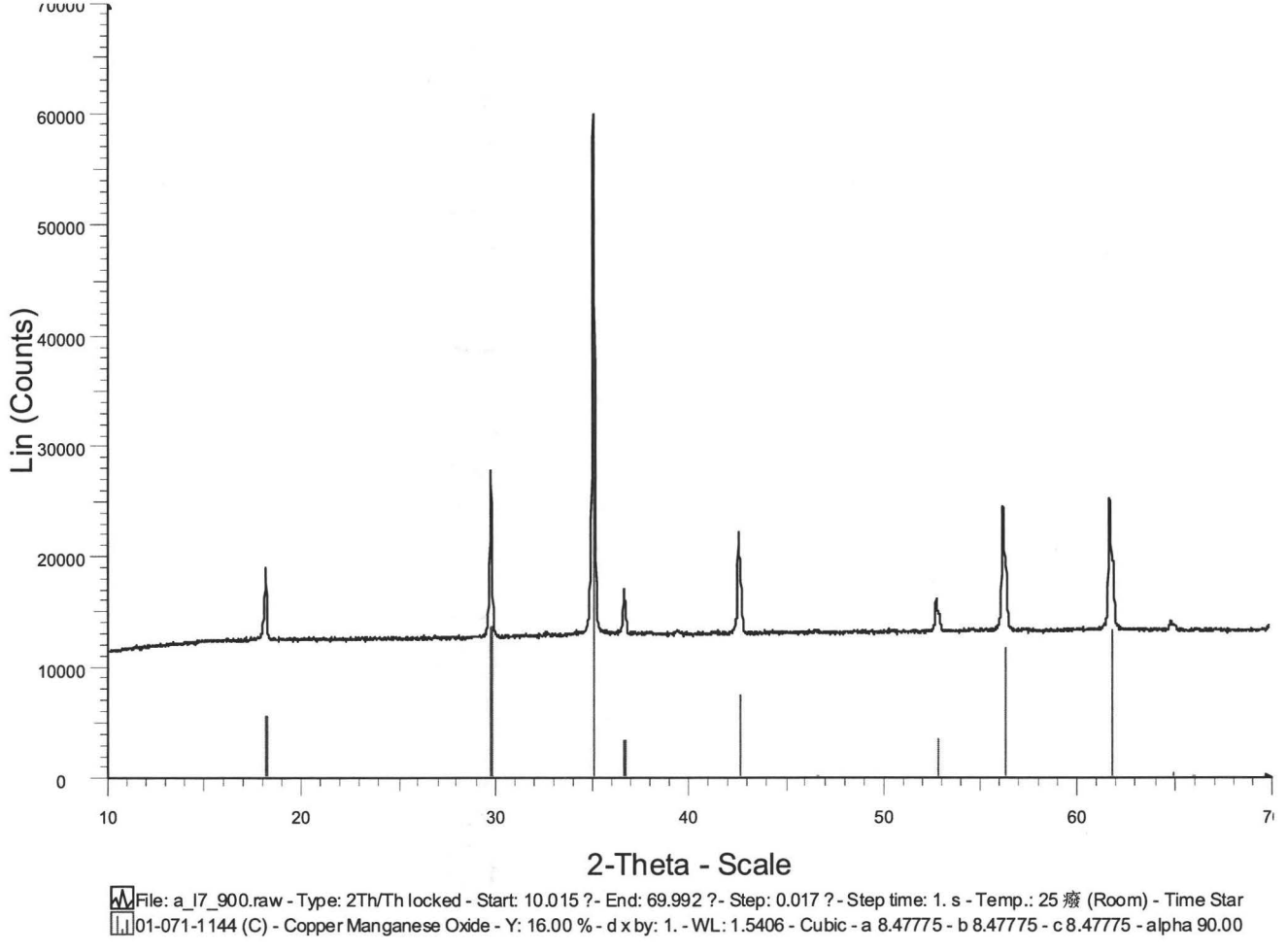

Figure 19 X-ray diffraction pattern of $Cu_{0.8}Mn_{2.2}O_4$ at 900°C at the beginning

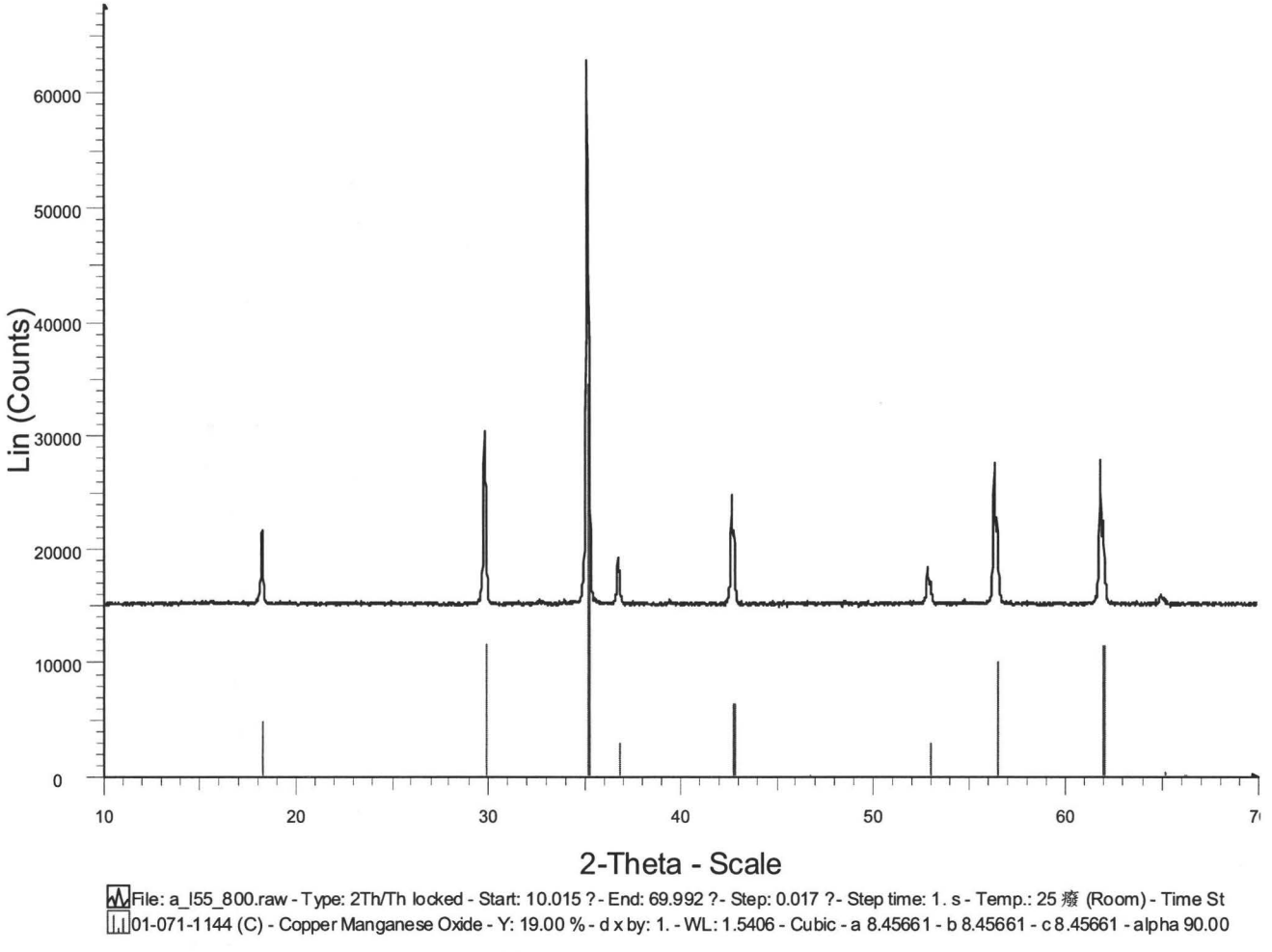

Figure 20 X-ray diffraction pattern of $Cu_{0.8}Mn_{2.2}O_4$ at 800°C

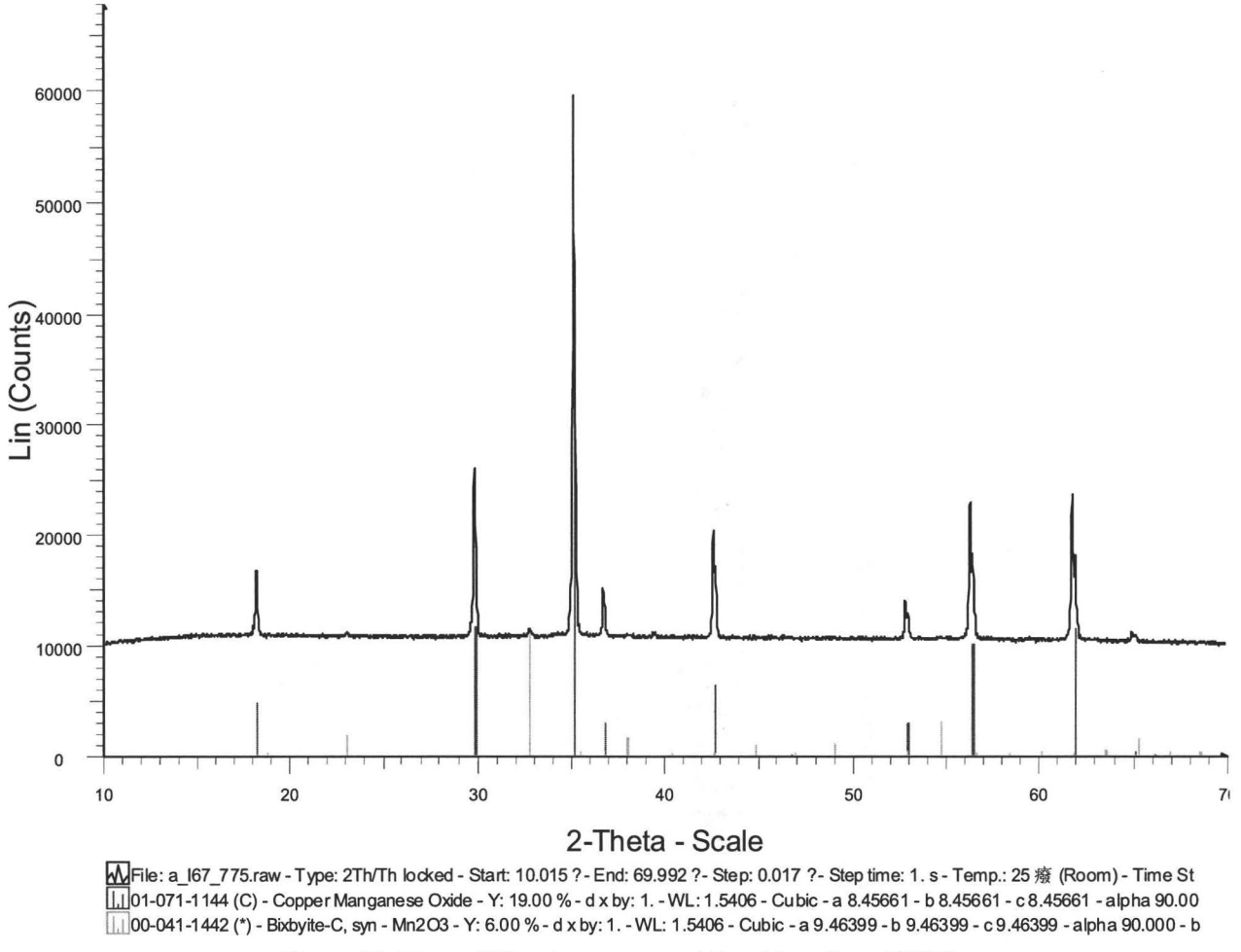

Figure 21 X-ray diffraction pattern of $Cu_{0.8}Mn_{2.2}O_4$ at 775°C

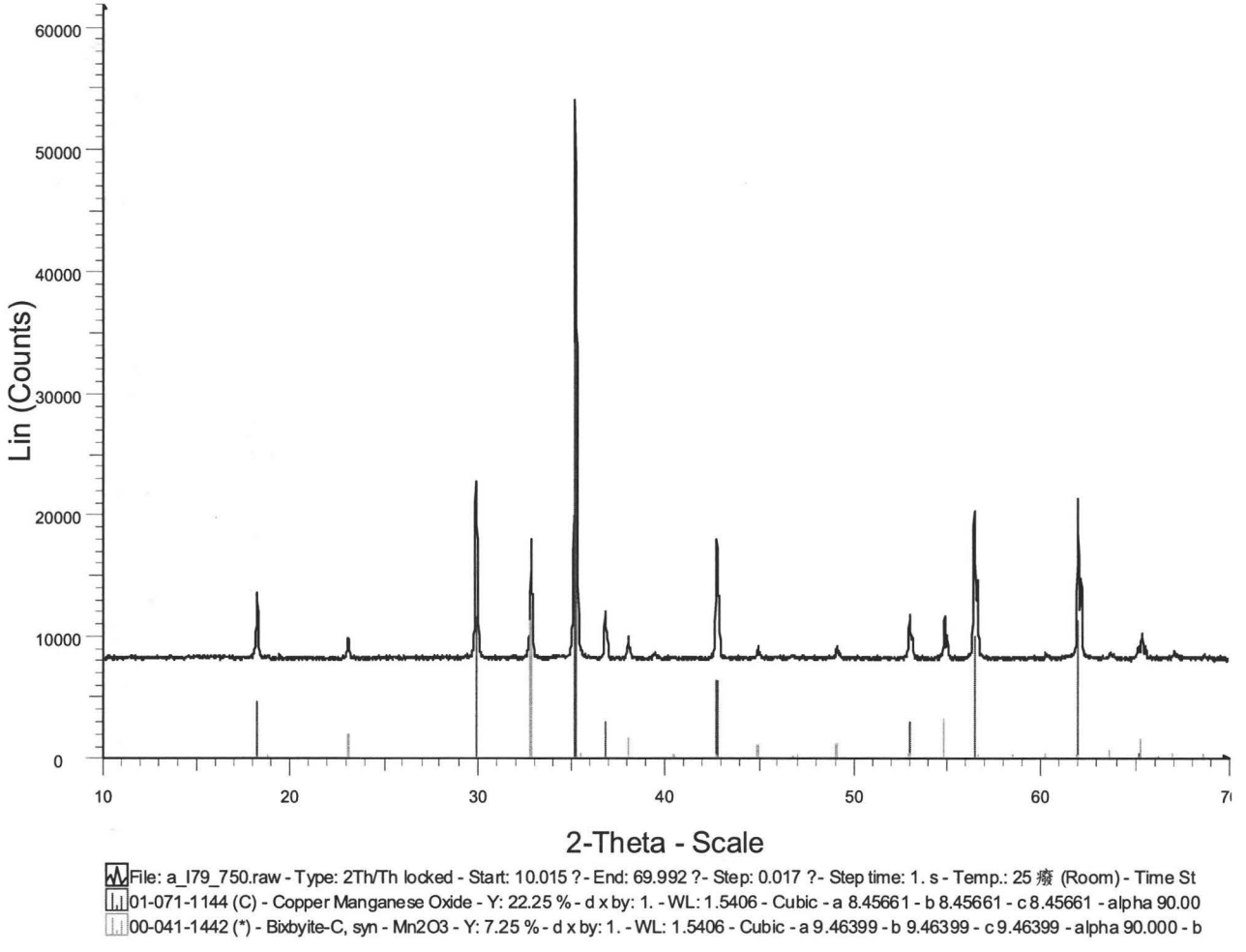

Figure 22 X-ray diffraction pattern of $Cu_{0.8}Mn_{2.2}O_4$ at 750°C

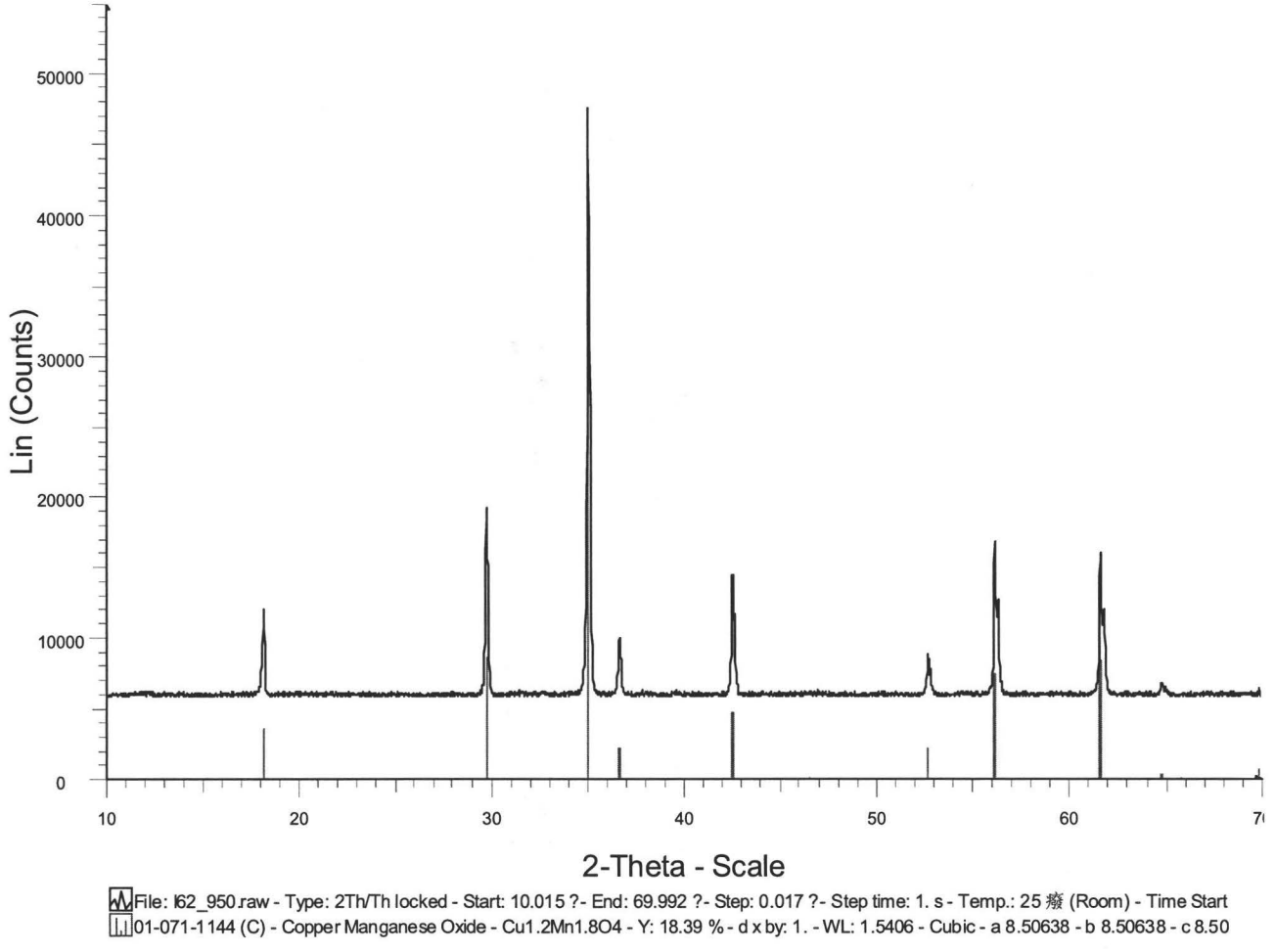

Figure 23 X-ray diffraction pattern of $Cu_{0.8}Mn_{2.2}O_4$ at 950°C

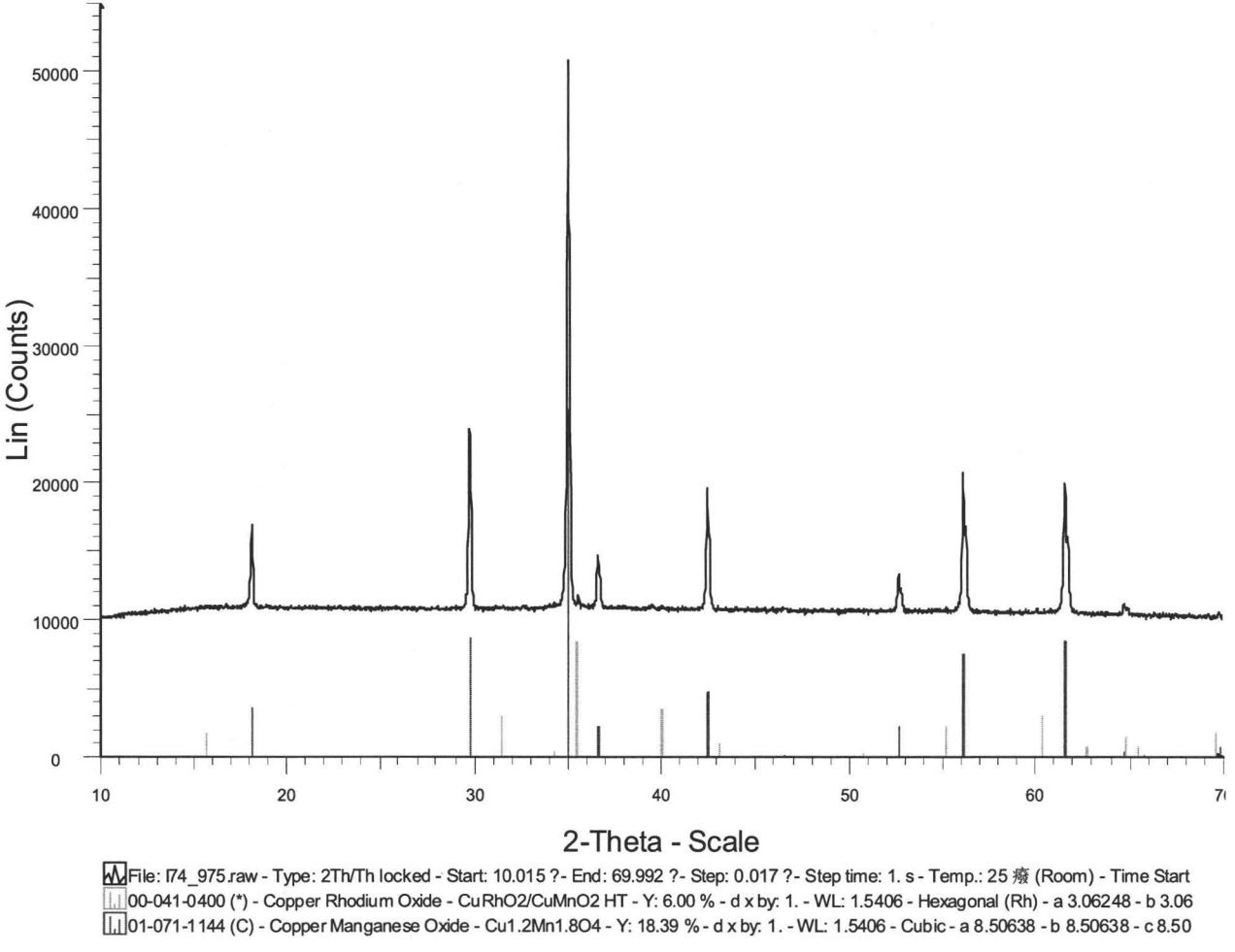

Figure 24 X-ray diffraction pattern of $Cu_{0.8}Mn_{2.2}O_4$ at 975°C

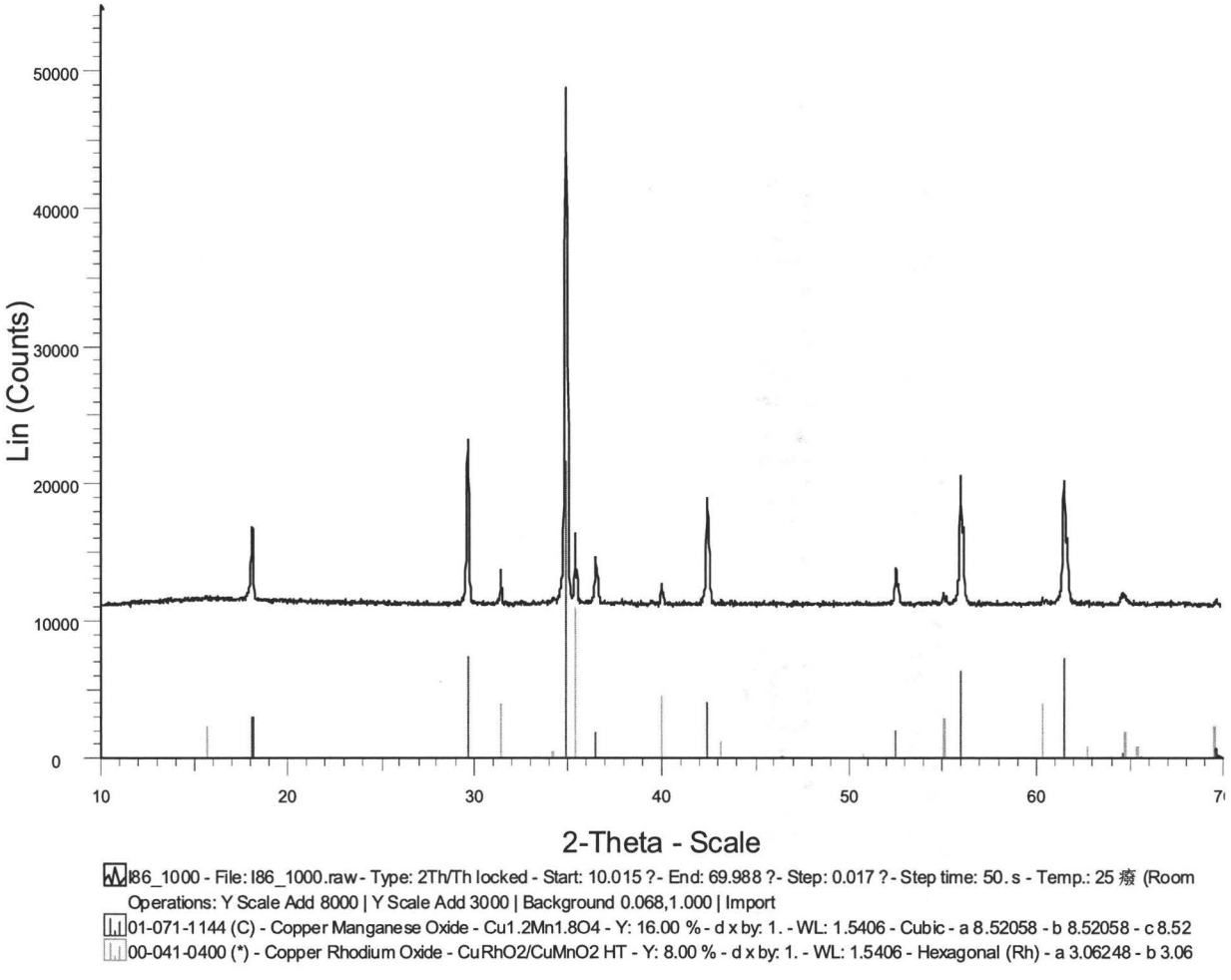

Figure 25 X-ray diffraction pattern of $Cu_{0.8}Mn_{2.2}O_4$ at 1000°C

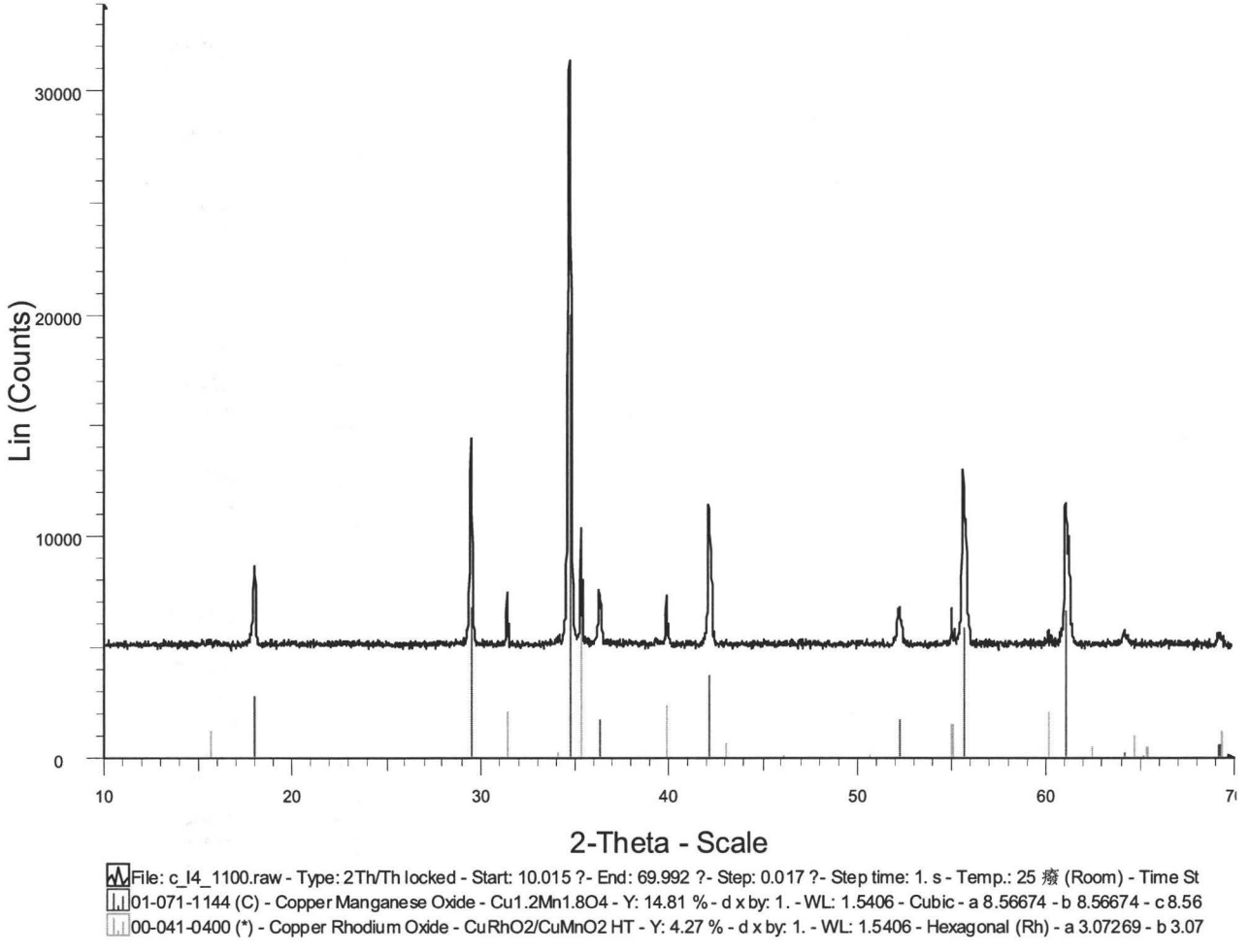

Figure 26 X-ray diffraction pattern of $Cu_{0.8}Mn_{2.2}O_4$ at 1100°C

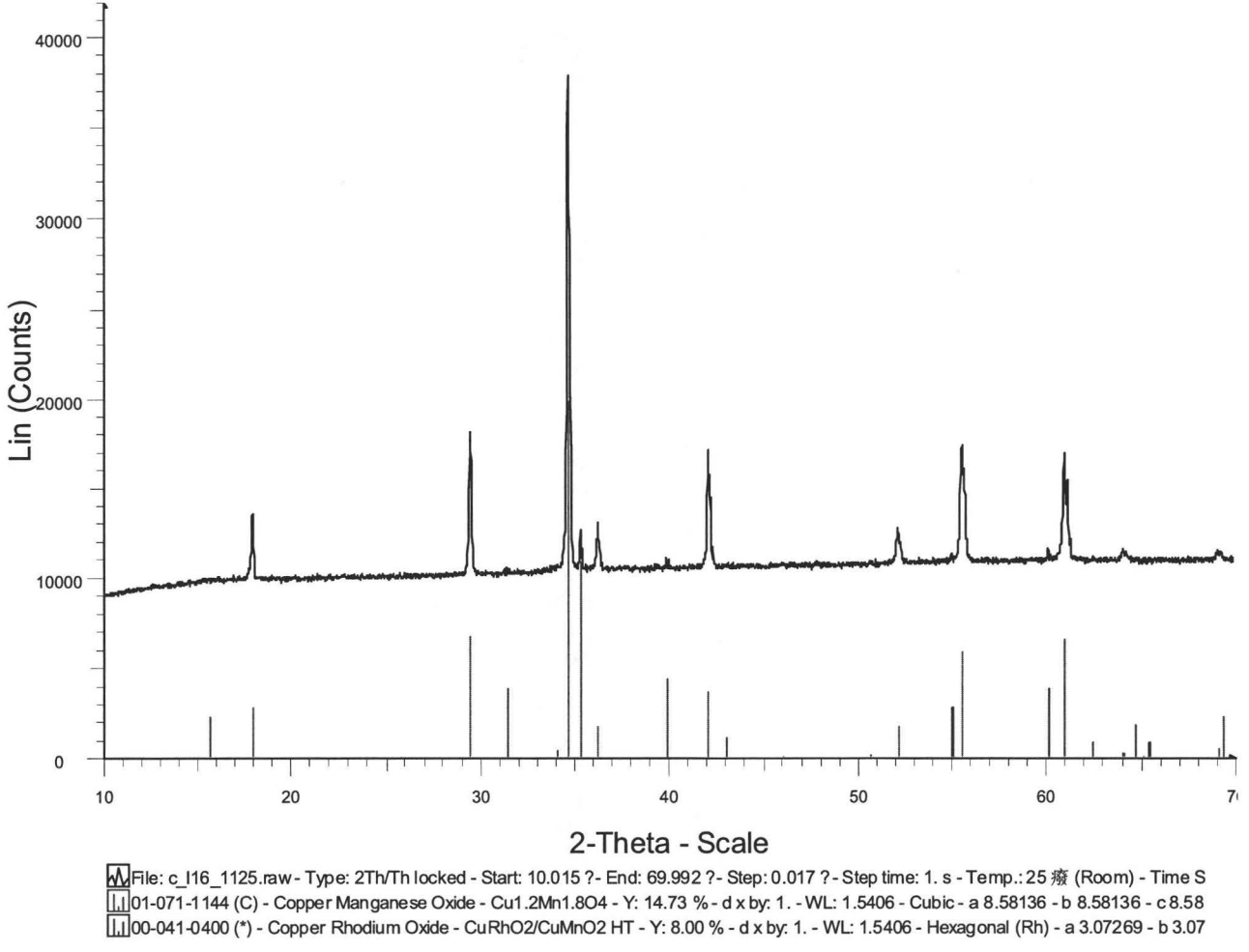

Figure 27 X-ray diffraction pattern of $Cu_{0.8}Mn_{2.2}O_4$ at 1125°C

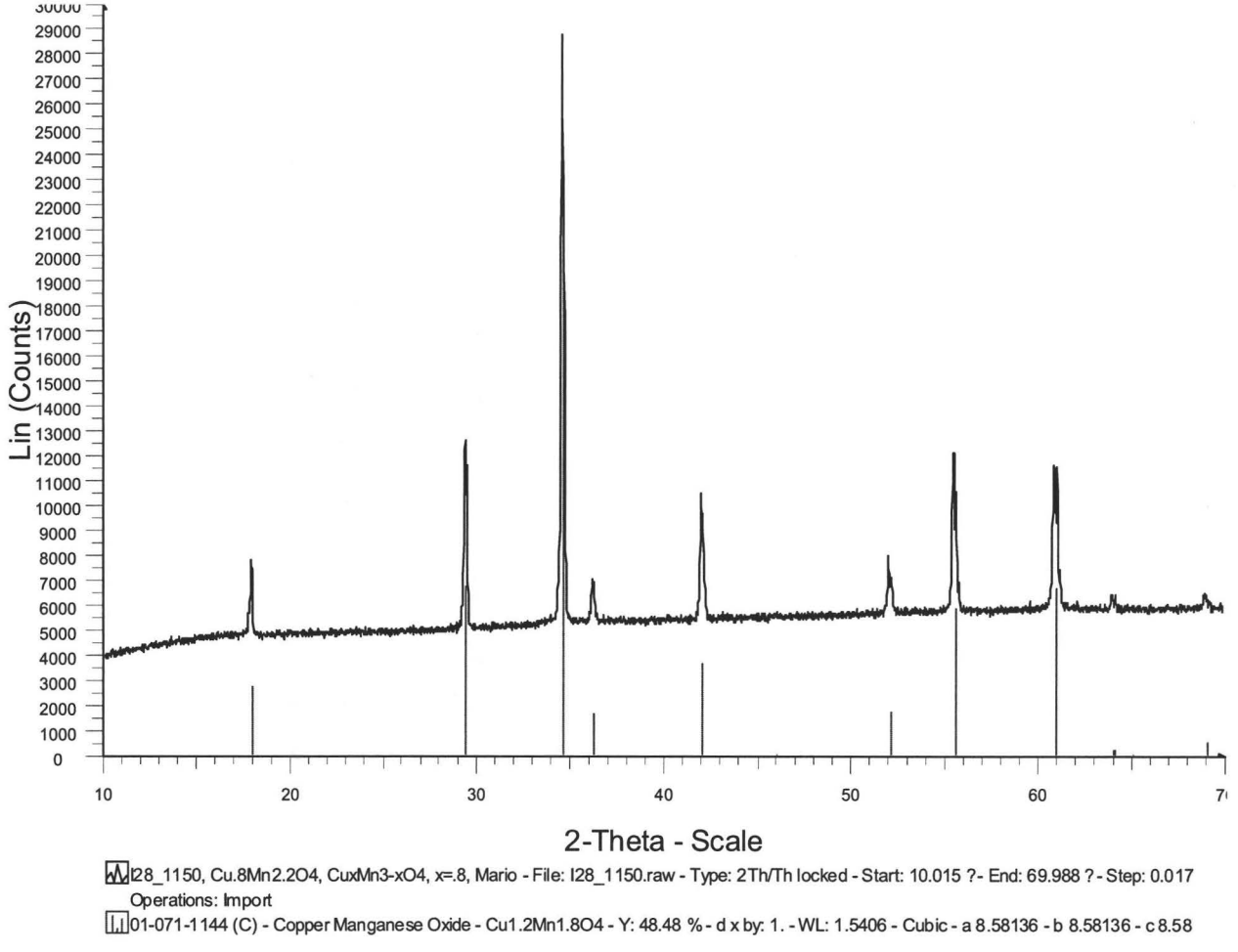

Figure 28 X-ray diffraction pattern of $Cu_{0.8}Mn_{2.2}O_4$ at 1150°C

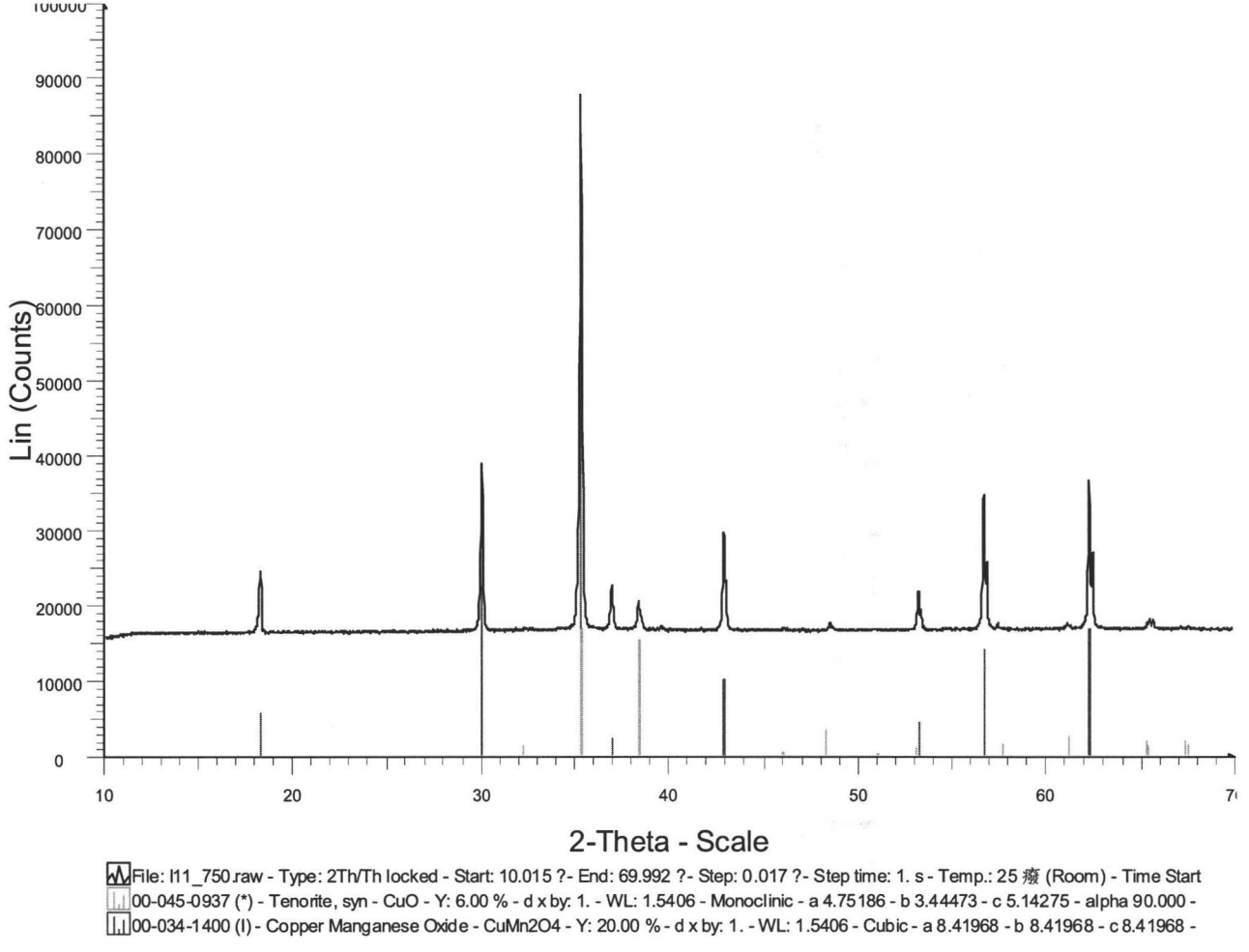

Figure 29 X-ray diffraction pattern of $Cu_{1.3}Mn_{1.7}O_4$ at 750°C

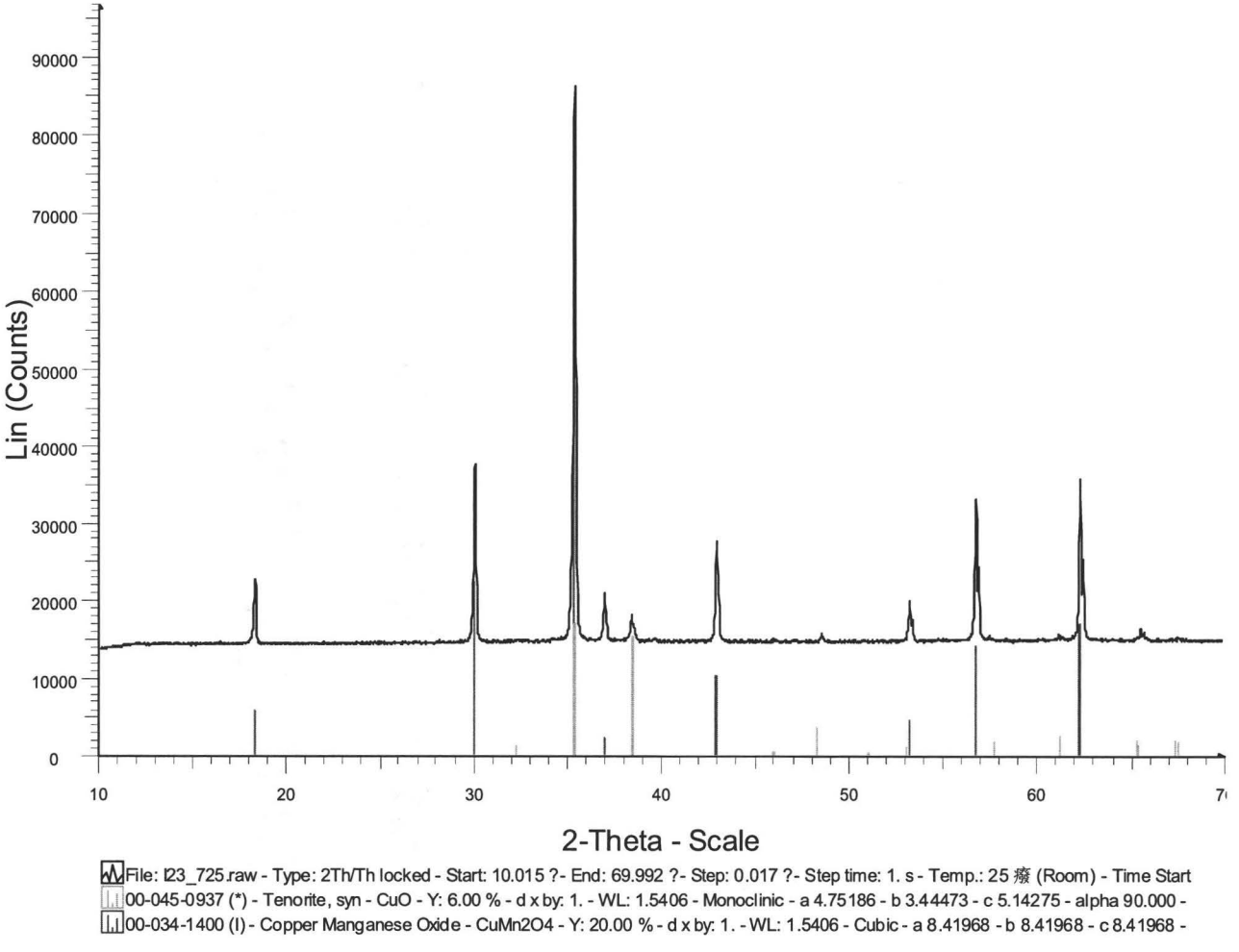

Figure 30 X-ray diffraction pattern of $Cu_{1.3}Mn_{1.7}O_4$ at 725°C

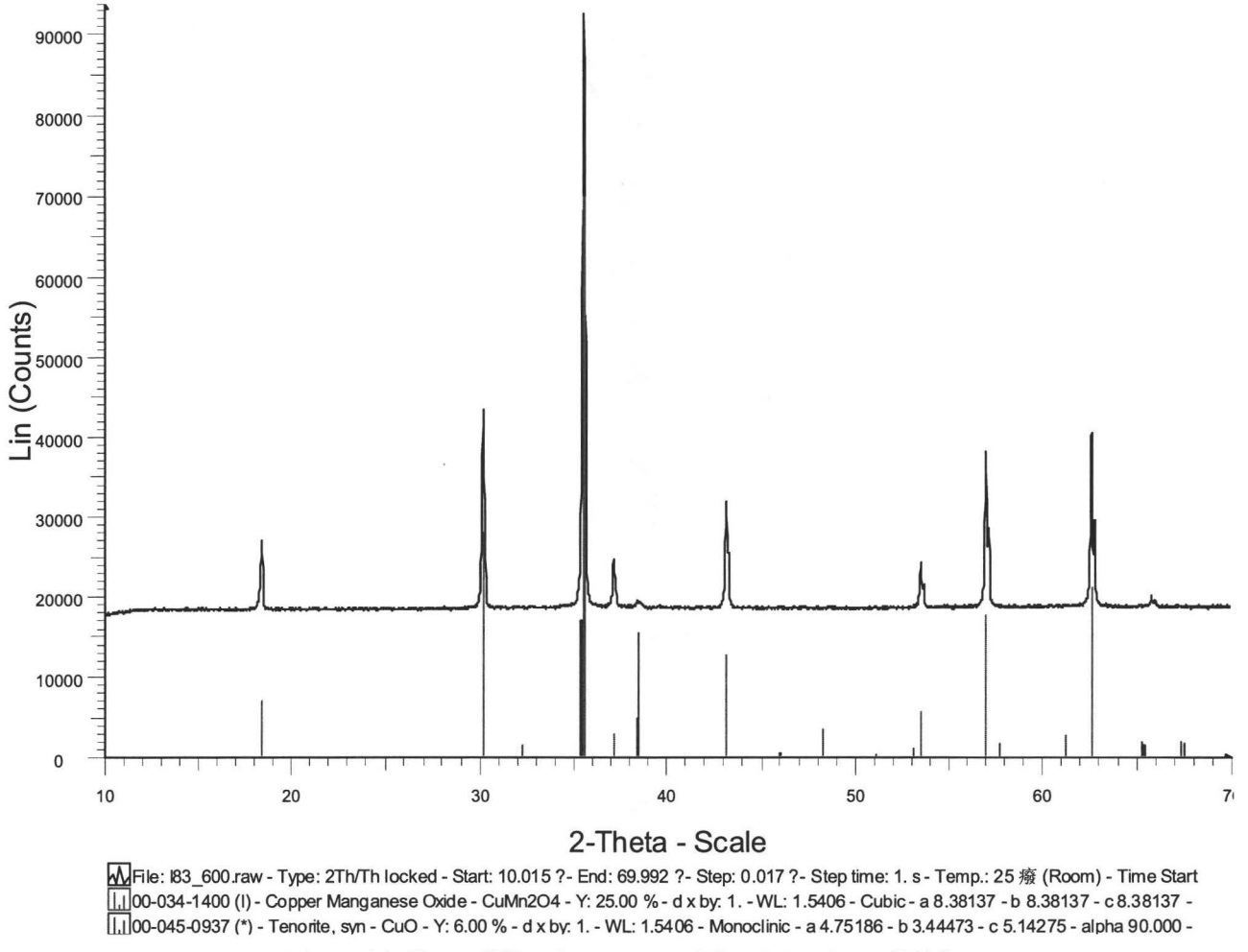

Figure 31 X-ray diffraction pattern of $Cu_{1.3}Mn_{1.7}O_4$ at 600°C

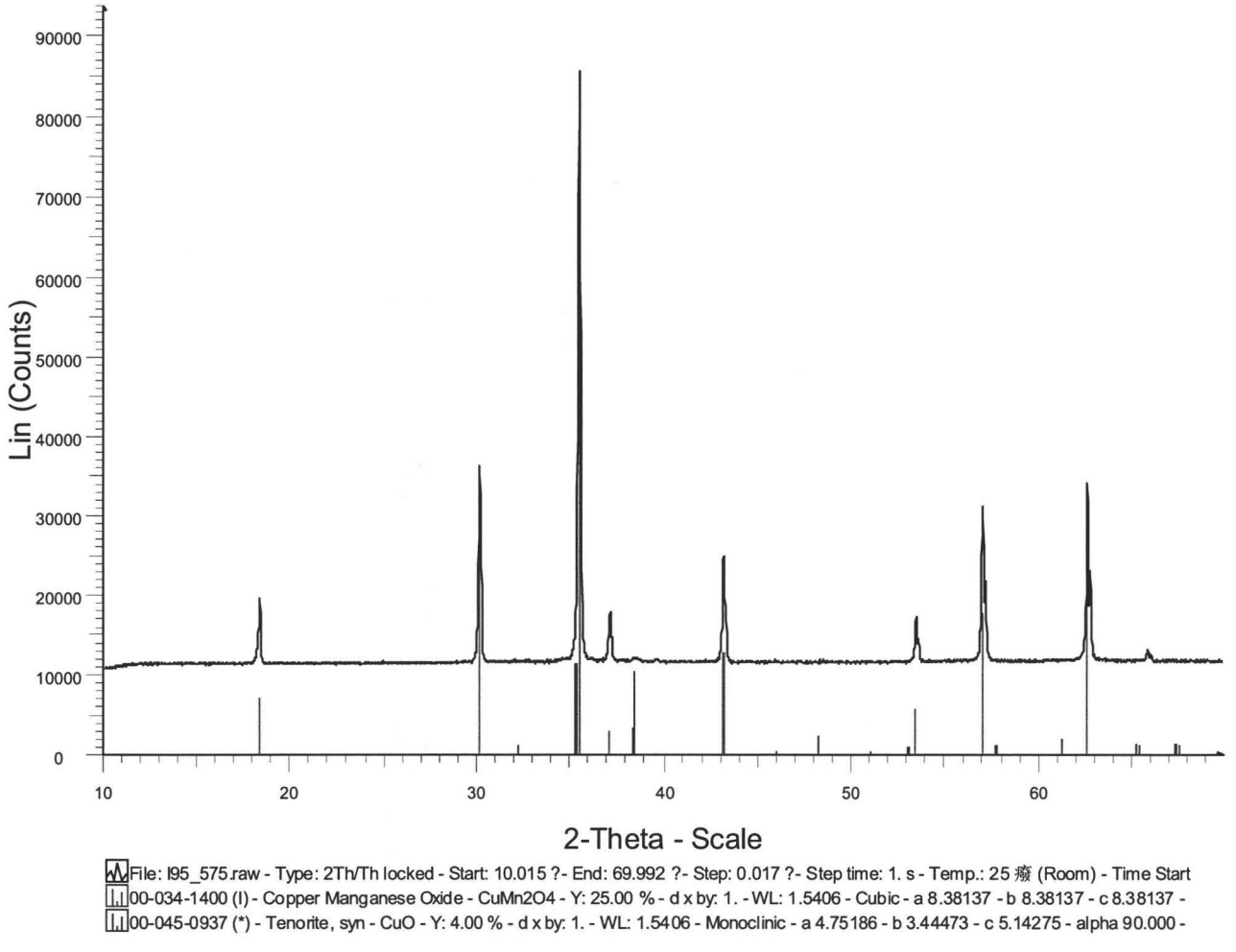

Figure 32 X-ray diffraction pattern of $Cu_{1.3}Mn_{1.7}O_4$ at 575°C

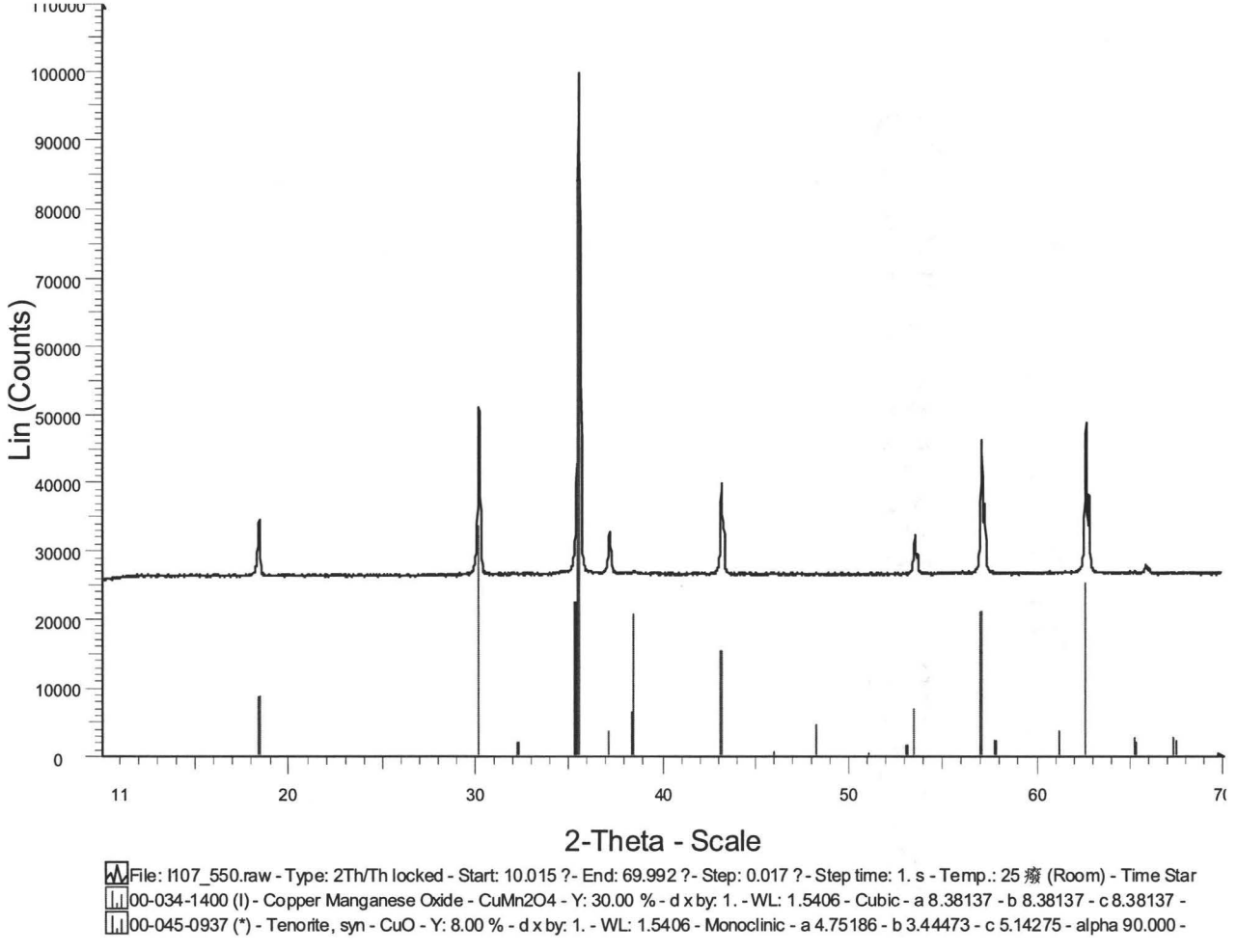

Figure 33 X-ray diffraction pattern of $Cu_{1.3}Mn_{1.7}O_4$ at 550°C

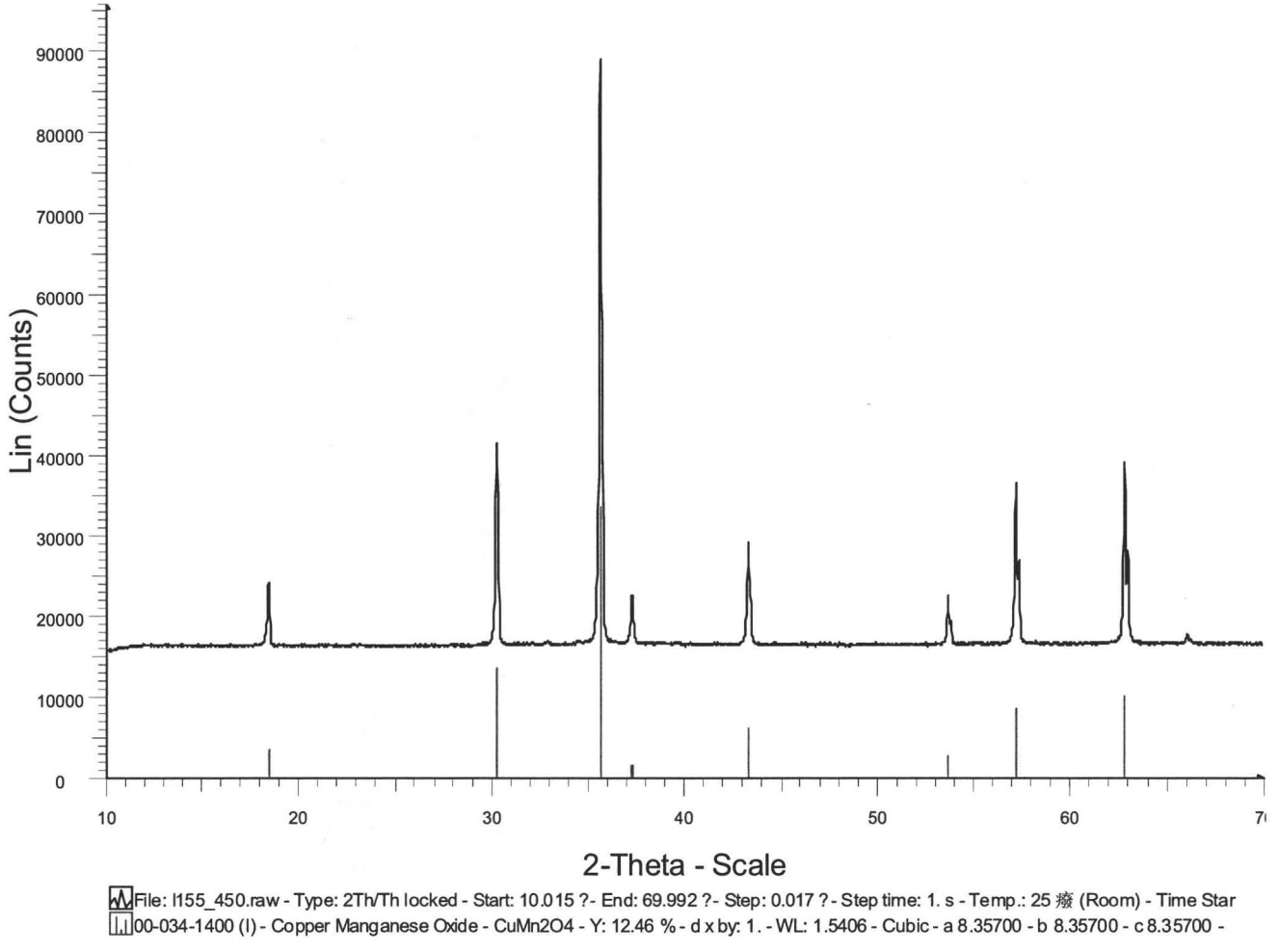

Figure 34 X-ray diffraction pattern of $Cu_{1.3}Mn_{1.7}O_4$ at 450°C

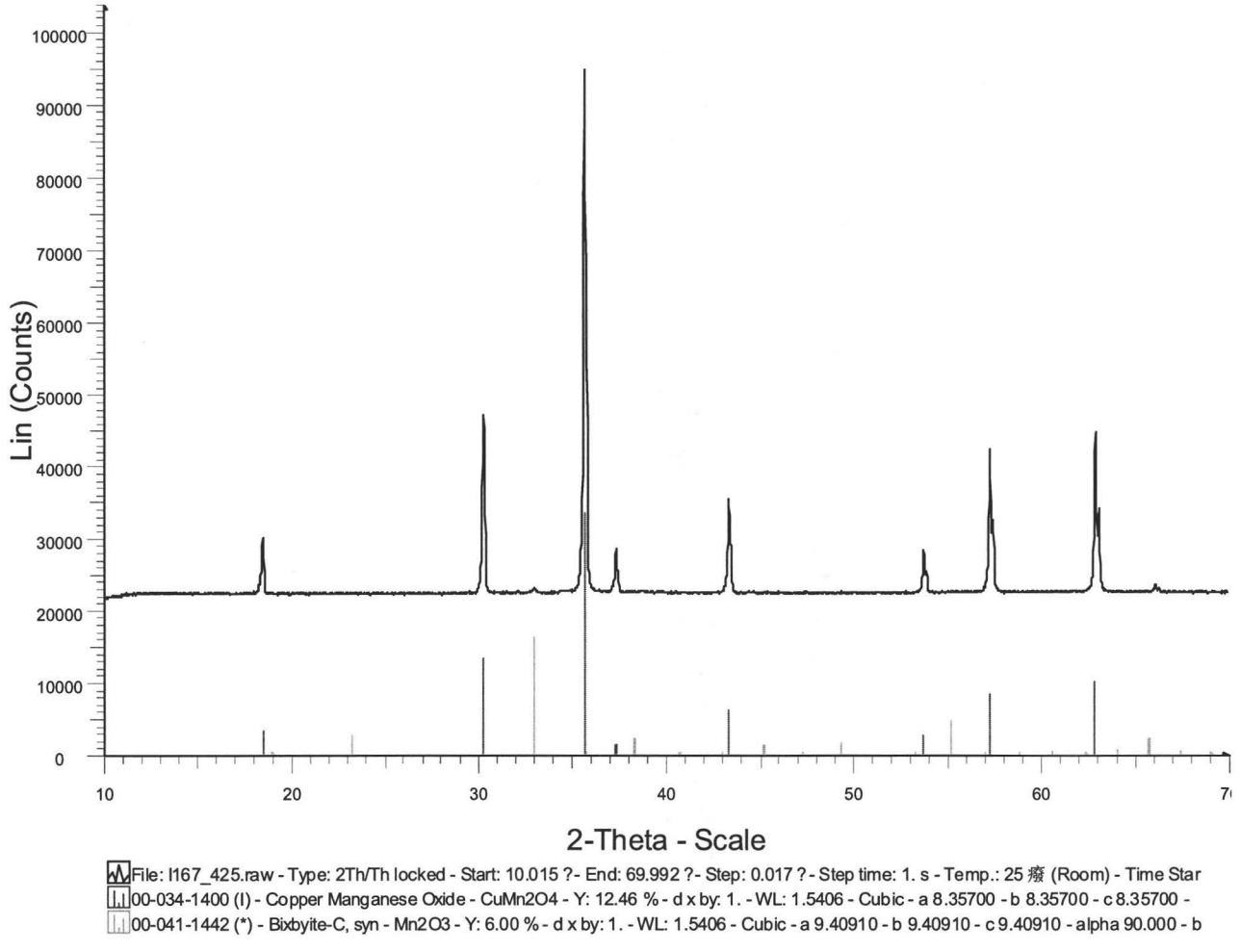

Figure 35 X-ray diffraction pattern of $Cu_{1.3}Mn_{1.7}O_4$ at 425°C

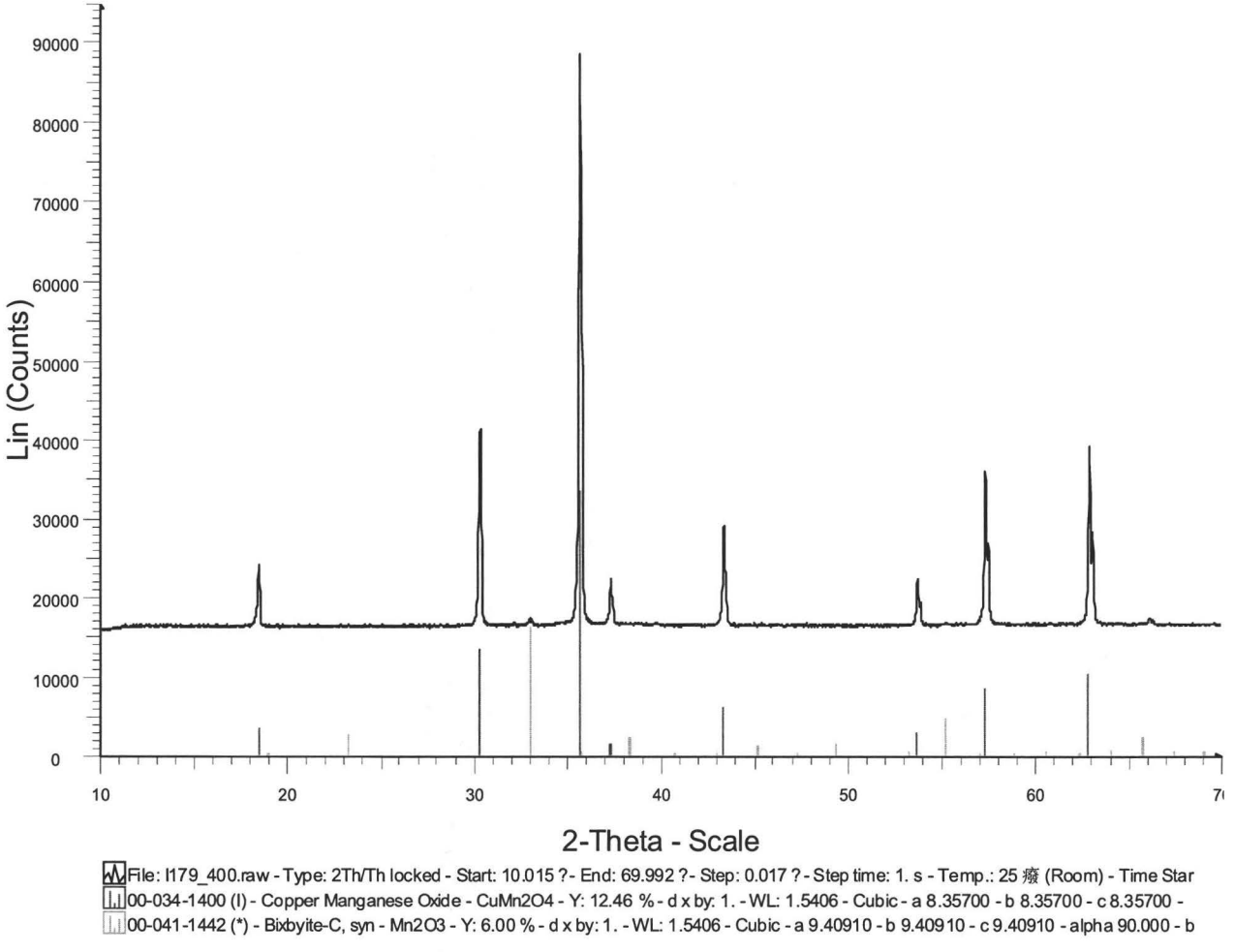

Figure 36 X-ray diffraction pattern of $Cu_{1.3}Mn_{1.7}O_4$ at 400°C

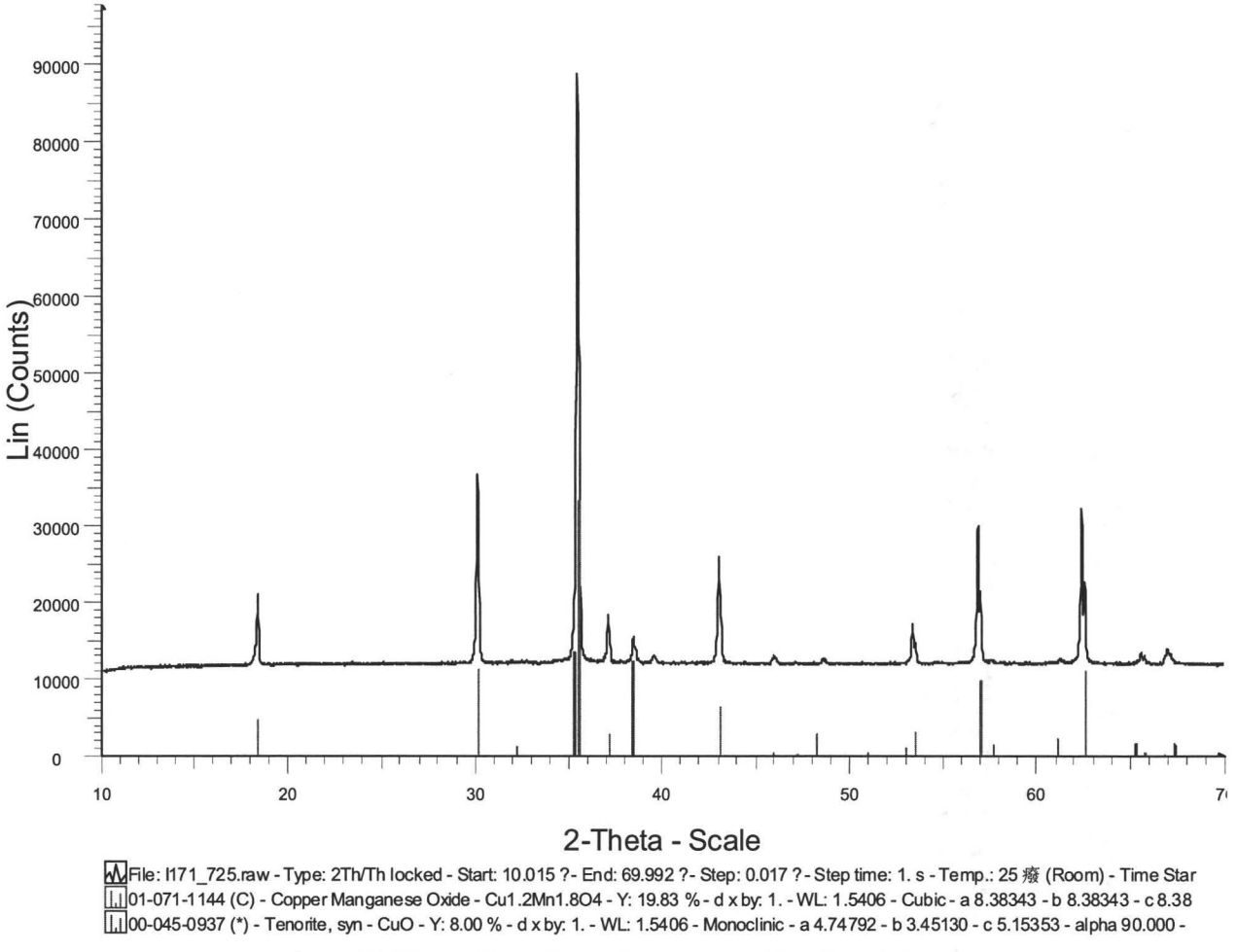

Figure 37 X-ray diffraction pattern of $Cu_{1.4}Mn_{1.6}O_4$ at 725°C

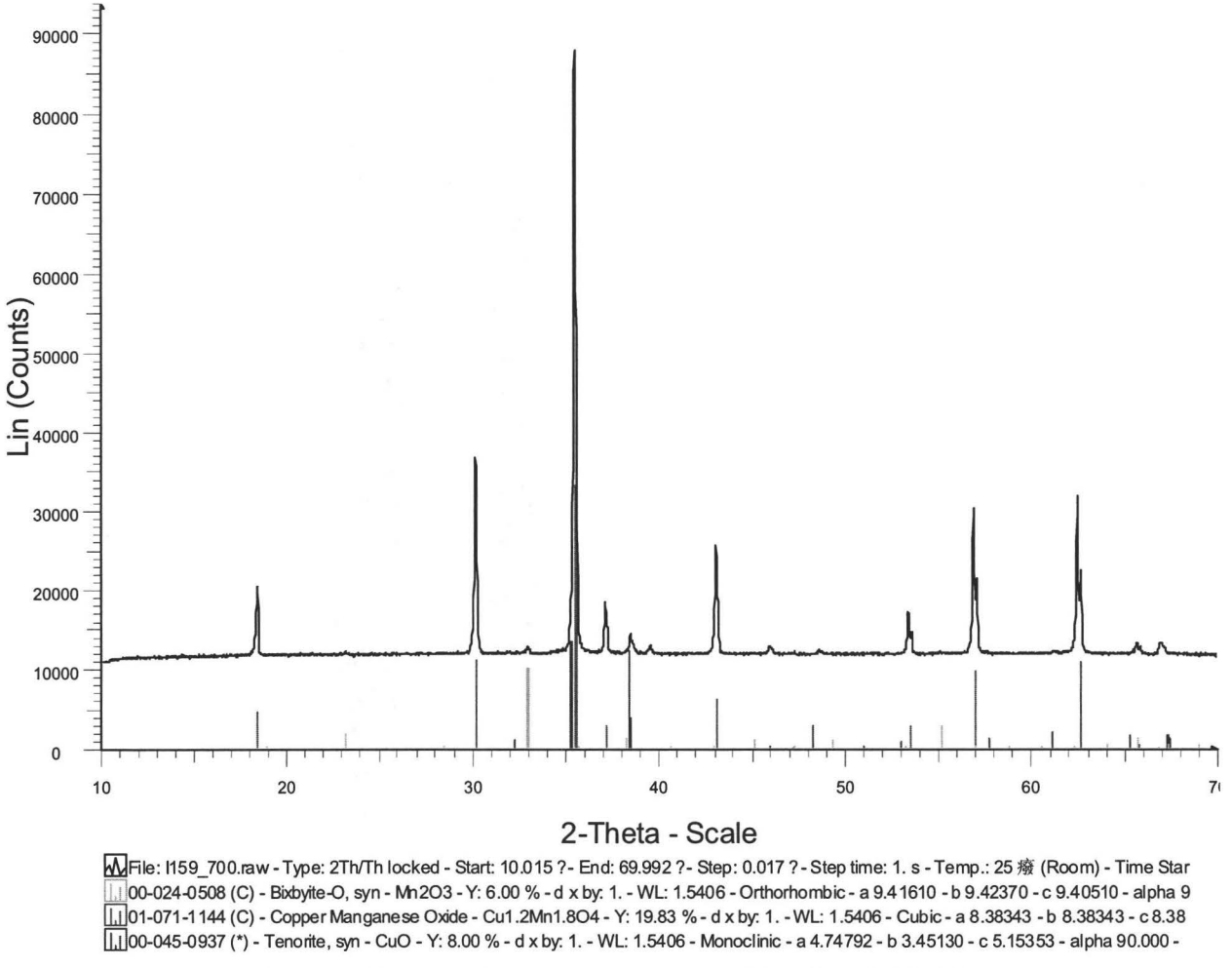

Figure 38 X-ray diffraction pattern of $Cu_{1.4}Mn_{1.6}O_4$ at 700C°C

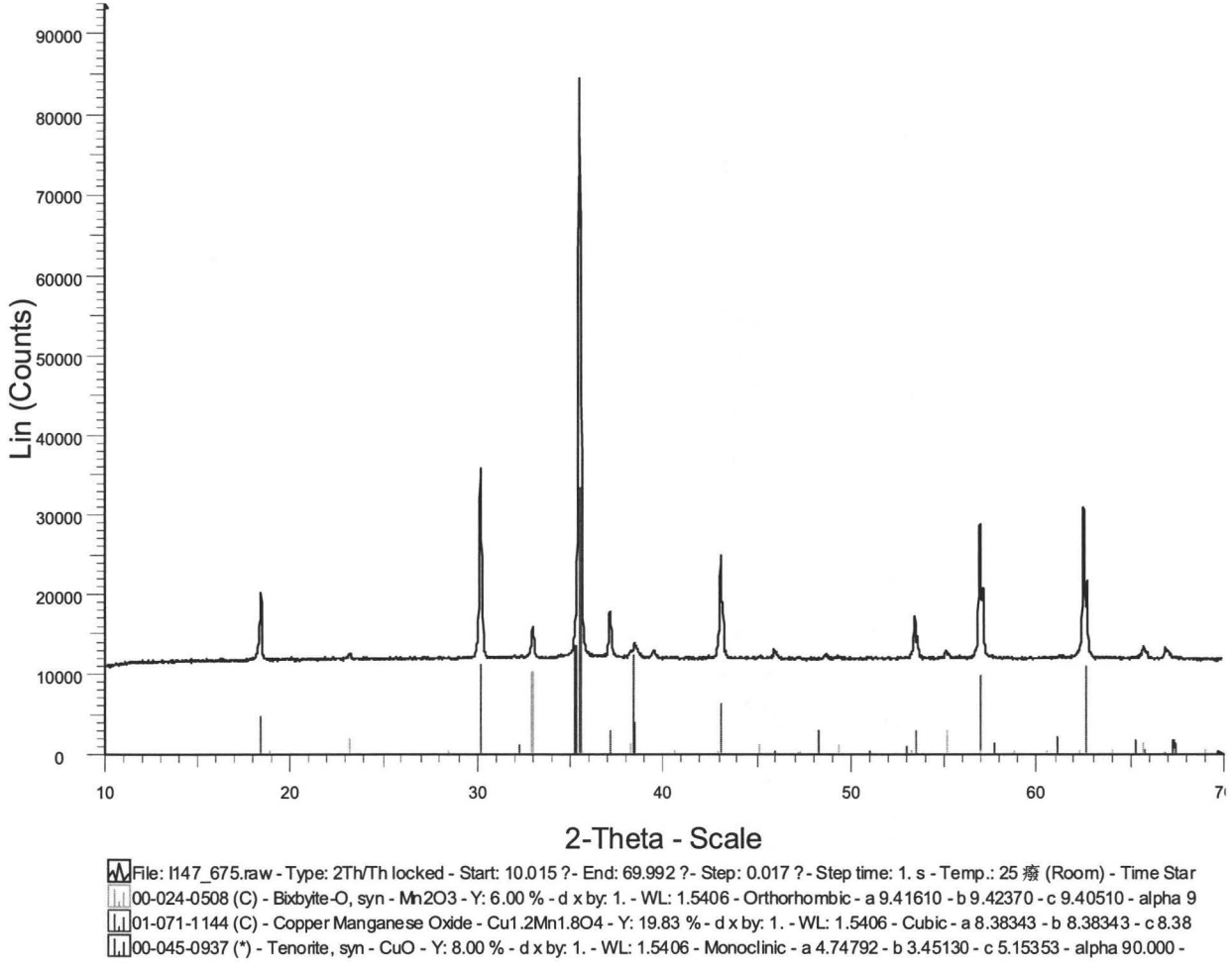

Figure 39 X-ray diffraction pattern of $Cu_{1.4}Mn_{1.6}O_4$ at 675°C

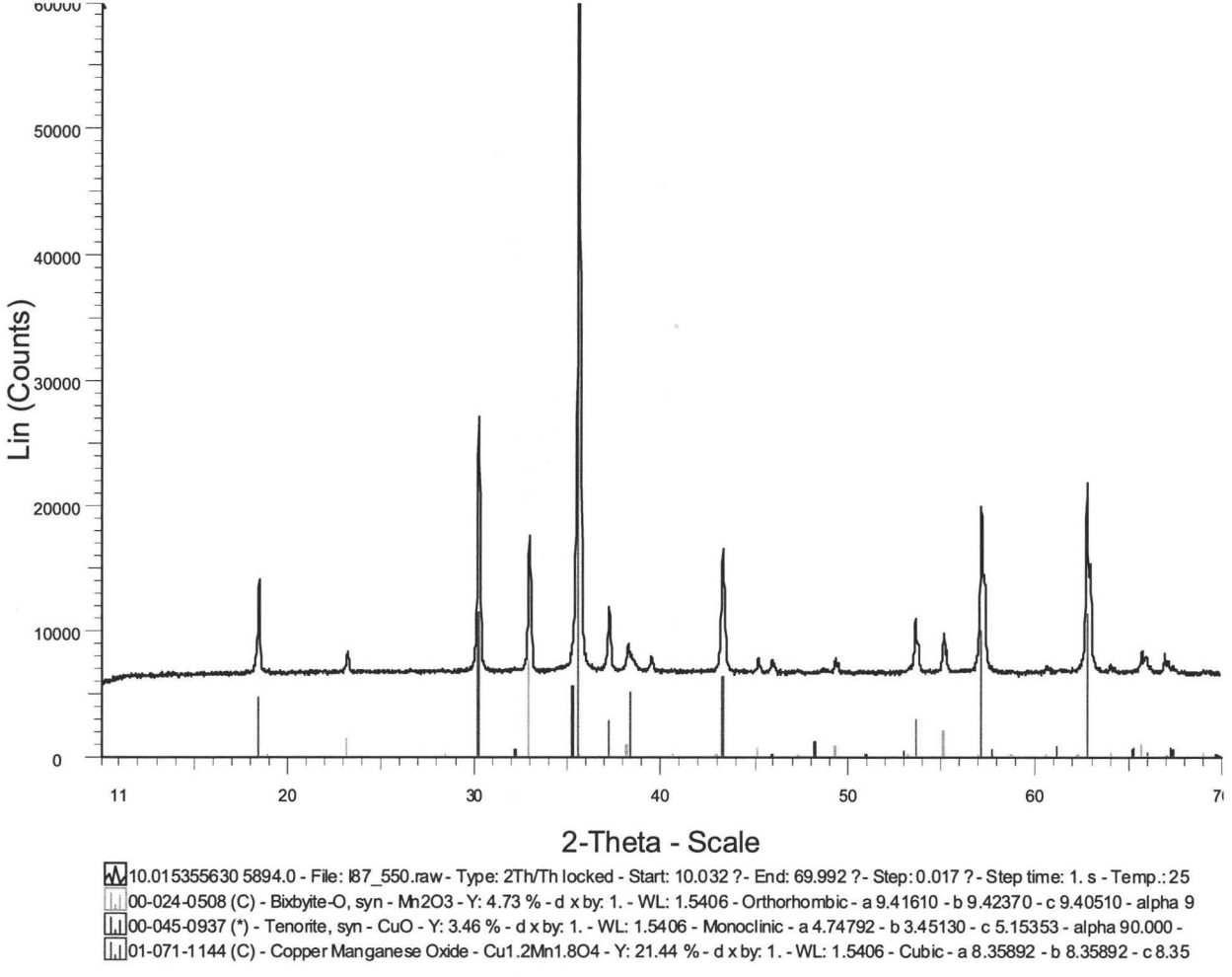

Figure 40 X-ray diffraction pattern of $Cu_{1.4}Mn_{1.6}O_4$ at 550°C

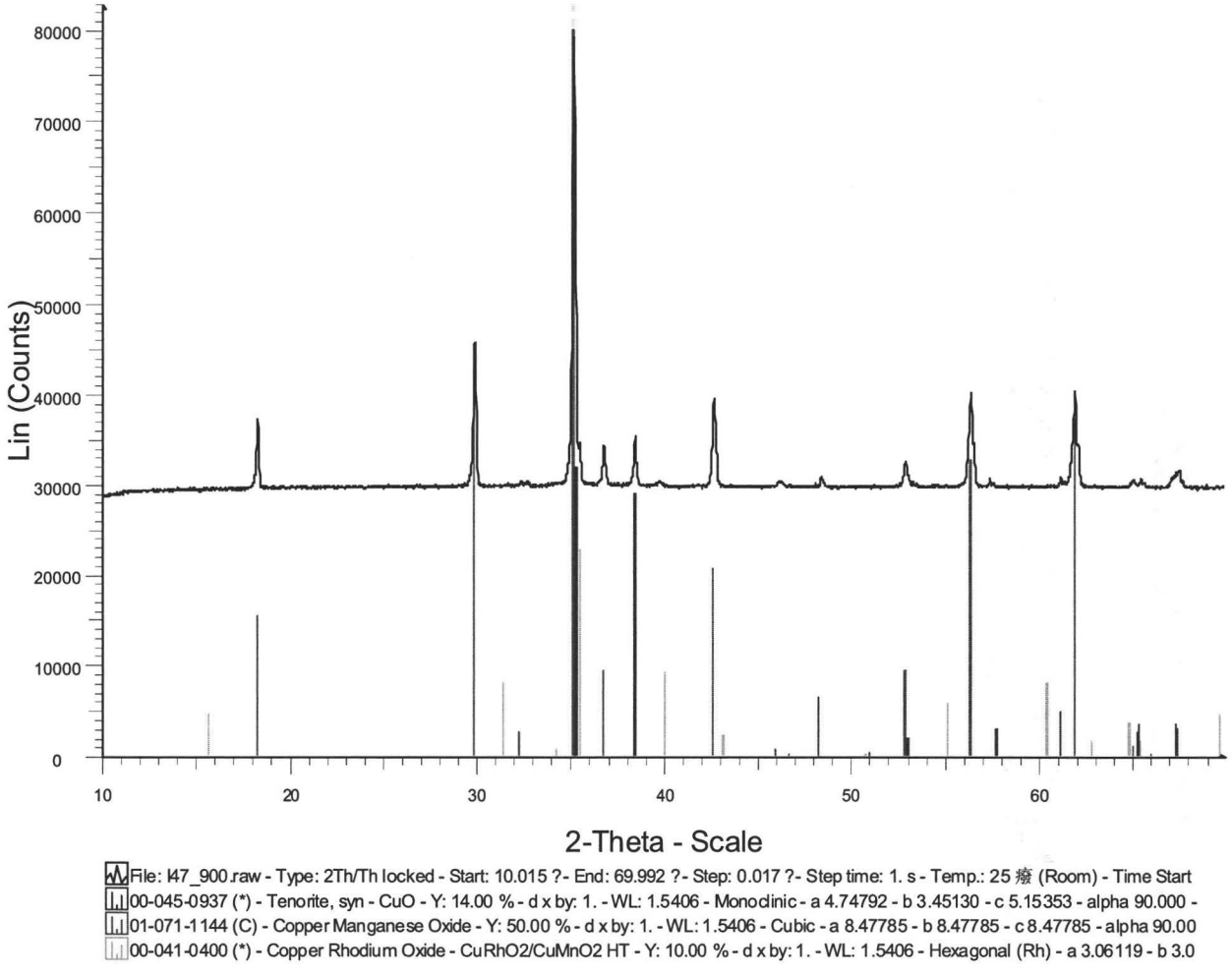

Figure 41 X-ray diffraction pattern of $Cu_{1.4}Mn_{1.6}O_4$ at 900°C

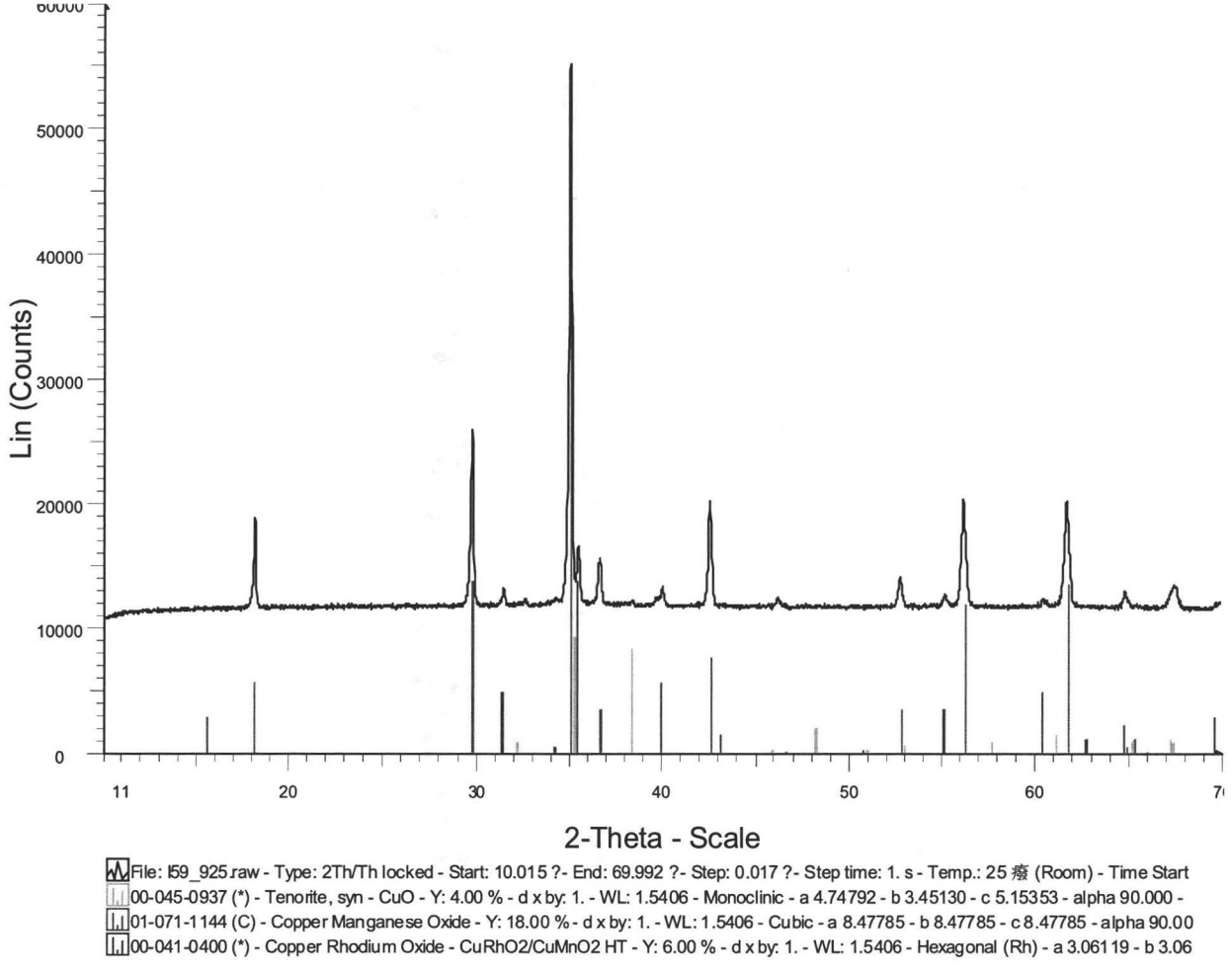

Figure 42 X-ray diffraction pattern of $Cu_{1.4}Mn_{1.6}O_4$ at 925°C

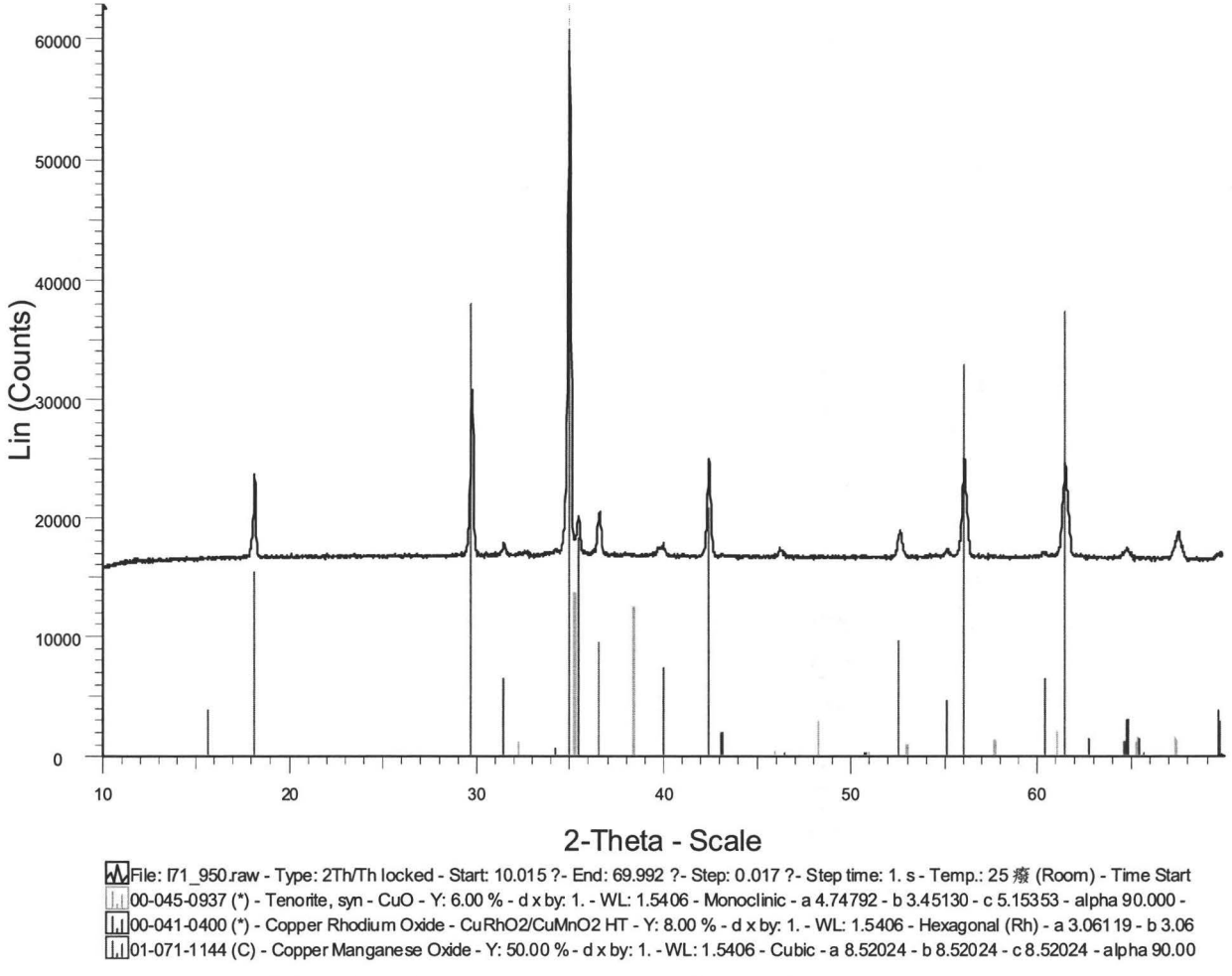

Figure 43 X-ray diffraction pattern of $Cu_{1.4}Mn_{1.6}O_4$ at 950°C

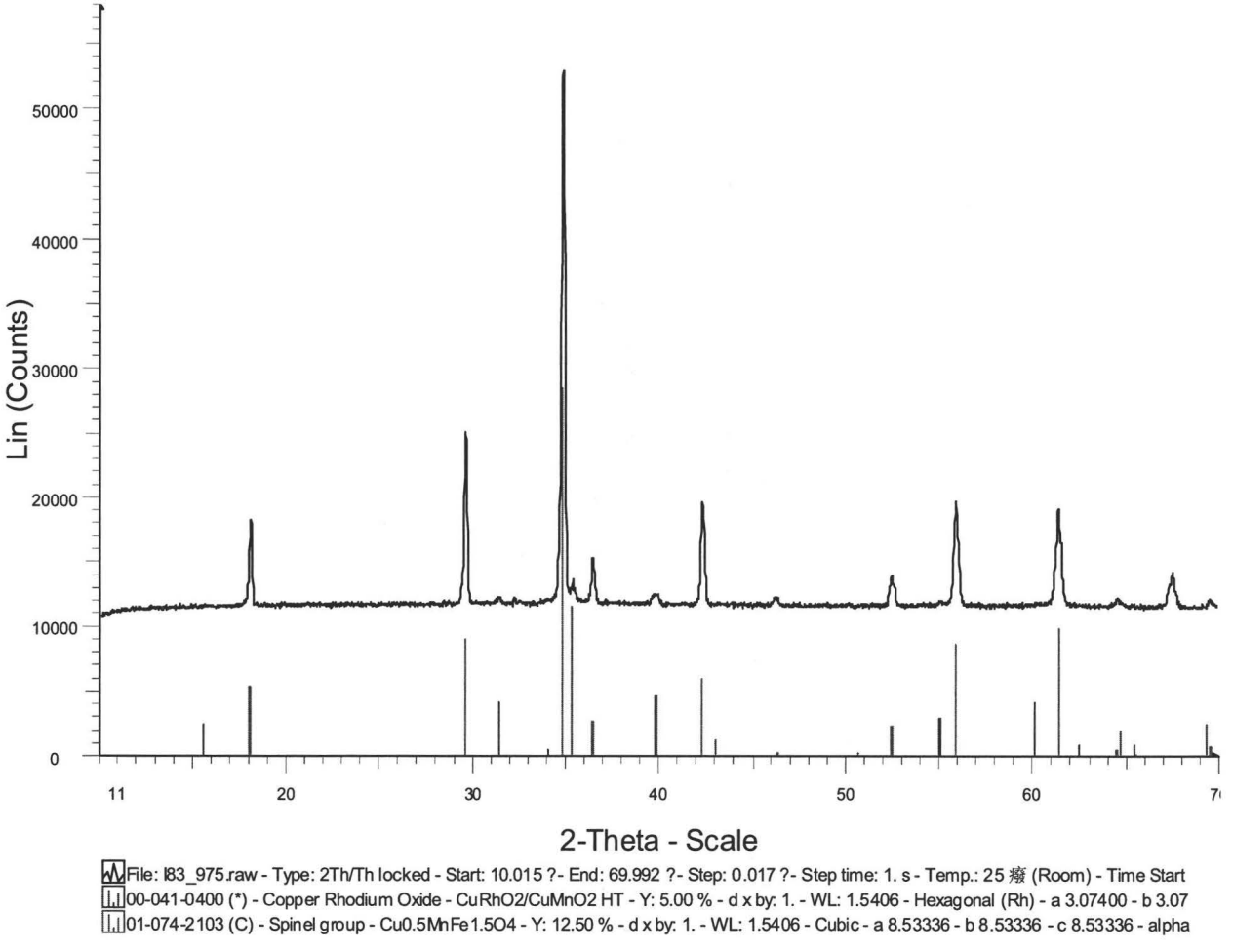

Figure 44 X-ray diffraction pattern of $Cu_{1.4}Mn_{1.6}O_4$ at 975°C

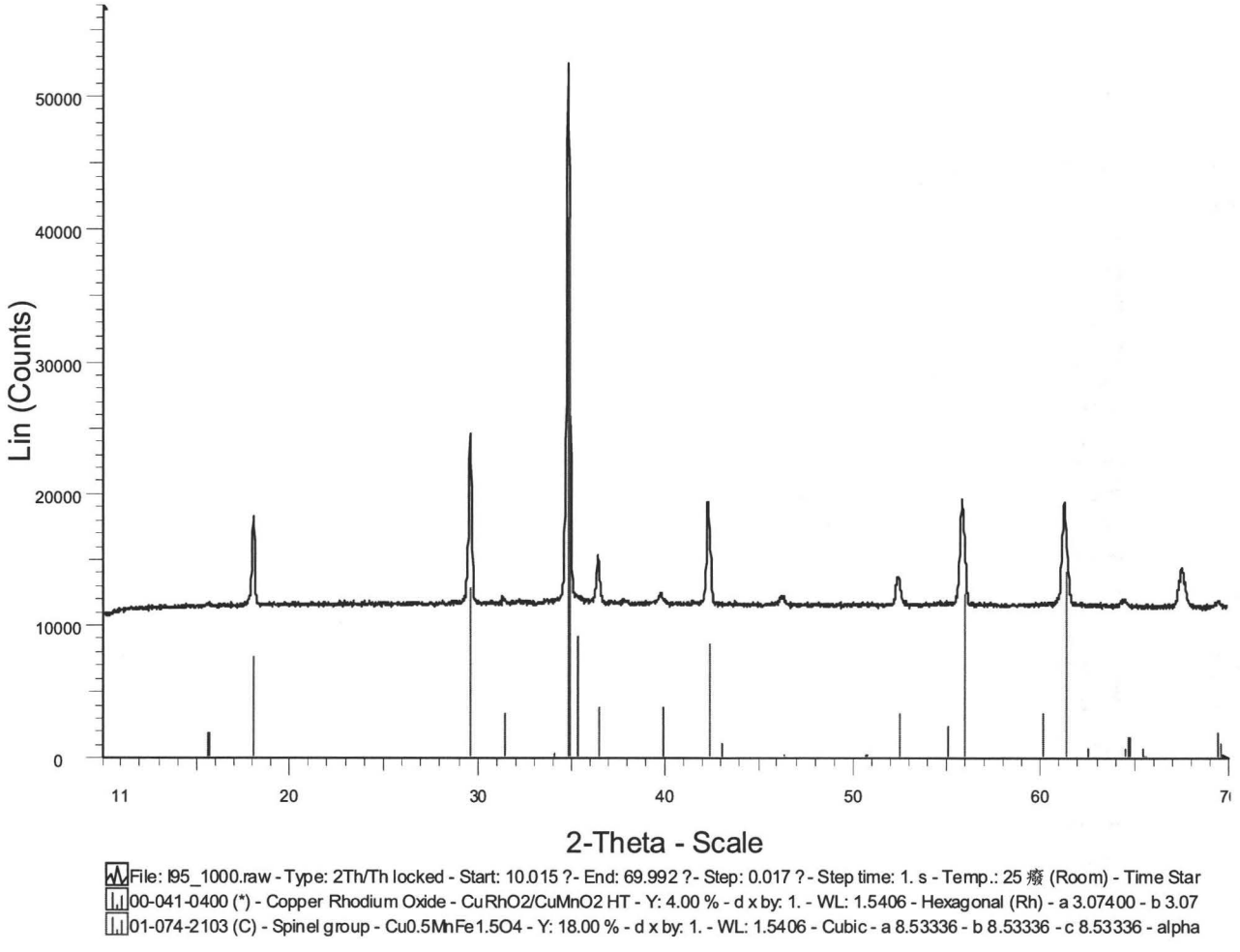

Figure 45 X-ray diffraction pattern of $Cu_{1.4}Mn_{1.6}O_4$ at 1000°C

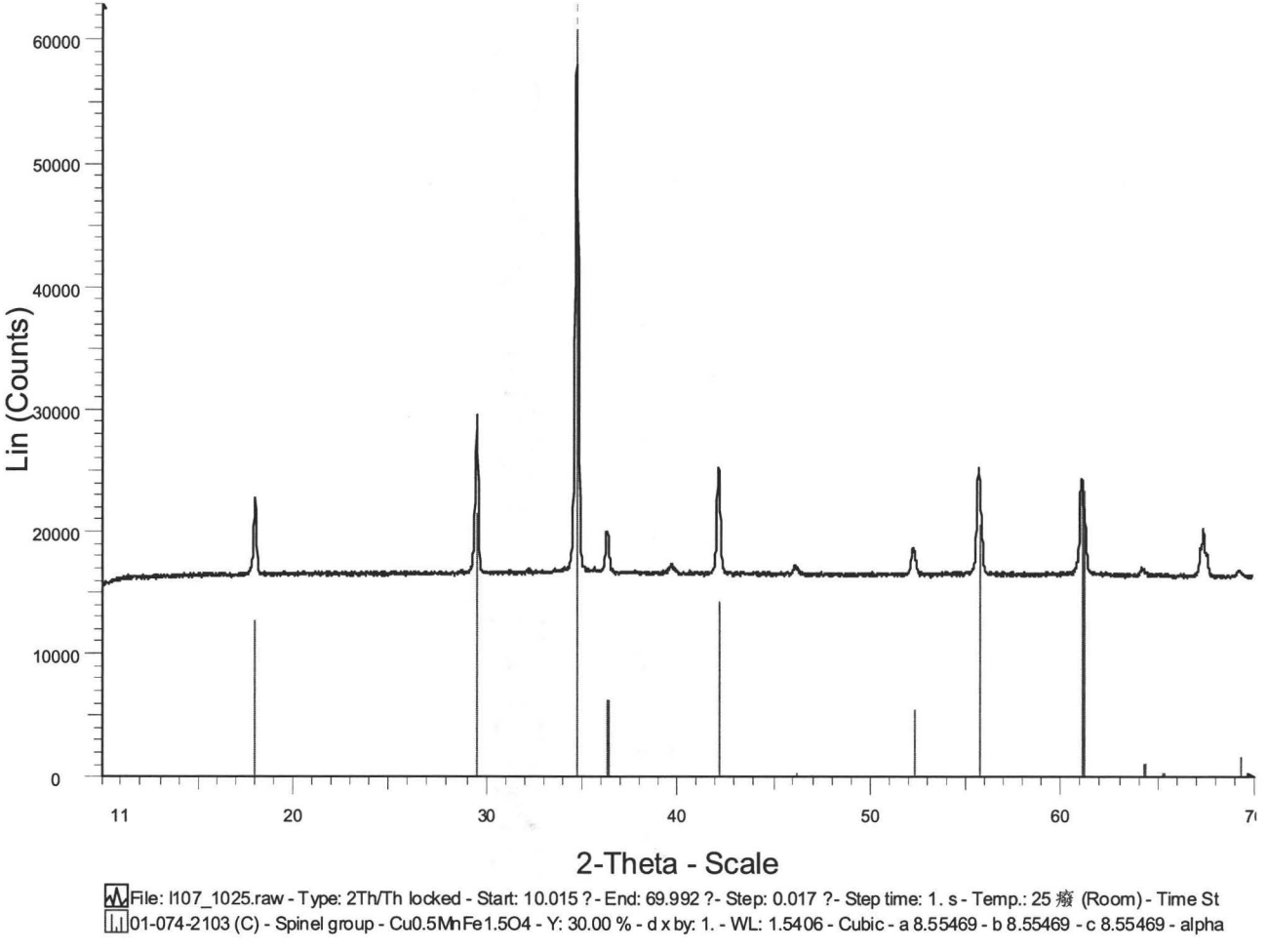

Figure 46 X-ray diffraction pattern of $Cu_{1.4}Mn_{1.6}O_4$ at 1025°C

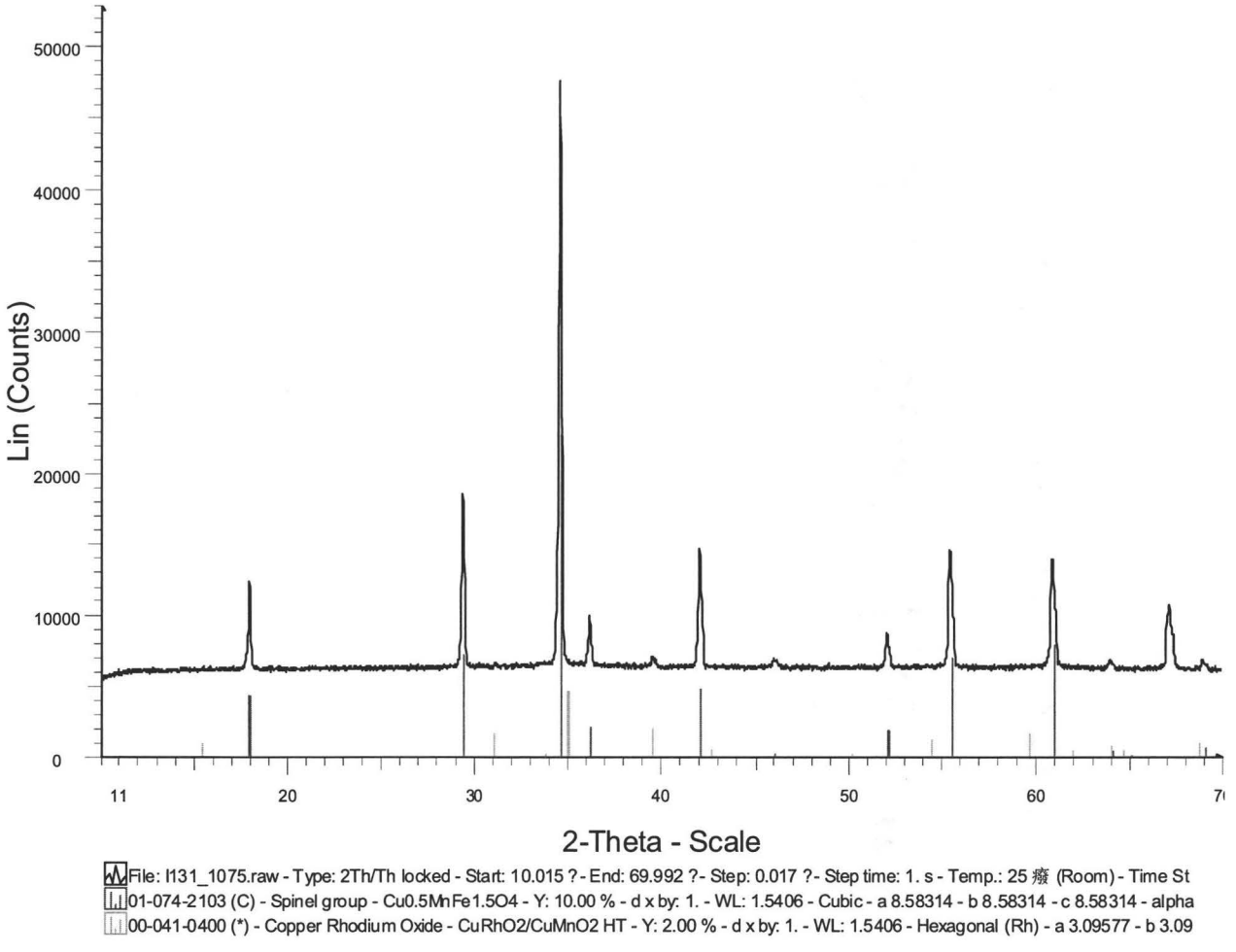

Figure 47 X-ray diffraction pattern of $Cu_{1.4}Mn_{1.6}O_4$ at 1075°C

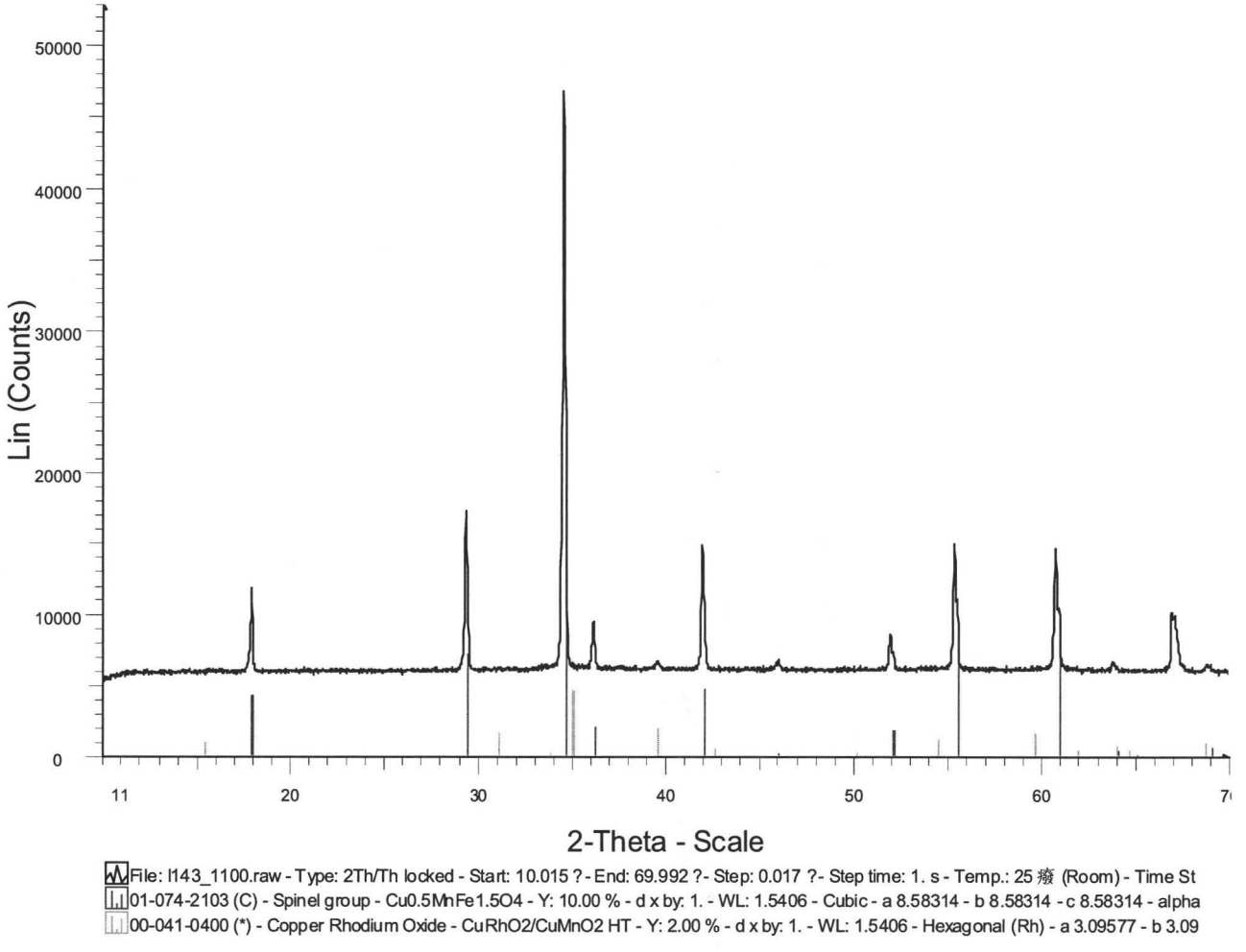

Figure 48 X-ray diffraction pattern of $Cu_{1.4}Mn_{1.6}O_4$ at 1100°C

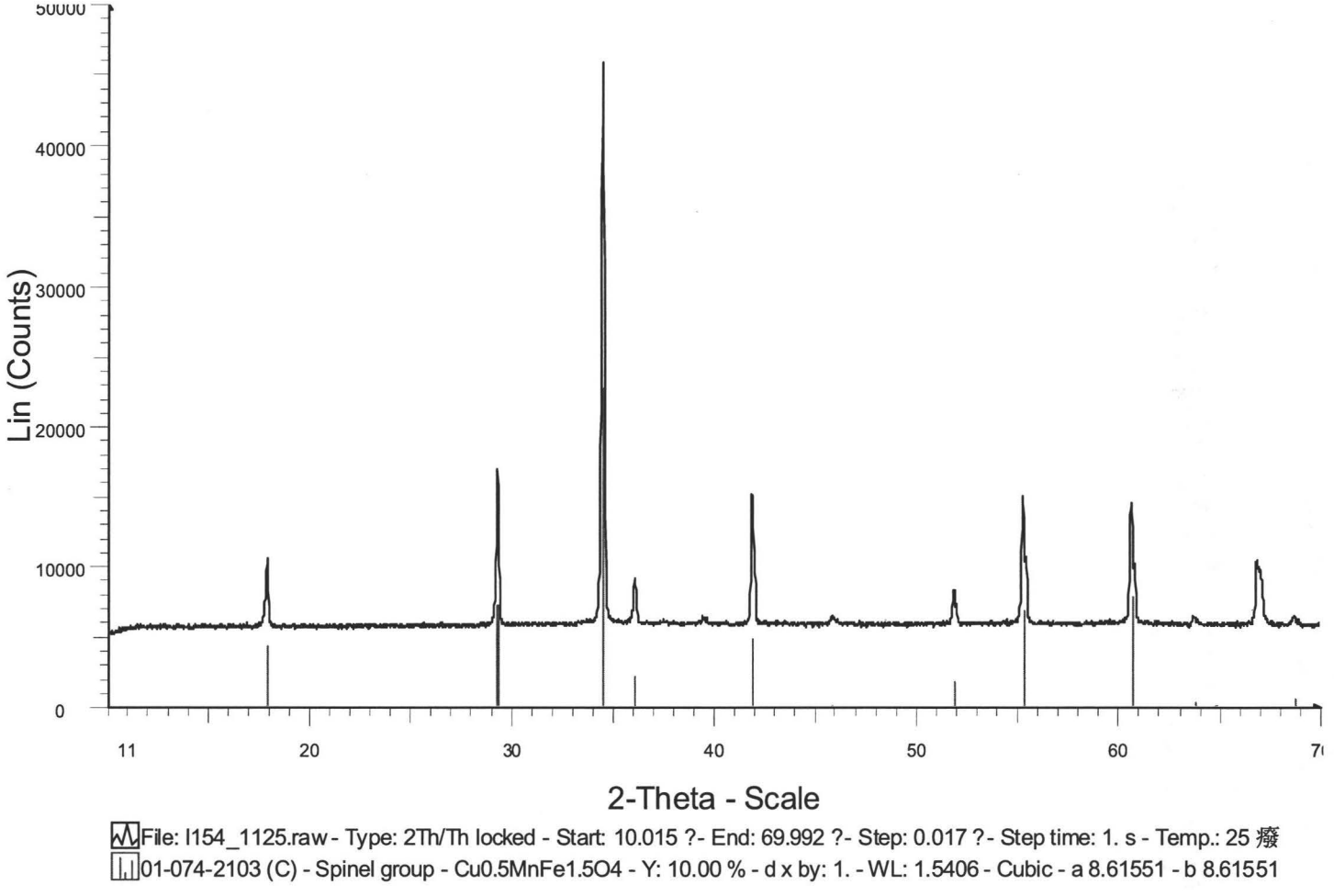

Figure 49 X-ray diffraction pattern of $Cu_{1.4}Mn_{1.6}O_4$ at 1125°C

Appendix 2

In-Situ Neutron Data Refinement

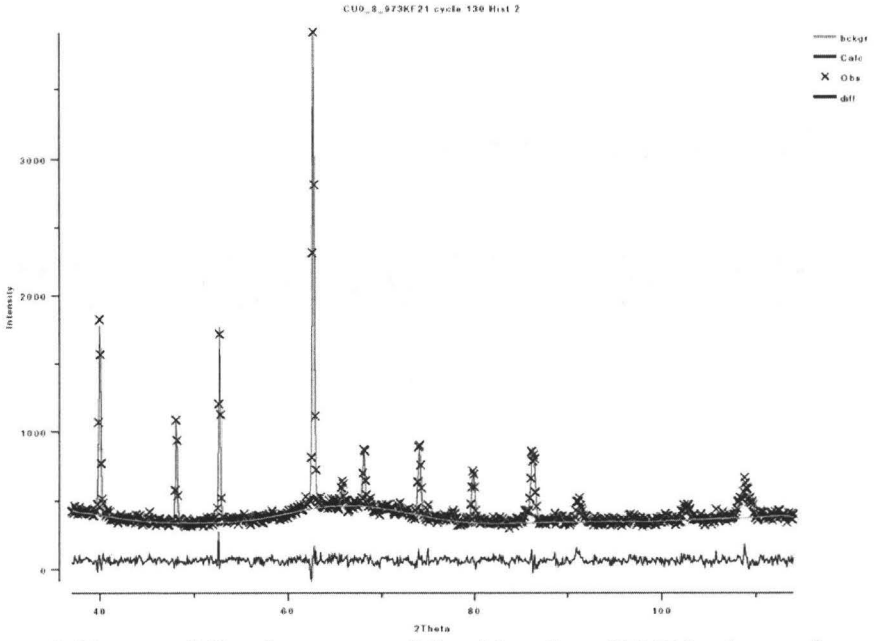

Figure 1 Neutron diffraction pattern of $Cu_{0.8}Mn_{2.2}O_4$ at 973 K in air superimposed with the calculated and difference spectra

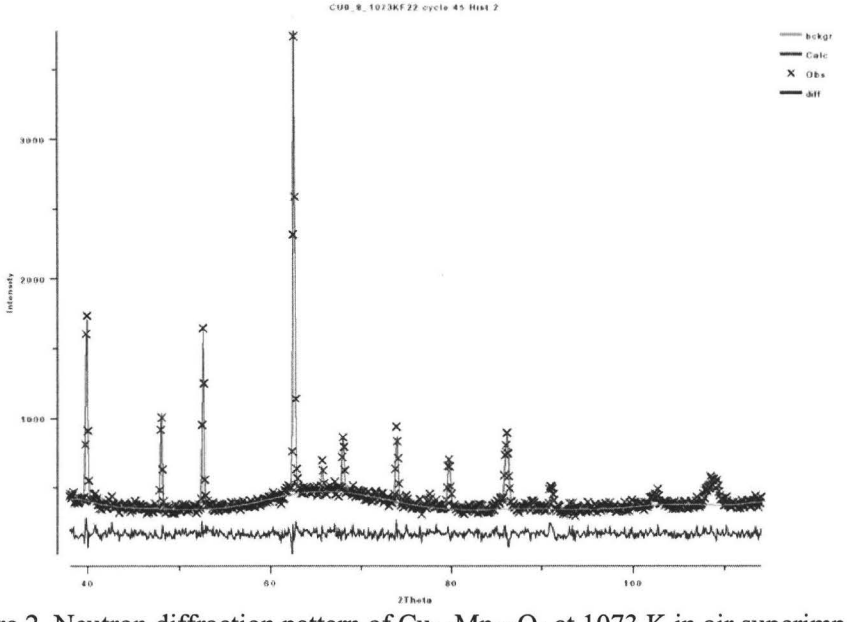

Figure 2 Neutron diffraction pattern of $Cu_{0.8}Mn_{2.2}O_4$ at 1073 K in air superimposed with the calculated and difference spectra

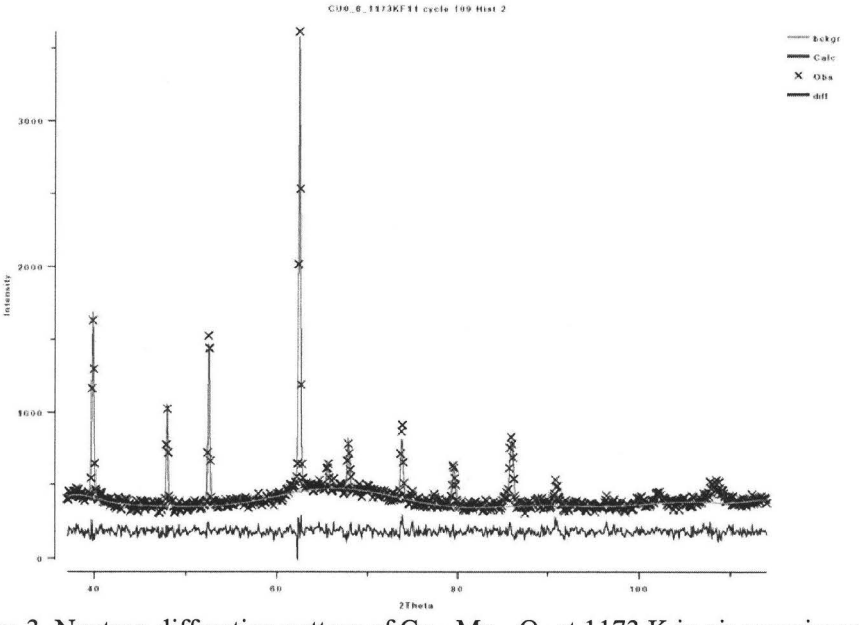

Figure 3 Neutron diffraction pattern of $Cu_{0.8}Mn_{2.2}O_4$ at 1173 K in air superimposed with the calculated and difference spectra

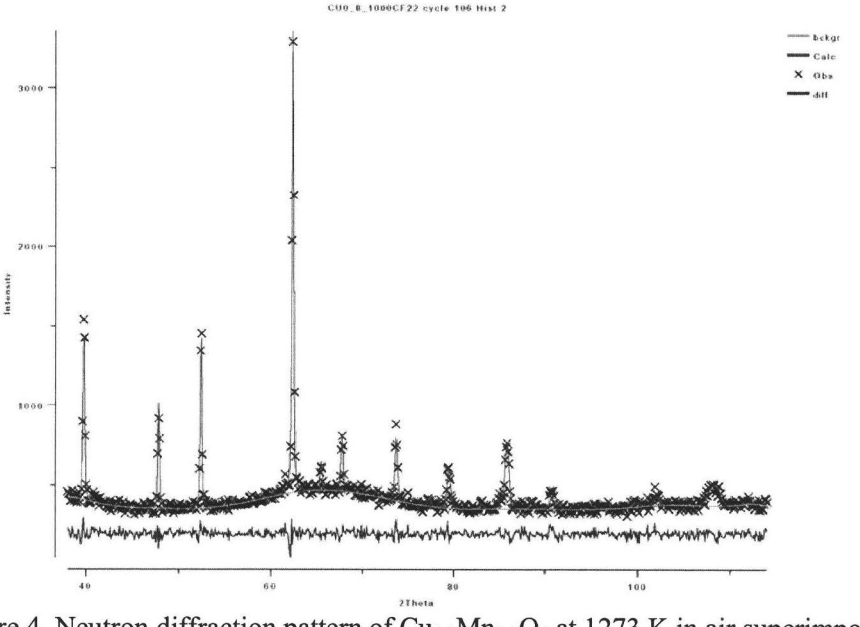

Figure 4 Neutron diffraction pattern of $Cu_{0.8}Mn_{2.2}O_4$ at 1273 K in air superimposed with the calculated and difference spectra

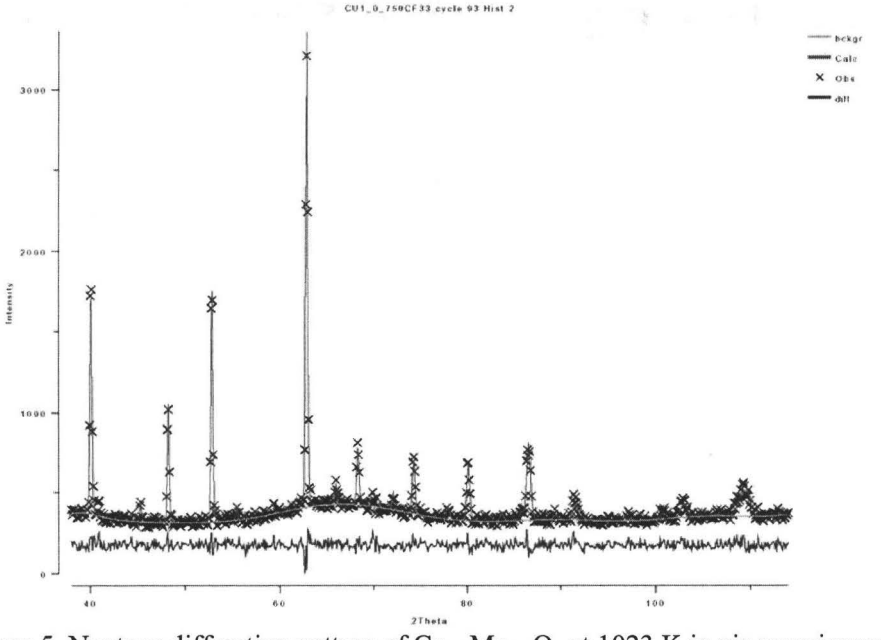

Figure 5 Neutron diffraction pattern of $Cu_{1.0}Mn_{2.0}O_4$ at 1023 K in air superimposed with the calculated and difference spectra

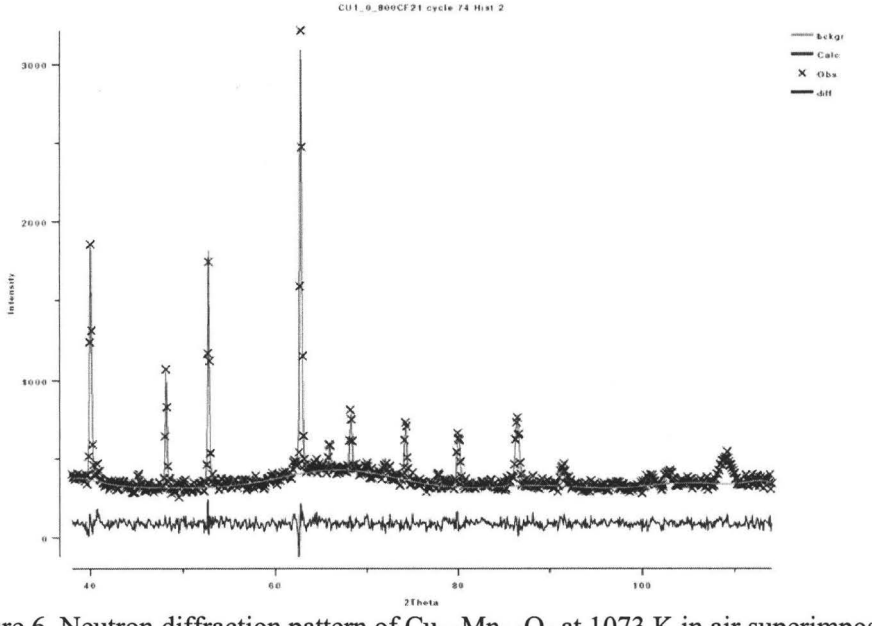

Figure 6 Neutron diffraction pattern of $Cu_{1.0}Mn_{2.0}O_4$ at 1073 K in air superimposed with the calculated and difference spectra

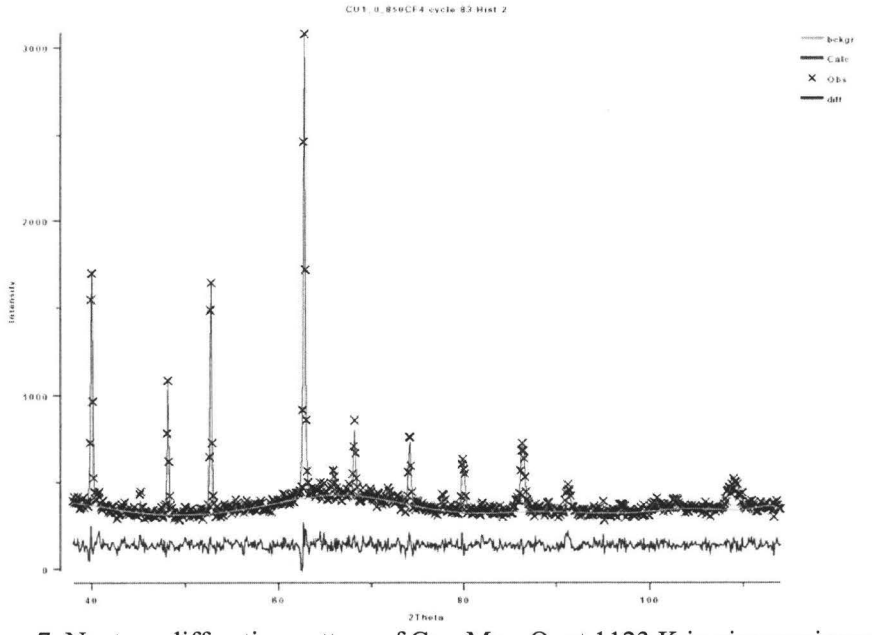

Figure 7 Neutron diffraction pattern of $Cu_{1.0}Mn_{2.0}O_4$ at 1123 K in air superimposed with the calculated and difference spectra

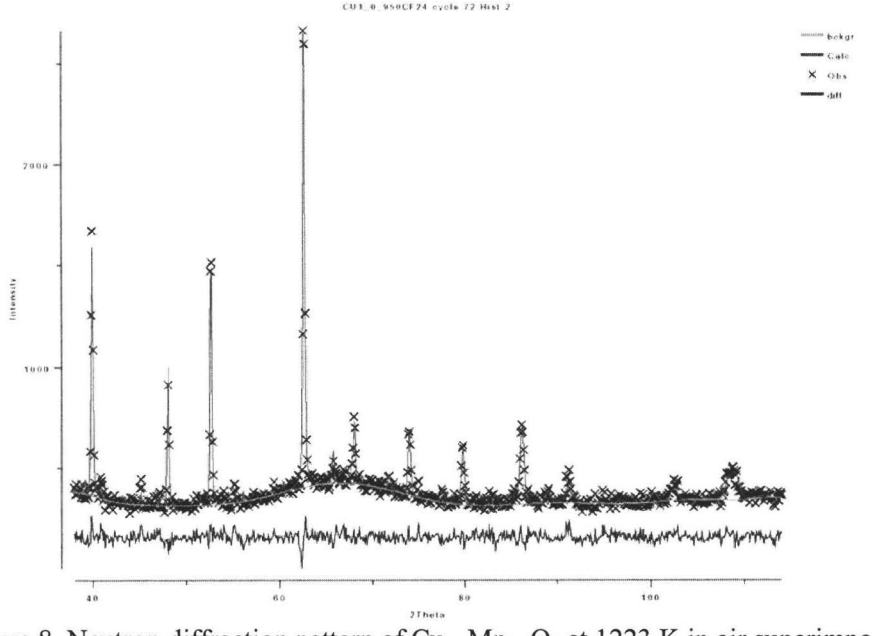

Figure 8 Neutron diffraction pattern of $Cu_{1.0}Mn_{2.0}O_4$ at 1223 K in air superimposed with the calculated and difference spectra

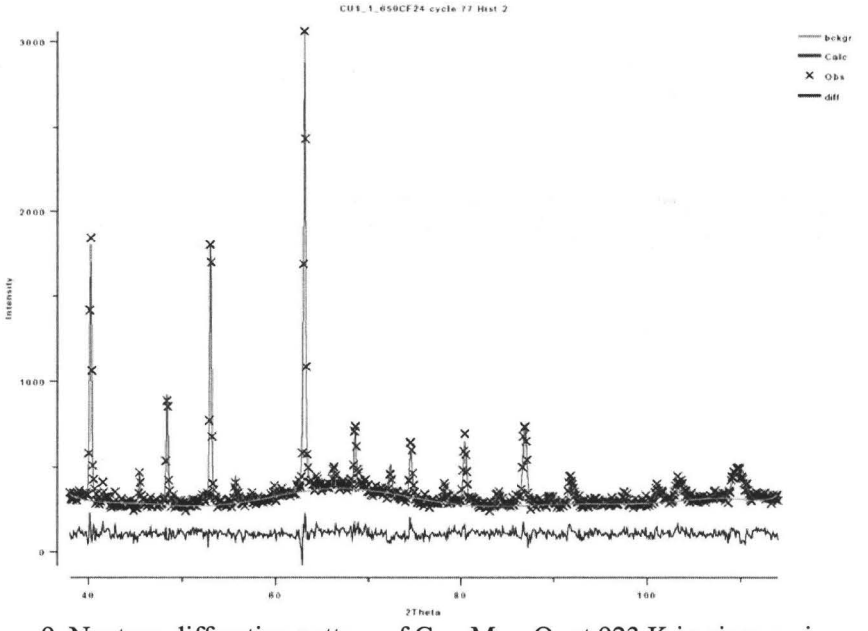

Figure 9 Neutron diffraction pattern of $Cu_{1.1}Mn_{1.9}O_4$ at 923 K in air superimposed with the calculated and difference spectra

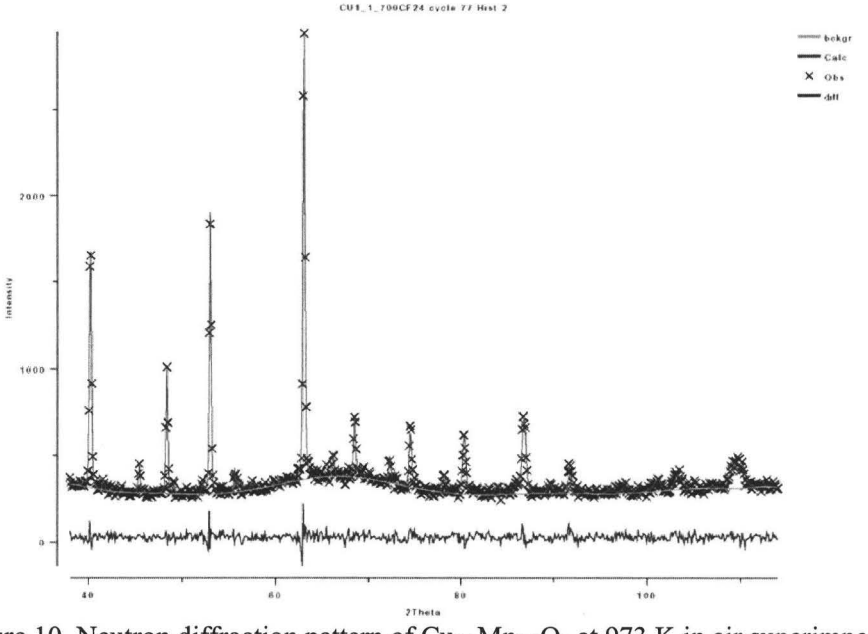

Figure 10 Neutron diffraction pattern of $Cu_{1.1}Mn_{1.9}O_4$ at 973 K in air superimposed with the calculated and difference spectra

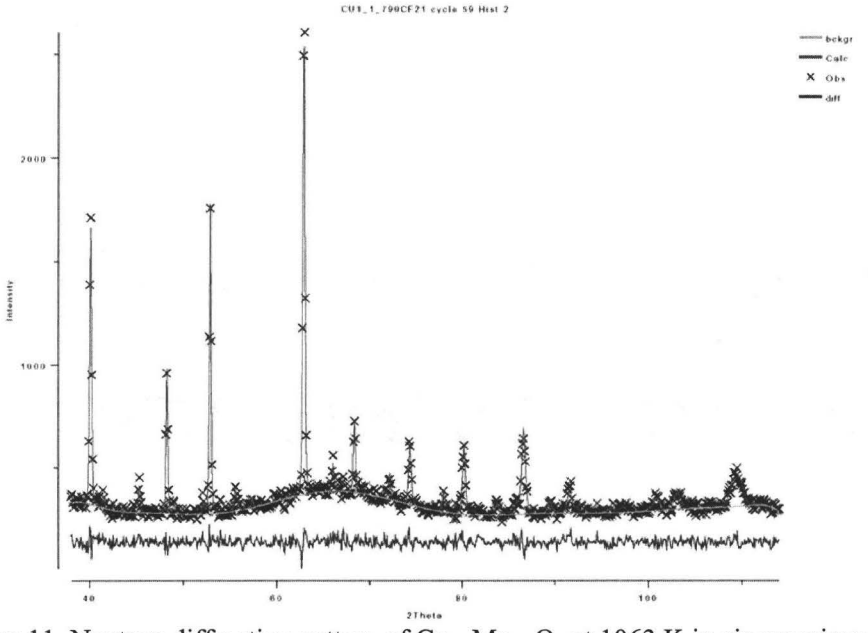

Figure 11 Neutron diffraction pattern of $Cu_{1.1}Mn_{1.9}O_4$ at 1063 K in air superimposed with the calculated and difference spectra

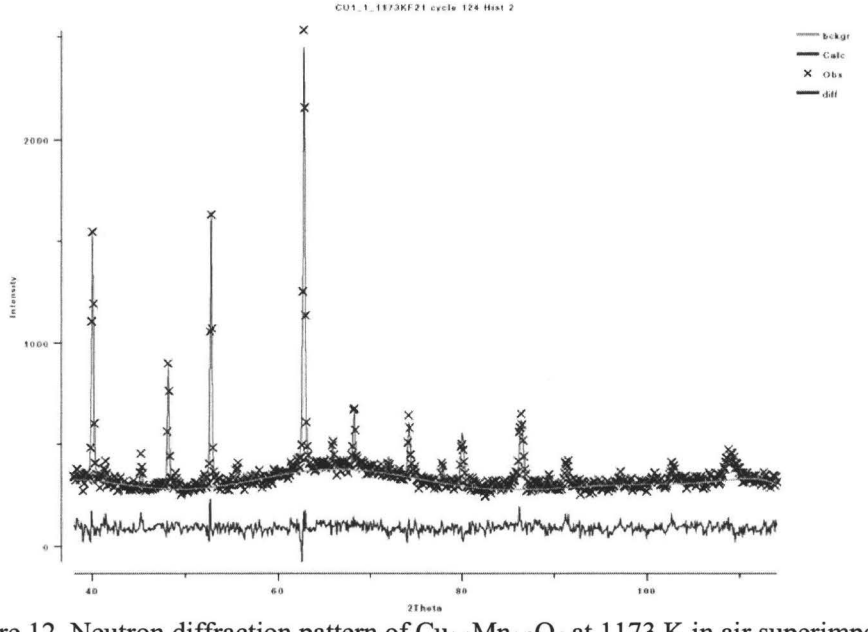

Figure 12 Neutron diffraction pattern of $Cu_{1.1}Mn_{1.9}O_4$ at 1173 K in air superimposed with the calculated and difference spectra

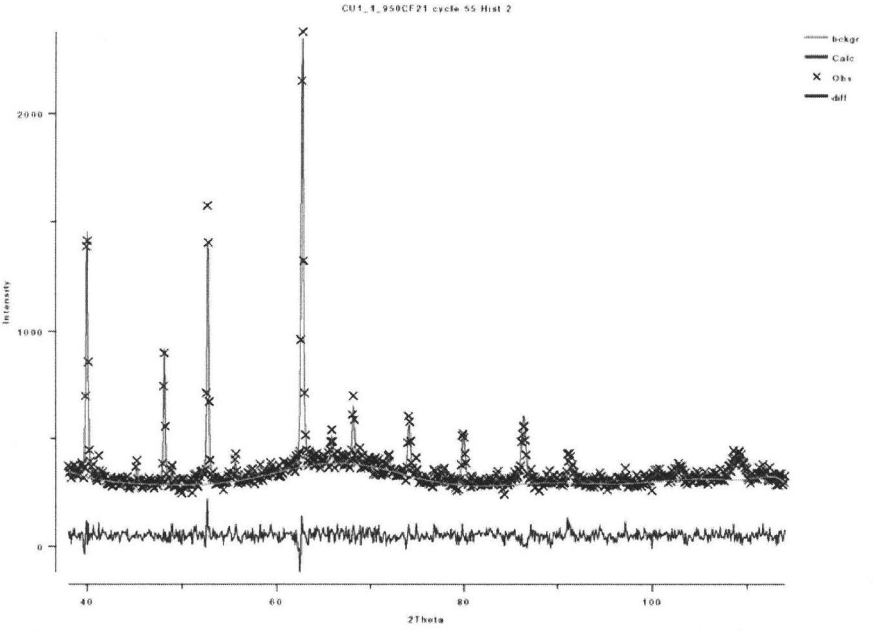

Figure 13 Neutron diffraction pattern of $Cu_{1.1}Mn_{1.9}O_4$ at 1223 K in air superimposed with the calculated and difference spectra

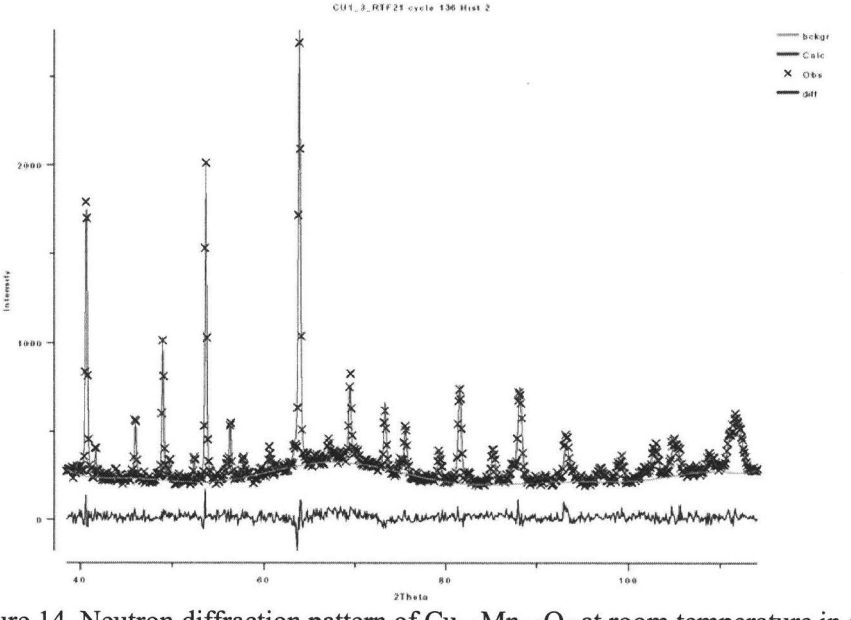

Figure 14 Neutron diffraction pattern of $Cu_{1.3}Mn_{1.7}O_4$ at room temperature in air superimposed with the calculated and difference spectra

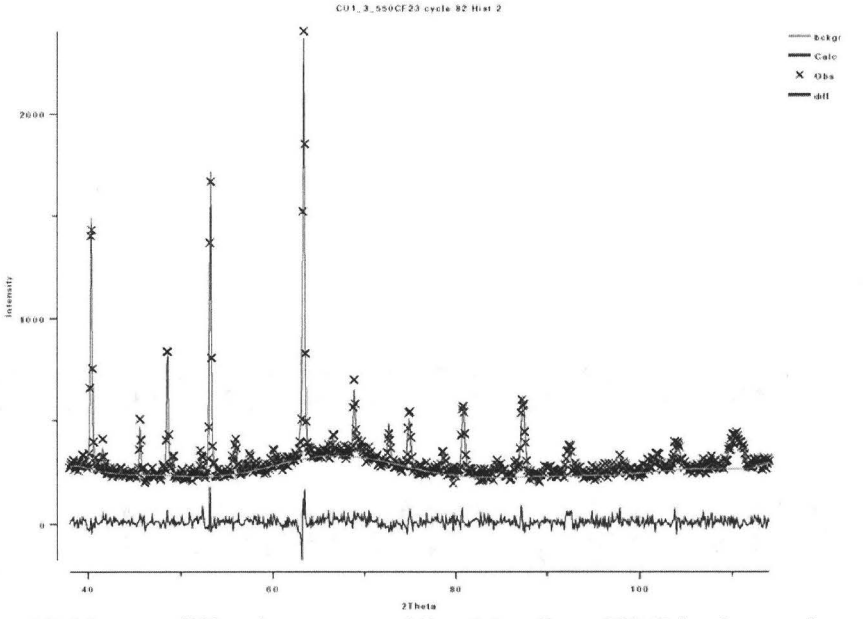

Figure 15 Neutron diffraction pattern of $Cu_{1.3}Mn_{1.7}O_4$ at 823 K in air superimposed with the calculated and difference spectra

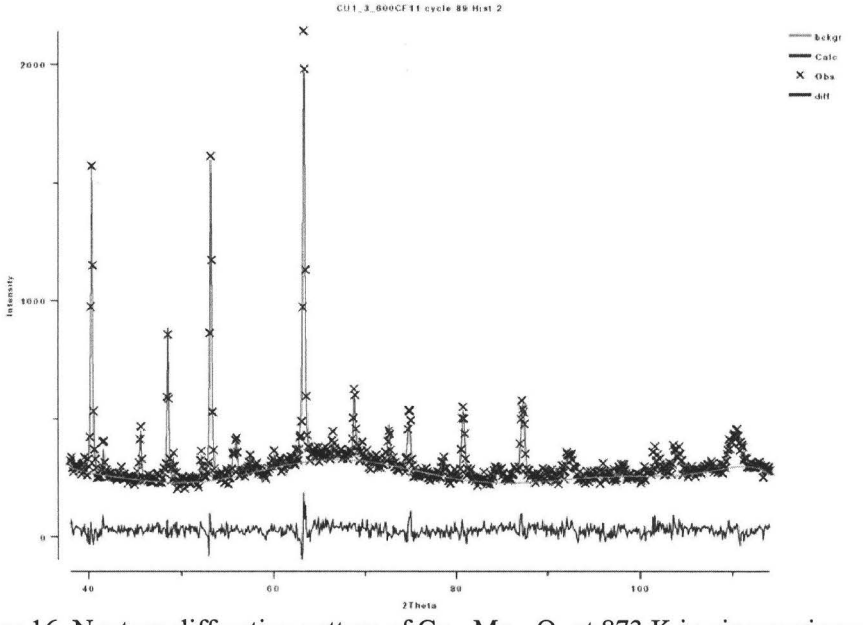

Figure 16 Neutron diffraction pattern of $Cu_{1.3}Mn_{1.7}O_4$ at 873 K in air superimposed with the calculated and difference spectra

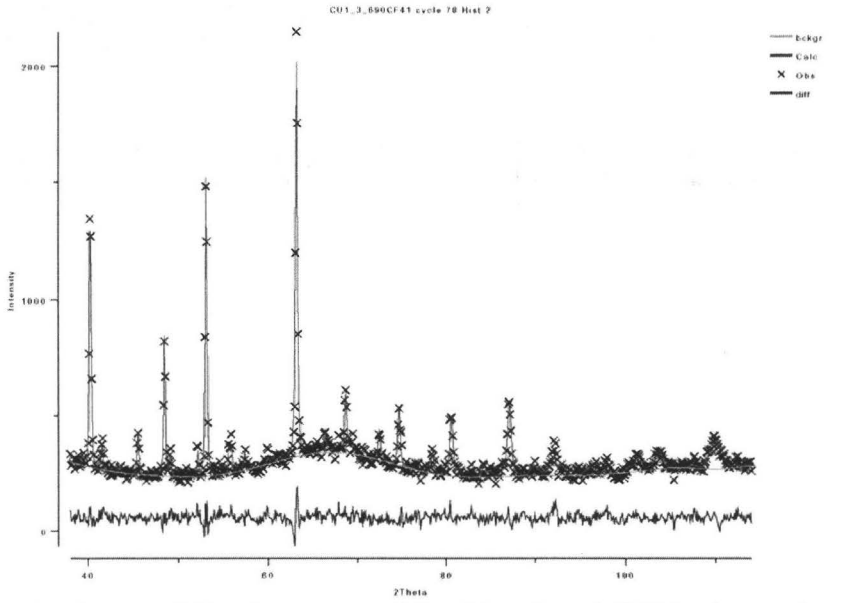

Figure 17 Neutron diffraction pattern of $Cu_{1.3}Mn_{1.7}O_4$ at 963 K in air superimposed with the calculated and difference spectra

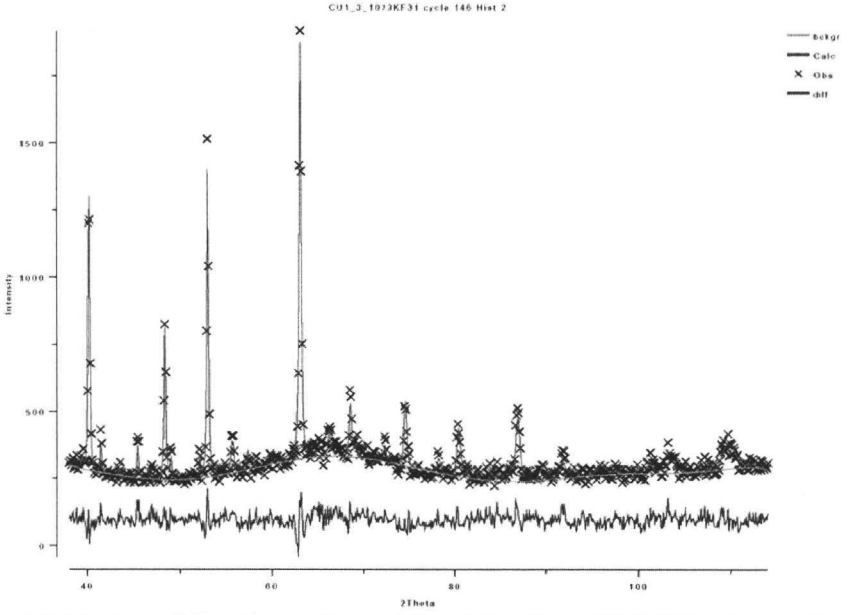

Figure 18 Neutron diffraction pattern of $Cu_{1.3}Mn_{1.7}O_4$ at 1073 K in air superimposed with the calculated and difference spectra

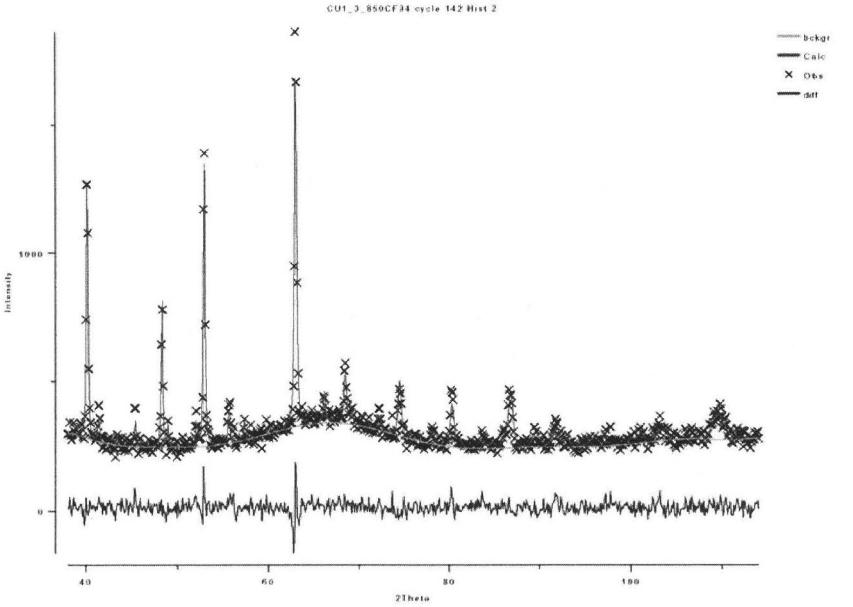

Figure 19 Neutron diffraction pattern of $Cu_{1.3}Mn_{1.7}O_4$ at 1123 K in air superimposed with the calculated and difference spectra